Applied Mathematical Sciences

Georges-Henri Cottet
Emmanuel Maitre
Thomas Milcent

# Level Set Methods for Fluid-Structure Interaction

Springer

# Applied Mathematical Sciences



Volume 210

The mathematization of all sciences, the fading of traditional scientific boundaries, the impact of computer technology, the growing importance of computer modeling and the necessity of scientific planning all create the need both in education and research for books that are introductory to and abreast of these developments. The purpose of this series is to provide such books, suitable for the user of mathematics, the mathematician interested in applications, and the student scientist. In particular, this series will provide an outlet for topics of immediate interest because of the novelty of its treatment of an application or of mathematics being applied or lying close to applications. These books should be accessible to readers versed in mathematics or science and engineering, and will feature a lively tutorial style, a focus on topics of current interest, and present clear exposition of broad appeal. A compliment to the Applied Mathematical Sciences series is the Texts in Applied Mathematics series, which publishes textbooks suitable for advanced undergraduate and beginning graduate courses.

Georges-Henri Cottet • Emmanuel Maitre •
Thomas Milcent

# Level Set Methods for Fluid-Structure Interaction

Springer

Georges-Henri Cottet
Laboratoire Jean Kuntzmann
Université Grenoble Alpes, CNRS,
Grenoble-INP*
Grenoble, France

Emmanuel Maitre
Laboratoire Jean Kuntzmann
Université Grenoble Alpes, CNRS,
Grenoble-INP*
Grenoble, France

Thomas Milcent
Institut de Mécanique de Bordeaux
Arts et Métiers, Université Bordeaux,
CNRS
Bordeaux, France

This work was supported by Agence Nationale de la Recherche (ANR-19-CE46-0001, ANR-17-CE23-0024)

ISSN 0066-5452 ISSN 2196-968X (electronic)
Applied Mathematical Sciences
ISBN 978-3-031-08658-8 ISBN 978-3-031-08659-5 (eBook)
https://doi.org/10.1007/978-3-031-08659-5

Mathematics Subject Classification: 35Q30, 65M22, 74F10, 76D05



This Springer imprint is published by the registered company Springer Nature Switzerland AG
The registered company address is: Gewerbestrasse 11, 6330 Cham, Switzerland

# Foreword

Fluid-structure interaction problems occur in many fields of engineering: mechanics of immersed structures, aeroelasticity, biomechanics, lubrication effects in pipe flows, particle transport, sediment transport, and erosion of shorelines.

From a mathematical and numerical point of view, these problems represent a real challenge insofar as fluids and solids are naturally described by models of a different nature: Eulerian models for fluids and Lagrangian models for solids. These models require adapted discretization methods. The traditional approach to deal with these problems, known as ALE (for Arbitrary Lagrangian Eulerian), is based on these various modelizations. It uses a Eulerian discretization of fluids and a Lagrangian discretization of solids, with adapted meshes and suitable coupling conditions to translate the continuity of velocity and forces at the interfaces.

In the last 15 years, alternatives to these methods have appeared, based on Eulerian models of the two types of media. Fluids and solids are considered as a single system with constitutive laws that vary in space and time. The interest of these methods is the possibility that they offer to use a single numerical model and a single mesh for the whole system, with the drawback of giving a less detailed description of the interface and the conditions that we impose on it.

The immersed boundary methods (IBM in short) proposed by Peskin in 1972 can be seen as a class of intermediate methods between the two approaches mentioned above. The solids are immersed in the fluid without the need to fit a fluid mesh on them, but are tracked in a Lagrangian fashion using markers advected by the fluid.

For a fairly complete review of these different methods, we refer to the recent book by T. Richter [119] for the ALE and Eulerian methods, and to the review article [92] for the immersed boundary methods.

The purpose of this book is to describe Eulerian models of the fluid-structure interaction based on Level Set functions. Level Set methods are well known since the works of Sethian [125] and Osher [112] in image processing and the computation of multi-phase flows. More recently, they have also been used with success in the context of shape optimization [4]. These methods allow implicit monitoring of Lagrangian interfaces (with physical advection fields for multiphase flows or virtual

flows in image processing or shape optimization) by solving partial differential transport equations.

For 10 years or so, a certain number of works, in particular by the authors of this book, have made it possible to use them to model the forces resulting from deformations of elastic solids or to treat contacts between objects and leading to numerical tools in fluid-structure interaction in a Eulerian framework. This book reviews these different works. Its objective is to describe the models. It does not focus on the numerical discretization methods, except for what concerns the explicit or implicit time discretizations which impact the stability of the models. In fact, one of the advantages of Eulerian methods is that they allow the use of conventional methods in fluid dynamics (finite differences, finite volumes, etc.) without involving questions specific to the coupling with solid structures. In this book, the spatial discretization techniques used are only briefly mentioned to describe numerical illustrations.

The plan of the book is as follows. In Chap. 1, we review the techniques for interface capturing or interface tracking. We show in particular how to use Level Set functions to translate surface forces into bulk forces, which is obviously a central point in these methods, and we specify how these methods allow in dimension two and three to account for curvatures. We develop the examples of Level Set methods mentioned previously in image processing and for multiphase flows, and we address the questions of stability in Level Set methods in the example of the treatment of surface tension terms, questions which will be taken up in the Chap. 3. Chapter 2 complements the reminders of Chap. 1 by notions of differential calculus on the trajectories in the Lagrangian and Eulerian descriptions. The conservation laws in these descriptions are also recalled.

Chapter 3 deals with the first example of fluid-structure interaction, that of an elastic membrane interacting with a fluid, first in the case of a membrane reacting to the variation of area then in the general case of a membrane also reacting to shear. It also evokes the case of elastic curves immersed in a space of dimension three. Finally, this chapter contains an example of code written in FreeFEM++ to allow the reader to experience these methods for himself.

Chapter 4 generalizes the Level Set approach to arbitrary elastic bodies, with a distinction between the cases of completely compressible or incompressible fluid-structure media.

Chapter 5 deals with the case of rigid solids, or solids deformable under the action of prescribed external forces. In these cases, the fluid-structure interaction is treated by the penalization method. Chapter 6 is concerned with the treatment by Level Set methods of contacts between objects, whether these objects are elastic or rigid. In particular, we describe a fast algorithm for processing multiple contacts. Finally, an appendix details certain technical elements of differential calculus and gives the demonstration of certain results used in the book. It also gives some basic tools concerning classical finite-difference for the resolution of transport equations.

Chapters 3–6 are largely independent of each other. Chapters 2 and 4 contain the elements of continuum mechanics (covering solids and fluids) necessary for the understanding of the book so as to make it accessible to students of Master of Numerical Analysis.

# Contents

# Chapter 1
# Level Set Methods and Lagrangian Interfaces


Throughout this chapter we are interested in following, in a given fluid, interfaces consisting of curves in $\mathbb{R}^2$ or surfaces in $\mathbb{R}^3$. We assume that $u$ is a $C^1$ vector field. To simplify the discussion, we will assume in this chapter, unless otherwise specified, that this field is defined in a bounded smooth domain $\Omega$ and vanishes on its boundary $\partial\Omega$, so that $\Omega$ is invariant under the action of the vector field. More precisely, we will make the following hypothesis

$$(H) \qquad u \in \mathcal{C}^1(\overline{\Omega} \times [0, T]) \text{ and } u = 0 \text{ on } \partial\Omega \times [0, T]$$

where $[0, T]$ is a fixed time interval.

Throughout the rest of this book we will denote the partial derivatives of the functions of several variables by an index of the corresponding variable, as in $\partial_t$.

For $\xi \in \Omega$ and $s \in ]0, T]$, we denote by $\tau \to X(\tau; \xi, s)$ the solution of the differential system $\partial_\tau X = \partial X/\partial\tau = u(X, \tau)$ provided with the initial condition $X(s) = \xi$. When there is no ambiguity on the initial time, we will use the notation $X(\tau, \xi)$. For an in-depth review of this notion of trajectory, we refer to the next chapter.

## 1.1 Interface Tracking or Interface Capturing

A natural way to monitor an interface is to write a parameterization that follows the speed of the interface. A Lagrangian interface, defined at time $t$, $\Gamma_t$, can be described by a parametrization

$$\theta \to \gamma(t, \theta)$$



G.-H. Cottet et al., *Level Set Methods for Fluid-Structure Interaction*, Applied Mathematical Sciences 210, https://doi.org/10.1007/978-3-031-08659-5_1

with

$$\partial_t \gamma = u(\gamma, t)$$

In two dimensions, $\theta$ is a real number and in three dimensions, $\theta = (\theta_1, \theta_2)$ is a vector in $\mathbb{R}^2$. Notable geometrical quantities related to the interface are, in 2D, its normal $n$ and its tangent $\mathbf{t}$:

$$\mathbf{t} = \frac{\partial_\theta \gamma}{|\partial_\theta \gamma|} \qquad n = \mathbf{t}^\perp, \tag{1.1}$$

and, in 3D, the normal vector

$$n = \frac{\partial_{\theta_1} \gamma \times \partial_{\theta_2} \gamma}{|\partial_{\theta_1} \gamma \times \partial_{\theta_2} \gamma|}$$

and the tangent plane defined by its orthogonal direction. These directions correspond to an orientation of the interface along increasing values of $\theta$ in 2D, or $\theta_1$ and $\theta_2$ in 3D.

This parameterization also gives access to the stretching of the interface during its movement. In 2D the stretching relative to the initial position of the curve at a point of the curve with parameter $\theta$ is given by

$$\mathcal{S}(t, \theta) = \frac{|\partial_\theta \gamma(t, \theta)|}{|\partial_\theta \gamma(0, \theta)|}.$$

In 3D the stretching on the surface relative to the variation of area is given by

$$\mathcal{S}(t, \theta) = \frac{|\partial_{\theta_1} \gamma(t, \theta) \times \partial_{\theta_2} \gamma(t, \theta)|}{|\partial_{\theta_1} \gamma(0, \theta) \times \partial_{\theta_2} \gamma(0, \theta)|}.$$

These quantities are involved in the curvilinear or surface integrals using the parametrization $\gamma(t, \theta)$.

From a numerical point of view, following these interfaces makes use of a finite number of markers of material points $\xi = \gamma(0, \theta)$ which correspond to discrete values of $\theta$. These markers move by the velocity field at the instant $t$ into $X(t, \xi) = \gamma(t, \theta)$. The reconstruction of regular interfaces from these markers can be done by various types of interpolation. The geometric properties of the interfaces can be calculated either by discretization on the markers of the above formulas, as illustrated in Fig. 1.1, or by using these interpolations.

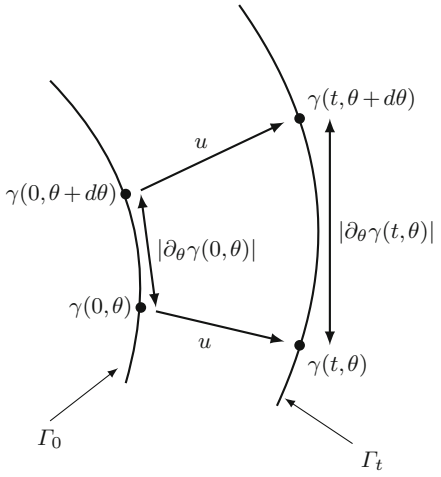


**Fig. 1.1** Transport and stretching of a Lagrangian interface

An alternative to the Lagrangian tracking of interfaces consists in considering these interfaces as level sets of a function, which by abuse of language we will call Level Set function. The justification of this implicit description of Lagrangian interfaces is given by the following result

**Proposition 1.1** *Let $\varphi_0$ be a continuous function defined on $\Omega$ and $\Gamma_0 = \{x \in \Omega, \varphi_0(x) = 0\}$. If $\varphi$ is solution to the transport equation*

$$\begin{cases} \partial_t \varphi + u \cdot \nabla \varphi = 0 & \text{on } \Omega \times ]0, T], \\ \varphi = \varphi_0 & \text{on } \Omega \times \{0\} \end{cases} \tag{1.2}$$

*we have*

$$\partial_t(\varphi(X(t;\xi,s),t) = 0 \text{ for all } \xi \in \Omega \text{ and } s \in [0,T]. \tag{1.3}$$

$$\Gamma_t = X(t;\Gamma_0,0) = \{x \in \Omega\ ,\ \varphi(x,t) = 0\} \text{ for all } t \in [0,T]. \tag{1.4}$$

***Proof*** Equation (1.3) follows directly, by derivation of the composition of functions, from (1.2) and the definition of characteristics. Equation (1.4) results from taking $s = 0$ and $\xi \in \Gamma_0$. □

Methods based on a description of Lagrangian interfaces by Level Set functions are called interface capturing methods, as opposed to the interface tracking methods described earlier.

## 1.2 Level Set Methods and Geometry of Surfaces

In this section, we develop how the notions of geometry of curves and surfaces can be expressed from implicit functions. We show in particular, starting from their parametric definition, how mean and Gaussian curvature can be expressed using Level Set functions.

Let us start by specifying the classical notions and regularity results of implicit surfaces.

**Definition 1.2** A hypersurface $S \subset \mathbb{R}^d$ is said of class $\mathcal{C}^k$ if any point of $S$ has a neighborhood $U$ such as the set $S \cap U$ can be represented by an equation of the form $x_i = f(x_1, \ldots, x_{i-1}, x_{i+1}, \ldots, x_d)$, where $f$ is of class $\mathcal{C}^k$.

The following proposition gives the regularity of the zero-level set of a function:

**Proposition 1.3** *Given an open set $\Omega$ in $\mathbb{R}^d$, let $\varphi : \Omega \to \mathbb{R}$, continuous on $\Omega$, and of class $C^k$ on an open set $U \subset \Omega$. We assume that $|\nabla\varphi|(x) > 0$ for all $x \in U$, and that $S = \{x \in \Omega, \varphi(x) = 0\}$ is a non-empty set included in $U$. Then $S$ is of class $\mathcal{C}^k$.*

For the proof of this result we refer the reader to the one given in [74], page 355.

**Proposition 1.4** *Let $S \subset \mathbb{R}^d$ a closed hypersurface of class $\mathcal{C}^k$, $k \geq 2$, and $d$ the signed distance (negative inside, for example) to $S$. Then there exists a neighborhood $U$ of $S$ such that $d$ is in $\mathcal{C}^k(U)$, satisfies $|\nabla d| = 1$ in $U$, and the projection $P_S(x)$ of $x \in U$ on $S$ is given by $P_S(x) = x - d(x)\nabla d(x)$. We therefore have for all $x \in U$, $d(x - d(x)\nabla d(x)) = 0$.*

For this type of result one can consult the publications of Delfour and Zolésio (see [47] and references therein) on the intrinsic geometry of surfaces. Intuitively, the distance function to a hypersurface, in a neighborhood thereof, has its gradient at a point directed towards its projection $P_S(x)$ on $S$. By moving in the direction opposite to this gradient, by definition of the distance, this distance decreases in equal amount of the displacement, which precisely means that its slope is 1. The distance ends up being canceled out when reaching the projection, which therefore must be equal to $P_S(x) = x - d(x)\nabla d(x)$, hence the last formula.

In the rest of this book, we will assume that a Level Set function is regular and has a non vanishing gradient everywhere in a neighborhood of its level set 0.

Let us now look at the particular case of a regular surface $S \subset \mathbb{R}^3$. Let $(\theta_1, \theta_2) \mapsto \gamma(\theta_1, \theta_2) \in \mathbb{R}^3$ a smooth parametrization of $S$. The vectors $\partial_{\theta_1}\gamma$ and $\partial_{\theta_2}\gamma$ define a basis of the tangent plane to the surface. We introduce the first fundamental form,

of general term

$$g_{ij} = \partial_{\theta_i}\gamma \cdot \partial_{\theta_j}\gamma. \tag{1.5}$$

This form, also called the metric of the surface, allows to calculate lengths, angles and areas on the surface. We also introduce the second fundamental form, of general term

$$h_{ij} = \partial^2_{\theta_i\theta_j}\gamma \cdot n \tag{1.6}$$

where

$$n = \frac{\partial_{\theta_1}\gamma \times \partial_{\theta_2}\gamma}{|\partial_{\theta_1}\gamma \times \partial_{\theta_2}\gamma|}$$

is the normal to the surface (orthogonal to the tangent plane). These two fundamental forms are $2 \times 2$ symmetric matrices. The curvature of a surface is intuitively related to the variation of the normal in the tangent plane and we can show that the matrix of the associated linear mapping, denoted $dn$, can be expressed using the two fundamental forms as

$$dn = [h_{ij}][g_{ij}]^{-1}. \tag{1.7}$$

The eigenvalues of this matrix are called the principal curvatures of the surface and we have the following definition:

**Definition 1.5** The mean curvature $H$ and the Gaussian curvature $G$ are defined by the formulas

$$H = \mathrm{Tr}(dn) \qquad , \qquad G = \det(dn).$$

We leave to the reader the proof that this definition does not depend on the chosen parameterization of the surface.

Let us now consider an implicit representation of this same surface $S \subset \mathbb{R}^3$. For a given smooth function $\varphi : \mathbb{R}^3 \to \mathbb{R}$, we consider $S = \{x \in \mathbb{R}^3 \ , \ \varphi(x) = 0\}$. In the parametric approach, we have access to the way in which the points of the surface are connected to each other through the parametrization, which yields a notion of metric. There is no similar notion in the implicit function approach because two points belonging to the surface are characterized by the fact that the function vanishes but there is no information about their proximity. However we will see that when we follow a surface over time it is possible to calculate its deformations with implicit functions. This property is the key point of the Eulerian formulation of elasticity and will be developed extensively in Chap. 3. Let us now look at some geometric quantities that can be calculated using an implicit representation of the surface. Note that the vector $\nabla\varphi$ is orthogonal to the level sets of $\varphi$ and therefore

we define the normal to the surface by

$$n(x) = \frac{\nabla\varphi}{|\nabla\varphi|}.$$

Since the curvature is defined by the variation of the normal along the surface, it seems natural that we can calculate this quantity using the second derivatives of the Level Set function. This statement is clarified and demonstrated in the following proposition:

**Proposition 1.6** *Let $S$ be a surface of $\mathbb{R}^3$ represented by the zero level of a Level Set function $\varphi$. The mean and Gaussian curvatures of $S$ are given by the formulas*

$$H = \mathrm{Tr}(\nabla_\Gamma n), \qquad G = \mathrm{Tr}(\mathrm{Cof}(\nabla_\Gamma n)),$$

*where $\nabla_\Gamma n = [\nabla n][\mathbb{I} - n \otimes n]$ with $n = \frac{\nabla\varphi}{|\nabla\varphi|}$.*

***Proof*** First note that $\nabla_\Gamma n(x)$ is a $3 \times 3$ matrix, defined for $x \in \mathbb{R}^3$, with a zero eigenvalue associated with the eigen-vector $n$, and $dn$ is a $2 \times 2$ matrix. By differentiating with respect to $\theta_i$ the equality $\varphi(\gamma(\theta_1, \theta_2)) = 0$ one gets

$$\frac{\nabla\varphi}{|\nabla\varphi|}(\gamma(\theta)) \cdot \partial^2_{\theta_j\theta_i}\gamma + \left(\nabla\left(\frac{\nabla\varphi}{|\nabla\varphi|}\right)(\gamma(\theta))\ \partial_{\theta_j}\gamma\right) \cdot \partial_{\theta_i}\gamma = 0.$$

Upon dividing by $|\nabla\varphi|$ (recall that this quantity is assumed to never vanish) then differentiating this equality one obtains

$$\frac{\nabla\varphi}{|\nabla\varphi|}(\gamma(\theta)) \cdot \partial^2_{\theta_j\theta_i}\gamma + \left(\nabla\left(\frac{\nabla\varphi}{|\nabla\varphi|}\right)(\gamma(\theta))\ \partial_{\theta_j}\gamma\right) \cdot \partial_{\theta_i}\gamma = 0.$$

We therefore have, according to definition (1.6), $h_{ij} = -\left([\nabla n](\gamma(\theta))\ \partial_{\theta_j}\gamma\right) \cdot \partial_{\theta_i}\gamma$. Let us now calculate the inverse of the first fundamental form (1.5)

$$[g_{ij}]^{-1} = \frac{1}{|\partial_{\theta_1}\gamma \times \partial_{\theta_2}\gamma|^2}\begin{pmatrix} |\partial_{\theta_2}\gamma|^2 & -\partial_{\theta_1}\gamma \cdot \partial_{\theta_2}\gamma \\ -\partial_{\theta_1}\gamma \cdot \partial_{\theta_2}\gamma & |\partial_{\theta_1}\gamma|^2 \end{pmatrix}.$$

If we denote by $\tau_i = \frac{\partial_{\theta_i}\gamma}{|\partial_{\theta_i}\gamma|}$ the unit tangent vectors associated with the parameterization of the surface, taking the trace of (1.7) yields

$$\mathrm{Tr}(dn) = \frac{([\nabla n]\tau_1) \cdot \tau_1 + ([\nabla n]\tau_2) \cdot \tau_2 - (\tau_1 \cdot \tau_2)(([\nabla n]\tau_1) \cdot \tau_2 + ([\nabla n]\tau_2) \cdot \tau_1)}{|\tau_1 \times \tau_2|^2}.$$

If we now consider the vector $\tilde{\tau_2} = \frac{\tau_2 - (\tau_1 \cdot \tau_2)\tau_1}{|\tau_1 \times \tau_2|}$ which satisfies $\tau_1 \cdot \tilde{\tau_2} = 0$ and $|\tilde{\tau_2}| = 1$, one obtains

$$\mathrm{Tr}(dn) = [\nabla n](\gamma(\theta)) : (\tau_1 \otimes \tau_1 + \tilde{\tau_2} \otimes \tilde{\tau_2}) = \mathrm{Tr}(\nabla_\Gamma n),$$

since $(\tau_1, \tilde{\tau_2}, n)$ is an orthonormal basis of $\mathbb{R}^3$, and, as a result, $\tau_1 \otimes \tau_1 + \tilde{\tau_2} \otimes \tilde{\tau_2} = \mathbb{I} - n \otimes n$.

Let us now turn to the case of the Gauss curvature. On the one hand, the determinant of (1.7) reads

$$\det(dn) = \frac{([\nabla n]\tau_1) \cdot \tau_1([\nabla n]\tau_2) \cdot \tau_2 - ([\nabla n]\tau_1) \cdot \tau_2([\nabla n]\tau_2) \cdot \tau_1}{|\tau_1 \times \tau_2|^2}.$$

On the other hand,

$$\begin{aligned} 2\,\mathrm{Tr}(\mathrm{Cof}(\nabla_\Gamma n)) &= \mathrm{Tr}(\nabla n(\tau_1 \otimes \tau_1 + \tilde{\tau_2} \otimes \tilde{\tau_2}))^2 \\ &\quad - \mathrm{Tr}(\nabla n(\tau_1 \otimes \tau_1 + \tilde{\tau_2} \otimes \tilde{\tau_2}) \nabla n(\tau_1 \otimes \tau_1 + \tilde{\tau_2} \otimes \tilde{\tau_2})). \end{aligned} \tag{1.8}$$

It suffices now to use the property $\mathrm{Tr}(A(b \otimes b)A(c \otimes c)) = (Ab) \cdot c \quad (Ac) \cdot b$ to obtain, after some straightforward calculations, the desired result. □

The following proposition allows to simplify the preceding formulas.

**Proposition 1.7** *Let $S$ be a surface represented by the zero level set of a function $\varphi$. We have*

$$H = \mathrm{Tr}(\nabla n) = \mathrm{div}\left(\frac{\nabla \varphi}{|\nabla \varphi|}\right), \tag{1.9}$$

$$G = \mathrm{Tr}(\mathrm{Cof}(\nabla n)) = \frac{1}{2}(\mathrm{Tr}(\nabla n)^2 - \mathrm{Tr}([\nabla n]^2)). \tag{1.10}$$

***Proof*** By differentiating the relation $n \cdot n = 1$ we obtain the identity $[\nabla n]^T n = 0$ which in turn implies that $([\nabla n]n) \cdot n = 0$. This property reveals that the invariants of $\nabla_\Gamma n$ are the same as those of $\nabla n$ and allows to conclude. □

In Sect. 7.1 of the appendix some explicit calculations of the curvature are given in the case of an ellipsoid and a torus. In the 2D case, the result remains valid and the curvature of a curve is given by $\mathrm{div}\left(\frac{\nabla \varphi}{|\nabla \varphi|}\right)$. To check this assertion it suffices to adapt the above demonstration: in this case the fundamental forms are scalars and using (1.1) we find the classical formula of the 2D curvature

$$dn = \partial^2_{\theta\theta}\gamma \cdot n\ (|\partial_\theta \gamma|^2)^{-1} = \frac{\partial^2_{\theta\theta}\gamma \cdot (\partial_\theta \gamma)^\perp}{|\partial_\theta \gamma|^3}.$$

## 1.3 Level Set Methods and Geometry of Curves in $\mathbb{R}^3$

Let us consider a curve $\Gamma \subset \mathbb{R}^3$. Let $\theta \mapsto \gamma(\theta) \in \mathbb{R}^3$ be a smooth parameterization of $\Gamma$. The tangent vector to the curve is defined by

$$\tau(\theta) = \frac{\gamma'(\theta)}{|\gamma'(\theta)|}. \tag{1.11}$$

The variation of the tangent vector is along the normal $n$ and proportional to the curvature $H$ of the curve. We therefore introduce

$$n(\theta) = \frac{\tau'(\theta)}{|\tau'(\theta)|} \quad , \quad \tau'(\theta) = H(\theta)|\gamma'(\theta)|n(\theta). \tag{1.12}$$

Note that with this definition the curvature is always non negative. By differentiating the relation $\tau(\theta).\tau(\theta) = 1$ with respect to $\theta$, we obtain that $\tau(\theta)$ and $n(\theta)$ are orthogonal. Computing $\tau'$ using the parametrization leads to $\tau'(\theta) = \frac{1}{|\gamma'(\theta)|}\big(\gamma''(\theta) - (\gamma'(\theta)\cdot\tau(\theta))\tau(\theta)\big)$. As a result, using (1.12) we get the following equivalent of (1.7) for the curves

$$H(\theta) = \frac{\gamma''(\theta)\cdot n(\theta)}{|\gamma'(\theta)|^2}. \tag{1.13}$$

We next introduce the binormal vector $b$

$$b(\theta) = \tau(\theta) \times n(\theta). \tag{1.14}$$

This vector is orthogonal to $\tau$ and $b$, and $(\tau, n, b)$ forms an orthonormal basis adapted to the parameterization, called the Frenet coordinate system. By differentiating the relations $b \cdot b = 1$ and $b \cdot \tau = 0$ it is straightforward to show that the components of $b'$ along $b$ and $\tau$ vanish. The variation of the binormal vector is therefore along the normal $n$ and proportional to the torsion $t_{ors}$ of the curve. We therefore introduce

$$b'(\theta) = -t_{ors}(\theta)|\gamma'(\theta)|n(\theta). \tag{1.15}$$

By differentiating $n \cdot n = 1$, we obtain that $n'$ has a zero component along $n$. Finally, differentiating the identity $n \cdot \tau = n \cdot b = 0$ then using (1.12) and (1.15) we finally obtain

$$\begin{cases} \tau'(\theta) = |\gamma'(\theta)|H(\theta)n(\theta), \\ n'(\theta) = |\gamma'(\theta)|(-H(\theta)\tau(\theta) + t_{ors}(\theta)b(\theta)), \\ b'(\theta) = -|\gamma'(\theta)|t_{ors}(\theta)n(\theta). \end{cases} \tag{1.16}$$

*Remark 1.8* One can show that if the curvature is zero then the curve locally resembles a straight line and if the torsion is zero the curve remains locally in a plane. When considering plane curves, that is when $\gamma(\theta) \in \mathbb{R}^2$, then $n = \tau^\perp$, which simplifies the computation of the curvature (1.13). Furthermore, there is no binormal vector or torsion.

Let us now consider an implicit representation of this same curve $\Gamma \subset \mathbb{R}^3$ using two surfaces. These surface are represented as the zero level of two functions $\varphi^i : \mathbb{R}^3 \longrightarrow \mathbb{R}$, $i = 1, 2$.

$$S_1 = \{x \in \mathbb{R}^3 / \varphi^1(x) = 0\}, \qquad S_2 = \{x \in \mathbb{R}^3 / \varphi^2(x) = 0\}.,$$

and $\Gamma = S_1 \cap S_2$.

Note that, unlike an expression based on a parameterization, this construction assumes that we only consider closed curves. The vector $\nabla\varphi^i$ gives the direction of the normal to $S_i$ and one thus defines the tangent vector to $\Gamma$ by

$$\tau(x) = \frac{\nabla\varphi^1 \times \nabla\varphi^2}{|\nabla\varphi^1 \times \nabla\varphi^2|}. \tag{1.17}$$

Let $x \mapsto v(x)$ be a vector field in $\mathbb{R}^3$. Using (1.11) we obtain the identity

$$(v(\gamma(\theta)))' = [\nabla v](\gamma(\theta))\ \gamma'(\theta) = [\nabla v](\gamma(\theta))\ \tau(\gamma(\theta))\ |\gamma'(\theta)|. \tag{1.18}$$

Thanks to the identity (1.18) with $v = \tau$ and (1.12), this leads to the following formulas for the normal and the curvature

$$H(x) = |[\nabla\boldsymbol{\tau}]\boldsymbol{\tau}|, \qquad n(x) = \frac{[\nabla\boldsymbol{\tau}]\boldsymbol{\tau}}{|[\nabla\boldsymbol{\tau}]\boldsymbol{\tau}|}. \tag{1.19}$$

We introduce the binormal vector given by the formula

$$b(x) = \tau(x) \times n(x). \tag{1.20}$$

By differentiating $|v|^2 = 1$ we get $[\nabla v]^T v = 0$ and by differentiating $v \cdot w = 0$ we get $[\nabla v]^T w = -[\nabla w]^T v$. Combining these relations for the vectors of the orthonormal basis $(\tau, n, b)$, the identity (1.18) with $v = b$ and $v = n$, and the definitions (1.16), we finally obtain

$$\begin{cases} [\nabla\tau]\tau = Hn, \\ [\nabla n]\tau = -H\tau + t_{ors}b, \\ [\nabla b]\tau = -t_{ors}n. \end{cases}$$

These constitue the Eulerian equivalent of formulas (1.16). In particular the curvature and the torsion can be calculated using Level Set functions by

$$H = ([\nabla\tau]\tau)\cdot n = -([\nabla n]\tau)\cdot\tau\ ,\ t_{ors} = -([\nabla b]\tau)\cdot n = ([\nabla n]\tau)\cdot b. \qquad (1.21)$$

*Remark 1.9* When considering plane curves, it suffices to choose $\varphi_2 = z$ and $\varphi^1$ only depending on $x, y$ to obtain $\nabla\varphi^1 \times \nabla\varphi^2 = (\partial_y\varphi^1, -\partial_x\varphi^1, 0)$ and, since $n = \tau^\perp$, we get $n = -\frac{\nabla\varphi^1}{|\nabla\varphi^1|}$. The curvature defined in the preceding formula can be rewritten as

$$H = -([\nabla n]\tau)\cdot\tau = -[\nabla n] : [\mathbb{I} - n\otimes n] = -\operatorname{div}(n) = \operatorname{div}\left(\frac{\nabla\varphi^1}{|\nabla\varphi^1|}\right). \qquad (1.22)$$

We thus find that the curvature in 2D is calculated like the divergence of the normal, as in (1.9) for the case of surfaces in 3D.

## 1.4 Expression of Surface Forces Using the Level Set Function

The question of the evaluation of energies or surface forces by means of the Level Set function is central in all these methods. In image processing, these forces are built to enforce the level sets to "stick" to the significant objects of an image, in order to segment this image, as illustrated in Fig. 1.3 on page 17. In fluid mechanics involving two-phase flows, these forces can result from the surface tension between phases. And, as we will see in more detail later in this book, in fluid structure interaction calculations, they can also represent elastic forces or contact forces between different objects.

Consider a curve in $\mathbb{R}^2$ or a surface in $\mathbb{R}^3$ noted $\Sigma$. We define the surface measure on $\Sigma$, noted $\delta_\Sigma$ by

$$\langle\delta_\Sigma\ ,\ \psi\rangle = \int_\Sigma \psi ds, \qquad (1.23)$$

for any function $\psi$ defined and continuous in $\Omega$. We then have the following fundamental result.

**Proposition 1.10** *Let $r \to \zeta(r)$ be a continuous function with support in $[-1, 1]$, such that $\int \zeta(r)\, dr = 1$, and $\varphi$ a function of class $C^2$ from $\Omega$ into $\mathbb{R}$ such that $|\nabla\varphi(x)| > 0$ for all $x$ in a neighborhood of $\{\varphi = 0\}$. Then*

$$\frac{1}{\varepsilon}\zeta\left(\frac{\varphi}{\varepsilon}\right)|\nabla\varphi| \underset{\varepsilon\to 0}{\rightharpoonup} \delta_{\{\varphi=0\}} \tag{1.24}$$

*in the space of measures. In other words we have*

$$\int_\Omega \frac{1}{\varepsilon}\zeta\left(\frac{\varphi}{\varepsilon}\right)|\nabla\varphi|\psi\, dx \underset{\varepsilon\to 0}{\longrightarrow} \int_{\{\varphi=0\}} \psi ds \tag{1.25}$$

*for any continuous test function $\psi$ defined on $\Omega$.*

***Proof*** Let us start by verifying that under the hypotheses of the proposition we have, in one dimension,

$$\frac{1}{\varepsilon}\zeta\left(\frac{x}{\varepsilon}\right) \underset{\varepsilon\to 0}{\rightharpoonup} \delta_0, \tag{1.26}$$

where $\delta_0$ is the 1D Dirac mass centered at 0. Indeed, for any test function $\psi \in C^0(\mathbb{R})$ one can write, by Lebesgue theorem

$$\int \frac{1}{\varepsilon}\zeta\left(\frac{x}{\varepsilon}\right)\psi(x)\, dx = \int \zeta(y)\psi(\varepsilon y)\, dy \underset{\varepsilon\to 0}{\longrightarrow} \int \zeta(y)\psi(0)\, dy = \psi(0) = \langle \delta_0\,,\ \psi\rangle.$$

For the rest of the proof, we propose three approaches: a first proof assuming that the level sets of $\varphi$ are parallel to an axis, a proof using a coordinate system adapted to the surface and finally an intrinsic proof. Although this last demonstration is the most general and the most concise, the first two demonstrations seem to us to be a natural way of understanding the result.

(a) **Case when** $\varphi(x_1, x_2, x_3) = rx_3$, $r > 0$. The level set $\varphi = 0$ corresponds to a plane of $\mathbb{R}^3$. Since $r > 0$, the orientation of $\Sigma$ defined by $\nabla\varphi$ corresponds to the orientation in the direction of increasing values of $x_3$ of this axis. Let $\psi$ be a test function defined on $\Omega$. We have

$$\int \frac{1}{\varepsilon}\zeta\left(\frac{\varphi}{\varepsilon}\right)|\nabla\varphi|\psi\, dx = \int dx_1 dx_2 \int \frac{r}{\varepsilon}\zeta\left(\frac{rx_3}{\varepsilon}\right)\psi(x_1, x_2, x_3)\, dx_3.$$

We deduce from (1.26) and Lebesgue theorem that

$$\int \frac{1}{\varepsilon}\zeta\left(\frac{\varphi}{\varepsilon}\right)|\nabla\varphi|\psi\, dx \underset{\varepsilon\to 0}{\longrightarrow} \int \psi(x_1, x_2, 0)\, dx_1 dx_2 = \int_{\{\varphi=0\}} \psi(x)\, ds.$$

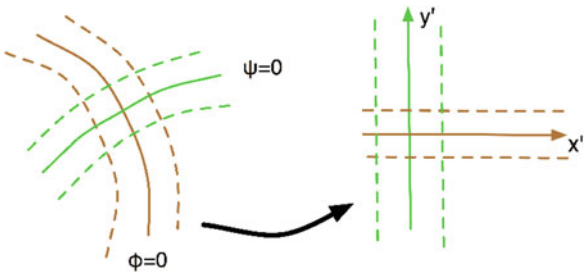


**Fig. 1.2** Mapping of level sets and orthogonal sets to a coordinate system

(b) **Proof using a parameterization adapted to the level sets of $\varphi$ around** $\{\varphi = 0\}$ [30]. The idea here is to come back to the above case by constructing a coordinate system adapted to the surface. This is achieved by defining directions orthogonal to the level sets of $\varphi$ (see Fig. 1.2), that is to say by finding a function $\psi$ such that $\nabla\psi$ does not take the value zero and

$$\nabla\varphi \cdot \nabla\psi = 0. \tag{1.27}$$

To simplify the exposition, we limit ourselves here to the two-dimensional case. Let us admit for now that such a function $\psi$ exists (the proof will be given below). The desired change of coordinates $(x, y) \to (x', y')$ will be written

$$x' = \psi(x, y)\ ,\ \ y' = \varphi(x, y).$$

This change of coordinates is well defined if its Jacobian is non-zero. The value of this Jacobian is given by

$$J(x, y) = \partial_x\varphi\partial_y\psi - \partial_y\varphi\partial_x\psi$$

which, since the gradients of $\varphi$ and $\psi$ are orthogonal, is equal, up to its sign, to the product of the norms of these two vectors. $J$ is therefore always non-zero.

Consider now a test function $w$. Using the change of variables that has just been defined we can write

$$\int \frac{1}{\varepsilon}\zeta\left(\frac{\varphi(x, y)}{\varepsilon}\right)|\nabla\varphi(x, y)|w(x, y)\,dxdy$$
$$= \int \frac{1}{\varepsilon}\zeta\left(\frac{y'}{\varepsilon}\right)|\nabla\varphi(x, y)|\tilde{w}(x', y')\frac{1}{|\nabla\varphi||\nabla\psi|}\,dx'dy',$$

where $\tilde{w}$ is defined by $w(x, y) = \tilde{w}(\psi(x, y), \varphi(x, y))$. According to (1.26) we thus have

$$\int \frac{1}{\varepsilon}\zeta\left(\frac{\varphi(x, y)}{\varepsilon}\right)|\nabla\varphi(x, y)|w(x, y)\,dxdy \to \int \frac{w(x', 0)}{|\nabla\psi(x, y)|}\,dx'.$$

The integral in the right hand side can be related to a curvilinear integral along $\Sigma$ by writing

$$x' = \psi(x(s), y(s))$$

where s is a curvilinear coordinate on $\Sigma$. This gives

$$dx' = |\nabla\psi \cdot \boldsymbol{\tau}| ds,$$

where $\boldsymbol{\tau}$ denotes a unit vector tangent to $\Sigma$. Since $\nabla\psi$ and $\boldsymbol{\tau}$ are collinear, we have $|\nabla\psi \cdot \boldsymbol{\tau}| ds = |\nabla\psi| ds$ and we finally get

$$\int \frac{1}{\varepsilon}\zeta\left(\frac{\varphi(x, y)}{\varepsilon}\right)|\nabla\varphi(x, y)| w(x, y)\, dxdy \to \int_{\Sigma} w\, ds.$$

It remains now to prove the existence of a change of variables $(x, y) \to (x', y')$. We first observe that since $\frac{1}{\varepsilon}\zeta\left(\frac{\varphi}{\varepsilon}\right)$ has a support of width $2\varepsilon$ it suffices to construct this change of variables in a neighborhood of the curve $\varphi = 0$. The idea consists of starting from a parameterization $s \to (x(s), y(s))$ of $\Sigma$ and to extend this parameterization in the neighborhood of $\Sigma$ by some functions $\tilde{x}(s, r), \tilde{y}(s, r)$ for $r \in [-\varepsilon, +\varepsilon]$. For this we wish to solve the differential equations

$$\begin{aligned} \tilde{x}(s, 0) = x(s) \quad , \quad \partial_r \tilde{x}(s, r) = \partial_x \varphi(\tilde{x}, \tilde{y}) \\ \tilde{y}(s, 0) = y(s) \quad , \quad \partial_r \tilde{y}(s, r) = \partial_y \varphi(\tilde{x}, \tilde{y}). \end{aligned}$$

Since $\varphi$ has been assumed to be of class $C^2$ on $\Omega$, this system is uniformly Lispchitzian and therefore has a unique global $C^2$ solution for $r \in [-\varepsilon, \varepsilon]$. It defines a valid change of variables, as the Jacobian of the transform $(x, y) \to (\tilde{x}, \tilde{y})$ satisfies

$$\begin{aligned} \left|\frac{\partial(\tilde{x}, \tilde{y})}{\partial(x, y)}\right| &= \partial_s x \partial_y \varphi(x(s), y(s)) - \partial_s y \partial_x \varphi(x(s), y(s)) + O(r) \\ &= |\nabla\varphi(x(s), y(s))| + O(r). \end{aligned}$$

The last equality results from the fact that the tangent $(x_s, y_s)$ to $\Sigma$ is orthogonal to $\nabla\varphi$. Since, by asumption, $\nabla\varphi$ never vanishes on $\Sigma$, we deduce that by continuity the Jacobian is non-zero in the neighborhood of $\Sigma$.

We conclude the proof by constructing $\psi$ as follows. We first consider on $\mathbb{R}$ a smooth, strictly increasing, function $\psi_0$ and we solve

$$\psi(\tilde{x}(s, r), \tilde{y}(s, r)) = \psi_0(s). \tag{1.28}$$

Due to the change of variable seen above, this defines a unique function $\psi$ in the neighborhood of $\Sigma$. By differentiating (1.28) with respect to $r$ we obtain

$$\partial_x \psi \partial_r \tilde{x} + \partial_y \psi \partial_r \tilde{y} = 0.$$

In other words we did check that

$$\nabla\varphi \cdot \nabla\psi = 0.$$

Moreover by differentiating (1.28) with respect to $s$ we obtain

$$\nabla\psi \cdot (\tilde{x}_s, \tilde{y}_s) = \psi_0'$$

which shows that $\nabla\psi$ never vanishes.

(c) **Intrinsic proof in the general case.** Given a test function $\psi$ let us set

$$g(r) = \int_{\{\varphi=r\}} \psi ds.$$

From (1.26) we have

$$\lim_{\varepsilon\to 0} \int_{\mathbb{R}} \frac{1}{\varepsilon}\zeta\left(\frac{r}{\varepsilon}\right) \int_{\{\varphi=r\}} \psi \, dsdr = \int_{\{\varphi=0\}} \psi \, ds,$$

that is,

$$\lim_{\varepsilon\to 0} \int_{\mathbb{R}} \int_{\{\varphi=r\}} \frac{1}{\varepsilon}\zeta\left(\frac{\varphi}{\varepsilon}\right) \psi \, dsdr = \int_{\{\varphi=0\}} \psi \, ds.$$

Since $\varphi$ has its support in $[-1, +1]$ we can write

$$\int_{\mathbb{R}} \int_{\{\varphi=r\}} \frac{1}{\varepsilon}\zeta\left(\frac{\varphi}{\varepsilon}\right) \psi \, dsdr = \int_{-\varepsilon}^{\varepsilon} \int_{\{\varphi=r\}} \frac{1}{\varepsilon}\zeta\left(\frac{\varphi}{\varepsilon}\right) \psi \, dsdr.$$

We can decompose, in the neighborhood of $x$, the volume $dx$ as $dx = ds \times dh$, where $dh$ is evaluated along the normal $\frac{\nabla\varphi}{|\nabla\varphi|}$. One next notices that

$$r \pm dr := \varphi\left(x \pm dh\frac{\nabla\varphi}{|\nabla\varphi|}\right) = \varphi(x) \pm dh|\nabla\varphi| + O(dh^2),$$

hence $dsdr = |\nabla\varphi| dx$ (see also Lemma 3.1 on page 57). As a result

$$\int_{\mathbb{R}} \int_{\{\varphi=r\}} \frac{1}{\varepsilon}\zeta\left(\frac{\varphi}{\varepsilon}\right)\psi \, dsdr = \int_{|\varphi(x)|<\varepsilon} \frac{1}{\varepsilon}\zeta\left(\frac{\varphi}{\varepsilon}\right)\psi|\nabla\varphi| \, dx$$
$$= \int_{\mathbb{R}^d} \frac{1}{\varepsilon}\zeta\left(\frac{\varphi}{\varepsilon}\right)\psi|\nabla\varphi| \, dx$$

which completes the proof.

□

Before giving examples which illustrate this result, one can notice that if in addition one assumes the function $\zeta$ even, which is always the case in practice, the convergence property (1.26) is stronger. If we assume $\psi$ of class $C^2$ we can indeed easily see that

$$\left| \int \frac{1}{\varepsilon}\zeta\left(\frac{x}{\varepsilon}\right)\psi(x) \, dx - \psi(0) \right| \leq |\psi|_{2,\infty} \int \frac{|x|^2}{\varepsilon}\zeta\left(\frac{x}{\varepsilon}\right) dx \leq C\varepsilon^2,$$

which shows that the computation of the forces using Level Set functions is second order with respect to the parameter $\varepsilon$.

### 1.4.1 Example 1: Image Processing

In image processing, the so-called active contour methods consist in isolating the characteristic objects of the image using curves. These curves (we limit ourselves in this discussion to the 2D case) must therefore stick as closely as possible to the significant contours of the image and "forget" the non-coherent part of the image (the noise). These methods are the subject of a vast literature that we cannot discuss here, and we particularly refer the reader to [112] and to the references given there. Level Set methods allow to implement this idea in a relatively simple way.

Given a Level Set function $\varphi$, we start by defining energies which reflect each of the above criteria. Suppose the image consists of two gray levels $c_1$ and $c_2$, respectively for the interior and exterior of the objects to be segmented. If we want to find the contour which best delimits these two gray levels, it is natural to minimize the following functional

$$\mathcal{E}_1(\varphi) = \int_\Omega |u_0 - c_1|^2 \mathcal{H}(\varphi) \, dx + \int_\Omega |u_0 - c_2|^2 \left(1 - \mathcal{H}(\varphi)\right) \, dx,$$

where $u_0$ denotes the gray level of the image to be processed and $\mathcal{H}$ denotes the Heaviside function. In the following, we will consider a regularized version of $\mathcal{E}_1$, keeping the same notation, obtained by replacing $\mathcal{H}$ by $\mathcal{H}_\varepsilon = \mathcal{H} \star \frac{1}{\varepsilon}\zeta(\frac{\cdot}{\varepsilon})$.

We assume here that the desired Level Set function satisfies $\varphi < 0$ inside the objects. To prevent the contour from stopping on objects of too small a scale (which mostly correspond to noise), a natural approach is also to minimize the length of the level set $\varphi = 0$. This length can be expressed as

$$l(\Sigma) = \int_{\Sigma} ds.$$

Thanks to Proposition 1.10 we can approach this length by the quantity

$$\mathcal{E}_2(\varphi) = \int \frac{1}{\varepsilon}\zeta\left(\frac{\varphi}{\varepsilon}\right)|\nabla\varphi|\,dx.$$

The goal is therefore to minimize with respect to $\varphi$ a functional of the form $\alpha\mathcal{E}_1(\varphi)+\beta\mathcal{E}_2(\varphi)$ where $\alpha$ and $\beta$ are two positive parameters to be adjusted to measure the respective importance of the two criteria just defined. An elementary calculation allows to calculate the differentials $\partial\mathcal{E}_1$ and $\partial\mathcal{E}_2$ of $\mathcal{E}_1$ and $\mathcal{E}_2$ as follows:

$$\begin{aligned} < \partial\mathcal{E}_2, \psi > &= \int \frac{1}{\varepsilon^2}\zeta'\left(\frac{\varphi}{\varepsilon}\right)|\nabla\varphi|\psi\,dx + \int \frac{1}{\varepsilon}\zeta\left(\frac{\varphi}{\varepsilon}\right)\frac{\nabla\varphi\cdot\nabla\psi}{|\nabla\varphi|}\,dx \\ &= \int \frac{1}{\varepsilon^2}\zeta'\left(\frac{\varphi}{\varepsilon}\right)|\nabla\varphi|\psi\,dx - \operatorname{div}\left[\frac{1}{\varepsilon}\zeta\left(\frac{\varphi}{\varepsilon}\right)\frac{\nabla\varphi}{|\nabla\varphi|}\right]\psi\,dx \\ &= -\int \frac{1}{\varepsilon}\zeta\left(\frac{\varphi}{\varepsilon}\right)\operatorname{div}\frac{\nabla\varphi}{|\nabla\varphi|}\psi\,dx. \end{aligned}$$

We deduce that

$$\partial\mathcal{E}_2 = -\frac{1}{\varepsilon}\zeta\left(\frac{\varphi}{\varepsilon}\right)\operatorname{div}\frac{\nabla\varphi}{|\nabla\varphi|}.$$

To differentiate $\mathcal{E}_1$ we start by noticing that $\mathcal{H}'_\varepsilon(\varphi) = \frac{1}{\varepsilon}\zeta\left(\frac{\varphi}{\varepsilon}\right)$ from which it results that

$$< \partial\mathcal{E}_1, \psi >= \int \frac{1}{\varepsilon}\zeta\left(\frac{\varphi}{\varepsilon}\right)(|u_0 - c_1|^2 - |u_0 - c_2|^2)\psi\,dx,$$

hence

$$\partial\mathcal{E}_1 = (|u_0 - c_1|^2 - |u_0 - c_2|^2)\frac{1}{\varepsilon}\zeta\left(\frac{\varphi}{\varepsilon}\right).$$

A classical gradient algorithm to minimize $\alpha\mathcal{E}_1(\varphi) + \beta\mathcal{E}_2(\varphi)$ can therefore be interpreted as the time discretization of the equation

$$\partial_t\varphi = \alpha\frac{1}{\varepsilon}\zeta\left(\frac{\varphi}{\varepsilon}\right)\operatorname{div}\frac{\nabla\varphi}{|\nabla\varphi|} + \beta(|u_0 - c_1|^2 - |u_0 - c_2|^2)\frac{1}{\varepsilon}\zeta\left(\frac{\varphi}{\varepsilon}\right). \tag{1.29}$$

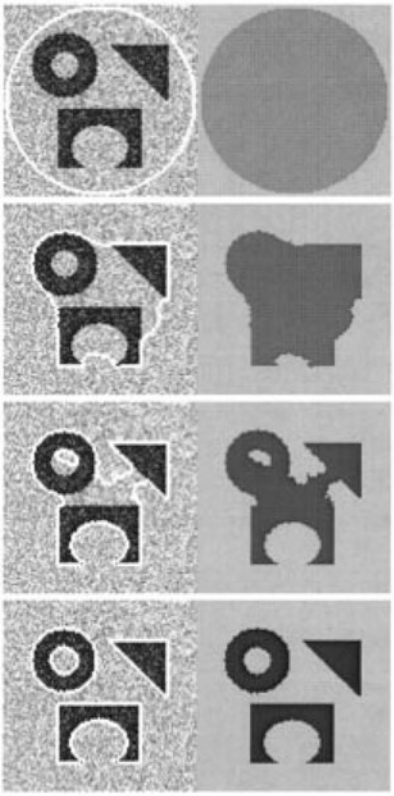

**Fig. 1.3** Application of active contour techniques to segment objects in a noisy image. Left column: initial image and successive stages of the contours. Right column: corresponding stages of the segmented image. From [112]

where the levels $c_1$ et $c_2$ are readily obtained by differentiating the energy:

$$c_1 = \frac{\int_\Omega u_0 \mathcal{H}_\varepsilon dx}{\int_\Omega \mathcal{H}_\varepsilon dx}, \quad c_2 = \frac{\int_\Omega u_0 (1 - \mathcal{H}_\varepsilon) dx}{\int_\Omega 1 - \mathcal{H}_\varepsilon dx}.$$

Figure 1.3 shows the contours obtained after several iterations of this algorithm on a noisy image. In particular, it highlights an important property of the Level Set methods, namely that the method is not topologically constrained: the initial contour is a circle and the final contour consists of several closed curves isolating the desired objects.

### *1.4.2 Exemple 2: Surface Tension*

We consider here the case of two incompressible fluids separated by an interface subject to surface tension [30]. This reference contains one of the very first

applications of Level Set methods in fluid mechanics. On either side of the interface $\Sigma$, which we will note the domains $\Omega_1$ and $\Omega_2$ with $\Omega = \Omega_1 \cup \Omega_2 \cup \Sigma$, the fluid is governed by the incompressible Navier–Stokes equations:

$$\rho(\partial_t u + u \cdot \nabla u) + \nabla p - \mathrm{div}(2\mu D(u)) = f \ , \ \mathrm{div}\, u = 0, \ \text{dans } \Omega_1 \cup \Omega_2. \tag{1.30}$$

In this equation $\mu$ denotes the viscosity (possibly different in each phase), and $D(u)$ the strain rate tensor

$$D(u) = \frac{1}{2}(\nabla u + \nabla u^T).$$

Fluid velocities are continuous along the interface and normal stresses are balanced by surface tension forces. If one notes $\boldsymbol{\sigma}$ the tensor of the fluid stresses, then

$$\boldsymbol{\sigma} = -p\, I + 2\mu D(u)$$

or equivalently:

$$\sigma_{ij} = -p\delta_{i,j} + \mu(\partial u_i/\partial x_j + \partial u_j/\partial x_i).$$

If $\lambda$ denotes the coefficient of surface tension, this equilibrium results in the relations

$$[\sigma_{ij} n_j]_\Sigma = \lambda H n_i$$

or, in a more compact form

$$[\boldsymbol{\sigma} \cdot n]_\Sigma = \lambda H n. \tag{1.31}$$

In the above expressions $n$ denotes as usual the normal to the interface, $H$ its mean curvature and $[\cdot]_\Sigma$ is the jump of a quantity across the interface. When the fluids are non-viscous ($\mu = 0$) this equilibrium means that the surface tension balances the pressure forces on either side of the interface:

$$[p]_\Sigma = \lambda H.$$

Starting from these jump relations, we can extend to the whole domain $\Omega$ the Navier–Stokes equations satisfied in each phase. For $u$ defined on $\Omega$ satisfying (1.31) the following equality holds

$$\mathrm{div}(2\mu D(u)) = U + \lambda H \delta_\Sigma n.$$

where we denote by $U$ the function which is equal to $\mathrm{div}(2\mu D(u))$ in $\Omega_1$ and in $\Omega_2$. We can therefore extend the Navier–Stokes equations to $\Omega$ into the following system

$$\rho(\partial_t u + u \cdot \nabla u) + \nabla p - \mathrm{div}(2\mu D(u)) = \rho\, \lambda\, H\, \delta_\Sigma\, n,$$
$$\mathrm{div}\, u = 0.$$

In view of Proposition 1.10, the Level Set formulation of this problem consists in solving in $\Omega$ the system

$$\rho(\partial_t u + u \cdot \nabla u) + \nabla p - \mathrm{div}(2\mu D(u)) = \rho(\varphi)\, \lambda\, H(\nabla\varphi)\, \frac{1}{\varepsilon}\zeta\left(\frac{\varphi}{\varepsilon}\right)\nabla\varphi, \quad (1.32)$$

$$\mathrm{div}\, u = 0, \quad (1.33)$$

$$\partial_t \varphi + u \cdot \nabla\varphi = 0, \quad (1.34)$$

where we recall that $H$ is a function of $\nabla\varphi$ given by

$$H = \mathrm{div}\, n, \ \text{with}\ n = \nabla\varphi/|\nabla\varphi|.$$

This system must be completed by boundary conditions, i.e., within the framework that we have set, $u = 0$ on $\partial\Omega$, and initial conditions $u(x,0) = u_0(x)$, $\varphi(x,0) = \varphi_0(x)$. Note that with this boundary condition on the velocity, it is not necessary to write a spatial boundary condition for $\varphi$ in the transport equation.

Figure 1.4 shows the transport under the effect of gravity of 2 bubbles of different densities and their fusion, illustrating the regularizing effect of surface tension on the shape of the interface. This figure again illustrates the fact that Level Set methods, unlike interface tracking methods, are not constrained by topology and allow the merging of objects. In this experiment, from [30], the coefficient of gravity is taken equal to 1, the density contrast between the 2 bubbles, initially circular, is equal to 10 (the lightest bubble is the lowest). The diameters of the bubbles are 0.2 and 0.3. The surface tension coefficient for the experiment on the right is equal to 0.02. As in [30], the Navier–Stokes equations are solved in the Boussinesq approximation. A semi-lagrangian particle method is used with a grid-size $h = 1/256$.

## 1.5 Numerical Aspects I: Consistency and Accuracy

As we have seen above, Level Set methods are based in the first place on the convergence of the approximation of a one-dimensional Dirac mass by a cut-off function, a convergence which itself results from the property (1.26) in one

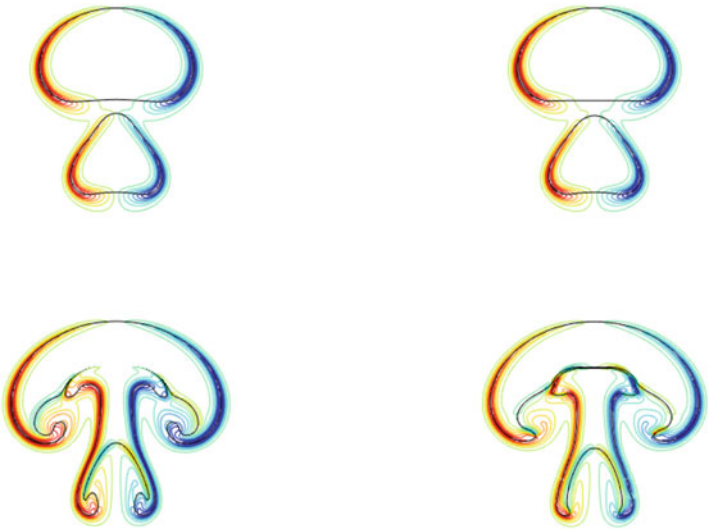

**Fig. 1.4** Merging of two bubbles with different densities, at two successive times ($t = 0.2$ for the top pictures and $t = 0.4$ for the bottom pictures). With (right pictures) or without (left pictures) surface tension. The color contour lines represent vorticity levels. See the text for the parameters of this experience

dimension. If we go back to the proof of this property and assume that $\varphi(x) = rx$ for a given constant $r$, we find

$$\left| \int \frac{1}{\varepsilon} \zeta\left(\frac{rx}{\varepsilon}\right) \psi(x)\, dx - \psi(0) \right| \leq \int \frac{1}{\varepsilon} \left| \zeta\left(\frac{rx}{\varepsilon}\right) \right| |\psi(x) - \psi(0)|\, dx$$
$$\leq \int \frac{|x|}{\varepsilon} \left| \zeta\left(\frac{rx}{\varepsilon}\right) \right| dx\ |\psi|_{1,\infty} \leq m_1 \frac{\varepsilon}{r} |\psi|_{1,\infty},$$

where $m_1 = \int |x\zeta(x)|\, dx$. Given that in this example $r = \varphi'(0)$ we can deduce that the approximation of the forces using a Level Set function will have a precision of order

$$O\left(\frac{\varepsilon}{\inf_{\{\varphi=0\}} |\nabla\varphi|}\right).$$

What we have just said assumes an exact calculation of the integrals. In practice these integrals must be evaluated by quadrature methods. Assuming these quadratures carried out for example by the mid-point method, on a grid of nodes $x_j$, with $j \in [0, N]^d$ where $d$ is the dimension of the space, of uniform grid-size $\Delta x$, the

error produced on the evaluation of a force of form (1.32) can be written with a first order estimate

$$\left| \int \frac{1}{\varepsilon}\zeta\left(\frac{\varphi}{\varepsilon}\right)\psi\, dx - \sum_j \frac{1}{\varepsilon}\zeta\left(\frac{\varphi(x_j)}{\varepsilon}\right)\psi(x_j) \right| \leq C\Delta x \left| \frac{1}{\varepsilon}\zeta\left(\frac{\varphi}{\varepsilon}\right)\right|_{1,1} |\varphi|_{1,\infty}$$

$$\leq C\frac{\Delta x}{\varepsilon}|\varphi|_{1,\infty}.$$

In view of the above, convergence will hold if, on the one hand, the convergence condition

$$\varepsilon \ll \inf_{\varphi=0} |\nabla\varphi|$$

is satisfied and, on the other hand,

$$\Delta x \ll \varepsilon/|\varphi|_{1,\infty}.$$

A second-order estimate of the quadrature error leads to similar conclusions. We deduce that a natural requirement to avoid taking too small values of the parameters $\varepsilon$ and $\Delta x$ is that the ratio

$$\frac{\inf_{\varphi=0}|\nabla\varphi|}{|\varphi|_{1,\infty}}$$

be as close to 1 as possible. The ideal case is when, at least in a neighborhood of size $\varepsilon$ of $\Sigma = \{\varphi = 0\}$, $|\nabla\varphi| = 1$(or another constant), which is the case if $\varphi$ is the signed distance to $\Sigma$ (see proposition 1.4).

While it is in general possible to initialize the value of $\varphi$ to such a value, it is obviously not possible to guarantee the property $|\nabla\varphi| \simeq 1$ for $t > 0$. To remedy this, two approaches are possible: either reset at any time $\varphi$ to a function which has this property, without altering the iso-surface $\{\varphi = 0\}$, or to renormalize $\varphi$ in the evaluation of the forces.

### *1.5.1 Redistancing of φ*

The first method consists in rectifying a given Level Set function $\varphi_0$ into a signed distance function at each time step. This idea appeared very quickly in Level Set methods [135, 136] and has undergone many developments (one can for example consult [31, 108, 121]). We will limit ourselves here to the outline of the method.

The redistancing of the Level Set function can typically be done by solving the following Hamilton–Jacobi equation:

$$\partial_\tau \varphi + \mathrm{sgn}(\varphi_0)(|\nabla \varphi| - 1) = 0. \tag{1.35}$$

with $\varphi_0$ as initial condition, and looking for a stationary state. In practice, due to the hyperbolicity of this equation, the rectificagtion of $\varphi$ is propagated starting from $\{\varphi = 0\}$ so that a few iterations are enough to reach $|\nabla \varphi| \approx 1$ in the neighborhood of $\{\varphi = 0\}$. Indeed, the above equation can be written as a transport equation with right hand side

$$\partial_\tau \varphi + \mathrm{sgn}(\varphi_0)\frac{\nabla}{\varphi}|\nabla \varphi| \cdot \nabla \varphi = -\mathrm{sgn}(\varphi_0). \tag{1.36}$$

The characteristics associated to this transport equation thus originate on $\{\varphi_0 = 0\}$ and are orthogonal to this interface. We can actually show that this equation does not modify the zero level set of the initial function, in other words $\{\varphi(\cdot, t) = 0\} = \{\varphi_0 = 0\}$ for all $t > 0$.

The drawback of this approach is, on the one hand, in the cost of solving this additional equation and, on the other hand, in the fact that its numerical discretization in practice leads to a displacement of the interface. This is a drawback that several contributions have attempted to overcome, to the detriment of the simplicity of the method [31, 56, 108, 121, 135]. One difficulty in particular lies in the numerical approximation of the sign function.

Other methods involve solving the Eikonal equation directly. Given an interface $\{\varphi_0 = 0\}$, where $\varphi_0$ is not a distance function, we look for $\varphi$ satisfying

$$\begin{cases} |\nabla \varphi| = 1 & \text{in } \Omega \\ \varphi = 0 & \text{on } \{\varphi_0 = 0\} \end{cases} \tag{1.37}$$

Among these methods, which historically began with the Fast Marching method [93, 123, 124], we find the Fast Sweeping method [117, 148] and, more recently, the method in [41].

Another approach is to transport $\varphi$ away from the interface in such a way that it always satisfies $|\nabla \varphi| = 1$. A method, initially introduced by Osher and collaborators [150] following an idea by Evans and Spruck [59], then taken up in [77] and, within the framework of shape optimization, in [47], consists in determining $\varphi$ as the solution to

$$\partial_t \varphi(x, t) + (u \cdot \nabla \varphi)(x - \varphi \nabla \varphi(x), t)) = 0.$$

This amounts, on the interface, to a transport equation, the solution of which is always a distance function if the initial function is. Unfortunately this equation is not local and difficult to use numerically.

In all these techniques, a drawback is that they deprive us of information on the gradients of the Level Set function advected by the flow, information which, as we will see later, is crucial for the treatment of the fluid-structure interaction by Level Set methods.

### 1.5.2 Renormalization of $\varphi$

The idea starts from the following observation: if $d(x,t)$ denotes the signed distance to the surface, the quantity $\frac{\phi}{|\nabla\phi|}$ approaches $d$ in the neighborhood of the interface.

Indeed as we mentioned in Proposition 1.4, for $d(x)$ small enough, the point $x - d(x)\nabla d(x)$ is on this surface, so that $\varphi(x - d(x)\nabla d) = 0$. By carrying out an expansion in the neighborhood of $d(x) = 0$ we have

$$\varphi(x) - d(x)\nabla\varphi \cdot \nabla d(x) + O(d(x)^2) = 0.$$

Furthermore, we have

$$\nabla d(x) = (\nabla d)(x - d(x)\nabla d) + d(x)[\nabla^2 d]\nabla d + O(d(x)^2),$$

and

$$\begin{aligned}(\nabla d)(x - d(x)\nabla d) &= \frac{\nabla\phi}{|\nabla\phi|}(x - d(x)\nabla d) \\ &= \frac{\nabla\varphi}{|\nabla\varphi|}(x) - d(x)\left[\nabla\left(\frac{\nabla\phi}{|\nabla\phi|}\right)\right]\nabla d + O(d(x)^2), \qquad (1.38)\end{aligned}$$

and thus

$$\nabla d(x) = \frac{\nabla\varphi}{|\nabla\varphi|}(x) + d(x)\left([\nabla^2 d] - \left[\nabla\left(\frac{\phi}{|\nabla\phi|}\right)\right]\right)\nabla d + O(d(x)^2).$$

Finally

$$\varphi(x) - d(x)|\nabla\varphi|(x) + O(d(x)^2) = 0,$$

that is

$$d(x) \approx \frac{\phi}{|\nabla\phi|}(x).$$

We thus have a simple way to estimate the distance from a point $x$ sufficiently close to $\{\varphi = 0\}$ to this curve, by dividing the value of $\varphi$ by the norm of its gradient. The function $\psi(x) = \frac{\phi}{|\nabla\phi|}(x)$ has, to first order in $\varphi$, a gradient of norm 1. On the other

hand, its zero level line coincides with that of $\varphi$. According to Proposition 1.10, we therefore have

$$\frac{1}{\varepsilon}\zeta\left(\frac{\psi}{\varepsilon}\right)|\nabla\psi| \rightharpoonup \delta_{\{\psi=0\}} = \delta_{\{\varphi=0\}} \quad \text{in } \mathcal{M}(\mathbb{R}^d).$$

which justifies the approximation of $\delta_{\{\varphi=0\}}$ by

$$\frac{1}{\varepsilon}\zeta\left(\frac{\varphi}{\varepsilon|\nabla\varphi|}\right).$$

To the first order in $\varphi$, this expression represents an approximation of the Dirac mass whose support remains of width $2\varepsilon$. Compared to the original method, the resulting method ultimately consists in replacing at each point $x$ the parameter $\varepsilon$ by local values $\varepsilon|\nabla\varphi|(x)$.

The interest of this method is that it can be interpreted as a post-processing of $\varphi$ which does not affect the location of the interface. Its downside is that it adds the singularity of $\nabla\varphi$ in the cut-off and that points where $|\nabla\varphi|$ is small can cause numerical concerns in the evaluation of forces.

A detailed study of this type of approximation was carried out by Tornberg, Enquist and Tsai [55], which allows to determine an optimal choice of the parameter $\varepsilon$. This consists of using the 1-norm of the vector and replacing $\varepsilon$ at each point by

$$\varepsilon(x) = |\nabla\varphi(x)|_1\varepsilon_0,$$

where $\varepsilon_0$ is fixed and $|\nabla\varphi(x)|_1 = |\partial_{x_1}\varphi(x)| + |\partial_{x_2}\varphi(x)| + |\partial_{x_3}\varphi(x)|$. Let us also indicate that the authors recommend the use of the hat function as an approximation of the Dirac measure, because it satisfies a second order discrete moment condition.

### *1.5.3 Comparison of the Two Approaches*

The advantages and drawbacks of redistancing approaches have been mentioned above. An additional interest of these methods, which appears as a side effect, is that because the gradients of $\varphi$ are brought close to 1 around the interface, the variations of $\varphi$ are somehow limited, which can have the effect of reducing the numerical errors in the treatment of the transport equation of $\varphi$ (and this independently of the numerical discretization method used to solve this equation).

Figure 1.5 illustrates both this effect and the drawback, already mentioned, that the discretization of Eq. (1.36) can lead to a shift of the interface.

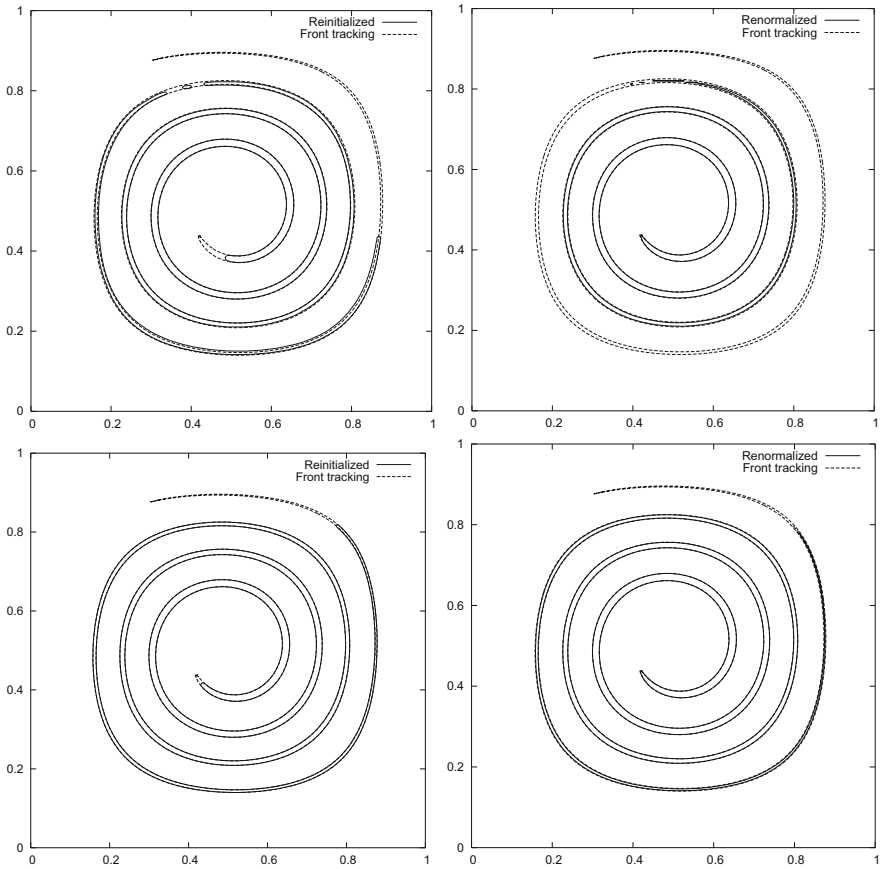


**Fig. 1.5** Interface computed with or without redistancing for the stretched blob, at $T = 5$, over a rectangular grid $N \times N$. Top pictures: $N = 256$. Bottom pictures: $N = 512$. From [36]

In this example, which is classically used to test Level Set methods and the numerical treatment of the transport equation (1.2) (see for example [56]), the velocity field is given by

$$u(x_1, x_2) = (-\sin^2(\pi x_1)\sin(2\pi x_2), \sin(2\pi x_1)\sin^2(\pi x_2)$$

and the initial interface is a circle centered at the point $(0.5, 0.75)$ and with radius 0.15. Although smooth, the velocity field produces as time goes on a significant stretching and a filamentation of the interface which makes it difficult to capture it for a time $T > 2$. In this figure, the reference solution is obtained at $T = 5$ with a purely Lagrangian method, very simple to implement in this particular case, using 1000 markers located on the interface.

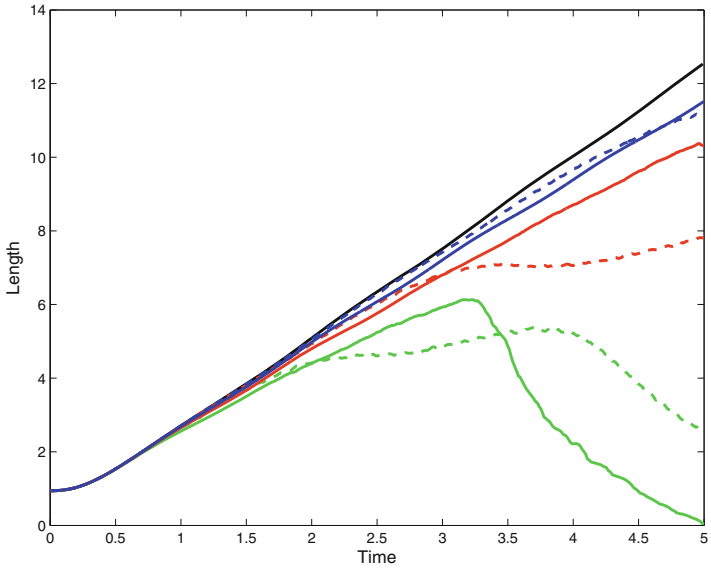


**Fig. 1.6** Comparison of the redistancing and renormalization methods in calculating the length of the filament for the experiment in Fig. 1.5. The results concern a resolution with 64 (green curves), 128 (red curves) and 256 (blue curves) discretization points in each direction. The black curve is the reference curve. Results obtained by redistancing (solid lines) and renormalization (dotted lines). From [36]

In the Level Set framework, the transport equations are solved by a WENO5 scheme on a structured mesh of size $256 \times 256$ or $512 \times 512$. We can see that in the thin parts of the filament, the interface is better captured by the redistancing method, which can be attributed to the fact that the discretization errors in the solution of the transport equation are large when $\varphi$ is stiff. On the other hand, in better resolved areas, we also see that the redistancing equation causes an artificial displacement of the interface.

To test the ability of the different methods above to allow a correct calculation of the forces, we take the same velocity field and calculate the length of the filament over time. This calculation here represents a surface force prototype that needs to be properly calculated. In Fig. 1.6, the upper curve, which shows an almost linear increase in length, is the reference curve obtained as before by following a large number of markers. The dotted curves are obtained by a renormalization method and the solid curves by the redistancing method.

The tests are conducted with 64, 128 and 256 grid points in each direction. We observe that at low resolution the redistancing method ends up making the filament completely disappear. At higher resolution, the redistancing and renormalization methods give comparable results. The renormalization method therefore appears as a method allowing a correct calculation of the forces, even in the event of strong stretching, without affecting the transport equation on the Level Set function.

**Table 1.1** Comparison of numerical errors produced in Smereka's methods [130] and in the renormalization method

| Grid | Smereka 1 | | Renormalization | | Smereka 2 | |
|---|---|---|---|---|---|---|
| size | Rel. error | Order | Rel. Error | Order | Rel. error. | Order |
| 0.2 | $9.38 \times 10^{-3}$ | | $1.5 \times 10^{-1}$ | | $2.68 \times 10^{-3}$ | |
| 0.1 | $2.23 \times 10^{-3}$ | 2.07 | $5 \times 10^{-3}$ | | $5.49 \times 10^{-4}$ | 2.29 |
| 0.05 | $8.12 \times 10^{-4}$ | 1.46 | $1.3 \times 10^{-3}$ | 1.9 | $1.32 \times 10^{-4}$ | 2.05 |
| 0.025 | $2.71 \times 10^{-4}$ | 1.58 | $3 \times 10^{-4}$ | 2.1 | $2.90 \times 10^{-5}$ | 2.18 |
| 0.0125 | $7.58 \times 10^{-5}$ | 1.83 | $8 \times 10^{-5}$ | 1.9 | $7.79 \times 10^{-6}$ | 1.90 |
| 0.00625 | $3.04 \times 10^{-5}$ | 1.32 | $2 \times 10^{-5}$ | 2 | $1.84 \times 10^{-6}$ | 2.08 |

A complementary example illustrating the behavior of the renormalization method relies on the test proposed by [130] to introduce a new way of approaching the Dirac measure. In this article, the author constructs two discrete Dirac functions approximating the measure to first and second order, then calculates the length of an ellipse whose orientation is randomly chosen to avoid grid effects. The average error made is then recorded. Table 1.1 demonstrates that the renormalization method behaves, from the point of view of accuracy, like the first approximation proposed by the author, and therefore constitutes, in view of its simplicity, an effective solution to approach an area measurement in the Level Set method. A complete study of the approximation of Dirac functions was carried out in [55].

### *1.5.4 Towers Method to Approximate Surface Integrals*

Another method has been introduced by Towers in a series of papers [139–142] to approximate surface integrals in a Level Set framework, which improved the order of accuracy. The idea is to introduce

$$I(\varphi) = \int_0^{\varphi} \mathcal{H}(r)dr = \max(\varphi, 0)$$

and to derive approximations of $\delta_{\{\varphi=0\}}$ and $\mathcal{H}(\varphi)$ from it, using the formulas:

$$\nabla I(\varphi) = \mathcal{H}(\varphi)\nabla\varphi, \qquad \Delta I(\varphi) = |\nabla\varphi|^2\delta_{\{\varphi=0\}} + \mathcal{H}(\varphi)\Delta\varphi,$$

which lead to

$$\mathcal{H}(\varphi) = \frac{\nabla I(\varphi)\cdot\nabla\varphi}{|\nabla\varphi|^2}, \ \delta_{\{\varphi=0\}} = \frac{\Delta I(\varphi) - \mathcal{H}(\varphi)\Delta\varphi}{|\nabla\varphi|^2} = \frac{\Delta I(\varphi)}{|\nabla\varphi|^2} - \frac{(\nabla I(\varphi)\cdot\nabla\varphi)\Delta\varphi}{|\nabla\varphi|^4}$$

Both expressions above are approximated by second order central differences, and convergence at order two is indeed reported by Towers for the computation of surface integrals with the rectangle method as quadrature. While $\varphi$ does not need to be a distance function, better behavior is reported in that case. One fundamental feature of these approximations is that they do not rely on a discretization parameter such as $\varepsilon$ appearing in the smoothed approach. While this approach is very efficient in computing integrals, its ability to be fully used in the pointwise computation of forces would have to be further investigated.

## 1.6 Numerical Aspects II: Stability

In the ALE methods which are currently used for fluid-structure interaction problems, the questions of stability arise in particular through phenomena known under the terms of added mass, when the densities of fluids and solids are close. In Level Set methods, the situation is very different. Added mass is not an issue but stability issues are instead related to the types of temporal discretizations, explicit or implicit, used to couple the transport and Navier–Stokes equations, and occur when the stiffness coefficients are large. To study these questions it seems difficult to have a completely general framework and it is necessary to specify the coupling under consideration. We will consider the case of the surface tension already mentioned above in a flow with uniform density and viscosity and which, as we will see, is also relevant to more general fluid-structure problems.

Stability issues in Level Set methods in this framework have been studied in particular in [21, 50, 71, 116]. We generalize here to the three-dimensional case the analysis made in [19, 37]. We will see later how the conclusions of this analysis are generalized to the case of elastic membranes.

The system (1.32)–(1.34) reduces in the case of constant density and viscosity to the following system:

$$\partial_t u + u \cdot \nabla u + \nabla p - \mu \Delta u = \lambda H(\nabla \phi) \frac{1}{\varepsilon} \zeta \left( \frac{\varphi}{\varepsilon} \right) \nabla \varphi, \tag{1.39}$$

$$\operatorname{div} u = 0, \tag{1.40}$$

$$\partial_t \varphi + (u \cdot \nabla) \varphi = 0. \tag{1.41}$$

In the sequel we will study the linear stability of certain temporal discretizations of this system, around a steady-state consisting of a fluid at rest with a plane interface (it should be noted that these are not the only equilibrium states because the condition of incompressibility allows equilibrium states which are not of zero curvature, like the spheres in 3D). Without restricting the generality one can suppose

that the interface coincides with an axial plane, which gives for example

$$\bar{\varphi}(x) = x_1. \tag{1.42}$$

This function obviously statisfies

$$|\nabla\bar{\varphi}| \equiv 1\ ,\ H(\nabla\bar{\phi}) \equiv 0.$$

The linearization of the right-hand side of (1.39) therefore only involves the term which comes from the linearization of $H$. In the following one will note $\varphi$ the variation of the level set around the equilibrium profile $\bar{\varphi}$. An elementary differential calculus gives us

$$H(\nabla\bar{\phi} + \nabla\phi) = \sum_i \sum_j \partial_j\varphi \left( \frac{\delta_{ij}}{|\nabla\bar{\varphi}|} - \frac{\partial_i\bar{\varphi}\partial_j\bar{\varphi}}{|\nabla\bar{\varphi}|^3} \right)$$

which, due to the particular form of $\bar{\varphi}$, yields

$$H(\nabla\bar{\phi} + \nabla\phi) = \sum \partial_{ii}\varphi - \sum_{i,j} [\partial_i\bar{\varphi}\partial_j\bar{\varphi}]\partial_{ij}\varphi = \Delta\varphi - \partial_{11}\varphi.$$

where we noted $\partial_i = \partial/\partial x_i$ for $i \in [1,3]$ and $\partial_{ij} = \partial^2/\partial x_i x_j$. As for the linearization of the transport equation of $\varphi$, it is given by

$$\partial_t\varphi + (u\cdot\nabla)\bar{\varphi} = 0.$$

If we therefore seek a solution of the form $(u = (u_1,u_2,u_3), p, \bar{\varphi} + \varphi)$ the linearization of the system (1.39)–(1.41) leads to the system

$$\partial_t u_1 - \partial_1 p - \mu\Delta u_1 = \lambda(\Delta\varphi - \partial_{11}\varphi)\frac{1}{\varepsilon}\zeta\left(\frac{\varphi}{\varepsilon}\right)(x_1), \tag{1.43}$$

$$\partial_t u_2 - \partial_2 p - \mu\Delta u_2 = 0, \tag{1.44}$$

$$\partial_t u_3 - \partial_3 p - \mu\Delta u_3 = 0, \tag{1.45}$$

$$\partial_1 u_1 + \partial_2 u_2 + \partial_3 u_3 = 0, \tag{1.46}$$

$$\partial_t\varphi + u_1 = 0. \tag{1.47}$$

As the fluid-interface interaction is limited to the support of $\frac{1}{\varepsilon}\zeta\left(\frac{\varphi}{\varepsilon}\right)$ and to simplify the Fourier analysis, we will consider the system (1.43)–(1.47) in a band $\Omega = [-\varepsilon,+\varepsilon]\times[-\pi,+\pi]^2$, supplemented by periodic boundary conditions on the boundaries of $\Omega$. We will further assume that $\zeta \equiv 1/2$ in its support. We then

readily see that the solution of this system satisfies

$$u_2 = u_3 = p = 0\ ,\ u_1 = u_1(x_2, x_3)\ ,\ \varphi = \varphi(x_2, x_3),$$

as long as the initial conditions are of this form, with

$$\partial_t u_1 - \mu\, \Delta' u_1 = \frac{\lambda}{2\varepsilon}\, \Delta' \varphi, \tag{1.48}$$

$$\partial_t \varphi + u_1 = 0, \tag{1.49}$$

where we noted $\Delta' = \partial_{22} + \partial_{33}$. This system is posed in the domain $\Omega' = [-\pi, +\pi]^2$.

The following stability analysis will focus on the solutions of this system. We can already notice that by replacing $u_1$ by $-\partial_t \varphi$ in the first equation we get

$$\partial^2_{tt} \varphi - \mu\, \Delta' \partial_t \varphi = \frac{\lambda}{2\varepsilon}\, \Delta' \varphi. \tag{1.50}$$

In particular, if $\mu = 0$, this is a wave equation for $\varphi$ in the directions that are transverse to the surface. Despite the assumptions and simplifications made to obtain these particular forms of solutions, we will see that they make it possible to highlight stability criteria which confirm numerical studies and other empirical analysis of the literature.

The discretization in time of (1.32)–(1.34) naturally leads to explicit and implicit schemes. Rather than linearizing the discrete equations obtained from (1.32)–(1.34), one can in an equivalent fashion discretize the linearized equations obtained above. This is the approach we are going to take.

In the following, we are given a time step $\Delta t$, a grid size $\Delta x$ and a uniform grid of the plane $(x_2, x_3)$ of $\Omega$ with nodes $x_{\mathbf{i}} = (-\pi + i_1 \Delta x, -\pi + i_2 \Delta x), \mathbf{i} = (i_1, i_2) \in [1, N]^2$ with $N \Delta x = 2\pi$.We will denote by $(u, \varphi)$ the solution of (1.48)–(1.49), $u^n_{\mathbf{i}}, \varphi^n_{\mathbf{i}}$ the discrete solution provided by the schemes at time $t_n = n\Delta t$ and at the grid point $\mathbf{i}\Delta x$. Finally, we will consider the discrete Fourier transform of a periodic sequence $(u_{\mathbf{i}}, \varphi_{\mathbf{i}})$ of period $N$ defined by

$$u^n_{\mathbf{j}} = \sum_{\mathbf{k} \in [1,N]^2} \hat{u}_{\mathbf{k}} \exp\left[\, i\ (< \mathbf{j} \cdot \mathbf{k} > \Delta x)\right]\ , \tag{1.51}$$

$$\varphi^n_{\mathbf{j}} = \sum_{\mathbf{k} \in [1,N]^2} \hat{\varphi}_{\mathbf{k}} \exp\left[\, i\ (< \mathbf{j} \cdot \mathbf{k} > \Delta x)\right] \tag{1.52}$$

### 1.6.1 Explicit Scheme

A natural explicit scheme for the system (1.48)–(1.49) reads

$$\begin{cases} \dfrac{u_{\mathbf{j}}^{n+1} - u_{\mathbf{j}}^{n}}{\Delta t} - \mu \Delta_d u_{\mathbf{j}}^{n+1} = -\dfrac{\lambda}{\varepsilon} \Delta_d \varphi_{\mathbf{j}}^{n} \\ \dfrac{\varphi_{\mathbf{j}}^{n+1} - \varphi_{\mathbf{j}}^{n}}{\Delta t} + u_{\mathbf{j}}^{n+1} = 0 \\ u_{\mathbf{j}}^{0} = f_{\mathbf{j}},\ \varphi_{\mathbf{j}}^{0} = g_{\mathbf{j}}, \end{cases} \tag{1.53}$$

where $\Delta_d$ denotes the classical centered Laplacian:

$$\Delta_d u_{\mathbf{j}} = \frac{u_{j_1+1,j_2} - 2u_{j_1,j_2} + u_{j_1-1,j_2}}{(\Delta x)^2} + \frac{u_{j_1,j_2+1} - 2u_{j_1,j_2} + u_{j_1 j_2-1}}{(\Delta x)^2}$$

for $\mathbf{j} = (j_1, j_2)$. Let us note that the above scheme is explicit as regards the coupling between $u$ et $\varphi$, it suffices to solve the first equation before the second, but, classically, implicit in dealing with the diffusion equation for $u$.

The stability of this scheme is described by the following result.

**Proposition 1.11** *A necessary condition for the stability of the scheme (1.53) is*

$$\Delta t \leq \frac{\mu\varepsilon + \sqrt{\mu^2\varepsilon^2 + \frac{\lambda}{2}\varepsilon\Delta x^2}}{\lambda} \tag{1.54}$$

***Proof*** In the Fourier decomposition (1.51)–(1.52), the system (1.53) can be translated, for each wave number $k = (k_1, k_2)$, into the linear system

$$\begin{cases} \left(1 + \dfrac{4\mu\Delta t}{\Delta x^2}\alpha_k\right) \hat{u}_k^{n+1} = \hat{u}_k^n + \dfrac{4\lambda\Delta t}{\varepsilon\Delta x^2}\,\alpha_k\,\hat{\varphi}_k^n \\ \hat{\varphi}_k^{n+1} + \Delta t\,\hat{u}_k^{n+1} = \hat{\varphi}_k^n, \end{cases} \tag{1.55}$$

with

$$\alpha_k = \sin^2\left(\frac{k_1\Delta x}{2}\right) + \sin^2\left(\frac{k_2\Delta x}{2}\right)$$

or, in matrix form,

$$\begin{pmatrix} \hat{u}_k^{n+1} \\ \hat{\varphi}_k^{n+1} \end{pmatrix} = \begin{pmatrix} \dfrac{1}{\delta_k} & \dfrac{\beta_k}{\delta_k} \\ -\frac{\Delta t}{\delta_k} & 1 - \Delta t \frac{\beta_k}{\delta_k} \end{pmatrix} \begin{pmatrix} \hat{u}_k^{n} \\ \hat{\varphi}_k^{n} \end{pmatrix} = A_k \begin{pmatrix} \hat{u}_k^{n} \\ \hat{\varphi}_k^{n} \end{pmatrix}$$

with $\beta_k = \frac{4\lambda\Delta t}{\varepsilon \Delta x^2}\alpha_k$ and $\delta_k = 1 + \frac{4\mu\Delta t}{\Delta x^2}\alpha_k = 1 + \frac{\mu\varepsilon}{\lambda}\beta_k$.
The eigenvalues of the matrix $A_k$ are the roots of the ploynomial

$$\left(1 + \frac{\mu\varepsilon}{\lambda}\beta_k\right) r^2 - \left(2 + \left(\frac{\mu\varepsilon}{\lambda} - \Delta t\right)\beta_k\right) r + 1. \tag{1.56}$$

Let us assume that

$$\Delta t > \frac{\mu\varepsilon + \sqrt{\mu^2\varepsilon^2 + \frac{\lambda}{2}\varepsilon\Delta x^2}}{\lambda}, \tag{1.57}$$

and show that one of the eigenvalues has a modulus greater than 1, which contradicts stability. The discriminant of the polynomial (1.56) is given by

$$\Delta_k = 4\Delta t\, \beta_k \left(\left(\frac{\mu\varepsilon}{\lambda} - \Delta t\right)^2 \frac{\lambda}{\varepsilon\Delta x^2}\alpha_k - 1\right).$$

From (1.57) we also have

$$\Delta t > \frac{\mu\varepsilon}{\lambda} + \Delta x\sqrt{\frac{\varepsilon}{2\lambda}}$$

and thus

$$\left(\frac{\mu\varepsilon}{\lambda} - \Delta t\right)^2 \frac{\lambda}{\varepsilon\Delta x^2} > \frac{1}{2}.$$

As a result, there are values of $k$ such that the discriminant of (1.56) is positive. For these modes the eigenvalues are therefore real. Denote by $r_-$ the smallest eigenvalue and show by the absurd that $r_- < -1$. We can write

$$\begin{aligned} & r_- \geq -1 \\ \Leftrightarrow\ & 2 + \left(\frac{\mu\varepsilon}{\lambda} - \Delta t\right)\beta_k - \sqrt{\beta_k}\sqrt{\left(\frac{\mu\varepsilon}{\lambda} - \Delta t\right)^2 \beta_k - 4\Delta t} \\ & \geq -2 - 2\frac{\mu\varepsilon}{\lambda}\beta_k \\ \Leftrightarrow\ & 4 + \left(\frac{3\mu\varepsilon}{\lambda} - \Delta t\right)\beta_k \geq \sqrt{\beta_k}\sqrt{\left(\frac{\mu\varepsilon}{\lambda} - \Delta t\right)^2 \beta_k - 4\Delta t} \geq 0 \end{aligned}$$

By taking the square of this inequality we obtain

$$r_- \geq -1 \Rightarrow \frac{\mu\varepsilon}{\lambda}\left(\frac{2\mu\varepsilon}{\lambda} - \Delta t\right)\beta_k^2 + \left(\frac{6\mu\varepsilon}{\lambda} - \Delta t\right)\beta_k + 4 \geq 0. \quad (1.58)$$

Consider now the polynomial in $\beta_k$ above. Since, according to (1.57), $\Delta t > 2\mu\varepsilon/\lambda$, its roots are real, of opposite signs and given by $\beta_- = -\dfrac{\lambda}{\mu\varepsilon}$, $\beta_+ = \dfrac{4}{\Delta t - \frac{2\mu\varepsilon}{\lambda}}$. From (1.57) one gets $\Delta t > \frac{2\mu\varepsilon}{\lambda}$ and $\beta_+ > 0$ and we deduce from (1.58) that we must have $\beta_k \leq \beta_+$. But if $\beta_k \leq \beta_+$ for all $k$ this implies

$$\frac{2\lambda\Delta t}{\varepsilon\Delta x^2} \leq \frac{1}{\Delta t - 2\mu\frac{\varepsilon}{\lambda}},$$

or

$$\lambda\Delta t^2 - 2\mu\varepsilon\Delta t - \frac{\varepsilon}{2}\Delta x^2 \leq 0.$$

We can easily see by considering the polynomial in $\Delta t$ above and its two real roots that this inequality in turn leads to the inequality

$$\Delta t \leq \frac{\mu\varepsilon + \sqrt{\mu^2\varepsilon^2 + \frac{\lambda}{2}\varepsilon\Delta x^2}}{\lambda}$$

which contradicts (1.57). We have therefore proved that $r_- < -1$, which shows that the scheme is not stable and completes this proof. □

*Remark 1.12* Let us make a few remarks about this stability result.

- In practice, one generally chooses $\varepsilon$ of the order of $\Delta x$, so that the dependence of the time step with respect to the grid size is in $\Delta x^{3/2}$.
- In the case of a vanishing viscosity, the stability condition (1.54) becomes

  $$\Delta t \leq \sqrt{\frac{\varepsilon}{2\lambda}}\Delta x,$$

  as one would expect from the wave equation (1.50) satisfied by $\varphi$ in this case. This condition agrees with the condition found in [21] for high Reynolds number flows.
- For large values of the viscosity (and/or small values of the surface tension), we obtain the condition

  $$\Delta t \leq \frac{2\mu}{\lambda}\varepsilon,$$

  a condition similar to the condition found in [71].

Finally, note that for the explicit scheme which would use $u^n$ instead of $u^{n+1}$ in the equation for $\varphi$ the condition of stability would be more demanding. In the case of zero viscosity, for example, the resulting scheme would be unconditionally unstable (see [19] for more details).

### 1.6.2 Implicit Scheme

A natural implicit scheme for the system (1.48)–(1.49) is to take $\varphi^{n+1}$ instead of $\varphi^n$ in the right hand side for the equation on $u$. We obtain the following scheme

$$\begin{cases} \dfrac{u_{\mathbf{j}}^{n+1} - u_{\mathbf{j}}^n}{\Delta t} - \mu \Delta_d u_{\mathbf{j}}^{n+1} = -\dfrac{\lambda}{\varepsilon} \Delta_d \varphi_{\mathbf{j}}^{n+1} \\ \dfrac{\varphi_{\mathbf{j}}^{n+1} - \varphi_{\mathbf{j}}^n}{\Delta t} + u_{\mathbf{j}}^{n+1} = 0 \\ u_j^0 = f_j, \varphi_j^0 = g_j. \end{cases} \tag{1.59}$$

This scheme requires the inversion of a linear system. In the case of the original system (1.32)–(1.34) it requires the calculation of a fixed point, which makes it expensive. The counterpart is in the following result.

**Proposition 1.13** *The scheme (1.59) is unconditionally stable.*

***Proof*** In the Fourier decomposition (1.51)–(1.52), and with the notations of the previous proof, the scheme (1.59) reads for each mode $k$:

$$\begin{aligned} \delta_k \, \hat{u}_k^{n+1} - \beta_k \, \hat{\varphi}_k^{n+1} &= u_k^n \\ \Delta t \, \hat{u}_k^{n+1} + \hat{\varphi}_k^{n+1} &= \hat{\varphi}_k^n, \end{aligned}$$

or

$$\begin{pmatrix} \hat{u}_k^{n+1} \\ \hat{\varphi}_k^{n+1} \end{pmatrix} = \frac{1}{\delta_k + \beta_k \Delta t} \begin{pmatrix} 1 & \beta_k \\ -\Delta t & \delta_k \end{pmatrix} \begin{pmatrix} \hat{u}_k^n \\ \hat{\varphi}_k^n \end{pmatrix} = A_k' \begin{pmatrix} \hat{u}_k^n \\ \hat{\varphi}_k^n \end{pmatrix}.$$

The eigenvalues of $A_k'$ are the roots of the polynomial

$$(\frac{1}{\delta_k + \beta_k \Delta t} - r)(\frac{\delta_k}{\delta_k + \beta_k \Delta t} - r) + \frac{\beta_k \Delta t}{\delta_k + \beta_k \Delta t} = r^2 - r(\frac{1 + \delta_k}{\delta_k + \beta_k \Delta t}) + \frac{1}{\delta_k + \beta_k \delta_k}.$$

If its discriminant is negative, its roots have modulus $(\delta_k + \beta_k \Delta t)^{-1} < 1$ and the system is stable. If its discriminant is positive, its two roots are positive, because they have positive product and sum, and the larger root is given by

$$r_+ = \frac{1 + \delta_k + \sqrt{(1-\delta_k)^2 - 4\beta_k \Delta t}}{2(\delta_k + \beta_k \Delta t)}.$$

For $k = 0$ we easily check that $\hat{u}_0^n = \hat{u}_0^0$ and $\hat{\varphi}_0^n = \hat{\varphi}_0^0 - n\Delta t \hat{u}_0^0$. If $k \neq 0$ then $\beta_k > 0$ and

$$r_+ < \frac{1 + \delta_k + \delta_k - 1}{2\delta_k} = 1.$$

The scheme is therefore unconditionally stable. □

### *1.6.3 Semi-Implicit Scheme*

We therefore have, on the one hand an explicit scheme, simple to implement and inexpensive, but which requires time steps with a dependence in $\Delta x^{3/2}$ which can turn out to be very drastic in the cases with low viscosity and/or large surface tension, and, on the other hand, an implicit scheme, unconditionally stable but expensive to implement. In this section we derive a semi-explicit scheme, of cost comparable to that of the explicit scheme but with better stability properties.

To write this scheme, we start from the implicit scheme (1.59) to write from the first equation

$$u_{\mathbf{j}}^{n+1} = u_{\mathbf{j}}^n + \mu \Delta t \Delta_d u_{\mathbf{j}}^{n+1} - \frac{\lambda}{\varepsilon} \Delta t \Delta_d \varphi_{\mathbf{j}}^{n+1}.$$

This allows to obtain from the second equation

$$\varphi_{\mathbf{j}}^{n+1} = \varphi_{\mathbf{j}}^n - \Delta t u_{\mathbf{j}}^n + \mu \Delta t^2 \Delta_d u_{\mathbf{j}}^{n+1} + \frac{\lambda}{\varepsilon} \Delta t^2 \Delta_d \varphi_{\mathbf{j}}^{n+1}.$$

The idea is then to calculate a predictor of $\varphi^{n+1}$ by forgetting the term in $\Delta_d u^{n+1}$ in the above equation. In other words, we start by solving

$$\frac{\psi_{\mathbf{j}}^{n+1} - \varphi_{\mathbf{j}}^n}{\Delta t} - \frac{\lambda}{\varepsilon} \Delta t^2 \Delta_d \psi_{\mathbf{j}}^{n+1} = -u_{\mathbf{j}}^n \tag{1.60}$$

then the equation on $u$

$$\frac{u_{\mathbf{j}}^{n+1} - u_{\mathbf{j}}^{n}}{\Delta t} - \mu \Delta_d u_{\mathbf{j}}^{n+1} = -\frac{\lambda}{\varepsilon} \Delta_d \psi_{\mathbf{j}}^{n+1} \tag{1.61}$$

and, finally, the transport equation on the Level Set $\varphi$

$$\frac{\varphi_{\mathbf{j}}^{n+1} - \varphi_{\mathbf{j}}^{n}}{\Delta t} + u_{\mathbf{j}}^{n+1} = 0. \tag{1.62}$$

We can notice that (1.60) consists of a time step of an implicit scheme for a diffusion equation, with initial condition $\varphi^n$ and diffusion coefficient $\Delta t\, \lambda/\varepsilon$. Compared to the explicit method seen previously, $\psi^{n+1}$ can be seen like a perturbation of $\varphi^n$ only used for the computation of the force of surface tension in the fluid.

It is important to note that the transport of the interface remains ensured by the original transport equation (1.62) and that $\psi^{n+1}$ intervenes only in an auxiliary way for the computation of the right side of the equation for $u$ (or for the Navier–Stokes equation when the scheme is used on the complete model).

The justification for this method is given by the

**Proposition 1.14** *The semi-implicit scheme (1.60), (1.61) and (1.62) is unconditionnally stable.*

***Proof*** We recall the notations already introduced for the previous methods. The scheme (1.60), (1.61), (1.62) is translated in the Fourier decomposition by the system

$$\alpha_k = \sin^2\left(\frac{k_1 \Delta x}{2}\right) + \sin^2\left(\frac{k_2 \Delta x}{2}\right),$$

$$\beta_k = \frac{4\lambda \Delta t}{\varepsilon \Delta x^2} \alpha_k, \quad \delta_k = 1 + \frac{4\mu \Delta t}{\Delta x^2} \alpha_k = 1 + \frac{\mu \varepsilon}{\lambda} \beta_k.$$

or, in matrix form after substitution of the first equation in the second,

$$A_k \begin{pmatrix} \hat{u}_k^{n+1} \\ \hat{\varphi}_k^{n+1} \end{pmatrix} = B_k \begin{pmatrix} \hat{u}_k^{n} \\ \hat{\varphi}_k^{n} \end{pmatrix}$$

with

$$A_k = \begin{pmatrix} \delta_k & 0 \\ \Delta t & 1 \end{pmatrix} \qquad B_k = \begin{pmatrix} \frac{1}{1+\Delta t \beta_k} & \frac{\beta_k}{1+\Delta t \beta_k} \\ 0 & 1 \end{pmatrix}.$$

Let us start with the case $k = 0$. In that case $\delta_0 = 1$ and $\beta_0 = 0$, and we immediately see that

$$\left[A_0^{-1} B_0\right]^n = \begin{pmatrix} 1 & 0 \\ -n\Delta t & 1 \end{pmatrix}$$

and the scheme is stable for this mode.

Let us now look at the general case $k \neq 0$. The eigenvalues of $A_k^{-1} B_k$ are the solutions of $\det(A_k^{-1} B_k - r\mathbb{I}) = 0$, or $\det(B_k - r A_k) = 0$. This leads to the equation

$$\beta'_k \delta'_k r^2 - r[1 + \beta'_k \delta'_k - \Delta t \beta_k] + 1 = 0$$

where we have set $\beta'_k = 1 + \Delta t \beta_k$. The product of the roots $r_1 r_2$ is equal to $1/(\beta'_k \delta'_k) < 1$ for $k \neq 0$. If the roots are not real, they are therefore of modulus strictly less than 1. If they are real they have the same sign, positive because their sum is equal to $1 + \beta'_k \delta_k - \Delta t \beta_k = 2 + \delta_k + \Delta t \beta_k \delta_k > 0$. We can moreover write, for $\Delta t > 0$,

$$\begin{aligned} r_i &\leq \frac{1 + \beta'_k \delta_k - \Delta t \beta_k + \sqrt{(1 + \beta'_k \delta_k - \Delta t \beta_k)^2 - 4\beta'_k \delta_k}}{2\beta'_k \delta_k} \\ &< \frac{1 + \beta'_k \delta_k + \sqrt{(1 + \beta'_k \delta_k)^2 - 4\beta'_k \delta_k}}{2\beta'_k \delta_k} \\ &< \frac{1 + \beta'_k \delta_k + \sqrt{(1 - \beta'_k \delta_k)^2}}{2\beta'_k \delta_k} = 1. \end{aligned}$$

The spectral radius of $A_k^{-1} B_k$ is therefore strictly less than 1 and the system is stable. □

We will provide in the next chapter numerical illustrations of the results given in this section and simultaneously extend the definitions of the methods to the case of the interaction of a fluid with an elastic membrane.

# Chapter 2
# Mathematical Tools for Continuum Mechanics


In this chapter we list a few of definitions and mathematical results relating to the notions of trajectories in a smooth velocity field. We also recall certain principles of conservation in continuous media.

We place ourselves under the assumption of a regular velocity field:

$$(H) \qquad u \in \mathcal{C}^1(\overline{\Omega} \times [0, T]) \text{ and } u = 0 \text{ on } \partial\Omega \times [0, T]$$

where $[0, T]$ is a fixed time interval.

## 2.1 Characteristics and Flows Associated with a Velocity Field

Let us start by giving some notations and recalling elementary results of differential calculus related to the trajectories associated with a velocity field. Given a function $f$ defined from $\mathbb{R}^d$ into $\mathbb{R}$, we note $Df$ its differential and $\nabla f$ its gradient. We therefore have for all $h \in \mathbb{R}^d$, $Df(x)(h) = \nabla f(x) \cdot h$. For a vector field $v : \mathbb{R}^d \to \mathbb{R}^d$, $[Dv]$ is the differential of $v$, that is the linear matrix $\nabla v = [\partial_{x_j} v_i]_{ij}$. With these notations, for $\varphi : \mathbb{R}^d \to \mathbb{R}$, $v : \mathbb{R}^d \to \mathbb{R}^d$ and $X : \mathbb{R}^d \times ]0, T[ \to \mathbb{R}^d$ we have the following chain rule formulas:

$$\partial_t(\varphi(X)) = \nabla\varphi(X) \cdot \partial_t X,$$

$$\nabla(\varphi(X)) = [\nabla X]^T (\nabla\varphi)(X),$$

$$\nabla(v(X)) = [\nabla v](X)[\nabla X],$$



G.-H. Cottet et al., *Level Set Methods for Fluid-Structure Interaction*, Applied Mathematical Sciences 210, https://doi.org/10.1007/978-3-031-08659-5_2

where the composition of the applications was noted by a multiplication. For $\xi \in \Omega$ and $s \in ]0, T]$, we denote by $\tau \to X(\tau; \xi, s)$ the solution of the differential system

$$\partial_\tau X = u(X, \tau)$$

supplemented with the initial condition

$$X(s) = \xi.$$

The solution of this system exists and is unique in the classical framework, for example under the assumption that the velocity field is lipschitzian at $x$, uniformly with respect to $t$. The no-slip condition at the boundary imposed on the velocity field implies that these trajectories do not reach the boundary of the domain. More general solutions, defined almost everywhere, have been introduced by Lions and DiPerna [51]. We have placed ourselves within the framework of a smooth velocity field (assumption $(H)$, which is stronger than $u$ uniformly Lipschitzian because $\Omega$ is bounded), so that we restrict ourselves here to classical solutions.

The physical interpretation of $X(\tau; \xi, s)$ is the position at time $\tau$ of a particle in the continuous medium located at time $s$ at position $\xi$. Let us start with the following result:

**Lemma 2.1** *Under the assumption $(H)$ we get*

$$\forall (t_1, t_2) \in [0, T]^2, \ \forall x \in \Omega, \qquad X(t_1; X(t_2; x, t_1), t_2) = x.$$

***Proof*** Let $\xi = X(t_2; x, t_1)$. Then $X(\tau; \xi, t_2)$ is solution to the differential system $\partial_\tau X = u(X, \tau)$ under the condition $X(t_2) = \xi$. But $X(\tau; x, t_1)$ is the solution of the same system and satisfies $X(t_2; x, t_1) = \xi$. According to $(H)$ the solution of this system is unique, and thus $X(\tau; x, t_1) = X(\tau; \xi, t_2)$. In particular we have the desired identity for $\tau = t_1$, since $X(t_1; x, t_1) = x$. □

The above property tells us that the mapping $x \to X(t_1; x, t_2)$ is invertible, with inverse $X(t_2; \cdot, t_1)$. As a matter of fact, we have more:

**Proposition 2.2** *The mapping $x \to X(t_1; x, t_2)$ is a $\mathcal{C}^1$-diffeomorphism in $\Omega$. Its Jacobian $J(t_1; x, t_2)$, is continuous and strictly positive in $x$, and such that $t \to J(t; x, t_2)$ is of class $C^1$ and satisfies*

$$\partial_t J(t_1; x, t_2) = (\operatorname{div} u)(X(t_1; x, t_2), t_1) J(t_1; x, t_2).$$

***Proof*** The invertibility of $x \to X(t_1; x, t_2)$ directly comes from the above lemma. The $\mathcal{C}^1$ regularity of $X$ is classical under the assumptions made on $u$; this indeed corresponds to a regularity result of the solution of a differential system with respect to the parameters. To see this, let us set $Z(\tau; x, t) = X(\tau + t; x, t) - x$. The differential system in $X$ is equivalent to the differential system $\partial_\tau Z = u(Z+x, \tau+t)$ with initial condition $Z(0) = 0$. Since $u$ has been assumed of class $\mathcal{C}^1$ in $(x, t)$ we deduce that $X$ is of class $\mathcal{C}^1$ with respect to $(\tau, x, t)$, for instance as a consequence of [48], p. 286, or theorem 3.6.1 in [28]. The reader is also referred to [49], pp. 182 to 192. By differentiating the relation of Lemma 2.1 with respect to $x$, we obtain

$$[DX](t_1; X(t_2; \xi, t_1), t_2)[DX](t_2; x, t_1) = \mathbb{I}_d,$$

where $\mathbb{I}_d$ represents the identity matrix of $M_d(\mathbb{R})$. By taking the determinant, we obtain

$$J(t_2; x, t_1) J(t_1; X(t_2; \xi, t_1), t_2) = 1,$$

which proves that $J$ never vanishes. For fixed $(x, t)$, since $M : \tau \to \nabla_x X(\tau; x, t)$ satisfies $\partial_\tau M = \nabla_x u(X(\tau; x, t), \tau) M$ with $M(t) = \mathbb{I}_d$, and $\tau \to \nabla_x u(X(\tau; x, t), \tau)$ is continuous, $\tau \to \nabla_x X(\tau; x, t)$ and therefore $\tau \to J(\tau; x, t)$ are of class $\mathcal{C}^1$. As $J(t; x, t) = 1$, and $J$ does not vanish, it is always strictly positive. To obtain the announced differentiation formula, we use the following elementary lemma

**Lemma 2.3** *Let $A : (0, T) \to M_d(\mathbb{R})$ be a field of matrices of class $\mathcal{C}^1$ in $(0, T)$. We have*

$$\frac{d}{dt} \det A(t) = \operatorname{tr}(Cof(A)^T A'(t)),$$

*where $Cof(A)$ is the matrix of cofactors of $A$. If $A$ has values in the set of invertible matrices, the above expression becomes*

$$\frac{d}{dt} \det A(t) = \det A(t) \operatorname{tr}(A^{-1}(t) A'(t)).$$

This lemma can be proved simply by expanding the determinant to obtain the relation $\det(A + tE_{ij}) = \det(A) + t[\mathrm{Cof}(A)]_{ij}$ where $E_{ij}$ denotes the vectors of the canonical basis of the matrices. This leads to $\det'(A)(H) = \sum_{i,j} [\mathrm{Cof}(A)]_{ij} H_{ij} = \mathrm{Tr}(\mathrm{Cof}(A)^T H) = \det(A)\,\mathrm{Tr}(A^{-1} H)$.

Applying this lemma to $A(t) = \nabla_\xi X(t; x, t_2)$ yields

$$\partial_t(\det(\nabla_\xi X(t;\xi,t_2))) = \det(\nabla_\xi X)\,\mathrm{Tr}([\nabla_\xi X]^{-1}\nabla_\xi(u(X(t,\xi),t))) \\ = \det(\nabla_\xi X)\,\mathrm{div}(u)(X(t,\xi),t).$$

□

*Remark 2.4* It will be interesting in the following to consider the function $t \to X(\tau; x, t)$, for fixed values of $\tau$ and $x$. If we differentiate with respect to $t$ the identity $X(\tau; X(t; x, \tau), t) = x$ shown in Lemma 2.1, we get

$$\partial_t X(\tau; X(t; x, \tau), t) + [DX](\tau; X(t; x, \tau), t)\partial_\tau X(t; x, \tau) = 0.$$

Furthermore $\partial_\tau X(\tau; x, t) = u(X(\tau; x, t), \tau)$ and we notice that $[DX]u$ can be rewritten in the form $u \cdot \nabla X$. By renaming $X(\tau; x, t)$ as $x$, we thus obtain

$$\partial_t X(\tau; x, t) + u(x, t) \cdot \nabla X(\tau; x, t) = 0. \tag{2.1}$$

The function $(x, t) \to X(\tau; x, t)$ therfore satisfies the transport equation $\partial_t X + u \cdot \nabla X = 0$ with the initial condition at $t = \tau$: $X(\tau; x, \tau) = x$.

With these notations, we call Lagrangian variables the couple $(t, \xi)$, and Eulerian variables the couple $(x, t)$ where $x = X(t; \xi, 0)$. In order to simplify we will use in the sequel the notation $X(t, \xi)$ for this quantity. Note that symmetrically, we have from the above lemma $\xi = X(0; x, t)$. This last quantity will be noted to simplify $Y(x, t)$. The order of the temporal and spatial variables in these two versions of characteristics is on purpose, to reflect the dynamic system underlying the Lagrangian coordinates (Fig. 2.1).

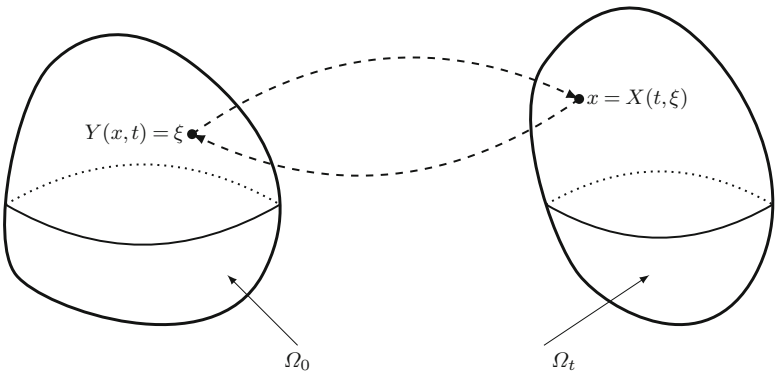


**Fig. 2.1** Initial and deformed configurations

In this framework, the regularity of the change of Eulerian-Lagrangian variables therefore makes it possible to switch from one representation to another in a seamless fashion. To summarize the properties of these functions that will be used constantly in the following, we have

$$X(t, Y(x,t)) = x, \qquad Y(X(t,\xi),t) = \xi, \tag{2.2}$$

and

$$\partial_t X = u(X,t), \qquad X(0,\xi) = \xi, \tag{2.3}$$

$$\partial_t Y + (u\cdot\nabla)Y = 0, \qquad Y(x,0) = x. \tag{2.4}$$

By differentiating (2.2) with respect to $x$ or $\xi$ we obtain

$$[\nabla_\xi X(t,\xi)] = [\nabla_x Y(x,t)]^{-1}. \tag{2.5}$$

This relationship is the key point of the Eulerian formulation of elasticity because the Lagrangian strain is calculated using the backward characteristics, which themselves are Level Set functions for the underlying flow.

The determinants of these Jacobian matrices satisfy dual equations. It is convenient to introduce additional notations for the Jacobians. From Proposition 2.2 we define the determinant $J_\ell(t,\xi) = J(t;\xi,0) = \det(\nabla_\xi X(t,\xi))$ and its Eulerian counterpart $J_e(x,t) = J_\ell(t,\xi) = \det(\nabla_x Y(x,t))^{-1}$ where $x = X(t,\xi)$.

The Jacobian $J_\ell$ satisfies a flow equation

$$\partial_t J_\ell(t,\xi) = J_\ell(t,\xi)(\operatorname{div} u)(X(t,\xi),t) \tag{2.6}$$

while its Eulerian analogue $J_e(x,t)$, satisfies the equation

$$\partial_t J_e(x,t) + u(x,t)\cdot\nabla J_e(x,t) = J_e(x,t)(\operatorname{div} u)(x,t). \tag{2.7}$$

## 2.2 Change of Variables

Under the assumption $(H)$, according to Proposition 2.2, the maps $X(t,\cdot)$ preserve the orientation, that is

$$J_\ell(t,\xi) = \det(\nabla_\xi X(t,\xi)) > 0.$$

This relation will make it possible to remove the modulus of the Jacobian in the change of variables to evaluate volume integrals.

**Proposition 2.5** *Let $f : \mathbb{R}^3 \to \mathbb{R}$ be a smooth function over a domain $\omega_t$ in $\mathbb{R}^3$ which is itself the image by a smooth application $X(t, \cdot)$ of a domain $\omega_0$ of $\mathbb{R}^3$. Then we have the change of variables formula*

$$\int_{\omega_t = X(t,\omega_0)} f(x,t)dx = \int_{\omega_0} f(X(t,\xi),t)\det(\nabla_\xi X(t,\xi))\,d\xi. \tag{2.8}$$

***Proof*** Consider a basis $(e_1, e_2, e_3)$ in $\mathbb{R}^3$. The volume element $d\xi$ of the associated parallelepiped is given by the mixed product or the determinant of the three vectors in the initial configuration: $d\xi = (e_1 \times e_2) \cdot e_3 = \det(e_1, e_2, e_3)$. These vectors are transformed in the deformed configuration into the vectors $a_i = [\nabla_\xi X]e_i$ because

$$X(\xi + h) = X(\xi) + [\nabla_\xi X]h + o(h) \tag{2.9}$$

The volume element $dx$ can be written in the deformed configuration as

$$\begin{aligned} dx &= \det(a_1, a_2, a_3) = \det([\nabla_\xi X]e_1, [\nabla_\xi X]e_2, [\nabla_\xi X]e_3) \\ &= \det([\nabla_\xi X])\det(e_1, e_2, e_3) = \det([\nabla_\xi X])\,d\xi. \end{aligned}$$

□

For surfaces, the general formula for change variables is given by the following proposition:

**Proposition 2.6** *Under the assumptions of Proposition 2.5, if $S_t$ (resp $S_0$) is the boundary of $\omega_t$ (resp $\omega_0$) we have*

$$\int_{S_t = X(t,S_0)} f(x,t)\,ds = \int_{S_0} f(X(t,\xi),t)|\operatorname{Cof}(\nabla_\xi X(t,\xi))n_0(\xi)|\,ds_0 \tag{2.10}$$

*where $n_0$ is a unit vector field normal to $S_0$.*

***Proof*** We use a parameterization of the surface to rewrite the surface integral as an integral on an open set of $\mathbb{R}^2$. Let us consider the vectors $e_1$ and $e_2$ associated with the parameterization in the initial configuration. These vectors form a basis of the tangent plane and are calculated by taking the derivatives of the parameterization. We then have $n_0(\xi) = e_1 \times e_2/|e_1 \times e_2|$ and the surface element in the initial

configuration is written $ds_0 = |e_1 \times e_2|$. These vectors are transformed in the deformed configuration into the vectors $a_i = [\nabla_\xi X]e_i$, and for any vector $v$

$$\begin{aligned}([\nabla_\xi X]e_1 \times [\nabla_\xi X]e_2) \cdot [\nabla_\xi X]v &= \det([\nabla_\xi X]e_1, [\nabla_\xi X]e_2, [\nabla_\xi X]v) \\ &= \det([\nabla_\xi X])(e_1 \times e_2) \cdot v.\end{aligned}$$

As a result

$$\begin{aligned}([\nabla_\xi X]e_1 \times [\nabla_\xi X]e_2) \cdot [\nabla_\xi X]v &= \det([\nabla_\xi X]e_1, [\nabla_\xi X]e_2, [\nabla_\xi X]v) \\ &= \det([\nabla_\xi X])(e_1 \times e_2) \cdot v.\end{aligned}$$

We thus have

$$n(X(t,\xi),t) = \frac{a_1 \times a_2}{|a_1 \times a_2|} = \frac{\mathrm{Cof}(\nabla_\xi X(t,\xi))n_0(\xi)}{|\mathrm{Cof}(\nabla_\xi X(t,\xi))n_0(\xi)|} \tag{2.11}$$

and the surface element $ds$ in the deformed configuration reads

$$ds = |a_1 \times a_2| = |\mathrm{Cof}([\nabla_\xi X])n_0||e_1 \times e_2| = |\mathrm{Cof}([\nabla_\xi X])n_0|\, ds_0.$$

We can easily deduce, for a matrix field $\sigma$,

$$\begin{aligned}&\int_{S_t = X(S_0,t)} \sigma(x,t)n(x,t)\, ds = \\ &\int_{S_0} \sigma(X(t,\xi),t)\,\mathrm{Cof}(\nabla_\xi X(t,\xi))n_0(\xi) ds_0,\end{aligned} \tag{2.12}$$

where $n(x,t)$ is the normal at $x \in S_t$ and $n_0(\xi)$ is the normal at $\xi \in S_0$. □

For curves, the general formula for change of variables is given by the following proposition:

**Proposition 2.7** *Let $f : \mathbb{R}^3 \to \mathbb{R}$ be a smooth function on a smooth curve $\Gamma_t$ in $\mathbb{R}^3$, image by a smooth mapping $X$ of a smooth curve $\Gamma_0$ in $\mathbb{R}^3$. We then have the change of variables formula*

$$\int_{X(t,\Gamma_0)=\Gamma_t} f(x,t)\, dl = \int_{\Gamma_0} f(X(t,\xi),t)|\nabla_\xi X(t,\xi)\tau_0(\xi)|\, dl_0, \tag{2.13}$$

*where $\tau_0$ is a field of unit tangent vectors to $\Gamma_0$.*

***Proof*** This formula is obtained by mapping the curve to an open set of $\mathbb{R}$ by an appropriate parametrization. We consider $e_1$ a tangent vector in the initial configuration, obtained by differentiating the parametrization. A unit tangent vector is given by $\tau_0(\xi) = e_1/|e_1|$ and the length element in the initial configuration is $dl_0 = |e_1|$. The vector $e_1$ is mapped in the deformed configuration into a vector $a_1 = [\nabla_\xi X]e_1$. We get the following relation

$$\tau(X(t,\xi),t) = \frac{a_1}{|a_1|} = \frac{[\nabla_\xi X]\tau_0(\xi)}{|[\nabla_\xi X]\tau_0(\xi)|} \tag{2.14}$$

and the length element $dl$ in the deformed configuration is

$$dl = |a_1| = |[\nabla_\xi X]e_1| = |[\nabla_\xi X]\tau_0|\, dl_0$$

□

*Remark 2.8* In the two-dimensional case we have a similarity between (2.13) and (2.10) as

$$|\operatorname{Cof}([\nabla_\xi X])n_0| = |[\nabla_\xi X]\boldsymbol{\tau}_0|.$$

Indeed, by taking the square of this identity we obtain, using the notation $C = [\nabla_\xi X]^T[\nabla_\xi X]$,

$$\det(C)(C^{-1}n_0)\cdot n_0 = (C\tau_0)\cdot\tau_0.$$

We conclude using the relation $\tau_0 \otimes \tau_0 = \mathbb{I} - n_0 \otimes n_0$ and the Cayley–Hamilton identity $A - \operatorname{Tr}(A)I + \det(A)A^{-1} = 0$ valid for $2 \times 2$ matrices.

In what follows, we consider a volume domain $\omega_t$ which moves over time with a velocity field $(x,t) \to u(x,t)$ satisfying the assumption $(H)$. In other words we have $\omega_t = X(t,\omega_0)$. To obtain the equations of the continuous medium, we will apply the principles of mechanics to this volume $\omega_t$. The variations of quantities such as mass, momentum or energy in the domain $\omega_t$ will therefore be carried out using time derivatives.

## 2.3 Reynolds Formulas

The Reynolds formulas that we recall and demonstrate below are the basis for the transcription as partial differential equations of the principles of conservation in continuum mechanics which will be stated in the following sections.

**Proposition 2.9** *Let an open set $\omega_0 \subset \Omega$, and let $\omega_t = X(t, \omega_0)$. Let $f \in \mathcal{C}^1(\overline{\Omega} \times [0, T])$. Then*

$$\frac{d}{dt}\int_{\omega_t} f(x,t)\,dx = \int_{\omega_t} \partial_t f + \operatorname{div}(fu)\,dx. \tag{2.15}$$

***Proof*** Indeed, according to (2.8),

$$\begin{aligned}\frac{d}{dt}\int_{\omega_t} f(x,t)\,dx &= \frac{d}{dt}\int_{\omega_0} f(X(t,\xi),t)J_\ell(t,\xi)\,d\xi \\ &= \int_{\omega_0} (\partial_t X(t,\xi)\cdot\nabla f(X(t,\xi),t) + \partial_t f(X(t,\xi),t))J_\ell(t,\xi) \\ &\qquad + f(X(t,\xi),t)\partial_t J_\ell(t,\xi)\,d\xi.\end{aligned}$$

From Proposition 2.2 we therefore have

$$\begin{aligned}\frac{d}{dt}\int_{\omega_t} f(x,t)\,dx &= \int_{\omega_0} (u(X(t,\xi),t)\cdot\nabla f(X(t,\xi),t) + \partial_t f(X(t,\xi),t))J_\ell(t,\xi) \\ &\qquad + f(X(t,\xi),t)(\operatorname{div} u)(X(t,\xi),t)J_\ell(t,\xi)\,d\xi \\ &= \int_{\omega_0} (\partial_t f + \operatorname{div}(fu))(X(t,\xi),t)J_\ell(t,\xi)\,d\xi = \int_{\omega_t} \partial_t f + \operatorname{div}(fu)\,dx.\end{aligned}$$

□

We have a similar result for a surface moving within a continuous medium:

**Proposition 2.10** *Let $S_0$ be a smooth surface included in $\Omega$ and $S_t = X(t, S_0)$. Let $f \in \mathcal{C}^1(\overline{\Omega} \times [0, T])$. Then*

$$\frac{d}{dt}\int_{S_t} f(x,t)\,ds = \int_{S_t} \partial_t f + \operatorname{div}(fu) - f(\nabla u\, n)\cdot n\,ds, \tag{2.16}$$

*where $n$ is a unit vector field normal to $S_t$.*

***Proof*** Indeed by using the change of variable formula (2.12),

$$\frac{\mathrm{d}}{\mathrm{d}t}\left(\int_{S_t} f(x,t)\,ds\right)$$
$$= \int_{S_0} \partial_t(f(X(t,\xi),t)\det([\nabla_\xi X(t,\xi)]))|[\nabla_\xi X(t,\xi)]^{-T} n_0(\xi)|\,ds_0$$
$$+ \int_{S_0} f(X(t,\xi),t)\det([\nabla_\xi X(t,\xi)])\partial_t(|[\nabla_\xi X(t,\xi)]^{-T} n_0(\xi)|)\,ds_0.$$

For the first term we use the previous calculations

$$\partial_t(f(X(t,\xi),t)\det([\nabla_\xi X(t,\xi)]))$$
$$= (\partial_t f + u\cdot\nabla f + f\,\mathrm{div}(u))(X(t,\xi),t)\det([\nabla_\xi X(t,\xi)]).$$

We have, with $(A^{-1})'(t) = -A^{-1}(t)A'(t)A^{-1}(t)$ and $\partial_t[\nabla_\xi X] = [\nabla_x u][\nabla_\xi X]$,

$$\partial_t([\nabla_\xi X(t,\xi)]^{-T}) = -[\nabla_\xi X(t,\xi)]^{-T}\partial_t([\nabla_\xi X(t,\xi)]^T)[\nabla_\xi X(t,\xi)]^{-T} \tag{2.17}$$
$$= [\nabla_x u]^T(X(t,\xi),t)[\nabla_\xi X(t,\xi)]^{-T}. \tag{2.18}$$

For the second term, using (2.18) we get

$$\partial_t(|[\nabla_\xi X(t,\xi)]^{-T} n_0(\xi)|) =$$
$$(\partial_t([\nabla_\xi X(t,\xi)]^{-T})n_0(\xi))\cdot\frac{[\nabla_\xi X(t,\xi)]^{-T} n_0(\xi)}{|[\nabla_\xi X(t,\xi)]^{-T} n_0(\xi)|}$$
$$= -\left([\nabla_x u]^T(X(t,\xi),t)\frac{[\nabla_\xi X(t,\xi)]^{-T} n_0(\xi)}{|[\nabla_\xi X(t,\xi)]^{-T} n_0(\xi)|}\right)\cdot[\nabla_\xi X(t,\xi)]^{-T} n_0(\xi).$$

In view of (2.11), we get

$$\partial_t(|[\nabla_\xi X(t,\xi)]^{-T} n_0(\xi)|) = -(([\nabla_x u]n)\cdot n)(X(t,\xi),t)|[\nabla_\xi X(t,\xi)]^{-T} n_0(\xi)|.$$

By putting together the above calculations we obtain

$$\frac{\mathrm{d}}{\mathrm{d}t}\left(\int_{S_t} f(x,t)ds\right) = \int_{S_0}(\partial_t f + u\cdot\nabla f + f\,\mathrm{div}(u) - f([\nabla_x u]n)\cdot n)(X(t,\xi),t)$$
$$|\,\mathrm{Cof}([\nabla_\xi X(t,\xi))\,n_0(\xi)|\,ds_0.$$

The change of variable (2.12) finally gives surface Reynolds formula (2.16). □

We have a similar result for a moving curve:

**Proposition 2.11** *Let $\Gamma_0$ be a regular curve in $\Omega \subset \mathbb{R}^3$ and $\Gamma_t = X(t, \Gamma_0)$. Let $f \in \mathcal{C}^1(\overline{\Omega} \times [0, T])$. Then*

$$\frac{d}{dt} \int_{\Gamma_t} f(x,t)\, dl = \int_{\Gamma_t} \partial_t f + u \cdot \nabla f + (\nabla u\ \tau) \cdot \tau\, dl, \tag{2.19}$$

*where $\tau$ is a field of unit vectors tangent to $\Gamma_t$.*

***Proof*** Using the change of variable formula (2.13)

$$\frac{\mathrm{d}}{\mathrm{d}t} \left( \int_{\Gamma_t} f(x,t)\, dl \right) = \int_{\Gamma_0} \partial_t (f(X(t,\xi),t)) |[\nabla_\xi X(t,\xi)]\tau_0(\xi)| + f(X(t,\xi),t) \partial_t (|[\nabla_\xi X(t,\xi)]\tau_0(\xi)|)\, dl_0.$$

For the first term we use the previous calculations, which gives

$$\partial_t (f(X(t,\xi),t)) = (\partial_t f + u \cdot \nabla f)(X(t,\xi),t).$$

For the second term, $\partial_t [\nabla_\xi X] = [\nabla_x u][\nabla_\xi X]$, we get

$$\begin{aligned} \partial_t (|[\nabla_\xi X(t,\xi)]\tau_0(\xi)|) &= (\partial_t ([\nabla_\xi X(t,\xi)])\tau_0(\xi)) \cdot \frac{[\nabla_\xi X(t,\xi)]\tau_0(\xi)}{|[\nabla_\xi X(t,\xi)]\tau_0(\xi)|} \\ &= \left( [\nabla_x u](X(t,\xi),t) \frac{[\nabla_\xi X(t,\xi)]\tau_0(\xi)}{|[\nabla_\xi X(t,\xi)]\tau_0(\xi)|} \right) \cdot [\nabla_\xi X(t,\xi)]\tau_0(\xi). \end{aligned}$$

We then deduce from (2.14)

$$\partial_t (|[\nabla_\xi X(t,\xi)]\tau_0(\xi)|) = ([\nabla_x u]\tau \cdot \tau)(X(t,\xi),t) |[\nabla_\xi X(t,\xi)]\tau_0(\xi)|.$$

Putting together the previous results, we obtain

$$\begin{aligned} &\frac{\mathrm{d}}{\mathrm{d}t} \left( \int_{\Gamma_t} f(x,t)\, dl \right) \\ &\quad = \int_{\Gamma_0} (\partial_t f + u \cdot \nabla f + f([\nabla u]\tau) \cdot \tau)(X(t,\xi),t) |[\nabla_\xi X(t,\xi)]\tau_0(\xi)|\, dl_0. \end{aligned}$$

It finally remains to use the change of variables formula (2.13) to obtain the Reynolds formula for curves (2.19). □

*Remark 2.12* In the two-dimensional case we have $\tau \otimes \tau = \mathbb{I} - n \otimes n$. There is therefore a correspondence between (2.19) and (2.16).

## 2.4 Conservation of Mass

To end this chapter we recall in this section and the following some principles of conservation in continuum mechanics as well as their Eulerian and Lagrangian formulation.

### *2.4.1 Mass Conservation in Eulerian Formulation*

The principle of conservation of mass states that the variation in mass in a moving volume $\omega_t$ is independent of time:

$$\frac{\mathrm{d}}{\mathrm{d}t}\left(\int_{\omega_t} \rho(x,t)dx\right) = 0,$$

where $\rho$ is the density.

Using Reynolds formula (2.15) with $f = \rho$ we get the mass conservation in the deformed configuration

$$\partial_t \rho + \mathrm{div}(\rho u) = 0. \tag{2.20}$$

### *2.4.2 Mass Conservation in Lagrangian Formulation*

It suffices to come back to the reference configuration with (2.8):

$$\frac{\mathrm{d}}{\mathrm{d}t}\left(\int_{\omega_0} \rho(X(t,\xi),t)\det(\nabla_\xi X(t,\xi))d\xi\right) = 0, \tag{2.21}$$

that we can write, since $X(0,\xi) = \xi$,

$$\rho(X(t,\xi),t)\det(\nabla_\xi X(t,\xi)) = \rho_0(\xi). \tag{2.22}$$

## 2.5 Conservation of Momentum

According to the fundamental principle of dynamics, the change in the momentum of a system is equal to the sum of the external forces acting on that system.

### 2.5.1 Momentum Conservation in Eulerian Formulation

This principle is applied to a volume $\omega_t$. The volume external forces, enforced on $\omega_t$, are noted $f(x,t)$. The surface external forces, enforced on $\partial\omega_t$ are noted $\sigma(x,t)n(x,t)$. The equilibrium of moments shows that $\sigma$ is a symmetric tensor. The conservation of momentum reads

$$\frac{\mathrm{d}}{\mathrm{d}t}\left(\int_{\omega_t}\rho(x,t)u(x,t)dx\right)=\int_{\partial\omega_t}\sigma(x,t)n(x,t)\,ds+\int_{\omega_t}f(x,t)dx \tag{2.23}$$

Reynolds formula (2.15) with $f=\rho u$ gives

$$\frac{\mathrm{d}}{\mathrm{d}t}\left(\int_{\omega_t}\rho u dx\right)=\int_{\omega_t}\partial_t(\rho u)+\mathrm{div}(\rho u\otimes u)dx \tag{2.24}$$

Using Stokes theorem for the surface integral we obtain the Eulerian equations in the deformed configuration $\omega_t$

$$\partial_t(\rho u)+\mathrm{div}(\rho u\otimes u)=\mathrm{div}\,\sigma+f. \tag{2.25}$$

By expanding this relation and using the mass conservation (2.20)

$$(\rho u)_t+\mathrm{div}(\rho u\otimes u)=\rho(\partial_t u+(u\cdot\nabla)u)+u(\partial_t\rho+\mathrm{div}(\rho u))=\rho(\partial_t u+(u\cdot\nabla)u).$$

The conservation equations for momentum can finally be rewritten

$$\rho(\partial_t u+(u\cdot\nabla)u)=\mathrm{div}\,\sigma+f. \tag{2.26}$$

### 2.5.2 Momentum Conservation in Lagrangian Formulation

To switch to a Lagrangian representation, it suffices to rewrite the preceding equations on the reference configuration. For the density, we use (2.8)

$$\int_{\omega_t}f(x,t)dx=\int_{\omega_0}f(X(t,\xi),t)\,\det(\nabla_\xi X(t,\xi))d\xi.$$

For the surface force we use the change of variable on surfaces (2.12)

$$\int_{\partial\omega_t} \sigma(x,t)n(x,t)\,ds = \int_{\partial\omega_0} \sigma(X(t,\xi),t)\,\mathrm{Cof}(\nabla_\xi X(t,\xi))n_0(\xi)\,ds_0.$$

Let us introduce the first Piola Kirchoff tensor $\mathcal{T}$ defined by

$$\mathcal{T}(t,\xi) = \sigma(X(t,\xi),t)\,\mathrm{Cof}(\nabla_\xi X(t,\xi)). \tag{2.27}$$

Note that, unlike $\sigma$, this tensor is not symmetric. Using Stokes theorem we get

$$\begin{aligned}\int_{\omega_t} \mathrm{div}_x(\sigma(x,t))dx &= \int_{\partial\omega_t} \sigma(x,t)n(x,t)\,ds \\ &= \int_{\partial\omega_0} \mathcal{T}(t,\xi)n_0(\xi)\,ds_0 = \int_{\omega_0} \mathrm{div}_\xi(\mathcal{T}(t,\xi))d\xi. \end{aligned}\tag{2.28}$$

For the momentum term we use (2.8) and (2.22) to obtain

$$\begin{aligned}\int_{\omega_t} \rho(x,t)u(x,t)dx &= \int_{\omega_0} \rho(X(t,\xi),t)u(X(t,\xi),t)\,\det(\nabla_\xi X(t,\xi))d\xi \\ &= \int_{\omega_0} \rho_0(\xi)u(X(t,\xi),t)d\xi.\end{aligned}$$

With (1.3), we get

$$\frac{\mathrm{d}}{\mathrm{d}t}\left(\int_{\omega_t} \rho(x,t)u(x,t)dx\right) = \int_{\omega_0} \rho_0(\xi)\partial_t^2 X(t,\xi)d\xi.$$

We finally obtain the Lagrangian equations in the reference configuration $\omega_0$

$$\rho_0(\xi)\partial_t^2 X(t,\xi) = \mathrm{div}_\xi(\mathcal{T}(t,\xi)) + f(X(t,\xi),t)\,\det(\nabla_\xi X(t,\xi)) \tag{2.29}$$

Unlike the Eulerian formulation, the conservation of mass does not require an additional equation, it is directly taken into account with the initial density. This is due to the fact that the equations are posed on the reference configuration.

In both the Eulerian and Lagrangian formulation, to close the systems of equations, we need to provide constitutive laws which allow to relate $\sigma$ to the other unknowns of the problem.

# Chapter 3
# Interaction of an Incompressible Fluid with an Elastic Membrane


In this chapter we consider the case of a thin elastic body, which we model as a surface in dimension 3 or a curve in dimension 2, immersed in an incompressible fluid and in interaction with it. The elastic body delimits an internal fluid and an external fluid which may have different properties (typically density and viscosity). In a first section we recall the immersed boundary model of Peskin which can be seen as a hybrid Lagrangian–Eulerian formulation of fluid-structure interaction. We then present in the second section a purely Eulerian formulation, first in the case when a membrane has a constitutive law that takes into account only the change of its local area. In this first case, the elastic forces are directly encoded in the Level Set function which captures the curve or the surface supporting the membrane. The extension to compressible flows is also presented in this section.

In general, an elastic membrane also responds to stresses acting in the tangent plane, which, in addition to the change in area, include shear stresses. The consideration of membrane with shear is the subject of the third section of this chapter.

This modeling part proceeds with a section devoted to the case of curves immersed in a three-dimensional space. We develop also for this case an Eulerian theory of elasticity and a Level Set formulation.

The chapter ends with an application to these fluid-membrane models of the schemes presented in Chap. 1. We also provide some numerical illustrations. Implementations of these algorithms in high level language such as FreeFEM++, Matlab, Octave are outlined. These can thus serve as hands on tutorials to support a teaching sequence for fluid-structure interaction problems.



G.-H. Cottet et al., *Level Set Methods for Fluid-Structure Interaction*, Applied Mathematical Sciences 210, https://doi.org/10.1007/978-3-031-08659-5_3

## 3.1 From the Immersed Boundary Method to Level Set Methods

The immersed boundary method (IBM) introduced by Pekin and collaborators [113, 114] allows to reduce the fluid-structure coupling of an incompressible fluid with elastic fibers to a pure fluid problem with a second member located on the structure and acting as a force term in the fluid. The method uses both Eulerian and Lagrangian variables. The Eulerian variables describe the velocity and the pressure of the fluid and the Lagrangian variables make it possible to track the curve(s) or immersed surfaces and to measure their stretching. The interaction between Eulerian and Lagrangian quantities is performed using a discrete Dirac measure located on the structure.

We use again here the notions and notations for the parameterizations of Lagrangian surfaces recalled in Sect. 1.1. We consider a smooth elastic surface $\overline{\Gamma}$ in $\mathbb{R}^3$ in a configuration at rest, that is free of any mechanical stress. This surface is represented by a smooth parameterization defined on $U = ]0, M[^2$, with $M > 0$, denoted by $\overline{\gamma} : \theta \in U \to \overline{\gamma}(\theta) \in \mathbb{R}^3$. The surface density of the membrane in this configuration is noted $\bar{m}(\theta)$

This surface moves with the velocity of the surrounding fluid between times $t = 0$ and $t = T$, and we denote by $\Gamma_t$ its position at time $t$. In particular $\Gamma_0$ is its initial position. Note that $\Gamma_0$ differs from $\overline{\Gamma}$ if the surface is not initially at rest.

Denote by $\theta \to \gamma_0(\theta)$ and $\theta \to \lambda_0(\theta)$ a smooth parameterization and a surface mass for $\Gamma_0$ such that $m_0|\partial_{\theta_1}\gamma_0 \times \partial_{\theta_2}\gamma_0| = \bar{m}|\partial_{\theta_1}\overline{\gamma} \times \partial_{\theta_2}\overline{\gamma}|$.

Let $\gamma : \theta \to \gamma(t, \theta)$ the advected smooth parameterization of $\Gamma_t$. This means that $\gamma(t, \theta) = X(t, \gamma_0(\theta))$ or, equivalently, is given by the following differential system

$$\begin{cases} \partial_t \gamma(t, \theta) = u(\gamma(t, \theta), t), & \theta \in U, t \in ]0, T] \\ \gamma(0, \theta) = \gamma_0(\theta), & \theta \in U. \end{cases} \tag{3.1}$$

The surface $\Gamma_t$ is immersed in an incompressible and homogeneous Newtonian fluid of density $\rho_f$ and viscosity $\nu$. With the notations of [114] adapted to the case of an elastic membrane, the immersed boundary method can be summarized by the following box:

**Immersed Boundary Method** Eulerian (resp. Lagrangian) description of the velocity of the surrounding fluid (resp. of the immersed elastic structure made of one-dimensional fibers), interpolated in the Eulerian domain.

- An Eulerian velocity field $(x, t) \in \Omega \times [0, T] \to u(x, t)$.

(continued)

- $(t, \theta) \in U \times [0, T] \to \gamma(t, \theta)$ the location of the points on the elastic structure $\Gamma_t$.
- The force density in the deformed configuration with respect to the surface measure in the reference configuration is a known function $\overline{F}(t, \theta)$ which can usually be written as a function of the partial derivatives of $\gamma$ and $\overline{\gamma}$ by an expression of the form $\overline{\mathcal{F}}[\gamma(t, \theta)]$.
- The surface mass in the reference configuration is a known function $\overline{m}(t, \theta)$.
- The equations of motion

$$(\rho_f + M)(\partial_t u + u \cdot \nabla u) - \nu \Delta u + \nabla p = f \tag{3.2}$$

$$\operatorname{div} u = 0 \tag{3.3}$$

$$f(x, t) = \int_U |\partial_{\theta_1} \overline{\gamma} \times \partial_{\theta_2} \overline{\gamma}| \overline{F}(t, \theta) \delta(x - \gamma(t, \theta)) d\theta \tag{3.4}$$

$$M(x, t) = \int_U |\partial_{\theta_1} \overline{\gamma} \times \partial_{\theta_2} \overline{\gamma}| \overline{m}(t, \theta) \delta(x - \gamma(t, \theta)) d\theta \tag{3.5}$$

$$\partial_t \gamma = u(\gamma(t, \theta), t) = \int_\Omega u(x, t) \delta(x - \gamma(t, \theta)) dx \tag{3.6}$$

Equation (3.4) expresses the Lagrangian force in the Eulerian domain; Eq. (3.6) converts the Eulerian velocity field into a velocity field at the Lagrangian points of the structure. The precise meaning of (3.4) can be written by considering a test function $\psi : \Omega \to \mathbb{R}$ and by integrating on $\Omega$:

$$\int_\Omega f(x, t) \psi(x, t) dx = \int_U |\partial_{\theta_1} \overline{\gamma} \times \partial_{\theta_2} \overline{\gamma}| \overline{F}(t, \theta) \int_\Omega \delta(x - \gamma(t, \theta)) \psi(x, t) dx d\theta$$

$$= \int_U |\partial_{\theta_1} \overline{\gamma} \times \partial_{\theta_2} \overline{\gamma}| \overline{F}(t, \theta) \psi(\gamma(t, \theta), t) d\theta = \int_{\Gamma_t} \overline{F}(t, \theta) \frac{|\partial_{\theta_1} \overline{\gamma} \times \partial_{\theta_2} \overline{\gamma}|}{|\partial_{\theta_1} \gamma \times \partial_{\theta_2} \gamma|} \psi(x, t) ds.$$

Therefore, formally

$$f(x, t) = \frac{|\partial_{\theta_1} \overline{\gamma} \times \partial_{\theta_2} \overline{\gamma}|}{|\partial_{\theta_1} \gamma \times \partial_{\theta_2} \gamma|} \overline{F}(t, \theta) \delta_{\Gamma_t} = F(t, \theta) \delta_{\Gamma_t}$$

for $x = \gamma(t, \theta)$ and if $F$ represents a surface density of force in the deformed configuration.

Similarly, from (3.5), $M$ is a measure defined by

$$M(x, t) = \frac{|\partial_{\theta_1} \overline{\gamma} \times \partial_{\theta_2} \overline{\gamma}|}{|\partial_{\theta_1} \gamma \times \partial_{\theta_2} \gamma|} \overline{m}(t, \theta) \delta_{\Gamma_t} = m(t, \theta) \delta_{\Gamma_t}, \qquad \text{with } x = \gamma(t, \theta).$$

For an elastic membrane reacting only to the local change of area, we can for example consider the following expression of the energy

$$\mathcal{E}[\gamma] = \int_U E\left(\frac{|\partial_{\theta_1}\gamma \times \partial_{\theta_2}\gamma|}{|\partial_{\theta_1}\overline{\gamma} \times \partial_{\theta_2}\overline{\gamma}|}\right) d\theta, \tag{3.7}$$

where $r \to E(r)$ is a given constitutive law representing the elastic properties of the membrane. Then, by differentiating the energy and applying the principle of virtual work, we can show that

$$F(t,\theta) = \nabla_{\Gamma_t} T(\theta) - T(\theta)\kappa n(\theta), \tag{3.8}$$

where

$$T(\theta) = E'\left(\frac{|\partial_{\theta_1}\gamma \times \partial_{\theta_2}\gamma|}{|\partial_{\theta_1}\overline{\gamma} \times \partial_{\theta_2}\overline{\gamma}|}\right) \frac{1}{|\partial_{\theta_1}\overline{\gamma} \times \partial_{\theta_2}\overline{\gamma}|}.$$

The energy $E$ is typically of the form $E(r) = k\max(r-1,0)^2$, for a stiffness coefficient $k > 0$. The immersed boundary method in this original formulation can be implemented to guarantee second order spatial accuracy in the case of thick interfaces, but is only first order in the case of sharp interfaces without thickness [82]. Stability analysis have been proposed in several works [14, 15, 132, 133].

The immersed boundary method just described is very simple and intuitive. However, the repeated passage between the Eulerian and Lagrangian coordinates may result in volume conservation problems. This is in part because the interpolation of the velocity field does not preserve its zero divergence. The advection of the markers on the interface can thus produce changes in volume. This is a known weakness of the method and which has been studied in [95, 96, 115]. These works propose modifications of the method which partly sacrifice its appealing simplicity.

The primary goal of the totally Eulerian formulation introduced in [35, 36] was precisely to retain the simplicity of the method by proposing an Eulerian localization of the membrane which avoids the back and forth convertions between the two coordinate systems.

Note also that an Eulerian formulation makes it possible to overcome the difficulties of parameterizing closed objects and to easily take into account variable viscosity values, unlike IBM methods. This is an important point for example in the case of biological cell models which are often considered with a contrast in viscosity between the inside and the outside of the cell, the greater viscosity inside being a simplified way of taking into account the presence of biological material in the cell.

In what follows we describe the Level Set models first in the simplest case of elastic surfaces which only respond to a variation of the local area. We consider in a second step the case of interfaces sensitive also to the effects of shear on their surface. We then evoke the questions of stability related to the discretization in time of the terms of coupling. The chapter concludes with numerical illustrations and

code examples produced using the FreeFEM++ software, allowing the reader to simply experiment with the methods.

## 3.2 Immersed Membrane: Case Without Shear

### 3.2.1 *Level Set Formulation of the Elastic Deformation of a Hypersurface Immersed in a Incompressible Fluid*

We will show that during the transport of a Level Set function by an incompressible velocity field, the norm of the gradient of the solution of the transport equation contains the information on the variation of the local areas (or lengths) of the level sets of the function. A proof of this result using a parametric representation of surfaces is given in [35]. We give here an intrinsic proof taken from [36].

To start with, let us recall the coarea formula:

**Lemma 3.1** *Let* $\varphi : \mathbb{R}^d \to \mathbb{R}$ *Lipschitzian on* $\mathbb{R}^d$ *and* $g : \mathbb{R}^d \to \mathbb{R}$ *integrable. We assume that there exists* $\eta_0 > 0$ *such that* $\inf \mathrm{ess}_{|\varphi|<\eta_0} |\nabla\varphi| > 0$. *Then for* $\eta \in ]0, \eta_0[$,

$$\int_{\{|\varphi(x)|<\eta\}} g(x)\, dx = \int_{-\eta}^{\eta} \int_{\{\varphi(x)=\nu\}} g(x) |\nabla\varphi|^{-1}\, ds d\nu.$$

This formula is quite natural because the volume $|\varphi| < \eta$ is calculated by integrating the area of the surface $\varphi = \nu$ multiplied by a factor $|\nabla\varphi|^{-1}$ which corresponds to the local distance between the level surfaces/lines of $\varphi$.

***Proof*** In [58], Proposition 3, page 118, it is shown under the assumptions of the lemma that

$$\frac{d}{d\nu}\left(\int_{\{\varphi>\nu\}} g(x)\, dx\right) = -\int_{\{\varphi=\nu\}} g|\nabla\varphi|^{-1}\, ds \qquad \text{for almost every } \nu.$$

The announced formula easily follows:

$$\begin{aligned}\int_{\{|\varphi(x)|<\eta\}} g(x)\, dx &= \int_{\{\varphi(x)>-\eta\}} g(x)\, dx - \int_{\{\varphi(x)>\eta\}} g(x)\, dx \\ &= \int_{\eta}^{-\eta} \frac{d}{d\nu}\left(\int_{\{\varphi>\nu\}} g(x)\, dx\right) = \int_{-\eta}^{\eta} \int_{\{\varphi=\nu\}} g|\nabla\varphi|^{-1}\, ds.\end{aligned}$$

□

By making the following regularity assumption on the level sets of $\varphi$,

$(H_\varphi)$ $\quad \forall t \in [0,T], \forall f \in \mathcal{C}_c(\mathbb{R}^n),$

$$v \to \int_{\{|\varphi(x,t)|<v\}} f(x)\ dx \text{ is } \mathcal{C}^1 \text{ in a neighborhood of } v = 0,$$

we have the following result:

**Proposition 3.2** *Let $u : \mathbb{R}^d \times [0,T] \to \mathbb{R}^d$ of class $\mathcal{C}^1$ with $\operatorname{div} u = 0$ and $\varphi$ a $\mathcal{C}^1$ solution of $\partial_t \varphi + u \cdot \nabla \varphi = 0$, $\varphi = \varphi_0$ with $|\nabla \varphi| \geq \alpha > 0$ and satisfying $(H_\varphi)$. Then for any continuous function $f$ with compact support,*

$$\int_{\{\varphi_0(\xi)=0\}} f(\xi)|\nabla \varphi_0|^{-1}(\xi)\, ds_0(\xi) = \int_{\{\varphi(x,t)=0\}} f(Y(x,t))|\nabla \varphi|^{-1}(x,t)\, ds(x). \tag{3.9}$$

In other words $|\nabla \varphi|/|\nabla \varphi_0|$ represents the variation of the surface measure of $\Gamma_t = \{x, \varphi(x,t) = 0\}$ relatively to $\Gamma_0$. This property is illustrated on Fig. 3.1.

***Proof*** The assumption $(H_\varphi)$ implies from the previous lemma that the application

$$s \to \int_{\{\varphi_0 = s\}} f(\xi)|\nabla \varphi_0|^{-1}(\xi)\, ds_0(\xi)$$

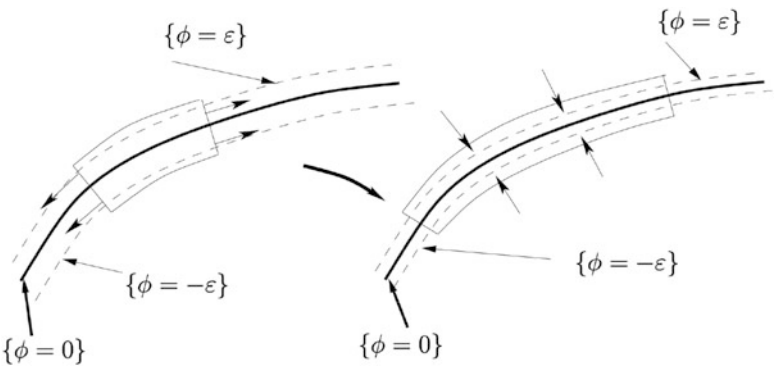


**Fig. 3.1** When an incompressible velocity field has the effect of stretching the level curves (or surfaces), then they necessarily tighten by conservation of volume. This stretching is precisely measured by the norm of the gradient of the Level Set function

is continuous. Thus, from Lemma 3.1,

$$\int_{\{\varphi_0(\xi)=0\}} f(\xi)|\nabla\varphi_0|^{-1}(\xi)\,ds_0(\xi)$$
$$= \lim_{\eta\to 0}\frac{1}{\eta}\int_{-\frac{\eta}{2}}^{\frac{\eta}{2}}\int_{\{\varphi_0=\nu\}} f(\xi)|\nabla\varphi_0|^{-1}(\xi)\,ds_0(\xi)\,d\nu = \lim_{\eta\to 0}\frac{1}{\eta}\int_{\{|\varphi_0|<\frac{\eta}{2}\}} f(\xi)\,d\xi.$$

We perform the change of variables $\xi = Y(x,t)$, with Jacobian $J_e(x,t)$ equal to 1, due to the fact that $\operatorname{div} u = 0$.

Since $\varphi$ is solution to the transport equation, we have $\varphi_0(Y(x,t)) = \varphi(x,t)$ and thus

$$\int_{\{\varphi_0(\xi)=0\}} f(\xi)\,ds_0(\xi) = \lim_{\eta\to 0}\frac{1}{\eta}\int_{\{|\varphi(x,t)|<\frac{\eta}{2}\}} f(Y(x,t))\,dx,$$

which gives the announced result thanks to Lemma 3.1. □

*Remark 3.3* Another proof of the previous proposition is possible by using the definition of the backward characteristics $Y$ (see remark 2.4) and the Reynolds differentiation formula for surfaces (2.16). Indeed this formula reads, for a function $g$ of class $\mathcal{C}^1$, and $u$ satisfying $\operatorname{div} u = 0$,

$$\frac{d}{dt}\int_{\{\varphi(x,t)=0\}} g(x,t)\,ds = \int_{\{\varphi(x,t)=0\}} \partial_t g + u\cdot\nabla g - g[\nabla u]n\cdot n\,ds;$$

and, taking the gradient of the transport equation for $\varphi$,

$$-\frac{1}{|}\nabla\varphi|\,(\partial_t|\nabla\varphi| + u\cdot\nabla|\nabla\varphi|) = [\nabla u]\frac{\nabla\varphi}{|\nabla\varphi|}\cdot\frac{\nabla\varphi}{|\nabla\varphi|} = [\nabla u]n\cdot n. \tag{3.10}$$

By grouping the terms together we have

$$\frac{d}{dt}\int_{\{\varphi(x,t)=0\}} g(x,t)\,ds = \int_{\{\varphi(x,t)=0\}} (\partial_t(g|\nabla\varphi|) + u\cdot\nabla(g|\nabla\varphi|))\frac{1}{|\nabla\varphi|}\,ds.$$

We then apply this formula to $g(x,t) = f(Y(x,t))|\nabla\varphi|^{-1}(x,t)$, after observing that, according to (2.4)

$$\partial_t(f(Y)) + u\cdot\nabla(f(Y)) = \nabla f\cdot\partial_t Y + u\cdot([\nabla Y]^T\nabla f) = \nabla f\cdot(\partial_t Y + u\cdot\nabla Y) = 0.$$

We therefore obtain

$$\frac{d}{dt}\int_{\{\varphi(x,t)=0\}} f(Y(x,t))|\nabla\varphi|^{-1}(x,t)\,ds = 0,$$

which, upon integrating from time 0 to $t$, is nothing but formula (3.9).

The above results can be interpreted on parametric representations of curves or surfaces. In two dimensions, recall that we are given a parameterization $\theta \in [0, M] \to \gamma(0,\theta) \in \mathbb{R}^2$ of $\Gamma_0$:

$$\int_0^M f(\gamma(0,\theta))|\nabla\varphi_0|^{-1}(\gamma(0,\theta))|\partial_\theta\gamma|(0,\theta)d\theta$$
$$= \int_0^M f(\gamma(0,\theta))|\nabla\varphi|^{-1}(\gamma(t,\theta),t)|\partial_\theta\gamma|(t,\theta)\,d\theta,$$

for any continuous function $f$ with compact support. Hence

$$\frac{|\nabla\varphi|(\gamma(t,\theta),t)}{|\nabla\varphi_0|(\gamma(0,\theta))} = \frac{|\partial_\theta\gamma(t,\theta)|}{|\partial_\theta\gamma(0,\theta)|}.$$

In three dimensions, if $\theta = (\theta_1,\theta_2) \in U \to \gamma(t,\theta_1,\theta_2) \in \mathbb{R}^3$ is (or is part of) a parametrization of $\Gamma_t$, then, since $Y(\gamma(t,\theta),t) = \gamma(0,\theta)$, we have

$$\int_\omega f(\gamma(0,\theta))|\nabla\varphi_0|^{-1}(\gamma(0,\theta))|\partial_{\theta_1}\gamma \times \partial_{\theta_2}\gamma|(0,\theta)d\theta$$
$$= \int_\omega f(\gamma(0,\theta))|\nabla\varphi|^{-1}(\gamma(t,\theta),t)|\partial_{\theta_1}\gamma \times \partial_{\theta_2}\gamma|(t,\theta)d\theta,$$

and thus

$$\frac{|\nabla\varphi|(\gamma(t,\theta),t)}{|\nabla\varphi_0|(\gamma(0,\theta))} = \frac{|\partial_{\theta_1}\gamma \times \partial_{\theta_2}\gamma|(t,\theta)}{|\partial_{\theta_1}\gamma \times \partial_{\theta_2}\gamma|(0,\theta)}.$$

In practice, $\varphi_0$ is constructed such that, on the one hand its zero level set represents $\Gamma_0$, and, on the other hand,

$$|\nabla\varphi_0|(\gamma(0,\theta)) = \frac{|\partial_{\theta_1}\gamma \times \partial_{\theta_2}\gamma|(0,\theta)}{|\partial_{\theta_1}\overline{\gamma} \times \partial_{\theta_2}\overline{\gamma}|(\theta)}.$$

This last equality means that $\varphi_0$ contains the amount of stretching of the initial membrane. We then have

$$|\nabla\varphi|(\gamma(t,\theta),t) = \frac{|\partial_{\theta_1}\gamma \times \partial_{\theta_2}\gamma|(t,\theta)}{|\partial_{\theta_1}\overline{\gamma} \times \partial_{\theta_2}\overline{\gamma}|(\theta)}. \tag{3.11}$$

If, for instance, the initial stretching does not depend on $\theta$, it suffices to initialize $\varphi_0$ as the signed distance to the interface multiplied by the stretching coefficient.

### 3.2.2 *Level Set Formulation of Elastic Energy and Fluid-Structure Coupling in the Incompressible Case*

From the expression of the stretching given by Proposition 3.2 and according to Proposition 1.10, it is natural to introduce the regularized elastic energy as

$$\mathcal{E}(\varphi) = \int_\Omega E(|\nabla\varphi|)\frac{1}{\varepsilon}\zeta\left(\frac{\varphi}{\varepsilon}\right) dx, \tag{3.12}$$

where $E$ is a constitutive law. The function $r \to E'(r)$ describes the strain-stress relationship, possibly nonlinear, within the elastic structure. For example, in the case of a single drop of a given fluid immersed in another fluid, this energy is given by $E(r) = \lambda r$ where $\lambda$ is the surface tension coefficient, and $E'(r) = \lambda$ is a constant. For a membrane subject to an elastic response to the change of local area, we use a quadratic law

$$E(r) = \frac{\lambda}{2}(r-1)^2 \tag{3.13}$$

which corresponds to $E'(r) = \lambda(r-1)$.

**Theorem 3.4** *The temporal variation of $E$ given by the principle of virtual work satisfies*

$$\partial_t \mathcal{E} = -\int_\Omega F \cdot u dx \tag{3.14}$$

*and corresponds to the following force:*

$$F = \nabla\left(E(|\nabla\varphi|)\frac{1}{\varepsilon}\zeta\left(\frac{\varphi}{\varepsilon}\right)\right) - \operatorname{div}\left(E'(|\nabla\varphi|)|\nabla\varphi| n \otimes n \frac{1}{\varepsilon}\zeta\left(\frac{\varphi}{\varepsilon}\right)\right). \tag{3.15}$$

*where we recall that the normal is defined by* $n = \dfrac{\nabla\varphi}{|\nabla\varphi|}$.

***Proof*** By differentiating (3.12) with respect to $t$ and combining the transport equation on $\varphi$ and (3.10), we obtain the following relation:

$$\partial_t \mathcal{E} = \int_\Omega E'(|\nabla\varphi|)(-u\cdot\nabla|\nabla\varphi| - [\nabla u] : |\nabla\varphi| n\otimes n)\frac{1}{\varepsilon}\zeta\left(\frac{\varphi}{\varepsilon}\right) dx + \int_\Omega E(|\nabla\varphi|)\frac{1}{\varepsilon^2}\zeta'\left(\frac{\varphi}{\varepsilon}\right)(-u\cdot\nabla\varphi)\, dx.$$

The integral over $\partial\Omega$ vanishes because $\zeta(\frac{\varphi}{\varepsilon}) = 0$ sur $\partial\Omega$. Integrating by parts the second term yields

$$\partial_t \mathcal{E} = -\int_\Omega u\cdot\nabla(E(|\nabla\varphi|))\frac{1}{\varepsilon}\zeta\left(\frac{\varphi}{\varepsilon}\right) - \operatorname{div}\left(E'(|\nabla\varphi|)|\nabla\varphi| n\otimes n\frac{1}{\varepsilon}\zeta\left(\frac{\varphi}{\varepsilon}\right)\right)\cdot u + E(|\nabla\varphi|)u\cdot\nabla\left(\frac{1}{\varepsilon}\zeta\left(\frac{\varphi}{\varepsilon}\right)\right) dx.$$

By grouping the first and last terms and using (3.14) we get the expression (3.15). □

The gradient terms in (3.15) can be absorbed into the pressure term of the incompressible Navier–Stokes equations. We can therefore rewrite the force under the form

$$F = \operatorname{div}\left(E'(|\nabla\varphi|)|\nabla\varphi|(\mathbb{I} - n\otimes n)\frac{1}{\varepsilon}\zeta\left(\frac{\varphi}{\varepsilon}\right)\right). \tag{3.16}$$

It may also be interesting to express this force along the normal and tangential directions to the surface.

By developing the divergence and using the fact that $(\mathbb{I} - n\otimes n)\nabla\varphi = 0$ we get $F = A\frac{1}{\varepsilon}\zeta\left(\frac{\varphi}{\varepsilon}\right)$ with $A = \operatorname{div}\left(E'(|\nabla\varphi|)|\nabla\varphi|(\mathbb{I} - n\otimes n)\right)$. We obtain by expanding this relation

$$A = -E'(|\nabla\varphi|)|\nabla\varphi|\operatorname{div}(n\otimes n) + \nabla_\Gamma\left(E'(|\nabla\varphi|)|\nabla\varphi|\right) \tag{3.17}$$

where we recall the definition $\nabla_\Gamma f = \nabla f - (\nabla f\cdot n)n$ which allows to calculate the variations of a function only in the tangent plane. It is important to note that this operator is defined on $\mathbb{R}^3$ and not just on the zero level set of $\varphi$. If $x\in\mathbb{R}^3$ lies on another level set of $\varphi$ then the surface gradient at this point is the projection of the classical gradient on the tangent plane defined on this level set.

Using the relationships

$$\operatorname{div}(n\otimes n) = Hn + [\nabla n]n\ ,\ [\nabla n]n = \frac{\nabla_\Gamma|\nabla\varphi|}{|\nabla\varphi|},$$

and absorbing the gradient term in the pressure, one finally obtains

$$F = \left(\nabla_\Gamma(E'(|\nabla\varphi|)) - E'(|\nabla\varphi|)H(\varphi)n\right)|\nabla\varphi|\frac{1}{\varepsilon}\zeta\left(\frac{\varphi}{\varepsilon}\right), \tag{3.18}$$

where $n = \dfrac{\nabla\varphi}{|\nabla\varphi|}$ and $H(\varphi) = \operatorname{div}\left(\dfrac{\nabla\varphi}{|\nabla\varphi|}\right)$ denotes the mean curvature.

Note that, as in Peskin's Lagrangian formulation, the curvature occurs in the normal component while stretching alone plays a role in the tangential direction. In the particular case where the dynamics is only driven by surface tension, which corresponds to $E'(r) = \lambda$, the tangential term vanishes and we find the Laplace force

$$-\lambda\, H(\varphi)\, n\, |\nabla\varphi|\frac{1}{\varepsilon}\zeta\left(\frac{\varphi}{\varepsilon}\right) \approx -\lambda\, H(\varphi)\, n\, \delta_{\{\varphi=0\}}.$$

We can now write a complete Level Set model for the fluid-structure coupling in the case considered in this chapter. In the following we will assume the surface mass, denoted by $m$, initially constant along the membrane.

We start by considering a regularized Heaviside function making it possible to locate the regions defined by the Level Set function and to assign them different density values $\rho_1$ and $\rho_2$. To fix ideas, we choose a regularization function $\zeta$ with support in $[-1, +1]$ and set

$$\mathcal{H}(r) = \int_{-\infty}^{r} \zeta(\alpha)d\alpha,$$

so that $\mathcal{H}(r) = 0$ for $r < -1$, and $\mathcal{H}(r) = 1$ for $r > 1$. We next write

$$\rho(\varphi) = \rho_1 + \mathcal{H}\left(\frac{\varphi}{\varepsilon}\right)(\rho_2 - \rho_1) + \frac{1}{\varepsilon}\zeta\left(\frac{\varphi}{\varepsilon}\right) m \tag{3.19}$$

and

$$\mu(\varphi) = \mu_1 + \mathcal{H}\left(\frac{\varphi}{\varepsilon}\right)(\mu_2 - \mu_1).$$

We then obtain the following model (written here with zero external force $f$): Find $(u, \varphi)$ solution in $\Omega\times]0, T[$ of

$$\rho(\varphi)(\partial_t u + u\cdot\nabla u) - \operatorname{div}(2\mu(\varphi)D(u)) + \nabla p = F(x,t), \tag{3.20}$$

$$\operatorname{div} u = 0, \tag{3.21}$$

$$\partial_t\varphi + u\cdot\nabla\varphi = 0, \tag{3.22}$$

where the elastic force $F$ is given either by (3.16), which is natural in a variational formulation, useful as we will see when dealing with finite element discretizations, or (3.18).

It should be noted that $\rho(\varphi)$ given by expression (3.19) also satisfies a transport equation and therefore satisfies mass conservation since $\operatorname{div} u = 0$. Formula (3.19) also translates that, as expected, the surface mass of the membrane evolves in a manner inversely proportional to its stretching.

We have therefore modeled the interaction of a fluid with an elastic membrane as the flow of a complex fluid whose stress tensor is modified near the surface. This model can be compared to that of Korteweg's fluids [137]. This is indeed from this remark that one can tackle the question of the existence of a solution to this problem. An important result is the following energy equality, which follows on the one hand from the conservation of mass that we have just mentioned, and on the other hand from the fact that the elastic force is derived from a potential:

**Proposition 3.5** *If $\varphi$ is such that $|\varphi| > \varepsilon$ on $\partial\Omega$, we have*

$$\begin{aligned}\frac{1}{2}\int_\Omega \rho(\varphi(x,T))u^2(x,T)\,dx + \int_\Omega E(|\nabla\varphi|)\frac{1}{\varepsilon}\zeta\left(\frac{\varphi}{\varepsilon}\right)dx \\ + \int_0^T\int_\Omega 2\mu(\varphi)D(u)^2\,dxdt \\ = \frac{1}{2}\int_\Omega \rho(\varphi_0(x))u_0^2(x)\,dx + \int_\Omega E(|\nabla\varphi_0|)\frac{1}{\varepsilon}\zeta\left(\frac{\varphi_0}{\varepsilon}\right)dx. \qquad (3.23)\end{aligned}$$

This property of energy conservation shows that the regularization of the force in the Level Set formulation does not induce energy dissipation over time. This will be illustrated numerically in Sect. 3.6.

An existence result for solutions of the system (3.20–3.22) is outlined in Sect. 3.2.5. The complete proof of this result can be found in [38].

### 3.2.3 Generalization to Compressible Flows

In the above, the representation of the stretching of a surface from the gradient of a Level Set function used to capture it makes a crucial use of the incompressibility of the flow. A generalization of the method to compressible flows has however been proposed in [8, 23].

To take into account the volume variations, let us start again from the Reynolds differentiation formula for surfaces (2.16). For a function $g$ of class $\mathcal{C}^1$,

$$\frac{d}{dt}\int_{\{\varphi(x,t)=0\}} g(x,t)\,ds = \int_{\{\varphi(x,t)=0\}} \partial_t g + \operatorname{div}(gu) - g[\nabla u]n\cdot n\,ds.$$

According to (2.7) the Eulerian Jacobian $J_e(x,t)$ verifies $\partial_t(J_e)+u\cdot\nabla J_e = J_e \operatorname{div} u$. We therefore obtain by using (3.10)

$$\operatorname{div}(u) - [\nabla u]n\cdot n = \frac{1}{J_e|\nabla\varphi|}\left(\partial_t(J_e|\nabla\varphi|) + u\cdot\nabla(J_e|\nabla\varphi|)\right).$$

It follows that

$$\frac{d}{dt}\int_{\{\varphi(x,t)=0\}} g(x,t)\,ds = \int_{\{\varphi(x,t)=0\}} \left(\partial_t(gJ_e|\nabla\varphi|) + u\cdot\nabla(gJ_e|\nabla\varphi|)\right)\frac{1}{J_e|\nabla\varphi|}\,ds.$$

We then apply this formula with $g(x,t) = f(Y(x,t))(J_e(x,t)|\nabla\varphi|)^{-1}(x,t)$, where $Y$ denote the backward characteristics. We observe that

$$\partial_t(gJ_e|\nabla\varphi|) + u\cdot\nabla(gJ_e|\nabla\varphi|) = \partial_t(f(Y)) + u\cdot\nabla(f(Y)) = 0$$

because $Y$ being the solution of the transport equation (2.4), so is $f(Y)$. We thus have

$$\frac{d}{dt}\int_{\{\varphi(x,t)=0\}} f(Y(x,t))(J_e(x,t)|\nabla\varphi|)^{-1}(x,t)\,ds = 0,$$

which, after integration between 0 and $t$, allows to generalize formula (3.9). In the compressible case we recover the results of [8, 23] which express the stretching as $J_e|\nabla\varphi|$. We finally deduce from what precedes the following Level Set formulation for the elastic energy:

$$\mathcal{E}(\varphi) = \int_\Omega E(J_e|\nabla\varphi|)\frac{1}{\varepsilon}\zeta\left(\frac{\varphi}{\varepsilon}\right)dx.$$

It remains now to differentiate this energy along the lines of the incompressible case to deduce a Level Set model for the fluid-structure interaction.

### 3.2.4 Taking into Account Curvature Forces

In many cases, such as in biophysics for the study of behavior of phospholipid vesicles, either in equilibrium or in a shear flow, the immersed membrane is in fact inextensible, and the prevailing energy is a bending energy. Phase field type methods have been extensively developed in the numerical physics community to deal with this problem [11–13, 99]. These methods consist in defining a phase function which takes the value 1 inside the volume surrounded by the immersed interface, and 0 outside, with a transition zone the thickness of which has to be controlled. Different approaches corresponding to different energies and strategies have been developed to control this thickness, the impact of which on the simulated dynamics is sometimes difficult to quantify.

The Level Set approach makes it possible to propose an interesting alternative to the phase field methods: the interface is the hypersurface $\{\varphi = 0\}$, which is the solution of a simple transport equation, and the regularization is not introduced into the model as a right hand side in the fluid equations.

From Proposition 1.10 a natural and general form for the bending energies is given by the formula

$$\mathcal{E}_c(\varphi) = \int_\Omega A(H(\varphi))|\nabla\varphi|\frac{1}{\varepsilon}\zeta\left(\frac{\varphi}{\varepsilon}\right)dx$$

where we recall that the mean curvature $H$ and the Gaussian curvature G are defined by (1.9) and (1.10)

$$H = \mathrm{Tr}(\nabla n) = \mathrm{div}(n) \qquad G = \mathrm{Tr}(\mathrm{Cof}(\nabla n)).$$

The most common case corresponds to $A(r) = r^2$.

Let us also recall the definition of surface operators which allows to take into account the variations of a scalar or a vector field only in the tangent plane

$$\nabla_\Gamma f = \nabla f - (\nabla f \cdot n)n \qquad \mathrm{div}_\Gamma(u) = \mathrm{div}(u) - ([\nabla u]n)\cdot n$$

and we define $\Delta_\Gamma f = \mathrm{div}_\Gamma(\nabla_\Gamma f)$.

By differentiating the energy $\mathcal{E}_c$ with respect to time we obtain

$$\partial_t\mathcal{E}_c(\varphi) = \int_\Omega A'(H(\varphi))\,\mathrm{div}\left(\frac{\nabla_\Gamma(\partial_t\varphi)}{|\nabla\varphi|}\right)|\nabla\varphi|\frac{1}{\varepsilon}\zeta\left(\frac{\varphi}{\varepsilon}\right)dx$$
$$+\int_\Omega A(H(\varphi))\frac{1}{\varepsilon}\zeta\left(\frac{\varphi}{\varepsilon}\right)\frac{\nabla\varphi}{|\nabla\varphi|}\cdot\nabla(\partial_t\varphi) + A(H(\varphi))|\nabla\varphi|\frac{1}{\varepsilon^2}\zeta'\left(\frac{\varphi}{\varepsilon}\right)\partial_t\varphi\,dx.$$

The terms of the second line can be grouped, since, by integrating the first term by parts, the second term appears with an opposite sign. Using $\mathrm{div}(A(H)n) = A(H)H + \nabla(A(H)) \cdot n$, the remaining terms combine to give

$$\partial_t \mathcal{E}_c(\varphi) = \int_\Omega \mathrm{div}\left(\frac{\nabla_\Gamma(\partial_t\varphi)}{|\nabla\varphi|}\right) A'(H(\varphi))|\nabla\varphi|\frac{1}{\varepsilon}\zeta\left(\frac{\varphi}{\varepsilon}\right) - \mathrm{div}\left(A(H(\varphi))\frac{\nabla\varphi}{|\nabla\varphi|}\right)\frac{1}{\varepsilon}\zeta\left(\frac{\varphi}{\varepsilon}\right)\partial_t\varphi\, dx.$$

In view of $\nabla_\Gamma(\partial_t\varphi)\cdot\nabla\varphi = 0$ the first term can be integrated by parts to give

$$-\int_\Omega \nabla\left(A'(H(\varphi))|\nabla\varphi|\right)\cdot\frac{\nabla_\Gamma(\partial_t\varphi)}{|\nabla\varphi|}\frac{1}{\varepsilon}\zeta\left(\frac{\varphi}{\varepsilon}\right) = -\int_\Omega \nabla_\Gamma\left(A'(H(\varphi))|\nabla\varphi|\right)\cdot\frac{\nabla(\partial_t\varphi)}{|\nabla\varphi|}\frac{1}{\varepsilon}\zeta\left(\frac{\varphi}{\varepsilon}\right)dx,$$

where we have used the symmetry of the operator $\nabla_\Gamma$. By integrating again by parts we finally find, using as before that the derivative of the energy is equal to the opposite of the work of the forces $\partial_t\mathcal{E}_c(\varphi) = -\int_\Omega F_c(x,t)\cdot u\, dx$,

$$F_c(x,t) = \mathrm{div}\left[-A(H(\varphi))\frac{\nabla\varphi}{|\nabla\varphi|} + \frac{1}{|\nabla\varphi|}\nabla_\Gamma(A'(H(\varphi))|\nabla\varphi|)\right]\frac{1}{\varepsilon}\zeta\left(\frac{\varphi}{\varepsilon}\right)\nabla\varphi.$$

We will now rewrite this force in another form, based only on surface operators. We have for the first term

$$\mathrm{div}(A(H)n) = A(H)H + A'(H)\nabla H\cdot n.$$

Using the relations $\frac{\nabla_\Gamma(|\nabla\varphi|)}{|\nabla\varphi|} = [\nabla n]n$, $\mathrm{div}([\nabla n]n) = \nabla H\cdot n + H^2 - 2G$ and $\nabla f\cdot([\nabla n]n) = -(\nabla(\nabla_\Gamma f)n)\cdot n$ we obtain

$$\begin{aligned} B &= \mathrm{div}\left(\frac{1}{|\nabla\varphi|}\nabla_\Gamma(A'(H(\varphi))|\nabla\varphi|)\right) = \mathrm{div}(A'(H)[\nabla n]n) + \mathrm{div}(\nabla_\Gamma(A'(H)))\\ &= A'(H)(\nabla H\cdot n + H^2 - 2G) + \nabla(A'(H))\cdot([\nabla n]n) + \mathrm{div}(\nabla_\Gamma(A'(H)))\\ &= A'(H)(\nabla H\cdot n + H^2 - 2G) + \Delta_\Gamma(A'(H)). \end{aligned}$$

We finally get

$$F_c(x,t) = \left(\Delta_\Gamma(A'(H)) + A'(H)(H^2 - 2G) - A(H)H\right)\frac{1}{\varepsilon}\zeta\left(\frac{\varphi}{\varepsilon}\right)\nabla\varphi.$$

If $A(r) = r^2$ one obtains a curvature force equal to $2\Delta_\Gamma H + H(H^2 - 4G)$ aligned along the normal direction. We find the classical result concerning the derivative of

the Willmore energy $\int H^2 ds$. However we used here a volume approach which will allow us to implement this force, just like the elastic forces, as a source term in the fluid equations. As will be see in Sect. 3.6, this will be convenient to compute the equilibrium forms of vesicles.

Recently, diffusion-redistancing type schemes have been implemented to numerically approach this curvature force which requires, as seen above, a 4th order derivative of the Level Set function. The PhD thesis of Arnaud Sengers [122] extends the diffusion-thresholding methods initiated by Bence, Merriman and Osher [103] and the diffusion-redistancing methods [57] to the case where the area and the surrounded volume must be preserved during the dynamics.

For more details on the calculations of shape derivatives for functionals defined on surfaces and depending on the normal and the mean and Gaussian curvatures, we refer the reader to the PhD thesis of Thomas Milcent [105].

### 3.2.5 *Korteweg Models and Existence of Solutions*

To use finite element-type numerical methods in order to discretize the membrane-fluid coupling problem, it is convenient to have a variational form of the elastic and curvature forces. Moreover, these forms are better suited to the mathematical analysis aiming at proving the existence of solutions. We recall that the elastic force in the form of divergence is given by (3.16). In this way we can formulate the fluid-structure coupling problem in the form of a complex fluid flow whose stress tensor has a fluid part and an elastic part located near the membrane:

$$\sigma = -p\mathbb{I} + \mu([\nabla u] + [\nabla u]^T) + E'(|\nabla\varphi|)\frac{\nabla\varphi \otimes \nabla\varphi}{|\nabla\varphi|}\frac{1}{\varepsilon}\zeta\left(\frac{\varphi}{\varepsilon}\right).$$

This formulation is used in [38] to prove the existence of a solution to this regularized coupling problem. To outline the principle of this proof, we consider the case $\epsilon = 1$, $\rho_1 = \rho_2$, $\mu_1 = \mu_2$ and the multiphysics model introduced above:

$$\rho(\varphi)\left(\partial_t u + (u \cdot \nabla)u\right) - \mu\Delta u + \nabla\pi = -\operatorname{div}\left(\Sigma(\varphi, \nabla\varphi)\right), \tag{3.24}$$

$$\partial_t\varphi + u \cdot \nabla\varphi = 0, \tag{3.25}$$

$$\operatorname{div}(u) = 0. \tag{3.26}$$

The stress tensor $\Sigma$ is written as a result of the constitutive law $E$ of the membrane as

$$\Sigma(\varphi, \nabla\varphi) = \frac{E^{'}(|\nabla\varphi|)}{|\nabla\varphi|}\zeta(\varphi)\nabla\varphi \otimes \nabla\varphi. \tag{3.27}$$

We are given initial conditions on $u$ and $\varphi$

$$u(x,0) = u_0(x)\ ,\ \varphi(x,0) = \varphi_0(x) \tag{3.28}$$

and homogeneous Dirichlet boundary conditions for $u$: $u = 0$ on $\partial\Omega$. So there is no boundary condition for $\varphi$ in the transport equation (note that the analysis readily extends to the case of periodic boundary conditions). We will assume that

$$r \to E'(r) \in \mathcal{C}^1([0,+\infty)). \tag{3.29}$$

For example, the case of a linear response (the material remains geometric-nonlinear) is given by $E'(r) = \lambda(r-1)$. Note that the formulation contains fluids of the Korteweg type [137] as a particular case, with $E'(r) = r$, the level set function then playing the role of density. Indeed if we introduce in this case a primitive $Z$ of $\sqrt{\zeta}$ and set $\psi = Z(\varphi)$ we have

$$\Sigma(\varphi, \nabla\varphi) = \zeta(\varphi)\nabla\varphi \otimes \nabla\varphi = \nabla\psi \otimes \nabla\psi.$$

The function $\psi$ is always a solution of the transport equation and, as $\mathrm{div}(\nabla\psi \otimes \nabla\psi) = \Delta\psi\nabla\psi + [D^2\psi]\nabla\psi = \Delta\psi\nabla\psi + \frac{1}{2}\nabla|\nabla\psi|^2$, we get the usual source term in Korteweg models [137][1] (up to a gradient term that can absorbed in the pressure term).

The following existence result is proved in the reference [38] and the PhD thesis of T. Milcent [105]:

**Theorem 3.6** *Let $\Omega$ be a smooth, open, bounded and connected set in $\mathbb{R}^3$. Let $p > 3$, $\varphi_0 \in W^{2,p}(\Omega)$, such that $|\nabla\varphi_0| \geq \alpha > 0$ in a neighborhood of $\{\varphi_0 = 0\}$, and $u_0 \in W_0^{1,p}(\Omega) \cap W^{2,p}(\Omega)$, with $\mathrm{div}\, u_0 = 0$. Then there exists $T^* > 0$, only depending on the initial conditions, such that a solution to (3.24), (3.25), (3.26) exists in $[0, T^*]$ with*

$$\varphi \in L^\infty(0,T^*; W^{2,p}(\Omega)),\ \nabla\pi \in L^p(0,T^*; L^p(\Omega)),$$
$$u \in L^\infty(0,T^*; W_0^{1,p}(\Omega)) \cap L^p(0,T^*; W^{2,p}(\Omega)).$$

The proof is based on a compactness argument. One first builds a sequence of solutions on a simpler problem on which we know how to show the existence of solutions. One introduces for that a temporal delay regularization of the velocity

[1] Korteweg models are often used to describe fluid media subjected to internal capillary forces [94].

(method also used in [25]) and a spatial regularization of the level set function. The delicate point consists in passing to the limit in the nonlinear term from the elastic force $\mathrm{div}(F(|\nabla\varphi|)\nabla\varphi\otimes\nabla\varphi)$. To simplify the presentation of the ideas, let us choose a Korteweg fluid for which $F = 1$. This assumption is not restrictive because the key point in the estimations lies in the fact that the term in the divergence is nonlinear in $\nabla\varphi$. Let us first look at the energy equality classically obtained by multiplying the momentum equation by $u$ and integrating

$$\frac{1}{2}\frac{d}{dt}(|u|^2_{L^2} + |\nabla\varphi|^2_{L^2}) + \mu|\nabla u|^2_{L^2} = 0. \tag{3.30}$$

This equality makes it possible to have $H^1$ estimates on $\varphi$ which will in turn allow to extract sub-sequences which converge weakly in $H^1$. This will however not allow to pass to the limit in the nonlinear elastic terms. To do this we need more regularity and obtain sequences such as $\nabla\varphi_n$ strongly converges in $L^\infty$. It is therefore necessary to obtain higher order estimates on $\varphi$. The space $H^1$ is not compact in $L^\infty$ and we need a stronger estimate.The Hilbert framework would require to differentiate several times the equations on the velocity and Level Set function, a strategy which would be cumbersome. The idea is instead to consider a non-Hilbertian framework and compact imbeddings $W^{1,p} \subset L^\infty$ for $p > 3$. One can obtain the desired estimates by differentiating only twice the transport equation and using Solonnikov's estimates [131] on the Stokes problem in $L^p$.

## 3.3 Immersed Membrane: The Case with Surface Shear

Until now, the immersed surfaces reacted only to a deformation causing a change of area. This is the case, for example, with phospholipid vesicles. However, in many applications, such as red blood cells, the immersed membrane also exhibits resistance to shear at each point in the tangent plane.

This is a difficulty for Level Set methods, because the dynamics of a function capturing the interface (3.31), by construction, completely ignores the tangential component of the velocity field, since $\nabla\varphi$ is normal to the interface. To hope to capture tangential deformations, it is necessary to be able to record the displacement of points on the interface using additional Level Set functions. This is what we describe below. To begin with we need to review the geometric description of a surface in terms of Level Set functions and to recast in an Eulerian framework the fundamentals of surface deformation and elasticity.

### *3.3.1 Level Set Approach for Surfaces*

Let us start by giving some additional geometry elements related to the Level Set methods. As usual we consider a surface $\Gamma_0$ which evolves in an Eulerian velocity

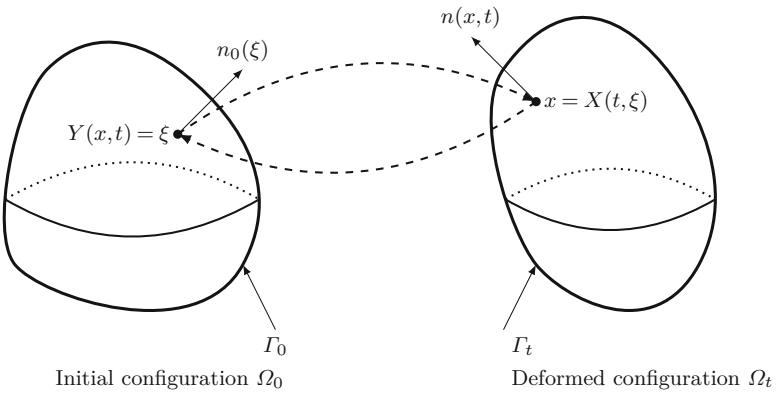


**Fig. 3.2** Initial and deformed configurations

field $u(x,t)$ and denote by $\Gamma_t$ the surface at time $t$. This surface is represented by a level set function $\varphi : \mathbb{R}^3 \times \mathbb{R}^+ \longrightarrow \mathbb{R}$

$$\Gamma_t = \{x \in \mathbb{R}^3 \ , \ \varphi(x,t) = 0\}.$$

We set $\varphi(\cdot, 0) = \varphi_0$. As the surface evolves with the velocity field $u$ one has already seen that its dynamic is written

$$\partial_t \varphi + u \cdot \nabla \varphi = 0. \tag{3.31}$$

Recalling the notation $Y$ for the backward characteristics, we obtain that the solution of (3.31) is

$$\varphi(x,t) = \varphi_0(Y(x,t)). \tag{3.32}$$

Let us note $n_0(\xi)$ the normal at the point $\xi \in \Gamma_0$ in the reference configuration and $n(x,t)$ the normal at the point $x \in \Gamma_t$ in the deformed configuration (see Fig. 3.2 which extends Fig. 2.1 by adding the normals to it). Recall that these normals are given by

$$n(x,t) = \frac{\nabla \varphi(x,t)}{|\nabla \varphi(x,t)|} \ , \qquad n_0(\xi) = \frac{\nabla_\xi \varphi_0(\xi)}{|\nabla_\xi \varphi_0(\xi)|}. \tag{3.33}$$

The identity (3.32) gives $\nabla \varphi(x,t) = [\nabla Y(x,t)]^T \nabla \varphi_0(Y(x,t))$. With (3.33) we can therefore write

$$n_0(Y(x,t)) = \frac{[\nabla Y(x,t)]^{-T} n(x,t)}{|[\nabla Y(x,t)]^{-T} n(x,t)|}. \tag{3.34}$$

Thanks to (2.5) we obtain the Lagrangian equivalent of (3.34):

$$n(X(t,\xi),t) = \frac{[\nabla_\xi X(t,\xi)]^{-T} n_0(\xi)}{|[\nabla_\xi X(t,\xi)]^{-T} n_0(\xi)|}. \tag{3.35}$$

Observe in passing that we recover the formula (2.11).

### 3.3.2 An Eulerian Tensor to Measure Surface Deformation

One thus wishes to measure the strain on the surface $\Gamma_t$. Relying on the Lagrangian formulation, more natural in this context, one starts by introducing the projection of the strain tensor on the tangent plane:

$$M(X(t,\xi),t) := [\nabla_\xi X(t,\xi)][\mathbb{I} - n_0(\xi) \otimes n_0(\xi)]. \tag{3.36}$$

$M$ acts as follows: if $v(\xi)$ is a vector defined at the point $\xi \in \Gamma_0$, this vector is first projected through the operator $[\mathbb{I} - n_0(\xi) \otimes n_0(\xi)]$ into a vector $v_\tau(\xi)$ which belongs to $T_\xi \Gamma_0$, the tangent plane to $\Gamma_0$ in $\xi$. Then the vector $v_\tau(\xi)$ is deformed through the action of $X$ into the vector $[\nabla_\xi X(t,\xi)]v_\tau(\xi)$ at $X(t,\xi)$. Notice that $Mv$ is already in $T_{X(t,\xi)}\Gamma_t$, the tangent plane to $\Gamma_t$ in $X(t,\xi)$. Indeed, using (3.35) and $v_\tau(\xi) \cdot n_0(\xi) = 0$, we have

$$(M(X(t,\xi),t)v(\xi)) \cdot n(X(t,\xi),t) = ([\nabla_\xi X]^T n(X(t,\xi),t)) \cdot v_\tau(\xi)) = 0.$$

The tensor (3.36) is written in its Eulerian form with (2.5)

$$M(x,t) := [\nabla Y(x,t)]^{-1}[\mathbb{I} - n_0(Y(x,t)) \otimes n_0(Y(x,t))].$$

Using the fact that $\mathbb{I} - n_0 \otimes n_0$ is a projector, therefore idempotent, the associated Cauchy–Green tensor is defined by

$$\mathcal{A} := MM^T = [\nabla Y]^{-1}(\mathbb{I} - n_0(Y) \otimes n_0(Y))[\nabla Y]^{-T}.$$

The right Cauchy–Green tensor will play an important role in the sequel. It is defined by

$$B = [\nabla_\xi X][\nabla_\xi X]^T = [\nabla Y]^{-1}[\nabla Y]^{-T}, \tag{3.37}$$

Using (3.34), the relations $A(v \otimes v)A^T = (Av) \otimes (Av)$ and $|[\nabla Y]^{-T} n|^2 = (Bn) \cdot n$, we finally obtain the expression of the surface strain tensor in Eulerian coordinates:

$$\mathcal{A} = B - \frac{(Bn) \otimes (Bn)}{(Bn) \cdot n}. \tag{3.38}$$

### 3.3.3 Invariants and Associated Elastic Force

We start by postulating that the invariants of the tensor $\mathcal{A}$ are the quantities carrying the relevant information to define the surface forces. Using (3.38) we have

$$\mathcal{A}n = 0. \tag{3.39}$$

As a result, 0 is an eigenvalue and $\det(\mathcal{A}) = 0$. The other invariants are $\mathrm{Tr}(\mathcal{A})$ and $\mathrm{Tr}(\mathrm{Cof}(\mathcal{A})) = \frac{1}{2}(\mathrm{Tr}(\mathcal{A})^2 - \mathrm{Tr}(\mathcal{A}^2))$. Since $\mathcal{A}$ is a real symmetric matrix, there exists an orthonormal basis of eigenvectors. In addition $\mathcal{A}$ is positive because $\mathcal{A}x \cdot x = |M^T x|^2 \geq 0$. We denote by 0, $\lambda_1^2$ and $\lambda_2^2$ the associated eigenvalues. We therefore have

$$\mathrm{Tr}(\mathcal{A}) = \lambda_1^2 + \lambda_2^2$$

and

$$\mathrm{Tr}(\mathrm{Cof}(\mathcal{A})) = (\lambda_1 \lambda_2)^2.$$

In the following, we will show that the following expressions allow us to capture the complete deformation of a membrane:

$$Z_1 = \sqrt{\mathrm{Tr}(\mathrm{Cof}(\mathcal{A}))} = |\lambda_1 \lambda_2|, \tag{3.40}$$

$$Z_2 = \frac{\mathrm{Tr}(\mathcal{A})}{2\sqrt{\mathrm{Tr}(\mathrm{Cof}(\mathcal{A}))}} = \frac{1}{2}\left(\left|\frac{\lambda_1}{\lambda_2}\right| + \left|\frac{\lambda_2}{\lambda_1}\right|\right). \tag{3.41}$$

In the reference configuration (often taken at time $t = 0$), we have $\mathcal{A}(0) = \mathbb{I} - n_0 \otimes n_0$, thus $\mathrm{Tr}(\mathcal{A}(0)) = 2$ and $\mathrm{Tr}(\mathrm{Cof}(\mathcal{A}(0))) = 1$. We have $Z_1 = Z_2 = 1$ at $t = 0$ and the inequalities $Z_1 \geq 0$, $Z_2 \geq 1$. Proposition 7.3, proved in the appendix, shows that $Z_1$ measures, in compressible as well as incompressible cases, the variation in the surface area. We also have from Proposition 7.4, also proved in the appendix, the relation

$$Z_1 = J_e \frac{|\nabla \varphi|}{|\nabla \varphi_0(Y)|}. \tag{3.42}$$

We therefore recover the result of Proposition 3.2 already obtained with the membranes reacting only to the variation of area: $|\nabla \varphi|$ measures the local variation in area for an incompressible flow. The $Z_2$ invariant is more difficult to justify in the general framework. To highlight its behavior, we propose in Sect. 7.2.2 a detailed study of its behavior during a prescribed deformation of a surface.

In the discussion and figures below, we illustrate in a simple way the behavior of these invariants for deformations of a planar surface in its plane. The proposed deformations are uniform in space in the sense that the invariants do not depend

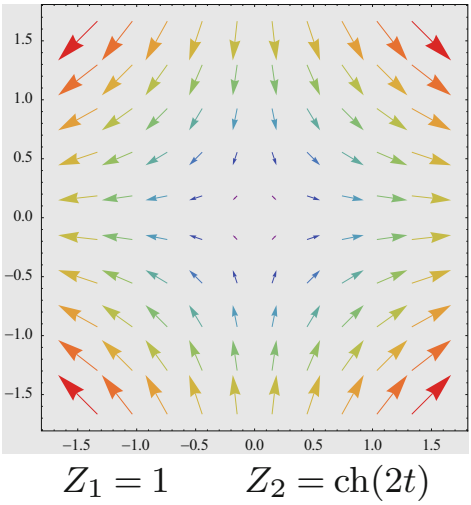


**Fig. 3.3** Velocity field $(x, -y, 0)$ for the deformation $\alpha = -1$ (TC1). From [106]

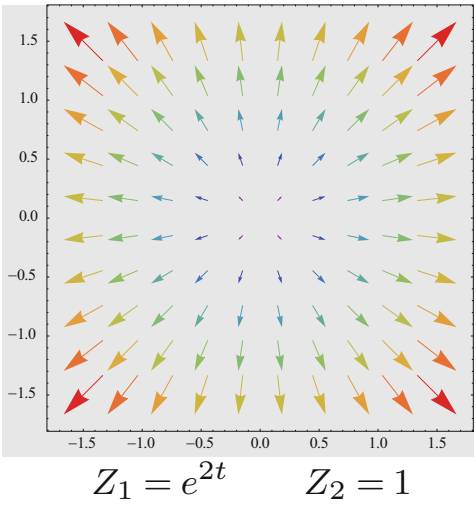


**Fig. 3.4** Velocity field $(x, y, 0)$ for the deformation $\alpha = 1$ (TC1). From [106]

on the spatial variables. The velocity field associated with each deformation is represented in the figures below with the corresponding values of $Z_1$ and $Z_2$ as a function of time $t$. We refer to the appendix for the references to the analytical formulas corresponding to the different test cases (numbered TC1 and TC2).

The deformation corresponding to $\beta = -1$ is a rotation and there is no variation in area and shear (see Fig. 3.7). The deformation $\alpha = 1$ is a pure expansion and only results in a variation of the area (see Fig. 3.4). The deformations $\beta = 0$, $\beta = 1$, $\alpha = -1$ correspond to different shear and no area variation (see Figs. 3.3, 3.6, and 3.8). The deformation $\alpha = 0$ is axial and induces both surface shear and area change (see Fig. 3.5). This may seem surprising at first glance, but when a surface is strained

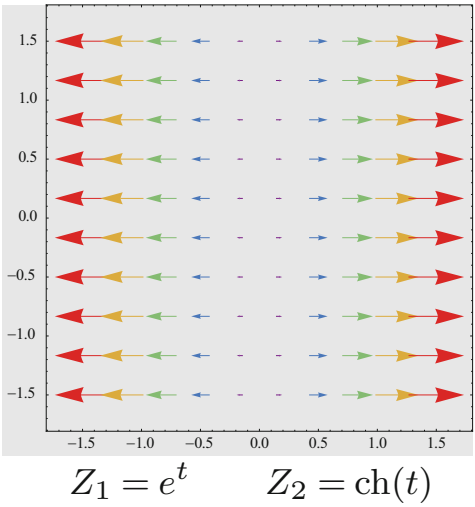


**Fig. 3.5** Velocity field $(x, 0, 0)$ for the deformation $\alpha = 0$ (TC1). From [106]

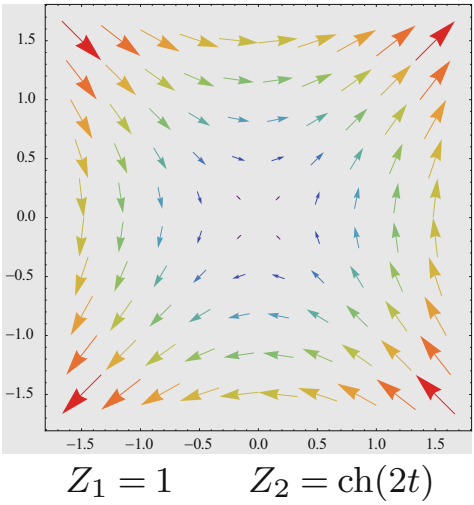


**Fig. 3.6** Velocity field $(y, x, 0)$ for the deformation $\beta = 1$ (TC2). From [106]

in two directions with different amplitude, so that $\alpha \neq 1$, it undergoes shear. The six illustrations in Figs. 3.3 to 3.8 are taken from [106].

*Remark 3.7* In the reference [106], the parametrization $(\theta_1, \theta_2) \mapsto \gamma(t, \theta_1, \theta_2)$ of the surface $S_t$ is introduced with $\gamma : \mathbb{R}^+ \times U \longrightarrow \mathbb{R}^3$ where $U$ is an open set in $\mathbb{R}^2$. One then defines the invariants

$$\mathcal{Z}_1(t) = \sqrt{\det(\mathcal{M}(t))} \qquad \mathcal{Z}_2(t) = \frac{\mathrm{Tr}(\mathcal{M}(t))}{2\sqrt{\det(\mathcal{M}(t))}} \tag{3.43}$$

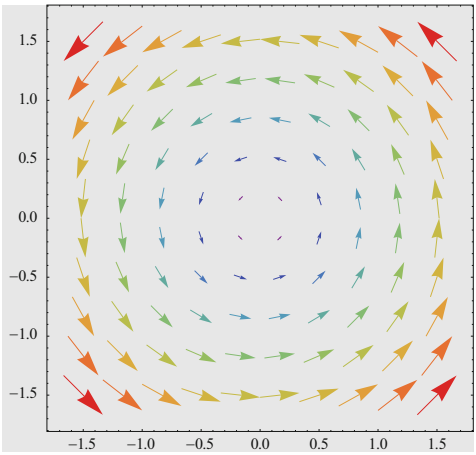


**Fig. 3.7** Velocity field $(-y, x, 0)$ for the deformation $\beta = -1$ (TC2). From [106]

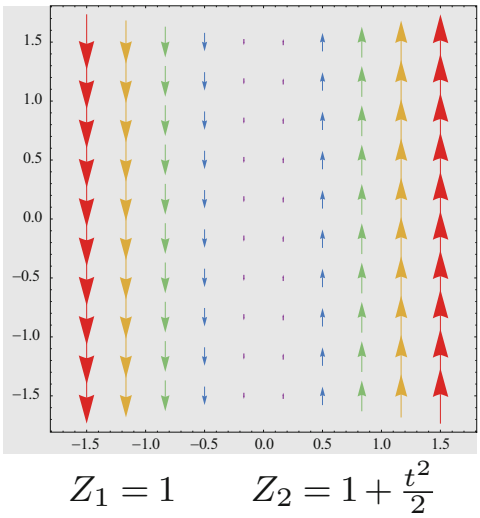


**Fig. 3.8** Velocity field $(0, x, 0)$ for the deformation $\beta = 0$ (TC2). From [106]

where $[\mathcal{M}(t)]_{ij} = \partial_{\theta_i}\gamma \cdot \partial_{\theta_j}\gamma$ is a $2 \times 2$ matrix called a metric. $\frac{\mathcal{Z}_1(t)}{\mathcal{Z}_1(0)}$ can be shown to correspond to the area variation and does not depend on the parametrization. As for the quantity $\frac{\mathcal{Z}_2(t)}{\mathcal{Z}_2(0)}$, it seems to measure the local shear but it depends on the chosen parameterization. This is due to a wrong choice of the invariants. The correct quantity to introduce in the Lagrangian framework is $\widetilde{\mathcal{A}}(t) = \mathcal{M}(t)\mathcal{M}(0)^{-1}$. One has

$$\widetilde{\mathcal{Z}}_1(t) = \det(\widetilde{\mathcal{A}}(t)) = \frac{\mathcal{Z}_1(t)}{\mathcal{Z}_1(0)}, \qquad \widetilde{\mathcal{Z}}_2(t) = \frac{\mathrm{Tr}(\widetilde{\mathcal{A}}(t))}{2\sqrt{\det(\widetilde{\mathcal{A}}(t))}} \neq \frac{\mathcal{Z}_2(t)}{\mathcal{Z}_2(0)}. \tag{3.44}$$

One can then show that this new invariant captures well the shear and does not depend on the chosen parameterization. It is thus possible to record shear deformations in a Lagrangian framework. However, as specified in [106], the Eulerian formulation allows the surface to be immersed in $\mathbb{R}^3$ and thus to overcome the problems related to surface singularities at the poles. Moreover the Eulerian approach allows more easily to deal with large deformations.

### 3.3.4 Energy and Coupling Model

Following the Level Set approach described in Sect. 1.4, we introduce the regularized energy

$$\mathcal{E}_i = \int_\Omega E_i(Z_i)\frac{1}{\varepsilon}\zeta\left(\frac{\varphi}{\varepsilon}\right)dx. \tag{3.45}$$

where $E_i$ is the constitutive law associated with the invariant $Z_i$.

**Theorem 3.8** *Using the principle of virtual work, the time variation of $\mathcal{E}_i$ is given by*

$$\partial_t \mathcal{E}_i = -\int_\Omega F_i \cdot u\, dx \tag{3.46}$$

*and corresponds to the following force:*

$$F_i = \nabla\left(E_i(Z_i)\frac{1}{\varepsilon}\zeta\left(\frac{\varphi}{\varepsilon}\right)\right) + \operatorname{div}\left(E_i'(Z_i)Z_i\mathcal{C}_i\frac{1}{\varepsilon}\zeta\left(\frac{\varphi}{\varepsilon}\right)\right). \tag{3.47}$$

***Proof*** By differentiation with respect to $t$ we obtain

$$\partial_t \mathcal{E}_i = \int_\Omega E_i'(Z_i)\partial_t(Z_i)\frac{1}{\varepsilon}\zeta\left(\frac{\varphi}{\varepsilon}\right)dx + \int_\Omega E_i(Z_i)\frac{1}{\varepsilon^2}\zeta'\left(\frac{\varphi}{\varepsilon}\right)\partial_t\varphi\, dx.$$

Using the transport equation on $\varphi$ and the equation $\partial_t Z_i + u\cdot\nabla Z_i = [\nabla u] : Z_i\mathcal{C}_i$ which follows from Proposition 7.2 proved in the appendix, we get

$$\partial_t \mathcal{E}_i = \int_\Omega E_i'(Z_i)(-u\cdot\nabla Z_i + [\nabla u] : Z_i\mathcal{C}_i)\frac{1}{\varepsilon}\zeta\left(\frac{\varphi}{\varepsilon}\right)dx + \int_\Omega E_i(Z_i)\frac{1}{\varepsilon^2}\zeta'\left(\frac{\varphi}{\varepsilon}\right)(-u\cdot\nabla\varphi)\,dx.$$

The integral over $\partial\Omega$ vanishes because $\zeta(\frac{\varphi}{\varepsilon}) = 0$ sur $\partial\Omega$ and integrating the second term by parts yields

$$\partial_t \mathcal{E}_i = -\int_\Omega u \cdot \nabla(E_i(Z_i))\frac{1}{\varepsilon}\zeta\left(\frac{\varphi}{\varepsilon}\right) + \operatorname{div}\left(E_i'(Z_i)Z_i\mathcal{C}_i\frac{1}{\varepsilon}\zeta\left(\frac{\varphi}{\varepsilon}\right)\right)\cdot u + E_i(Z_i)u\cdot\nabla\left(\frac{1}{\varepsilon}\zeta\left(\frac{\varphi}{\varepsilon}\right)\right)dx.$$

By grouping the first and last terms together and using (3.46) we get the expression (3.47). □

Note that, omitting the pressure term, the force relative to the area variation can be decomposed in the normal and tangential directions by

$$F_1 = \left(\nabla_\Gamma\left(\frac{E_1'(Z_1)J_e}{|\nabla\varphi_0(Y)|}\right) - \frac{E_1'(Z_1)J_e}{|\nabla\varphi_0(Y)|}Hn\right)|\nabla\varphi|\frac{1}{\varepsilon}\zeta\left(\frac{\varphi}{\varepsilon}\right). \tag{3.48}$$

This formula is clearly a generalisation of (3.18) when the flow is compressible ($J_e \neq 1$) and the initial Level set is not a distance function ($|\nabla\varphi_0(Y)| \neq 1$). The proof of this formula follows the lines of the one given for (3.18) and the relation (3.42).

The complete fluid-structure model can thus be formulated as follows in the case with constant density and uniform fluid viscosity:

$$\begin{cases} \partial_t u + u\cdot\nabla u - \mu\Delta u + \nabla p = F_1(\varphi, Y) + F_2(\varphi, Y) & \text{in } \Omega\times]0,T], \\ \operatorname{div} u = 0 & \text{in } \Omega\times]0,T], \\ \partial_t Y + u\cdot\nabla Y = 0 & \text{in } \Omega\times]0,T]. \end{cases} \tag{3.49}$$

This complex fluid type of model, which takes into account the complete elasticity of the membrane (area variation and shear), can therefore be seen as an extension of the Navier–Stokes equations with an elastic source term which is calculated using Level Set functions (the components of the vector $Y$) advected by the flow.

In typical implementations, the numerical discretization schemes to compute the solution of Eqs. (3.49) are based on a finite difference discretization on a staggered Cartesian grid of MAC type. A projection method is used to solve the incompressible Navier–Stokes equations and WENO schemes for the transport part of the backward characteristics. The terms appearing in the Navier–Stokes equations are discretized in space with standard finite difference schemes. The elastic force is localized on the membrane with a discretized Dirac mass.

## 3.4 Curves Immersed in $\mathbb{R}^3$

In this section, we propose an Eulerian approach for the elasticity of one-dimensional curves in $\mathbb{R}^3$. The use of Level Set functions to represent curves in space has been considered for example in [24] with potential applications to image processing. Level Set functions can also be used in fracture mechanics to represent a crack front [80]. We are interested here in the application of this formalism in the context of fluid-structure interaction.

We first introduce an invariant which measures the variation in length of a curve during a deformation, then we introduce an elastic energy and finally deduce the associated elastic force. We do not present in this book numerical simulations associated with this model but it could be implemented in a rather simple way, like the other Eulerian elastic models proposed in this book, as a source term in the Navier Stokes equations.

The aim of this example is to show how the tools and the formalism of the Level Set functions introduced in this book allow to define more general energies in Eulerian formulation and how to calculate the associated forces.

To go further, we could also consider energies which depend on geometric quantities such as curvature and torsion and which can be expressed using Level Set functions following (1.21). A potential application that one can have in mind is the simulation of the influence of aquatic vegetation on coastal flows with the ambition of controlling the silting up of the coastal line.

### *3.4.1 An Eulerian Tensor to Measure Strains Along Curves*

We are interested in a parameterized curve $\Gamma_0$ which is deformed into $\Gamma_t = X(t, \Gamma_0)$ through the mapping $X$. We note $\boldsymbol{\tau}_0(\xi)$ the tangent vector to the curve at a point $\xi \in \Gamma_0$ and $\boldsymbol{\tau}(X(t,\xi), t)$ the tangent vector to $\Gamma_t$ at the point $X(t,\xi)$. According to (2.14), these vectors are related through the relation

$$\boldsymbol{\tau}(X(\xi,t),t) = \frac{[\nabla_\xi X(t,\xi)]\boldsymbol{\tau}_0(\xi)}{|[\nabla_\xi X(t,\xi)]\boldsymbol{\tau}_0(\xi)|} \tag{3.50}$$

or, written in Eulerian form using (2.5),

$$\boldsymbol{\tau} = \frac{[\nabla Y]^{-1}\boldsymbol{\tau}_0(Y)}{|[\nabla Y]^{-1}\boldsymbol{\tau}_0(Y)|} \qquad \boldsymbol{\tau}_0(Y) = \frac{[\nabla Y]\boldsymbol{\tau}}{|[\nabla Y]\boldsymbol{\tau}|}. \tag{3.51}$$

One wishes to measure the strain on the curve $\Gamma_t$. Relying on the Lagrangian formulation, more natural in this context, one starts by introducing the projection of

the strain tensor along the tangent vector $\tau_0$:

$$\widetilde{M}(X(t,\xi),t) := [\nabla_\xi X(t,\xi)][\boldsymbol{\tau}_0(\xi) \otimes \boldsymbol{\tau}_0(\xi)]. \tag{3.52}$$

$\tilde{M}$ acts as follows: let $v(\xi)$ defined at a point $\xi \in \Gamma_0$. This vector is first projected along the tangent $\boldsymbol{\tau}_0$ with the operator $[\boldsymbol{\tau}_0(\xi) \otimes \boldsymbol{\tau}_0(\xi)]$ into a vector $v_{\boldsymbol{\tau}}(\xi)$. Then the vector $v_{\boldsymbol{\tau}}(\xi)$ is deformed through $X$ into the vector $[\nabla_\xi X(t,\xi)]v_{\boldsymbol{\tau}}(\xi)$ at $X(t,\xi)$. This vector is therefore parallel to $\boldsymbol{\tau}$ by virtue of (3.50).

With (2.5) we can write the tensor (3.52) in the Eulerian form

$$\widetilde{M}(x,t) := [\nabla Y(x,t)]^{-1}[\boldsymbol{\tau}_0(Y(x,t)) \otimes \boldsymbol{\tau}_0(Y(x,t))].$$

The associated Cauchy–Green tensor is defined by

$$\mathcal{L} := \widetilde{M}\widetilde{M}^T = [\nabla Y]^{-1}(\boldsymbol{\tau}_0(Y) \otimes \boldsymbol{\tau}_0(Y))[\nabla Y]^{-T}.$$

The second equality above results from the fact that $\boldsymbol{\tau}_0 \otimes \boldsymbol{\tau}_0$ is a projection.

Considering the tensor $B = [\nabla_\xi X][\nabla_\xi X]^T = [\nabla Y]^{-1}[\nabla Y]^{-T}$ and using (3.51), we obtain the following relation

$$|[\nabla Y]^{-1}\boldsymbol{\tau}_0(Y)|^{-2} = |[\nabla Y]\boldsymbol{\tau}|^2 = (B^{-1}\boldsymbol{\tau}) \cdot \boldsymbol{\tau}. \tag{3.53}$$

The identity $A(v \otimes v)A^T = (Av) \otimes (Av)$, combined with (3.53), leads to the following expression for the tensor of one-dimensional strains in Eulerian coordinates:

$$\mathcal{L} = \frac{\boldsymbol{\tau} \otimes \boldsymbol{\tau}}{(B^{-1}\boldsymbol{\tau}) \cdot \boldsymbol{\tau}} \tag{3.54}$$

### 3.4.2 *Invariants and Associated Elastic Force*

If $x$ is a vector orthogonal to $\tau$, then $\mathcal{L}x = 0$. The plane orthogonal to $\tau$ is therefore an eigenspace of dimension 2 associated with the eigenvalue 0 of the operator $\mathcal{L}$. As $\mathcal{L}$ is non-negative, because $\mathcal{L}x \cdot x = |\tilde{M}^T x|^2 \geq 0$, we denote by $\lambda_1^2 = \mathrm{Tr}(\mathcal{L})$ its non-zero eigenvalue. We introduce the invariant

$$Z_3 = \sqrt{\mathrm{Tr}(\mathcal{L})} = \sqrt{\frac{1}{(B^{-1}\boldsymbol{\tau}) \cdot \boldsymbol{\tau}}}. \tag{3.55}$$

In the reference configuration (often taken at time $t = 0$), we have $\mathcal{L}(0) = \tau_0 \otimes \tau_0$ hence $\mathrm{Tr}(\mathcal{L}(0)) = 1$. We have $Z_3 = 1$ at $t = 0$ and the inequality $Z_3 \geq 0$ for all times. Proposition 7.6, shown in the appendix, proves that $Z_3$ measures, in both compressible and incompressible regimes, the variation in length of the curve. We

also have from Proposition 7.7, also shown in the appendix, the relation

$$Z_3 = J_e \frac{|\nabla\varphi^1 \times \nabla\varphi^2|}{|\nabla\varphi_0^1(Y) \times \nabla\varphi_0^2(Y)|} \tag{3.56}$$

where $\varphi^1, \varphi^2$ are two Level Set functions such that the intersection of the associated zero level sets represents the curve. One can thus calculate the local variation of length using only the gradient of these two functions. This result can be seen as the equivalent of (3.42) for the curves.

We introduce the regularized energy

$$\mathcal{E}_3 = \int_\Omega E_3(Z_3) \frac{1}{\varepsilon^2} \zeta\left(\frac{\varphi^1}{\varepsilon}\right) \zeta\left(\frac{\varphi^2}{\varepsilon}\right) dx, \tag{3.57}$$

where $E_3$ is the constitutive law associated with the invariant $Z_3$. Thanks to the volume approximation formula (7.44) we deduce that this energy converges towards the perimeter of the parametrized curve for the constitutive law $E_3(r) = r$. This corresponds to the equivalent for the curves of the surface tension energy for surfaces.

According to Proposition 7.13, proved in the appendix, the associated force is given by

$$F_3 = \nabla\left(E_3(Z_3) \frac{1}{\varepsilon^2} \zeta\left(\frac{\varphi^1}{\varepsilon}\right) \zeta\left(\frac{\varphi^2}{\varepsilon}\right)\right) + \operatorname{div}\left(E_3'(Z_3) Z_3 \boldsymbol{\tau} \otimes \boldsymbol{\tau} \frac{1}{\varepsilon^2} \zeta\left(\frac{\varphi^1}{\varepsilon}\right) \zeta\left(\frac{\varphi^2}{\varepsilon}\right)\right).$$

We also show in the appendix Proposition 7.14 which allows to break down this force as follows

$$F_3 = \left(\left(\nabla\left(\tilde{E}_3'\right) \cdot \boldsymbol{\tau}\right) \boldsymbol{\tau} + \tilde{E}_3' H n\right) |\nabla\varphi^1 \times \nabla\varphi^2| \frac{1}{\varepsilon^2} \zeta\left(\frac{\varphi^1}{\varepsilon}\right) \zeta\left(\frac{\varphi^2}{\varepsilon}\right), \tag{3.58}$$

where $\tilde{E}_3' = \frac{E_3'(Z_3) J_e}{|\nabla\varphi_0^1(Y) \times \nabla\varphi_0^2(Y)|}$.

It is interesting to note that the force is written in the basis $(\boldsymbol{\tau}, n)$ and that there is therefore no component along the binormal vector $b$. We recall that the definitions of these geometric notions for parameterized curves in $\mathbb{R}^3$ using Level Set functions are given in Sect. 1.3.

## 3.5 Explicit and Semi-implicit Time Discretizations

We have seen in Sect. 1.6 that the time discretization technique chosen to simultaneously advect the Level Set function and take into account the capillary forces in the Navier–Stokes equations impacted the stability of the methods, and that a semi-implicit scheme could prove profitable from this point of view. This is again the case in the fluid-structure interaction models discussed in this chapter. This is not surprising because the elastic forces supported by the membranes can be seen as generalizations of the capillary forces.

We describe in the following the transcription in the case of shear-free membranes covered in Sect. 3.2 the explicit and semi-implicit schemes seen in Sect. 1.6 and we provide numerical illustrations of their behavior. Note that, and this is an important remark, it is not necessary to give linear stability analysis of these schemes. Indeed the linearizations and approximations of the coupling terms performed in Sect. 1.6 lead to the same models as in the case of multi-phase fluids and therefore would lead to the same conclusions on the conditions of linear stability of the schemes.

### *3.5.1 Explicit Schemes*

We recall the expression (3.18) of the elastic force as it appears in the right side of the Navier–Stokes equation, expressed in tangential and normal components:

$$F[\varphi] = \left( \nabla_\Gamma (E'(|\nabla\varphi|)) - E(|\nabla\varphi|) H(\varphi) \frac{\nabla\varphi}{|\nabla\varphi|} \right) |\nabla\varphi| \frac{1}{\varepsilon} \zeta\left(\frac{\varphi}{\varepsilon}\right).$$

The explicit scheme consists in alternating the resolutions of the Navier–Stokes equations where the elastic forces are evaluated from the values of $\varphi$ at the preceding time-step, followed by a transport equation where the velocity field results from the former stage :

$$\begin{cases} \dfrac{u^{n+1} - u^n}{\Delta t} = F[\varphi^n] + R(u^n, u^{n+1}), \\ \operatorname{div} u^{n+1} = 0, \\ \dfrac{\varphi^{n+1} - \varphi^n}{\Delta t} + u^{n+1} \cdot \nabla\varphi^{n+1} = 0. \end{cases} \tag{3.59}$$

### 3.5.2 Semi-implicit Scheme

We now extend the semi-implicit scheme (1.60)–(1.62) to the general case of an elastic interface immersed in an incompressible fluid. We proceed as in the case with surface tension, and start by writing an implicit time step in diffusion and explicit in convection for the Navier–Stokes equation

$$\begin{cases} \dfrac{u^{n+1}-u^n}{\Delta t} = F[\varphi^{n+1}] + \mu\Delta u^{n+1} - u^n\cdot\nabla u^n - \nabla p^{n+1}, \\ \operatorname{div} u^{n+1} = 0, \\ \dfrac{\varphi^{n+1}-\varphi^n}{\Delta t} + u^{n+1}\cdot\nabla\varphi^{n+1} = 0, \end{cases} \tag{3.60}$$

from which we build the following predictor of $u^{n+1}$:

$$\tilde{u}^{n+1} = u^n + \Delta t\, F[\varphi^{n+1}].$$

By inserting this expression in the advection equation for $\varphi$ we see that the tangential component of the force gives no contribution. Keeping only higher-order terms, we are left with

$$\frac{\tilde{\varphi}^{n+1}-\varphi^n}{\Delta t} - E'(|\nabla\varphi^n|)\frac{\Delta t}{\varepsilon}\Delta\tilde{\varphi}^{n+1} = -u^n\cdot\nabla\varphi^n. \tag{3.61}$$

The semi-implicit method is thus summarized in the following substeps:

Sub-step 1: implicit diffusion on $\varphi$

$$\frac{\tilde{\varphi}^{n+1}-\varphi^n}{\Delta t} - E'(|\nabla\varphi^n|)\frac{\Delta t}{\varepsilon}\Delta\tilde{\varphi}^{n+1} = -u^n\cdot\nabla\varphi^n. \tag{3.62}$$

Sub-step 2: discretization of the Navier–Stokes equations

$$\frac{u^{n+1}-u^n}{\Delta t} - \mu\Delta u^{n+1} + u^n\cdot\nabla u^n + \nabla p^{n+1} = F[\tilde{\varphi}^{n+1}]\ ;\ \operatorname{div} u^{n+1} = 0. \tag{3.63}$$

Sub-step 3: explicit advection of $\varphi$

$$\frac{\varphi^{n+1}-\varphi^n}{\Delta t} + u^{n+1}\cdot\nabla\varphi^n = 0. \tag{3.64}$$

### 3.5.3 Numerical Validation

Let us first consider the case of a viscous droplet subjected to surface tension. As already seen, this case can be seen as a particular case of an elastic membrane with a linear elastic potential. In this case, the semi-implicit scheme reduces in its predictive part to a simple diffusion equation.

Let us look more precisely at the case of an initial interface of elliptical shape, with an axis of sizes 0.5 and 0.75 respectively. Under the effect of surface tension, the elliptical drop relaxes to a circular shape with the same surface area. This test case, although simple, is a useful benchmark to check the conservation properties of the method.

Throughout this section, $\Delta t$ is the time step used to solve the Navier–Stokes equation with the elastic force. As already mentioned, depending on its value, sub-iterations can be used in the advection equation in order to satisfy the appropriate CFL condition in a grid-based method.

The surface tension coefficient (or stiffness coefficient for an elastic membrane with linear potential) is taken equal to 1. All the tests are carried out with a constant time step $\Delta t = 0.0025$. The width of the interface is $\varepsilon = 6\Delta x$. Figure 3.9 compares for $N = 256$ the evolution of the two axes of the ellipse obtained by the Level Set method in the case of a semi-implicit and explicit scheme. For these parameters, the semi-implicit scheme, unlike the explicit scheme, is found to be stable.

Figure 3.10 illustrates the numerical convergence of the semi-implicit scheme when the grid is refined. In this figure, the evolution of the small and large axes is shown for $N = 256$ and $N = 512$.

The Eulerian model has good volume conservation properties because it is based on a projection scheme on a staggered grid, which ensures to machine precision a zero divergence of the velocity field. To illustrate this property, we show in Fig. 3.10 the loss of volume in the drop for resolutions ranging from $N = 64$ to $N = 512$. We can see that the loss of volume during the oscillations is kept below 1.5% for the coarsest resolution and below 0.1% for the highest resolution. This can

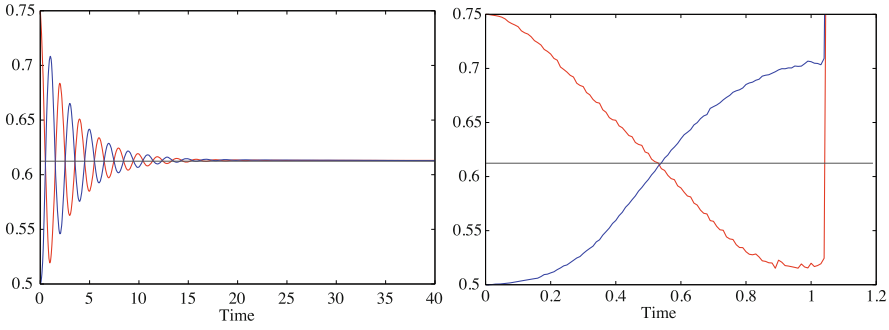


**Fig. 3.9** Oscillating drop for $N = 256$ and $\Delta t = 0.0025$. Time evolution variation of the axes lengths with the semi-implicit stable scheme (left picture) and explicit (right picture). From [37]

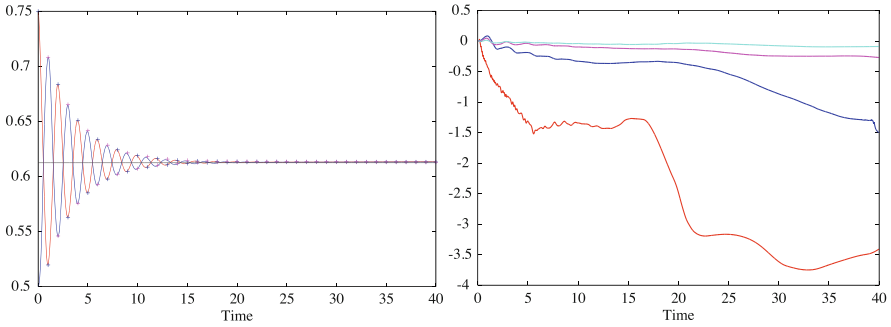


**Fig. 3.10** Oscillating drop with the semi-implicit scheme. Left: time evolution of the horizontal (blue) and vertical (red) axes lengths, for $N = 256$ (crosses) and $N = 512$ (continuous lines). Right: time eveolution of the volume inside the membrane (in percentage) for $N = 64$ (red), $N = 128$ (blue), $N = 256$ (magenta) and $N = 512$ (cyan). From [37]

be considered as satisfactory, given that volume conservation is a known issue in Immersed Boundary Methods (see for instance [95]).

Consider now an elastic membrane whose behavior is described by the quadratic elastic potential of (3.13). The value of the stiffness coefficient $\lambda$ is taken equal to 10. We consider the same test case as previously, borrowed from [36, 95]. The elliptical membrane, whose major and minor axes are again equal to 0.75 and 0.5, respectively, is stretched from a state of circular equilibrium. This corresponds to a uniform stretching rate of around 1.262.

We first study the stability properties of the semi-implicit scheme. To this end, we present two sets of refinement studies. In the first series of tests, we kept for the semi-implicit scheme the same time step for the Level Set equation for all the resolutions, with a value $\Delta t = 0.01$. In the second series of tests, the time step chosen for the semi-implicit scheme was specified using a CFL condition with a CFL number equal to 0.25, while, for the explicit scheme, it had to be defined on the basis of the stability condition (1.54). Table 3.1 shows the values of the resulting time steps for the explicit and semi-implicit schemes.

Figure 3.11 shows the relaxation of the membrane, for resolutions corresponding to a number of grid points in each direction ranging between $N = 64$ and $N = 256$, when the semi-implicit scheme is used with the time-step equal to 0.01. These experiments confirm the stability of the semi-implicit approach, but also show that,

**Table 3.1** Time step values used in the $2D$ experiment for the explicit and semi-implicit schemes

| N | Explicit | Semi-implicit |
|---|---|---|
| 64 | $3.5\,10^{-3}$ | $10^{-2}$ |
| 128 | $1.5\,10^{-3}$ | $8.\,10^{-3}$ |
| 256 | $6.5\,10^{-4}$ | $4.\,10^{-3}$ |
| 512 | $2.\,10^{-4}$ | $2.\,10^{-3}$ |

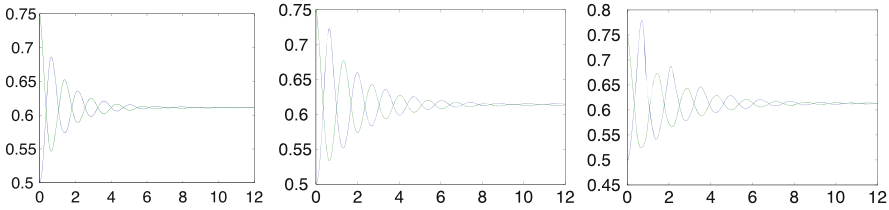


**Fig. 3.11** Relaxation of an elliptical elastic membrane. Time evolution of large and small axes using the semi-implicit scheme for $\Delta t = 10^{-2}$ and, from left to right, for $N = 64, 128, 256$. From [37]

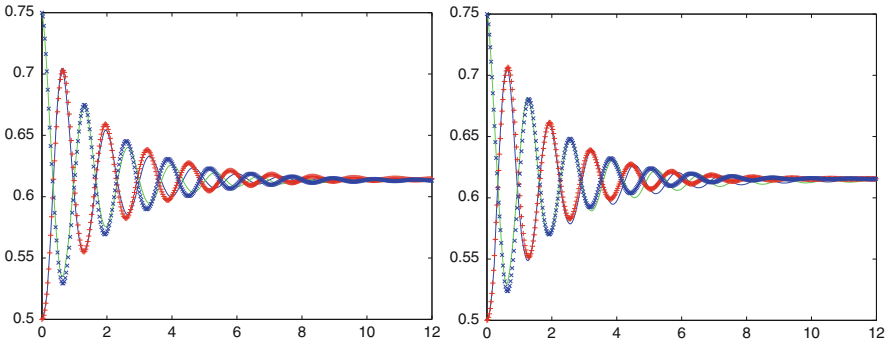


**Fig. 3.12** Relaxation of a 2D elliptical membrane. Temporal variation of the axes lengths. Semi-implicit (continuous line) vs explicit ($\times$ and $+$) schemes for $N = 128$ (left picture) and 256 (right picture). From [37]

for relatively small grid size and large time steps the membrane starts by undergoing non physical oscillations, before relaxing to its equilibrium position.

The reason is that, for large values of $\Delta t$, the elastic force, obtained from the filtered value of $\varphi$, is enforced at a location which significantly differs from its actual position. It can be noted, however, that if one is mainly interested in the state of equilibrium, rather than the dynamics of the oscillations, large values of the time step remain admissible.

The second series of refinement tests compare, as illustrated in Fig. 3.12, for the time steps given in Table 3.1, the results obtained with the explicit and semi-implicit schemes, for $N = 128$ and $N = 256$. On the left, for $N = 128$, we used $\Delta t = 1.5 \times 10^{-3}$ for the explicit scheme and $\Delta t = 8 \times 10^{-3}$ for the semi-implicit scheme. On the right, we have chosen $\Delta t = 6.5 \times 10^{-4}$ for the explicit scheme and $\Delta t = 4 \times 10^{-3}$ for the semi-implicit scheme. For $N = 256$ the time step for the semi-implicit scheme is eight times larger than for the explicit scheme, with very close results concerning the amplitudes. These experiments confirms the gain offered by the semi-implicit method. The slight time shift visible over long simulation times can be related the shift, already observed in Fig. 3.11, between the

physical position of the interface and the location of the force, when the time step is large.

## 3.6 Numerical Illustrations and Sample Code

In this section we successively review the different cases studied above: membrane without shear, membrane with bending energy and membrane with shear.

### *3.6.1 Shear-Free Membrane*

#### 3.6.1.1 2D Oscillating Elastic Membrane: FreeFEM++ and Matlab Codes

Let us come back to this case already evoked to study the stability of the discretization methods in time. We give below a code based on the FreeFEM++[84] finite element library which demonstrates the simplicity of implementing Level Set methods in this context. The goal here is educational, and the codes are given in their simplest version: the discretization in time is made by an explicit Euler method, the time step is constant and the transport equation for the Level Set function is solved by the characteristic method. The targeted test case is the one already used in [95] for the study of the immersed boundary methods.

As already observed, the form (3.16) of the elastic force

$$F = \operatorname{div}\left(E'(|\nabla\varphi|)|\nabla\varphi|\left(\mathbb{I} - \frac{\nabla\varphi \otimes \nabla\varphi}{|\nabla\varphi|^2}\right)\frac{1}{\varepsilon}\zeta\left(\frac{\varphi}{\varepsilon}\right)\right)$$

is natural for a variational formulation of the model.

The program below proposes an implementation in less than one hundred lines of this simple fluid-structure problem, using the finite element method and the FreeFEM++ software. The fluid mechanics equations are solved by a so-called P2-P1 discretization and the Level Set function is discretized into P2 elements (lines 20–22 of the code).

The test case consists of a stretched ellipse which relaxes towards a circle. We start by calculating a signed distance function to this ellipse from an implicit equation, by solving a Hamilton–Jacobi equation (lines 43–50). Note that this step can alternatively be carried out directly under FreeFEM++, which makes it possible to calculate the distance to any hypersurface described by a level set.

The variational formulation of the fluid problem is described in lines 61–71, in monolithic version. The software convect function, which implements the characteristic method, is used to solve both the transport equations of the level-set

function and the convective part of the fluid equations. Note that this part of the code does not require a CFL condition.

```
load "iovtk"

// settings
real xm=2; // Size of the box in x-direction
real ym=2; // Size of the box in y-direction
int n=30, m=30; // Number of points in each direction
real A=0.75, B=0.5; //  Ellipse axis lengths
real LARGINT=1.5; // Interface width relative to grid-size
real lambda=1; //  Stiffness coefficient
real Re=100; // Reynolds number=1 / viscosity
real ETIRINI=1.26253110; // Initial stretching
real tmax=10; // Simulation time
real dtaff=0.2; // Time between successive visualizations
real CFL=0.2; // CFL number for the Hamilton Jacobi equation
real dt=5.e-3; // Time step for level set and Navier-Stokes
    equations
real eps1=0.001; // Small parameter used to compute the normal

// Mesh
mesh Th=square (n,m, [xm*x, ym*y],flags=1);
fespace Velocity(Th,P2);
fespace  Pressure(Th,P1);
fespace LevelSet(Th,P2);

Velocity u1,u2,v1,v2,u1n,u2n;
Pressure p, q, pp;
LevelSet phi,M,M2,S,phiinit,nabla,N1,N2,zet,aux;

// Definition of the initial ellipse
func phi0=sqrt ((x-xm / 2)^2 /(A^2)+(y-ym/2)^2/(B^2))-1;
phi=phi0;
u1n=0; u2n=0;

// Calculation of the distance function to this ellipse
// NB: recent versions of FreeFEM$++$ implement a
// calculation of the distance to an interface described by a
// level line which can replace these few lines.

Pressure h1=hTriangle;
real h=h1[].max; // Maximum size of a triangle in the mesh
real epsil=LARGINT*xm/n;
int iterinit;
real TT=CFL*h;  // time step for re-initialization
for (iterinit=1;iterinit< 50*LARGINT;iterinit=iterinit+1)
{
        nabla=(dx(phi))^2+(dy(phi))^2;
        S=phi/(sqrt(phi^2+h*h*nabla)); //approximation of sign(
            phi)
        M1=dx(phi)/(sqrt(nabla+eps1^2)); //approximation of the
            normal
```

```
        M2=dy(phi)/(sqrt(nabla+eps1^2));
        phi=convect([-S*M1,-S*M2],TT,phi)+TT*S;
};

// zeta function
func real zeta(real r) {
  return (((r>-1)&&(r<1))?0.5*(1+cos(pi*r)):0);
}
// r -> E'(r) deformation / constraint law
func real Ep(real r) {
   return(lambda*(r-1));
}

// Variational problem
problem IBM([u1,u2,p],[v1,v2,q])=
    // Navier-Stokes
            int2d(Th)(u1*v1/dt+u2*v2/dt
            +1/Re*(dx(u1)*dx(v1)+dy(u1)*dy(v1) + dx(u2)*dx(v2)+
                dy(u2)*dy(v2)))
            + int2d(Th)(dx(p)*v1 + dy(p)*v2 + q*(dx(u1)+dy(u2)) -
                 1e-10*p*q)
            -int2d(Th)(convect([u1n,u2n],-dt,u1n)/dt*v1+convect([
                u1n,u2n],-dt,u2n)/dt*v2)
    // Elastic tensor
            + int2d(Th)(Ep(nabla)*(dy(phi)*dy(phi)*dx(v1)-dx(phi)
                *dy(phi)*(dx(v2)+dy(v1))+dx(phi)*dx(phi)*dy(v2))/
                nabla*zet)
    // Boundary conditions
            + on(1,2,3,4,u1=0,u2=0);

// Main loop
real t=0, taff=0;
for (t=0; t <tmax; t +=dt) {
   cout << "t=" << t << " Volume variation (%)= " << (vol-vol0)/
       vol0*100 << endl;
   //  Navier-Stokes equations
   IBM;
   u1n=u1; u2n=u2;
   // Transport of phi
   aux=convect([u1,u2],-dt,phi);
   phi=aux; vol=int2d(Th)(phi<0);
   nabla=sqrt((dx(phi))^2+(dy(phi))^2+eps1^2);
   zet=1./(nabla*epsil)*zeta(phi/(nabla*epsil));

   if (t>taff) {
      pp=p-p[].min;
      string vtkout="results/memb_t="+t+".vtk";
      savevtk(vtkout,Th,pp,phi,[u1,u2,0],dataname="Pressure
          LevelSet Velocity");
      taff=taff+dtaff;
      Th=adaptmesh(Th,p);
   }
}
```

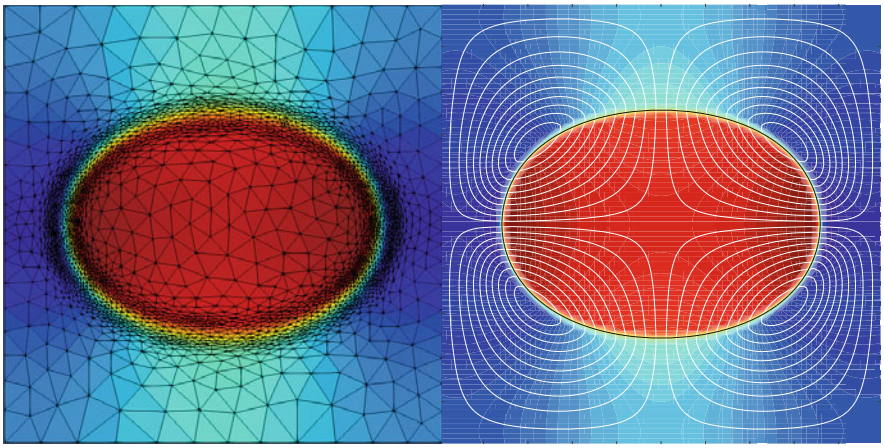

**Fig. 3.13** Pressure field calculated by FreeFEM++ (left figure) and Matlab (right figure) at $t = 0.4$

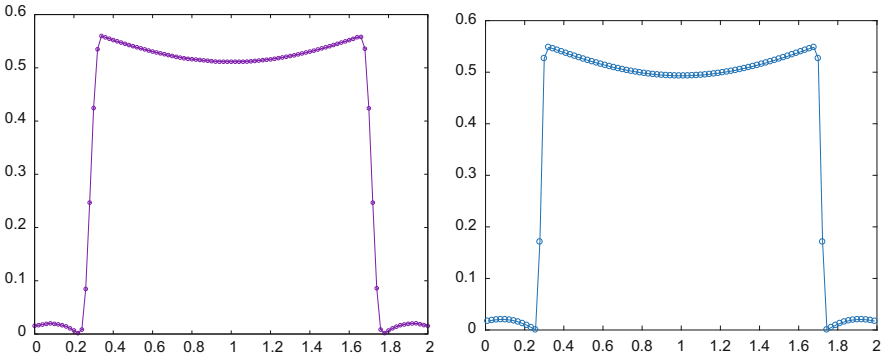


**Fig. 3.14** Pressure profile obtained by FreeFEM++ (left picture) and Matlab (right picture) at $t = 0.4$

The figures below correspond to the execution of this FreeFEM++ program up to $t = 0.4$. They show the mesh and the contours of the pressure field (left picture in Fig. 3.13) and the pressure profile along the axis $y = 1$ passing though the center of the ellipse (left picture in Fig. 3.14).

A finite difference code has also been implemented in Matlab, and is available on line.[2] It implements a Chorin-type projection method. The Level-Set package from Baris Sumengen is also used, where we have updated a WENO scheme to its WENO-Z version [3, 29] for the advection part (this scheme is described in the appendix).

[2] http://level-set.imag.fr.

The code is thus based on quite different methods from those involved the finite element code. We nevertheless obtain (see right pictures of Figs. 3.13 and 3.14) remarkably close numerical results, taking into account the fact that the linear interpolation of the *convect* function in the FreeFEM++ method induces as expected a greater numerical spreading of the interface, visible on the pressure profile. One can see that for the finite-difference method the pressure gradient is essentially captured on one grid point. This confirms what was already mentioned concerning energy conservation, namely that the spreading of the force, which is part of the Level Set formulation, does not induce a build up in time of numerical dissipation.

#### 3.6.1.2 Membrane with Bending Energy

One of the applications of Level Set methods, and more generally of fluid-structure coupling methods, concerns the study of the dynamics of red blood cells in shear flows. To reproduce the behavior of these objects in the blood flow, we can consider in a first approach that the associated energy is purely a bending energy (which is the case for phospholipid membranes), with a constraint of constant length of the membrane. One way to approach this problem is to operate by penalization, considering a very steep area change energy.

A classical setting is to place a vesicle in a symmetrical shear flow (by this we mean the shear of the flow and not that of the surface as studied in the next section) and to study its behavior as a function of the viscosity ratio of the fluids inside and outside the membrane. Below a certain threshold, it is known that the stationary behavior is a "tank-treading" regime with an angle relative to the flow direction which depends on the viscosity ratio. Beyond this threshold, the motion is an almost rigid rotation of the membrane and of the fluid within the membrane, relatively to the flow outside the membrane (the so-called "tumbling" regime).

Another application consists in calculating the 3D equilibrium shapes of vesicles according to their volume ratio, that is to say their volume compared to the volume of a sphere having the same area. In this application, the time step in the transport and Navier–Stokes equations acts as an iteration increment for an optimization algorithm.

Figures 3.15, 3.16 and 3.17 illustrate the results obtained by Level Set methods in these different situations. We refer to [98, 99] for a more detailed discussion of these results.

Much work has been carried out on this topic, using either phase field methods or the Level Set methods, and relying on the finite element library FEEL ++ [104] (available at https://docs.feelpp.org). We refer to the PhD thesis of Vincent Doyeux [53] and the references therein.

More recently diffusion-redistanciation methods for interface motion using geometry based energies have been implemented in the PhD thesis of Arnaud Sengers [122] in the framework of FEEL++.

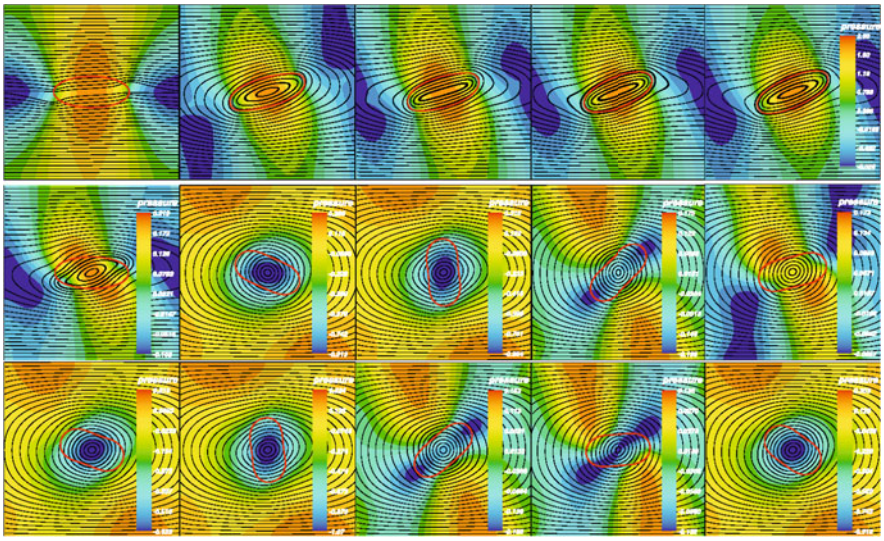

**Fig. 3.15** Tank-treading (top pictures) and tumbling (two bottom lines) motion of a vesicle with a filling rate of 0.7 in a shear flow, depending on the ratio between inside and outside viscosity values (respectively 1 and 8). The vesicle is represented by a red line on top of pressure contour lines. From [99]

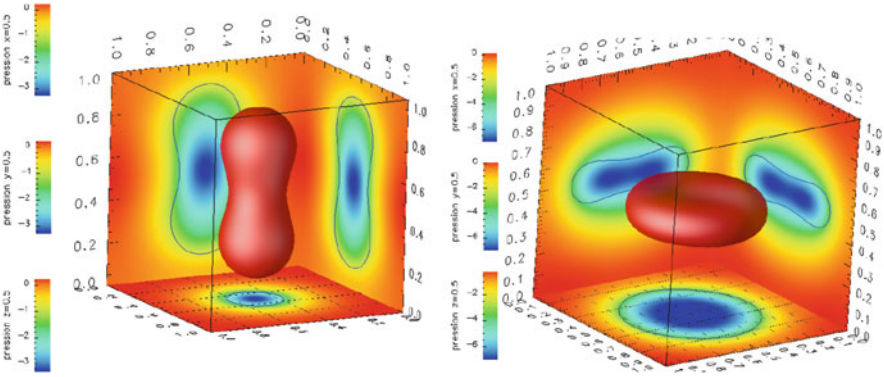

**Fig. 3.16** Three-dimensional equilibrium shape depending on the volume ratio. Left picture: 0.77; right picture: 0.6. From [98]

### *3.6.2 Membrane with Shear*

To illustrate this case, the following linear elastic laws are used in the simulations of this section

$$E_1'(r) = \lambda_1(r-1) \qquad E_2'(r) = \lambda_2(r-1) \tag{3.65}$$

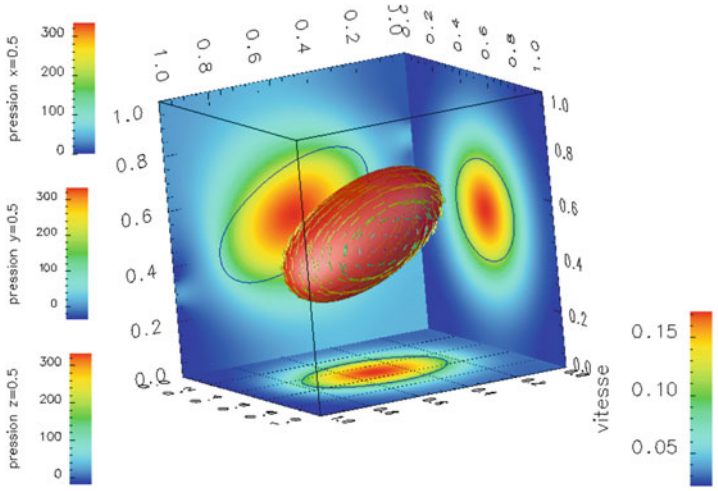


**Fig. 3.17** Three-dimensional vesicle in a shear flow. From [105]

where $\lambda_1$ and $\lambda_2$ are the elastic area and shear modulus as defined in Sect. 3.3.3. Note that, although the elastic energies are linear, the model is still strongly nonlinear because of the geometric nonlinearities and the coupling with the Navier–Stokes equations.

In this section, we are interested in the test case of a sheared elastic sphere. The domain $Q = [-1, 1]^3$ is discretized on a Cartesian mesh using 128 points in each direction. We choose in this simulation a viscosity $\mu = 0.01$, an area modulus of elasticity $\lambda_1 = 1$ and a shear modulus $\lambda_2 = 1$. The parameter $\varepsilon$ is equal to $3.5\Delta x$ in simulations where $\Delta x$ is the grid size. The time step is $\Delta t = 1,3\,10^{-3}s$. A vanishing velocity is taken for the initial and boundary conditions. The initial immersed surface is a sphere, so that

$$\varphi_0(x, y, z) = \sqrt{x^2 + y^2 + z^2} - 0.5. \tag{3.66}$$

However this sphere is preloaded with the backward characteristic field

$$Y(x, y, z, 0) = (x\cos(t_0 z) + y\sin(t_0 z), -x\sin(t_0 z) + y\cos(t_0 z), z) \tag{3.67}$$

This corresponds to a deformation of the sphere when a three-dimensional circular shear (see the expression of $Y$ for TC4 in Table 7.1 and Fig. 7.2) is applied up to $t = t_0$. Here we take $t_0 = \pi$. Although this initial deformation was imposed (artificially) with no area variation (the sheared surface is still geometrically a sphere), the area will change locally when the sphere begins to relax, so the force $F_1$ is also involved. The motion is however initially controlled by the shear force $F_2$.

Numerical results at different times are shown in Fig. 3.18. In order to visualize the local displacement of the points, we represented on the deformed surface a grid

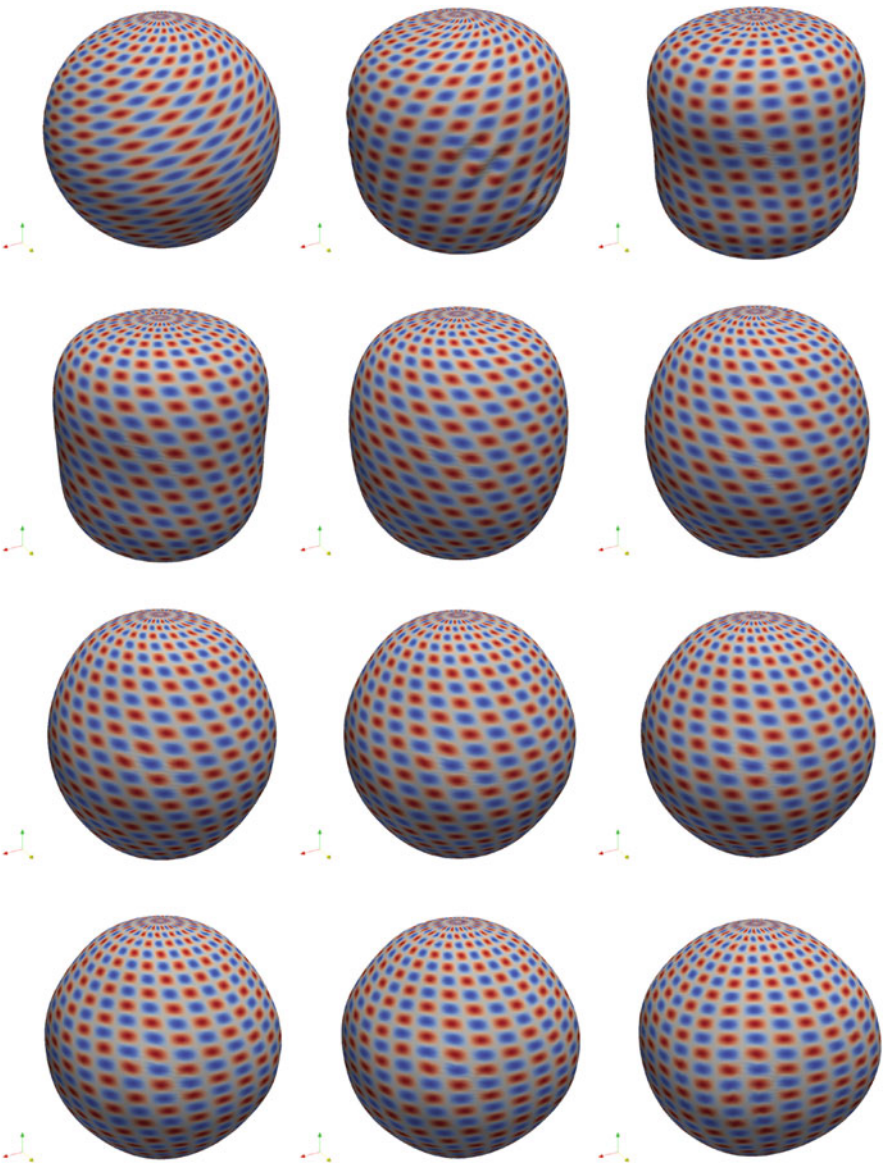

**Fig. 3.18** Relaxation of a sphere subject to shear, from time $t = 0$ to $t = 9$ with increments of 0.5 (from left to right, top to bottom). Lagrangian markers are used to show the return to the unconstrained state of equilibrium. From [106]

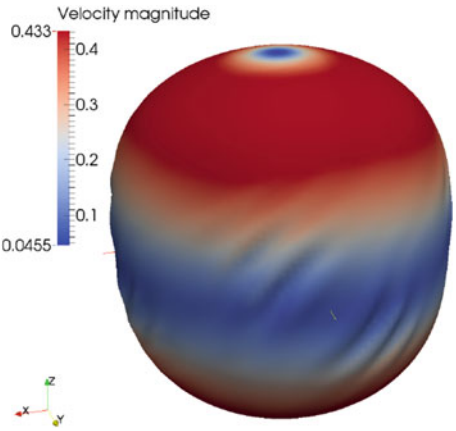


**Fig. 3.19** Velocity magnitude at $t = 0.5$ for the sphere under shear. From [106]

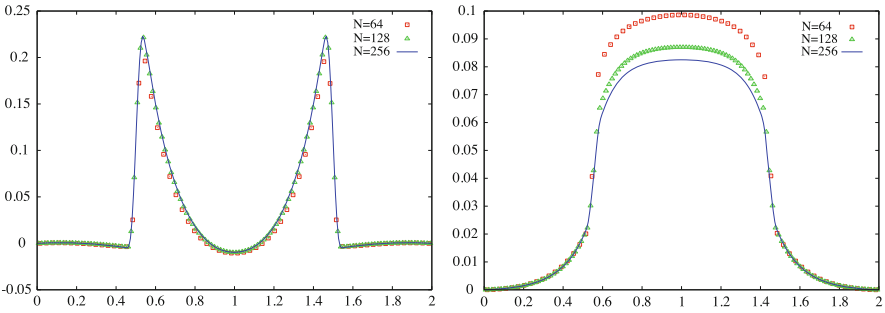


**Fig. 3.20** Spherical membrane under shear. Pressure along the $x$ axis at time $t = 0.1$ (left picture) and $t = 1.2$ (right picture) for $N = 64, 128, 256$. From [106]

which was followed with markers. In Fig. 3.19, we draw on the surface the norm of the velocity at $t = 0.5$. Due to the high shear imposed, the surface undergoes a complex deformation involving some folding. This type of ripple was also observed in [146] in the simulation of a capsule subjected to simple shear. An interesting feature of this method is its ability to converge to a stable solution even in absence of any curvature energy. Note that the sphere does not seem to return to its initial state since it is not initially pressurized. If an initial pressure jump is prescribed across the membrane, by setting the initial area variation above one, it will drive the equilibrium state back to the sphere. Similarly to the 2D experiment in Fig. 3.12, we then observe that the membrane does relax to its initial shape (see the corresponding movie in http://level-set.imag.fr).

To analyze in a more precise way the numerical convergence of the method, Figs. 3.20 and 3.21 show pressure profiles along the $x$ and $z$ axes during this relaxation at times $t = 0.1$ and $t = 1.2$. Similarly, Fig. 3.22 represents the variation of the vertical radius over time. The calculations were carried out with $N$ points in

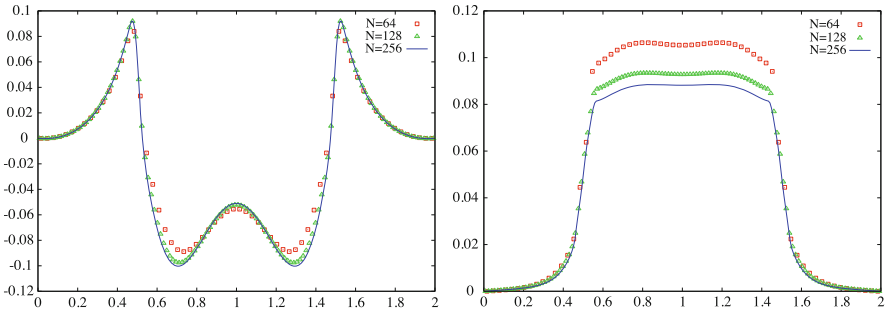


**Fig. 3.21** Spherical membrane under shear. Pressure along the $z$ axis at time $t = 0.1$ (left picture) and $t = 1.2$ (right picture) for $N = 64, 128, 256$. From [106]

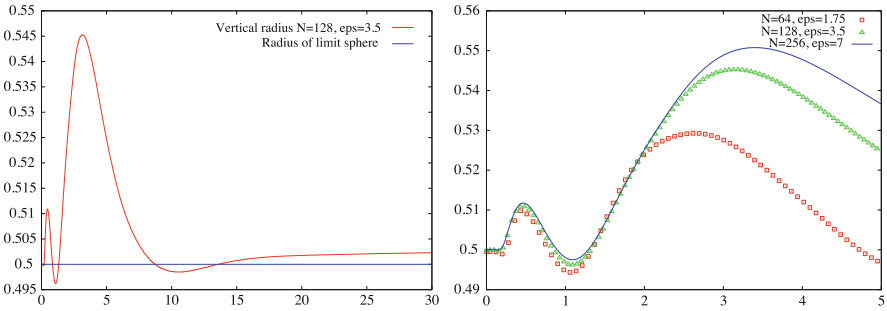


**Fig. 3.22** Spherical membrane under shear. Left picture: vertical radius up to $t = 30$. Right picture: zoom on values of $t \in [0, 5]$ for $N = 64, 128, 256$. From [106]

each direction with $N = 64$, 128 and 256. In all these, in order to keep a constant physical thickness and observe numerical convergence as the grid is refined, the width of the numerical interface was kept constant. As a consequence, its value $\varepsilon$ is equal to $1.75\Delta x$, $3.5\Delta x$, $7\Delta x$, depending on the value of $N$, where $\Delta x$ is the corresponding grid size.

Since the flow is incompressible, the function $Y(\cdot, t) : \Omega \to \Omega$ conserves the volume, that is, $\det(\nabla Y) = 1$ at the continuous level. However, after discretization in time and space, and due to numerical errors introduced when solving the transport equations on $Y$, this constraint cannot be exactly imposed. In Figs. 3.23 and 3.24, we represent the $L^2$ norm of $\det(\nabla Y) - 1$ as a function of time, over the whole domain and at the interface. More precisely the plotted quantities are respectively:

$$RMS_\Omega(t) = \left( \frac{1}{|\Omega|} \int_\Omega |\det \nabla Y(x,t) - 1|^2 \, \mathrm{d}x \right)^{\frac{1}{2}},$$

$$\text{and } RMS_{\Gamma_t}(t) = \left( \frac{1}{|\Gamma_t|} \int_{\Gamma_t} |\det \nabla Y(x,t) - 1|^2 \, \mathrm{d}s \right)^{\frac{1}{2}}. \tag{3.68}$$

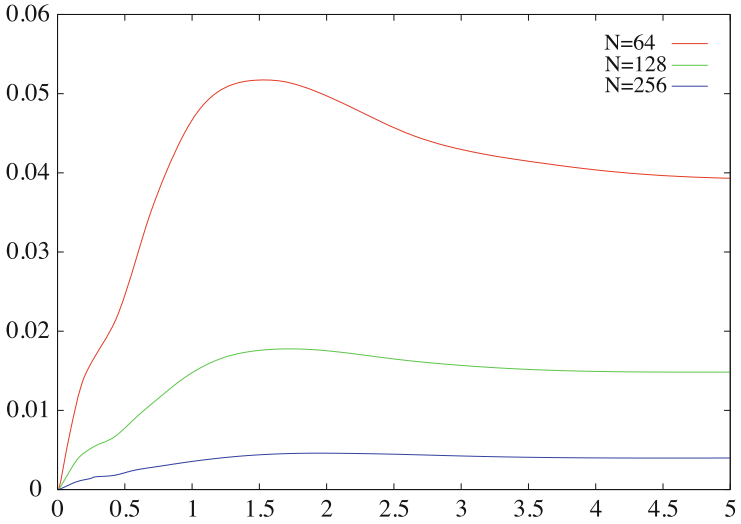


**Fig. 3.23** Spherical membrane under shear. Time evolution for $N = 64, 128, 256$ of $t \rightarrow RMS_{\Omega}(t)$ defined in (3.68). From [106]

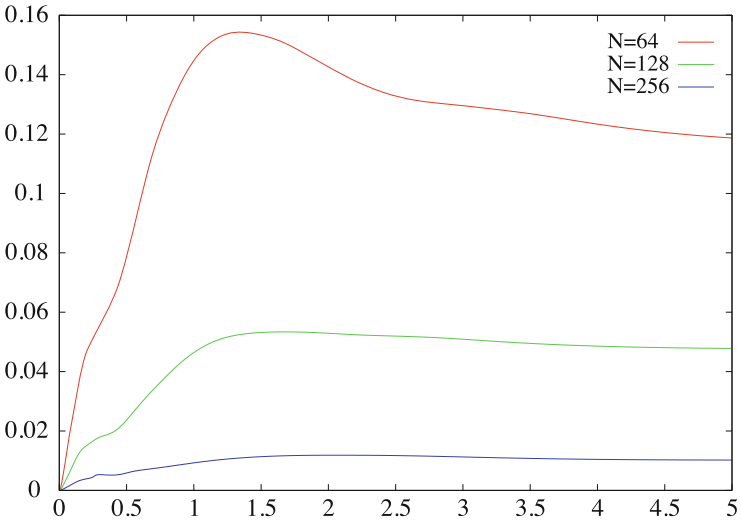


**Fig. 3.24** Spherical membrane under shear.Time evolution for $N = 64, 128, 256$ of $t \rightarrow RMS_{\Gamma_t}(t)$ defined in (3.68). From [106]

Although the $N = 64$ case is clearly under-resolved these figures show that numerical conservation dramatically improves as the grid is refined.

# Chapter 4
# Immersed Bodies in a Fluid: The Case of Elastic Bodies


In this chapter we are interested in the modeling and the simulation of fluid-structure interactions in the case where the elastic solid has a finite thickness as opposed to the case of the surface membranes studied in the previous chapter.

Several strategies have been developed in the literature to resolve this type of interaction. In the ALE methods [52], which are the most commonly used, see for instance [18, 64–68, 70, 79], the physical domain is discretized on a moving mesh which follows the motion of the interface. The formulation and implementation of numerical methods in this context is tricky, especially in three dimensions. The generation and partitioning of meshes can also be problematic when solids are subjected to large deformations. The immersed boundary methods mentioned in the previous chapter can be extended to the case of volume elasticity [16], in general by considering volumes made up of mono-dimensional fibers. We refer to [81] for a recent review of these methods.

As in the case of membranes, it is possible to rely on an Eulerian formulation of elasticity that will couple in a simple way the elastic solids with fluids, which are already naturally described in an Eulerian formulation. The interest of Eulerian models lies in the possibility of discretizing them on a fixed grid, typically Cartesian, which allows a simple implementation and parallelization as well as taking into account large deformations in the solid. In addition, the fluids and solids considered in these interactions can be incompressible (and possibly viscous) or compressible. We refer to [119] for a recent review of these methods.

In the more specific point of view which concerns us in this book, a Level Set function will be used in order to follow in an Eulerian way the interface between the fluid and the solid, completed by additional Level Set functions to account for the deformations and elastic forces. It is these methods that we will describe in this chapter.

For compressible and incompressible media, the models are of a different nature: hyperbolic for the compressible case and parabolic for the incompressible case. Their natural numerical treatment is therefore based on very different numerical



G.-H. Cottet et al., *Level Set Methods for Fluid-Structure Interaction*, Applied Mathematical Sciences 210, https://doi.org/10.1007/978-3-031-08659-5_4

schemes: discretization by finite volume method using Riemann solvers for the compressible case; finite difference or finite-element and projection methods for the incompressible case. This is why models and discretizations are natural for interactions where the fluid and the solid are both compressible or both incompressible. The case of a compressible solid coupled to an incompressible viscous fluid could also be taken into account by the type of methods relevant to this book, but to the detriment of their simplicity because it would be necessary to impose the constraint of zero divergence of the velocity field on only a part of the domain. We will mostly ignore this case here. However an example falling into this category for rigid solids will be discussed in Sect. 5.5.

After a general presentation of the equations of hyperelastic solids in Lagrangian and Eulerian formulation, we will focus on the fluid-structure interactions, first in the compressible then in the incompressible case. We will end this chapter by presenting two illustrations of fluid-structure interactions, one in the incompressible case, the other in the compressible case.

## 4.1 Hyperelastic Materials in Lagrangian Formulation

We are now interested in the modeling of elastic materials. The Lagrangian formulation is *a priori* the most suitable framework for several reasons:

- the free surface limiting the unknown elastic solid $\Omega_t$ is taken into account by bringing it back to the reference configuration $\Omega_0$,
- the forward characteristics $X(t,\xi)$ make it possible to follow the position of the points of the solid from their initial position $\xi$ and the tensor $\nabla_\xi X$ allow to locally calculate the deformations of the medium,
- the first Piola-Kirchhoff stress tensor $\mathcal{T}$, defined by (2.27) is expressed as a function of the strain tensor $\nabla_\xi X$, which provides a closure to the elasticity system.

For a more detailed description of the concepts mentioned in this section, the reader can consult [85].

Let $W : M_3(\mathbb{R}) \to \mathbb{R}$ be a function defined over the set of $3 \times 3$ square matrices. The Taylor expansion of $W$ reads

$$W(F+H) = W(F) + \frac{\partial W}{\partial F}(F) : H + o(|H|) \tag{4.1}$$

and by definition $\left[\dfrac{\partial W}{\partial F}\right]_{ij} = \dfrac{\partial W}{\partial F_{ij}}$ where $A : B = \mathrm{Tr}(A^T B)$ denotes the usual scalar product of matrices. A material is said to be hyper-elastic if the first Piola Kirchoff tensor is given by the derivative with respect to $\nabla_\xi X$ of a volume energy

per unit of volume $W$

$$\mathcal{T}(t,\xi) = \frac{\partial W}{\partial F}(\nabla_\xi X). \tag{4.2}$$

The energies that are considered in practice are not arbitrary but must obey certain physical principles.

### 4.1.1 Principle of Material Indifference

We note $F = \nabla_\xi X$ and $Q$ any rotation belonging to $SO(3)$. The energy must verify the principle of material indifference which can be written

$$\forall Q \in SO(3) \quad W(QF) = W(F). \tag{4.3}$$

The geometric interpretation of this definition is as follows: the energy is invariant if we apply a rotation after the deformation (see Fig. 4.1). We can show that the energy associated with a material which satisfies the principle of material indifference is written

$$W = \tilde{W}(C(t,\xi)), \tag{4.4}$$

where $C$ indicates the right Cauchy–Green tensor

$$C(\xi,t) = [\nabla_\xi X]^T [\nabla_\xi X]. \tag{4.5}$$

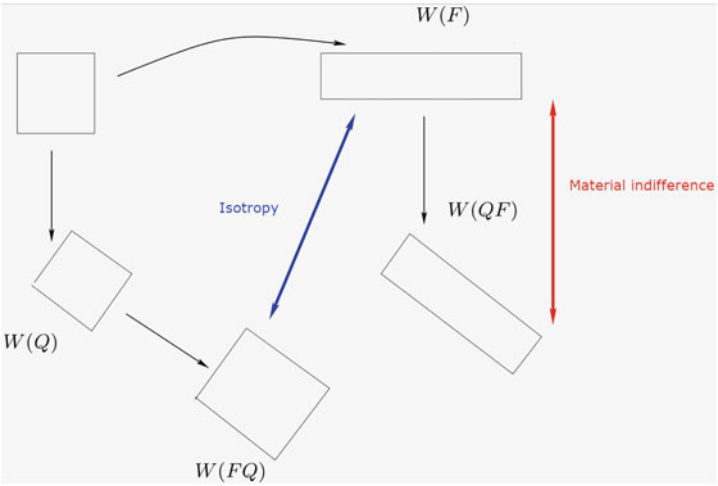


**Fig. 4.1** Illustration of material indifference and isotropy

This energy only depends on $C = F^T F$, so we have to find a way to calculate $\mathcal{T}$. To do this we introduce $W(F) = \tilde{W}(F^T F)$. We have the following expansion

$$W(F+H) = \tilde{W}(F^T F + F^T H + (F^T H)^T + H^T H)$$
$$= \tilde{W}(F^T F) + \frac{\partial \tilde{W}}{\partial C}(C) : (F^T H + (F^T H)^T) + o(|H|).$$

Since $C$ is symmetric, $\frac{\partial \tilde{W}}{\partial C}$ is a symmetric matrix and the linear term in $H$ reads $2[F\frac{\partial \tilde{W}}{\partial C}(C)][H]$. Upon comparing with (4.1) we thus obtain

$$\mathcal{T} = [\nabla_\xi X]\Sigma, \tag{4.6}$$

where $\Sigma$ indicates the second Piola Kirchhoff tensor defined by

$$\Sigma = 2\frac{\partial \tilde{W}}{\partial C}(C). \tag{4.7}$$

This relation is one of the reasons for introducing this tensor.

### *4.1.2 Isotropic Materials*

Materials often verify symmetry properties. They are said to be isotropic if they behave in the same way in all directions. To simplify the exposition, we will place ourselves in this section mainly in this case. However, we will also give below (Sect. 4.3.2) a numerical illustration for a case of anisotropic elasticity. In the isotropic case, the associated energy satisfies

$$\forall Q \in SO(3) \quad W(FQ) = W(F). \tag{4.8}$$

The geometric interpretation of this definition is as follows: the energy is invariant if we apply a rotation and then a deformation (see Fig. 4.1). When this relationship is only verified for certain rotations, the material is said to be anisotropic. We can show that the energy of a material which is isotropic and which satisfies the principle of material indifference is written

$$W = W(\iota_{C(t,\xi)}) \tag{4.9}$$

where $\iota_C = (\mathrm{Tr}(C), \mathrm{Tr}(\mathrm{Cof}(C)), \det(C))$ are the three invariants of $C$. It is easy to show that an energy of the type (4.9) satisfies (4.3) and (4.8). The converse is more delicate and the proof is purely algebraic. In the case of an anisotropic material, the

energy depends on $C$ but also on tensors constructed with $C$ and some privileged directions of anisotropy.

### 4.1.3 Computation of the Stress Tensor in a Lagrangian Framework

Let us now compute the stress tensor associated to the energy (4.9). Using (4.7) we get

$$\frac{\Sigma}{2} = \frac{\partial W(\iota_C)}{\partial C} = \frac{\partial W}{\partial a}\frac{\partial \operatorname{Tr}(C)}{\partial C} + \frac{\partial W}{\partial b}\frac{\partial \operatorname{Tr}(\operatorname{Cof}(C))}{\partial C} + \frac{\partial W}{\partial c}\frac{\partial \det(C)}{\partial C}.$$

We have the following expansions (recall that $C$ is symmetric)

$$\begin{aligned}
\operatorname{Tr}(C+H) &= \operatorname{Tr}(C) + \operatorname{Tr}(H),\\
\operatorname{Tr}(\operatorname{Cof}(C+H)) &= \operatorname{Tr}(\operatorname{Cof}(C)) + \operatorname{Tr}((\operatorname{Tr}(C)I - C)H) + o(|H|),\\
\det(C+H) &= \det(C) + \det(C)\operatorname{Tr}(C^{-1}H) + o(|H|).
\end{aligned}$$

We therefore obtain

$$\frac{\Sigma}{2} = \left(\frac{\partial W}{\partial a} + \operatorname{Tr}(C)\frac{\partial W}{\partial b}\right) I - \frac{\partial W}{\partial b}C + \frac{\partial W}{\partial c}\det(C)C^{-1}. \tag{4.10}$$

The Cayley–Hamitlon theorem reads

$$C^3 - \operatorname{Tr}(C)C^2 + \operatorname{Tr}(\operatorname{Cof}(C))C - \det(C)I = 0. \tag{4.11}$$

We thus have $\det(C)C^{-1} = C^2 - \operatorname{Tr}(C)C + \operatorname{Tr}(\operatorname{Cof}(C))I$, which allows to write the stress tensor as function of $(I, C, C^2)$ if needed. The elasticity equations are finally given by

$$\rho_0 \partial_{tt}^2 X = \operatorname{div}([\nabla X]\Sigma), \tag{4.12}$$

where $\Sigma$ depends in a nonlinear way on $X(t,\xi)$ through (4.10).

These equations are posed in the reference domain $\Omega_0$ and are supplemented by initial conditions and appropriate boundary conditions. Note here that if we consider an incompressible elastic medium, we must impose the condition

$$J_\ell(t,\xi) = \det(\nabla_\xi X(t,\xi)) = 1, \tag{4.13}$$

which is not trivial because this constraint is a nonlinear equation. To do this, we must write the first tensor of Piola Kirchhoff under the form $\mathcal{T} = -p[\nabla X]^{-T} +$

$\tilde{\mathcal{T}}$ where $p$ denotes the scalar Lagrange multiplier needed to impose the constraint (4.13). We will see later that this incompressibility condition becomes linear in an Eulerian framework and is simpler to impose numerically through a zero divergence condition on the velocity field.

## 4.2 Hyperelastic Materials in Eulerian Formulation

### *4.2.1 Computation of the Stress Tensor in an Eulerian Framework*

The tensor $\mathcal{T}$ (or equivalently the tensor $\Sigma$) allows to calculate the stresses in the reference configuration. However, the stress tensor in the deformed configuration is easier to interpret on physical grounds. In this case, the tensor $\sigma$ must be calculated using the forward characteristics $X(t,\xi)$. To do this we use the relation $\sigma\,\mathrm{Cof}([\nabla X]) = \mathcal{T}$, (2.27) combined with (4.7) to get

$$\sigma(X(t,\xi),t) = J_\ell(t,\xi)^{-1}[\nabla_\xi X(t,\xi))]\Sigma(t,\xi)[\nabla_\xi X(t,\xi))]^T. \tag{4.14}$$

After having introduced the left Cauchy–Green tensor

$$\tilde{B}(t,\xi) = [\nabla_\xi X(t,\xi))][\nabla_\xi X(t,\xi))]^T \tag{4.15}$$

we have the following relationships

$$[\nabla_\xi X]I[\nabla_\xi X]^T = \tilde{B},\ [\nabla_\xi X]C^{-1}[\nabla_\xi X]^T = I,\ [\nabla_\xi X]C[\nabla_\xi X]^T = \tilde{B}^2. \tag{4.16}$$

Using (4.10) et (4.16), the expression (4.14) becomes (we also use the fact that $B$ and $C$ have the same invariants)

$$\sigma(X(t,\xi),t) = 2J_\ell^{-1}\left(\frac{\partial W}{\partial c}\det(\tilde{B})I + \left(\frac{\partial W}{\partial a} + \mathrm{Tr}(\tilde{B})\frac{\partial W}{\partial b}\right)\tilde{B} - \frac{\partial W}{\partial b}\tilde{B}^2\right). \tag{4.17}$$

Observe that this Cauchy tensor is written on the deformed configuration but that it is calculated in a Lagrangian way as it depends on the forward characteristics $X(t,\xi)$. In order to write this tensor in Eulerian formulation we are going to use the backward characteristics $Y(x,t)$. Recall that these characteristics satisfy $Y(X(t,\xi),t) = \xi$ and that the differentiation of this equation with respect to $t$ and $\xi$ gives

$$\partial_t Y + (u\cdot\nabla)Y = 0, \qquad [\nabla_\xi X(t,\xi)] = [\nabla_x Y(x,t)]^{-1}.$$

In the Eulerian formulation we have an additional equation related to the conservation of mass (2.20). Starting from (2.22) and using $Y$, we obtain

$$\rho(x,t) = \det(\nabla_x Y(x,t))\rho_0(Y(x,t)). \tag{4.18}$$

It is therefore possible to recover the density using backward characteristics. Using the relation (4.2.1), the left Cauchy Green tensor (4.15) is rewritten at $\xi = Y(x,t)$

$$\tilde{B}(t, Y(x,t)) = [\nabla_x Y(x,t)]^{-1}[\nabla_x Y(x,t)]^{-T} = B(x,t). \tag{4.19}$$

We also remind that $J_e(x,t) = J_\ell(t, Y(x,t))$. The Eulerian expression of the Cauchy tensor is therefore given by

$$\sigma(x,t) = 2J_e^{-1}\left(\frac{\partial W}{\partial c}\det(B)I + \left(\frac{\partial W}{\partial a} + \mathrm{Tr}(B)\frac{\partial W}{\partial b}\right)B - \frac{\partial W}{\partial b}B^2\right). \tag{4.20}$$

This Cauchy tensor is written on the deformed configuration. It is here calculated in an Eulerian way because it relies on the backward characteristics $Y(x,t)$.

It is interesting in practice to decompose the energy into a part which depends only on volume variations and an isochoric part which only depends on the shear. This formulation is very useful in the compressible case because it allows to model gases (perfect, of Van der Waals type etc), non-viscous fluids (with so-called stiffened gas laws) as well as elastic solids (Neo-Hookean for example). Let us break down the energy as follows:

$$W = W_{\mathrm{vol}}(J_e) + W_{\mathrm{iso}}(\mathrm{Tr}(\overline{B}), \mathrm{Tr}(\mathrm{Cof}(\overline{B}))), \tag{4.21}$$

where $\overline{B}(x,t) = \frac{B(x,t)}{\det(B(x,t))^{\frac{1}{3}}}$ and $J_e(x,t) = \det(B(x,t))^{\frac{1}{2}}$. Notice that $\det(\overline{B}) = 1$ and this is why we use the term isochoric for this part of the energy. To write the stresses it suffices to rely on the formula (4.20) with

$$W(a,b,c) = W_{\mathrm{vol}}(c^{\frac{1}{2}}) \qquad \text{and} \qquad W(a,b,c) = W_{\mathrm{iso}}(c^{-\frac{1}{3}}a, c^{-\frac{2}{3}}b).$$

We obtain with the formula (4.20)

$$\sigma(x,t) = W'_{\mathrm{vol}}(J_e)I + 2J_e^{-1}\left(\overline{\sigma}_{\mathrm{iso}} - \frac{\mathrm{Tr}(\overline{\sigma}_{\mathrm{iso}})}{3}I\right), \tag{4.22}$$

with

$$\overline{\sigma}_{\mathrm{iso}} = \frac{\partial W_{\mathrm{iso}}}{\partial a}\overline{B} - \frac{\partial W_{\mathrm{iso}}}{\partial b}\overline{B}^{-1}.$$

### 4.2.2 Elastic Constitutive Laws for Elastic Media

The constitutive laws of elasticity are phenomenological, in the sense that, unlike in gases, they do not arise from microscopic statistical physics. The constitutive laws obey physical principles (material indifference, isotropy, etc.) and their choice depends on the behavior of the material in small/large deformations, compression, shearing, etc. We can mention the law of Mooney–Rivlin

$$W_{\text{iso}} = \chi_1(\text{Tr}(\overline{B}) - 3) + \chi_2(\text{Tr}(\overline{B}^{-1}) - 3),$$

with, as a particular case, the Neo-Hookean law which corresponds to the value $\chi_2 = 0$. Let us also mention the Saint-Venant Kirchoff law

$$W_{\text{iso}} = \frac{\chi_1}{2}\,\text{Tr}(E)^2 + \chi_2\,\text{Tr}(E^2) \qquad \text{with} \qquad E = \frac{1}{2}(C - I).$$

In these energies, the parameters $\chi_i$ are the elastic coefficients measured in Pascal unit.

There are also anisotropic laws that model materials which do not behave in the same way in all directions. For example, a material with a privileged direction $\tau$ whose elastic response is invariant under rotation around this direction and also when replacing $\tau$ by $-\tau$ (a case often encountered for biological tissues as we will see below) is said to be transverse isotropic. In this case the energy depends on $(\text{Tr}(B), \text{Tr}(B^{-1}))$ as well as on $\tau^T B^{-2}\tau$ and $\tau^T B^{-1}\tau$, and the stress tensor $\sigma$ depends on the quantities $(\nabla Y^{-1}\tau) \otimes (\nabla Y^{-1}\tau)$ and $(\nabla Y^{-1}\tau) \otimes (B\nabla Y^{-1}\tau) + (B\nabla Y^{-1}\tau) \otimes (\nabla Y^{-1}\tau)$ [111]. An example of such a law is given in the case of the contraction of a heart cell which will be considered in (4.33).

There is a considerable literature on elastic constitutive laws and we refer again to the work [85] and the references therein for more details.

### 4.2.3 Eulerian Elasticity in the Incompressible Case

A medium is said to be incompressible if it satisfies the condition $J_\ell = \det(\nabla X) = 1$ everywhere. Using a Reynolds formula ((2.15) with $f = 1$), one can then show that the Eulerian equivalent corresponds to the constraint $\text{div}(u) = 0$. It is interesting to note that this constraint is linear, unlike the constraint $J_\ell = 1$ in the Lagrangian framework which is non linear.

In order to impose this constraint, it is natural to introduce a pressure $p$ as a Lagrange multiplier associated with the constraint $\text{div}(u) = 0$. One can then show that the stress tensor (4.22) is written

$$\sigma(x, t) = -pI + \sigma_{\text{iso}}(\nabla Y). \tag{4.23}$$

Since the zero divergence constraint is linear, it is relatively easy to find $p$ with a projection method, for example. In the case of small deformations, one can use the models of linear elasticity which depend on two elastic parameters $\lambda$ and $\mu$, the so-called Lamé coefficients, or, equivalently, on $E$ and $\nu$, the Young's modulus and the Poisson ratio. One can show that if $\nu$ is close to $1/2$ then, for an infinitesimal strain, the volume is almost locally conserved. However we must always have $\nu < 1/2$ because the formulas are singular for the value $1/2$. Let us insist on the fact that these two notions of incompressibility are different. The one involving zero divergence of the velocity allows to impose exactly $J = 1$ while remaining valid even if the solid undergoes large deformations. Note also that in an incompressible regime the energy equation is not coupled to the momentum equation.

We finally obtain the following equations for an incompressible elastic medium (we use here the non-conservative forms of the equations)

$$\begin{cases} \rho(\partial_t u + (u \cdot \nabla)u) + \nabla p = \operatorname{div}(\sigma_{\text{iso}}(\nabla Y)), \\ \operatorname{div}(u) = 0, \\ \partial_t Y + (u \cdot \nabla)Y = 0. \end{cases} \tag{4.24}$$

This complex fluid-type model can be seen an extension of the Navier–Stokes equations with an elastic source term which is calculated using three Level Set functions (the three components of the $Y$ vector) advected by the flow.

### 4.2.4 Eulerian Elasticity in the Compressible Case

Compressible elasticity equations are used when materials are subject to local changes in volume. They are most often used for the study of transient phenomena. When looking at compressible media, the energy equation is no longer decoupled from the equations translating the conservation of mass and momentum. It is also important to consider the conservative forms of the equations because the solutions of these equations can develop finite-time discontinuities (shock waves or contact discontinuities), in which case the non conservative forms are generally ill-posed. In this compressible context we introduce, by analogy with gas modeling, a formulation with an energy per unit of mass $\varepsilon = \rho W$ rather than per unit of volume. Moreover, thermodynamics are used only in the solid part by introducing the entropy $s$

$$\varepsilon = \varepsilon_{\text{vol}}(\rho, s) + \varepsilon_{\text{iso}}(\operatorname{Tr}(\overline{B}), \operatorname{Tr}(\operatorname{Cof}(\overline{B}))). \tag{4.25}$$

We then obtain using (4.22) and, due to (2.22), $J_e(x,t) = \frac{\rho_0(Y(x,t))}{\rho(x,t)}$

$$\sigma = -p(\rho, s)I + \sigma_{\text{iso}}(\nabla Y), \tag{4.26}$$

where the pressure is defined by $p(\rho, s) = \rho^2 \frac{\partial \varepsilon}{\partial \rho}$ and where the derivative is calculated for a given value of the entropy. The two previous equations allow to close the following system of conservation laws for the compressible elasticity in Eulerian formulation

$$\begin{cases} \partial_t \rho + \operatorname{div}(\rho u) = 0, \\ \partial_t (\rho u) + \operatorname{div}(\rho u \otimes u - \sigma) = 0, \\ \partial_t (\nabla Y) + \nabla (u \cdot \nabla Y) = 0, \\ \partial_t (\rho e) + \operatorname{div}(\rho e u - \sigma^T u) = 0. \end{cases} \tag{4.27}$$

Indeed, Eq. (4.25) allows to evaluate $s$ as a function of $\varepsilon, \rho$ and $\nabla Y$. By substituting this expression for $s$ in (4.26) and in view of the definition $e = \varepsilon - \frac{1}{2}|u|^2$ of the total energy we obtain $\sigma$ as a function of $\rho, u, \nabla Y$ and $e$. As $\sigma$ directly depends on $\nabla Y$ we took the gradient of the transport equation on the backward characteristics in order to write the set of Eqs. (4.27) as a system of conservation laws of the form $\partial_t \Psi + \operatorname{div}(F(\Psi)) = 0$. This form will make it possible to study the properties of hyperbolicity (speed of waves, shocks, expansion waves, etc.) and to derive adapted numerical schemes.

## 4.3 Fluid-Structure Coupling Model in the Incompressible Case

We are now interested in the coupling between an elastic structure and an incompressible viscous fluid. The completely Eulerian formulation of elasticity will make it possible to model the fluid-structure interaction as a complex fluid. The elastic forces are added into the fluid equations as a source term and discretized on the same grid as the fluid. Let us insist here on the fact that the solid is also supposed to be incompressible and that the constraint of free divergence is thus applied on the whole domain.

This formulation of Eulerian elasticity has been developed by several teams [38, 118, 134, 144]. The approach is based on the three components of the backward characteristics $Y$ (also called reference map in [144]) which is simply advected by the velocity of the fluid and its spatial derivatives make it possible to calculate the elastic stress. In [134] the authors used, instead of the backward characteristics, an Eulerian equation on the six components of the elastic symmetric tensor $B = [\nabla Y]^{-1}[\nabla Y]^{-T}$. This advection equation also contains two additional terms involving the velocity gradients.

In this Eulerian context, the backward characteristics, and therefore the elastic tensor, are calculated over the whole domain, which includes the fluid region. The fluid near the interface can be subjected to large shear, which can in turn cause exponential growth of some components of the backward characteristics. These

distortions in the fluid, if they are used in the numerical scheme in the vicinity of the fluid-solid interface, can cause numerical instabilities because the stress tensor is generally diffused on a few points of the mesh inside the fluid.

To address this difficulty, different discretization strategies have been developed in the literature. In [118], the fluid-structure equations are discretized on an unstructured finite element mesh and the Eulerian deformations are extrapolated linearly in the fluid. In [134], the model is discretized with a finite difference scheme on a Cartesian mesh and the elastic tensor is smoothed in the fluid. In [134], the fluid-structure equations are discretized with finite differences on a Cartesian mesh and the characteristics are extrapolated in the fluid.

In the example described below, a linear extrapolation of the backward characteristics is chosen in the fluid with the method of Aslam [6]. The details of this method as well as numerous validations and numerical simulations of these models are developed in the thesis of Julien Deborde [45] and in the article [46].

### 4.3.1 Model and Constitutive Law in the Incompressible Case

A level set function $\varphi$ is used to capture the interface separating the fluid and the solid and verifies the transport equation

$$\partial_t \varphi + u \cdot \nabla \varphi = 0. \tag{4.28}$$

The complete model is given by

$$\begin{cases} \rho\left(\partial_t u + (u \cdot \nabla)u\right) + \nabla p = \operatorname{div}(\sigma), \\ \operatorname{div}(u) = 0, \\ \partial_t Y + (u \cdot \nabla)Y = 0, \\ \partial_t \varphi + u \cdot \nabla \varphi = 0. \end{cases} \tag{4.29}$$

Note that the equation on $\varphi$ is redundant because knowing $Y$ gives the solution to solve any transport equation (because $\varphi(x,t) = \varphi_0(Y(x,t))$). However, we can choose to monitor both quantities for numerical reasons: one may wish to use the redistancing algorithm on $\varphi$ and extrapolations of $Y$ in the fluid. This choice will be made in the example described below. The fluids and solids considered here are viscous and thus

$$\sigma = \mu([\nabla u] + [\nabla u]^T) + \mathcal{H}\left(\frac{\varphi}{\varepsilon}\right)\sigma_S \tag{4.30}$$

where $\mathcal{H}$ is a regularized Heaviside function, typically given by

$$\mathcal{H}(r) = \begin{cases} 1 & \text{si } r \leq -1, \\ \frac{1}{2}\left(1 - r - \frac{\sin(\pi r)}{\pi}\right) & \text{if } -1 \leq r \leq 1, \\ 0 & \text{if } r \geq 1. \end{cases} \tag{4.31}$$

and $2\varepsilon$ is the width of the interface between the solid and the fluid. As a result, $\varphi > \varepsilon$ corresponds to the fluid domain and $\varphi < -\varepsilon$ corresponds to the solid domain. In our simulations, $\varepsilon$ has a fixed value equal to $2\Delta x$, which is a standard value used in the literature to diffuse the interface.

### *4.3.2 Numerical Illustrations*

In the following examples, with the exception of that of the heart cell, the numerical schemes for the resolution of Eqs. (4.29) are based on a discretization by finite differences or finite volumes on a staggered Cartesian grid of MAC type. A projection method is used to solve the incompressible Navier–Stokes equations and WENO schemes take care of the transport of the backward characteristics. These two parts of the system are decoupled in time in an explicit way. The terms of transport and diffusion are discretized in space in a classic way with upwind or centered schemes. The elastic force is discretized with a centered scheme. Let us insist on the fact that one uses exactly the same methods as for the elastic membranes with explicit discretization in time of the coupling, with the difference that the elastic force is localized on the whole the elastic domain through a Heavyside function, instead of being localized on a surface using a regularized Dirac mass.

#### 4.3.2.1 Elastic Ball in a Driven Cavity

In this paragraph, we present a 2D simulation of the deformation of an elastic ball in a driven cavity taken from [46]. This benchmark case was originally proposed in [149] et [134]. The initial configuration and physical parameters are given in Fig. 4.2 and Table 4.1. The initial velocity is zero inside the domain while a horizontal velocity of 1 $m.s^{-1}$ is imposed at the top and a no-slip condition is imposed on the other boundaries. The computation is carried out on a regular Cartesian mesh using $1024^2$ discretization points. The time step of this simulation is fixed at $\Delta t = 10^{-4}s$. In these simulations the elasticity is driven by the Neo-Hookean constitutive law given in 2D by (4.22) with $J_e = 1$ and $W = \chi(\mathrm{Tr}(B) - 2)$. In other words

$$\sigma_S = 2\chi\left(B - \frac{\mathrm{Tr}(B)}{2} I\right), \tag{4.32}$$

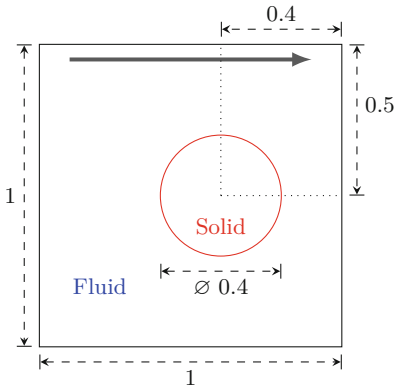


**Fig. 4.2** Initial configuration in 2D of the elastic ball in a driven cavity. The computational domain is $[0, 1] \times [0, 1]$

**Table 4.1** Physical parameters

| Medium | $\rho$ (kg.m$^{-3}$) | $\mu$ (Pa.s) | $\chi$ (Pa) |
|---|---|---|---|
| Fluid | 1 | $10^{-2}$ | – |
| Solid | 1 | $10^{-2}$ | 0.05 |

where $\chi$ denotes the elastic modulus. Note that the term proportional to identity will be absorbed in the pressure for this incompressible version of the model.

On Fig. 4.3, the zero level set is presented at various times and compared to the results of [134] using the same mesh but different numerical schemes (transport of the tensor $B$ in [134] and transport of the backward characteristics $Y$ in our Level Set method).

#### 4.3.2.2 Flapping of an Elastic Rod

We present in this section a simulation of the flapping of an elastic rod taken from [46]. In this test case, initially presented in [143], a fine elastic bar is fixed to a circular rigid solid and immersed in a fluid. The initial configuration and physical parameters are described in Fig. 4.4 and Table 4.2. A horizontal Poiseuille profile $u_L(y) = \frac{1.5y(0.41-y)}{\left(\frac{0.41}{2}\right)^2}$ is imposed on the left side. No-slip conditions are imposed at the top and bottom and a Neumann condition on the right ensures a free outlet of the flow. A horizontal initial velocity $U = 1.4$ (resp. $U = 1.6$) is imposed in the upper part $y > 0.2$ (resp in the lower part $y < 0.2$). The Reynolds number based on the diameter of the cylinder is taken equal to 100. The wake generated behind the elastic structure is therefore laminar.

The computation is carried out on a non-uniform Cartesian mesh with $1100 \times 400$ grid points with a mesh refinement in the region where the bar will move (30 grid points are used across the elastic structure). The penalization method described in Sect. 5.1 is used to impose a zero velocity inside the cylinder. The time step used in this simulation is taken equal to $10^{-5}$. The very small value of this time step is

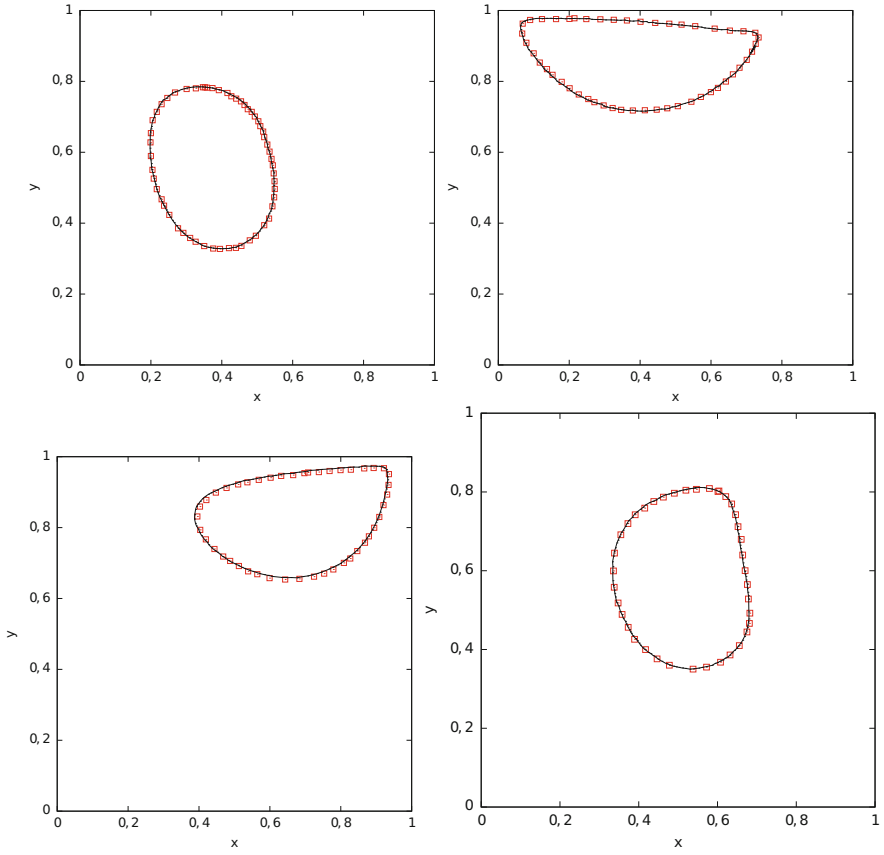


**Fig. 4.3** Comparison between the Level Set method (black line) and the method in [134] (red squares) for the location of the interface at times $t = 2.34, 4.69, 5.86, 8.20$ (from left to right, top to bottom). From [46]

imposed by the high value of stiffness of the elastic bar, reflected by a high value of the parameter $\chi$ (of the order of $10^6$). This makes this case very expansive in terms of computational time.

We present in Fig. 4.5 the zero isovalue of the Level Set function, giving the position of the elastic bar, as well as the vorticity at different times.

The horizontal and vertical displacements of the bar end over the time interval $[4.4, 5.8]$ are shown in Fig. 4.6. From this graph, we can estimate the vertical and horizontal displacements and frequencies and compare them with the existing literature in Table 4.3. The method used in [143] is an ALE method and the one used in [10] couples a finite element method in the elastic bar in Lagrangian formulation to an immersed boundary method for the fluid part.

Some caution must be exercised when comparing the different results. Indeed, [143] and [10] use a compressible model of elasticity (with Saint Venant-Kirchhoff

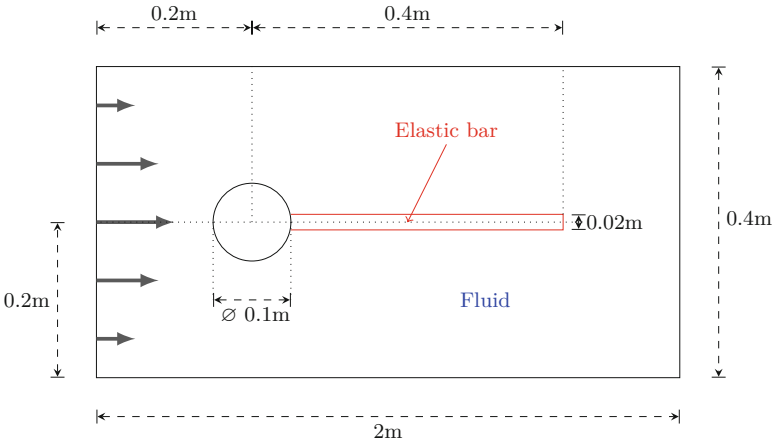


**Fig. 4.4** Initial configuration for the test of the flapping rod. The computational domain is $[0, 2.5] \times [0, 0.4]$

**Table 4.2** Physical parameters for the test case of the flapping rod

| Medium | $\rho$ (kg.m$^{-3}$) | $\mu$ (Pa.s) | $\chi$ (Pa) |
|---|---|---|---|
| Fluid | $10^3$ | 1 | – |
| Solid | $10^4$ | 1 | 0.375 $10^6$ |

laws) whereas the Eulerian Level Set model is completely incompressible for both the solid and the fluid. The parameter $\chi$ has been set empirically to reproduce a comparable physical behavior between the different models. Despite variations between the different computations on the values of the amplitude, all computations agree to give a ratio close to 2 between the horizontal and vertical frequencies.

#### 4.3.2.3 Wave Damping by Elastic Structures

In this section we present the simulations reported in [45] et [46] of wave damping through elastic devices. This kind of simulation can be useful for the design and calibration of coastal protection systems.

The initial configuration and physical parameters are given in Figs. 4.7, 4.8, and Table 4.4. The velocity, pressure and free surface profile are initially calculated with a theoretical third order solitary wave solution [97]. The initial water depth is $d = 0.5$ and we have $H/d = 0.06644$, where $H$ is the amplitude of the wave. The speed of the initial wave is $c = 2.29$ and its peak is located at $x = 2$. A Neumann condition is imposed on the right edge and a no-slip condition is imposed on the other edges. The computation is carried out on a regular Cartesian mesh using $7000 \times 230$ discretization points. In this simulation the Neo-Hookean constitutive law given in 2D by (4.32) is chosen.

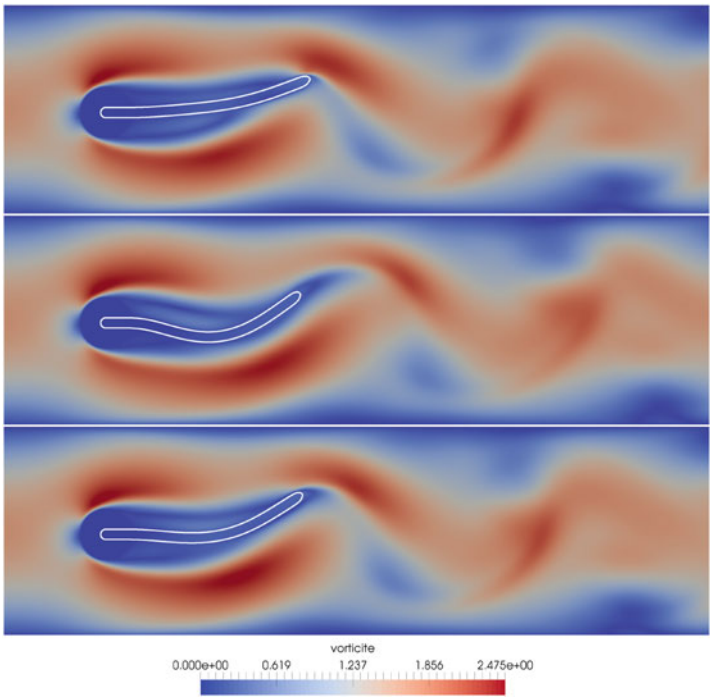


**Fig. 4.5** Deformations of the elastic bar at times $t = 13.96$, 14.06 et 18.06. From [45]

We present in Fig. 4.9 the zero contour of the Level Set function as well as the vorticity at different times. The energy of the wave deforms the structures and the stored elastic energy is then released in the form of vortices which are confined by the presence of the free surface. This induces turbulence in the upper part of the water column (with vortices and high velocity gradients), while the structures result in a blocking effect of the flow in the lower part.

Figure 4.10 next allows to compare the decay of the kinetic energy with rigid or elastic structures. In the case of solid structures, as in the previous example, a method of penalization is used to impose the no-slip condition at the walls of the fluid. One can observe an increase in the damping effect with elastic strucutres of about 50%.

#### 4.3.2.4 Fluid-Structure Interaction in the Contraction of a Cardiac Muscle Cell

The 3-dimensional example we are giving now is in the field of biophysics and concerns the contraction of a heart muscle cell under the influence of local variations in calcium concentration. The previous cases illustrated the capacity of the Level

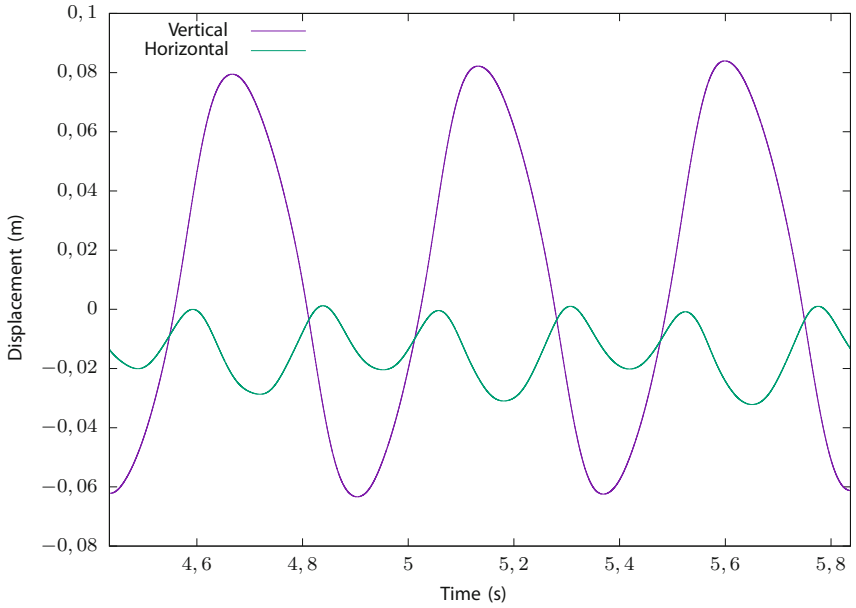


**Fig. 4.6** Time evolution of horizontal and vertical displacements of the tip of the bar. From [45]

**Table 4.3** Comparison of the motion of the tip of the bar between the Level Set method and the literature for the flapping rod test case. Vertical (first column) and horizontal (second column) amplitudes. Horizontal (third column) and vertical (fourth column) frequencies. From [45]

| | V ampl [m] | H ampl [m] | H freq $[s^{-1}]$ | V freq $[s^{-1}]$ |
|---|---|---|---|---|
| Level Set method | 0.073 | 0.016 | 4.30 | 2.11 |
| [143] | 0.083 | 0.012 | 3.87 | 1.9 |
| [10] | 0.092 | 0.018 | 3.88 | 1.9 |

Set methods to deal with large deformations. Here, the interest of an Eulerian model of elasticity stems in particular from the fact that the equations which govern the concentration of calcium are of the reaction-diffusion type and therefore naturally posed in an Eulerian framework.

An additional interesting feature of this example is the anisotropy of the medium, as the heart cells are aligned along the fibers of the heart muscle. To take this anisotropy into account, the stress tensor is generalized in the form:

$$\sigma_0 = -p\mathbb{I} + 2\alpha\, B + 2\beta\, (\mathrm{tr}(B)B - B^2) + 2\gamma\, \nabla Y^{-1}\tau \otimes \nabla Y^{-1}\tau, \tag{4.33}$$

where $\alpha$, $\beta$ and $\gamma$ are coefficients. The presence of calcium in the cell results in active stresses which appear in the coefficient $\gamma$ and can be modeled as follows

$$\gamma = \gamma_0 + \gamma'(Z(x,t))$$

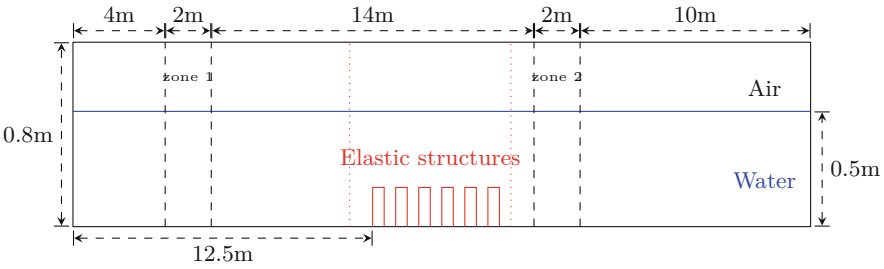


**Fig. 4.7** Initial configuration for the wave-damping test case. The domain is $[0, 32] \times [0, 0.8]$

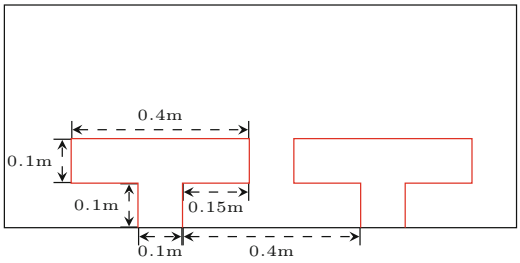


**Fig. 4.8** Dimensions of the T-shaped elastic structure

**Table 4.4** Physical parameters for the wave-structure interaction

| Medium | $\rho$ (kg.m$^{-3}$) | $\mu$ (Pa.s) | $\chi$ (Pa) |
|---|---|---|---|
| Air | 1.177 | 1.85 $10^{-5}$ | – |
| Water | $10^3$ | $10^{-3}$ | – |
| Structure | $10^3$ | $10^{-3}$ | 300 |

where $Z$ denotes the intracellular concentration of $Ca^{2+}$ ions, which is given by a reaction-diffusion equation, and $\gamma'$ is a sigmoid function. For the justification and the details of the model as well as the numerical values of the parameters we refer to [98]. Figure 4.11 shows the cell shape and calcium levels at three successive times. This example and this model have also been used in a finite element implementation in two dimensions in [120].

## 4.4 Fluid-Structure Coupling in the Compressible Case

We are interested in the numerical simulation of transient phenomena such as the propagation of shock waves at gas-water interfaces, the propagation of nonlinear elastic waves from a hyperelastic solid to a fluid and vice versa. These phenomena can be modeled by an entirely Eulerian system of conservation laws which applies to all materials which are all supposed to be compressible; only the constitutive law can change, reproducing the mechanical characteristics of the medium considered. For

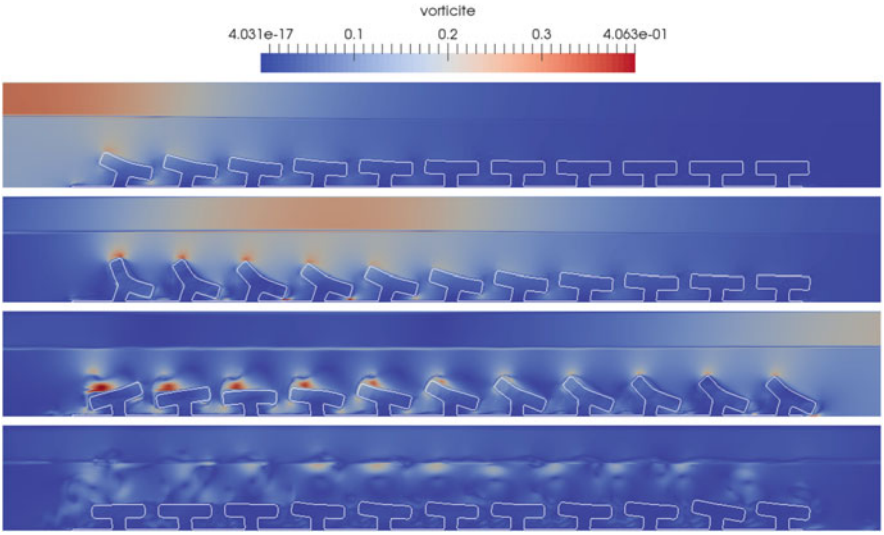


**Fig. 4.9** Propagation of a solitary wave in an arrangement of 11 elastic T-shaped structures. From [46]

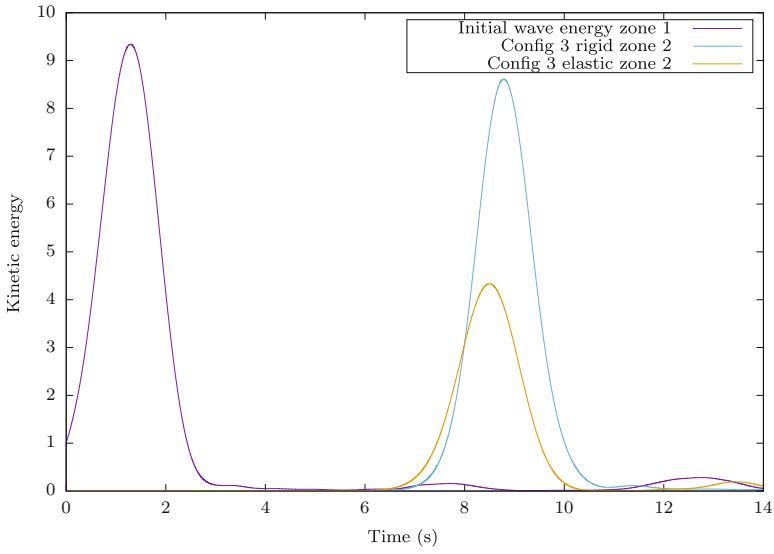


**Fig. 4.10** Comparison of kinetic energy damping with rigid or elastic structures. From [46]

example, an elastic material or a gas will be modeled by the same set of quasi-linear hyperbolic partial differential equations, except for the constitutive law connecting the strain of the material and the stress tensor.

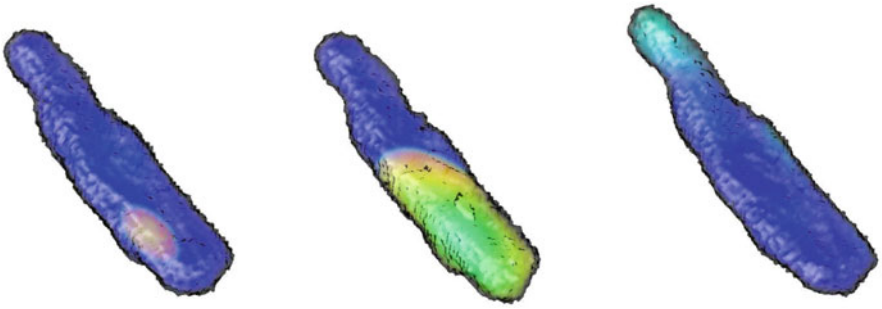

**Fig. 4.11** Heart cell at 3 successive instants. The colors represent the concentration of calcium inside the cell. From [98]

The systematic derivation of such models from the principles of continuum mechanics, their thermodynamic coherence and the corresponding wave propagation models were initially studied in [76]. Their numerical simulation is delicate because the classical Godunov schemes already lead in the case of multi-fluids to pressure oscillations at the level of the contact discontinuity. In [1], the pressure perturbation mechanism at the origin of this phenomenon was explained and a first solution has been proposed. In [56] an efficient solution is presented to solve this difficulty with the *ghost fluid* method which involves sharp interface between materials. For multi-fluids, improvements to this approach requiring less storage have been proposed in [2], with a diffuse interface, and [60], with a sharp interface.

The common idea of these methods is to define a ghost fluid that has continuous mechanical characteristics on the interface, but the same thermodynamic state or the same equation of state as the real fluid. This assumption leads to locally non-conservative, stable schemes, without spurious oscillations at the interface of materials. A different method was proposed in [107], where a conservative *cut cell* type technique was developed for hyperelastic and multi-material plastic simulations. This scheme is the basis for many subsequent works in the literature. Another approach is introduced in [62] for the interactions between hyperelastic solids and fluids. The authors design a conservative model of out-of-equilibrium mixing that adapts to desired multi-material conservation laws. In this approach, the stiffness of the material interface is compromised to avoid oscillations and to apply an HLLC solver previously developed for a single material in [72]. Other developments of this method include plasticity modeling [63] and an approach dividing the system into hyperbolic subsystems [61], where each subsystem has only three waves instead of seven.

The approach described below uses a discretization of Eulerian conservation laws of hyperelastic compressible materials which simplify the computations of numerical fluxes at the material interface. No ghost material is defined and no mixing model is necessary to obtain a non-oscillatory scheme. Details of this method as well as simulations on bubble shock and projectile impacts (modeled with plasticity) are presented in [43, 44, 78] and in the PhD thesis of Alexia de

Brauer [42]. We present in the following the discretization of the equations as well as an example of 3D numerical simulation of the impact of a copper projectile in the air.

### 4.4.1 Model and Constitutive Law in the Compressible Case

A Level Set function is used to follow the interface between two materials.

$$\partial_t \varphi + u \cdot \nabla \varphi = 0. \tag{4.34}$$

Conservation of mass, momentum and energy are given by (4.27):

$$\begin{cases} \partial_t \rho + \operatorname{div}(\rho u) = 0, \\ \partial_t (\rho u) + \operatorname{div}(\rho u \otimes u - \sigma) = 0, \\ \partial_t (\nabla Y) + \nabla (u \cdot \nabla Y) = 0, \\ \partial_t (\rho e) + \operatorname{div}(\rho e u - \sigma^T u) = 0. \end{cases} \tag{4.35}$$

Using Eqs. (2.22) and (2.5) we get the relation $\rho = \rho_0(Y) \det(\nabla Y)$. If $\rho_0$ is constant, the conservation of mass is redundant with the equation on $\nabla Y$. Moreover, applying the gradient of the equation on $Y$ makes it possible to put the equations in the form of a hyperbolic system but imposes the new constraint $\nabla \times \nabla Y = 0$. This constraint is sometimes called involutive constraint and characterizes the fact that the quantity $\nabla Y$ must remain a gradient for all time. Some authors impose this constraint by penalizing the equations [107] which complicates the models and their numerical implementtion. One may prefer to choose to ignore this constraint. It is indeed shown in [107] (Table 3 p. 137) that the numerical schemes make it possible to satisfy it within the precision of the schemes.

In what follows [107] we choose a general constitutive law which will allow to model gases, fluids and elastic solids with internal energy per unit of mass $\varepsilon = e - \frac{1}{2}|u|^2$ given by

$$\varepsilon(\rho, s, \nabla Y) = \overbrace{\underbrace{\underbrace{\frac{e^{\frac{s}{c_v}}}{\gamma - 1}\left(\frac{1}{\rho} - b\right)^{1-\gamma}}_{\text{van der Waals gas}} - a\rho}_{\text{stiff gas}} + \frac{p_\infty}{\rho} + \frac{\chi}{\rho_0}(\operatorname{Tr}(\overline{B}) - 3)}^{\text{Neo-Hookean elastic solid}}. \tag{4.36}$$

We then obtain with (4.26)

$$\sigma(\rho, s, \nabla Y) = -p(\rho, s)I + 2\chi J_e^{-1}\left(\overline{B} - \frac{\mathrm{Tr}(\overline{B})}{3}I\right), \tag{4.37}$$

where

$$p(\rho, s) = -p_\infty - a\rho^2 + \kappa(s)\left(\frac{1}{\rho} - b\right)^{-\gamma}. \tag{4.38}$$

Here $c_v$, $\gamma$, $p_\infty$, $a$, $b$ and $\chi$ are positive constants which characterize a given material. The parameters $a$ and $b$ correspond to the van der Waals parameters. The constant $p_\infty$ makes it possible to model fluid or solid materials where intermolecular forces are present. The last term of the energy expression represents a Neo-Hookean elastic solid where the constant $\chi$ is the shear elasticity modulus.

### 4.4.2 Numerical Scheme

Let $x = (x_1, x_2, x_3)$ be the coordinates in the canonical basis of $\mathbb{R}^3$. The system of Eqs. (4.27) can be rewritten in a compact way

$$\partial_t \Phi + \partial_{x_1}(G^1(\Phi)) + \partial_{x_2}(G^2(\Phi)) + \partial_{x_3}(G^3(\Phi)) = 0. \tag{4.39}$$

We discretize (4.39) with a finite volume method on a Cartesian mesh. Let $\Delta x_i$ be the grid size in the $x_i$ direction and $\Omega_{i,j,k}$ the control volume centered at the node $(i\Delta x_1, j\Delta x_2, k\Delta x_3)$. The semi-discretization in space of (4.39) on $\Omega_{i,j,k}$ is given by

$$\partial_t \Phi_{i,j,k} + \frac{G^1_{i+1/2,j,k} - G^1_{i-1/2,j,k}}{\Delta x_1} + \frac{G^2_{i,j+1/2,k} - G^2_{i,j-1/2,k}}{\Delta x_2} + \frac{G^3_{i,j,k+1/2} - G^3_{i,j,k-1/2}}{\Delta x_3} = 0. \tag{4.40}$$

The fluxes in (4.40) are computed by approximate one-dimensional Riemann solvers in the direction orthogonal to the faces of the cells of the Cartesian mesh. We thus have

$$G^1_{i-1/2,j,k} \approx \mathcal{F}(\Phi_{i-1,j,k}; \Phi_{i,j,k}) \quad G^1_{i+1/2,j,k} \approx \mathcal{F}(\Phi_{i,j,k}; \Phi_{i+1,j,k}) \tag{4.41}$$

$$G^2_{i,j-1/2,k} \approx \mathcal{F}(\Phi_{i,j-1,k}; \Phi_{i,j,k}) \quad G^2_{i,j+1/2,k} \approx \mathcal{F}(\Phi_{i,j,k}; \Phi_{i,j+1,k}) \tag{4.42}$$

$$G^3_{i,j,k-1/2} \approx \mathcal{F}(\Phi_{i,j,k-1}; \Phi_{i,j,k}) \quad G^3_{i,j,k+1/2} \approx \mathcal{F}(\Phi_{i,j,k}; \Phi_{i,j,k+1}) \tag{4.43}$$

where $\mathcal{F}(\cdot\ ;\ \cdot)$ is the numerical flux. The fluxes are the same in the three spatial directions, so it is enough to consider the one-dimensional problem in the $x_1$ direction

$$\partial_t \Psi + \partial_{x_1}(F(\Psi)) = 0. \tag{4.44}$$

One can then show that the wave speeds (the eigenvalues of $F'(\Psi)$) are of the form

$$\Lambda^E = \left\{ u_1, u_1, u_1 \pm \sqrt{\frac{\alpha_1}{\rho}}, u_1 \pm \sqrt{\frac{\alpha_2}{\rho}}, u_1 \pm \sqrt{\frac{\alpha_3}{\rho}} \right\}, \tag{4.45}$$

where $\alpha_1, \alpha_2$ et $\alpha_3$ depend on the conservative variables. We will refer to [43] for an exact expression of these wave speeds.

Consider Eq. (4.44) with the initial condition

$$\Psi(x, t = 0) = \begin{cases} \Psi_l \text{ if } x \leq 0, \\ \Psi_r \text{ if } x > 0. \end{cases} \tag{4.46}$$

The numerical flux $\mathcal{F}(\Psi_l; \Psi_r)$ is determined at interface $x = 0$ using an approximate Riemann HLLC solver [138]. Although the exact model involves seven distinct waves (see (4.45)), the solver approximates the solution using only three waves, namely the contact discontinuity $u_1^\star$ and the fastest waves $s_l$ and $s_r$. This only involves two intermediate states $\Psi^-$ et $\Psi^+$, as shown on Fig. 4.12.

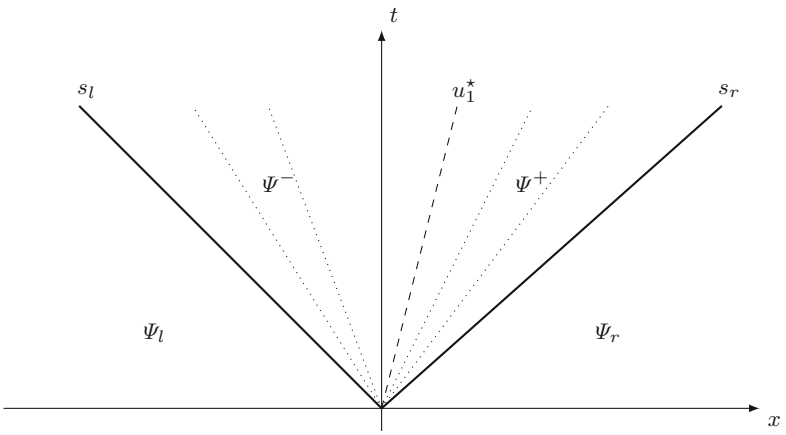


**Fig. 4.12** Representation of the waves in the HLLC solver

The HLLC scheme is based on the assumption that each wave is a shock and the Rankine-Hugoniot relations give

$$\begin{cases} F(\Psi_r) - \mathcal{F}^+ = s_r(\Psi_r - \Psi^+), \\ \mathcal{F}^+ - \mathcal{F}^- = u_1^*(\Psi^+ - \Psi^-), \\ \mathcal{F}^- - F(\Psi_l) = s_l(\Psi^- - \Psi_l). \end{cases} \tag{4.47}$$

These relations allow to completely determine the states $\Psi^\pm$ and their associated fluxes $\mathcal{F}^\pm$. The numerical flux at $x = 0$ is then given by

$$\mathcal{F}(\Psi_l; \Psi_r) = \begin{cases} F(\Psi_l) & \text{if} \quad 0 \le s_l, \\ \mathcal{F}^- & \text{if} \quad s_l \le 0 \le u_1^\star, \\ \mathcal{F}^+ & \text{if} \quad u_1^\star \le 0 \le s_r, \\ F(\Psi_r) & \text{if} \quad s_r \le 0. \end{cases} \tag{4.48}$$

At the interface between the two materials, one uses the fluxes $\mathcal{F}^\pm$ which leads, as for the ghost fluid schemes, to a locally non-conservative scheme because $\mathcal{F}^- \neq \mathcal{F}^+$. It is however consistent as $\mathcal{F}^\pm$ are fairly regular states to the left and right of the interface and $\mathcal{F}^+ = \mathcal{F}^-$ when these states are identical. In [78] it was indeed shown that the conservation error is negligible because the number of cells for which a non-conservative numerical flux is used is always negligible compared to the total number of cells. The scheme is extended to second order in space using a MUSCL piecewise linear reconstruction with a minmod limiter. A second order Runge-Kutta time stepping is used and the time-step is limited for numerical stability on the basis of the speeds of the fastest waves. Finally, the level set equation solved to capture the interface between the different media is discretized with a fifth order WENO scheme using also a second order Runge-Kutta scheme.

### *4.4.3 Numerical Illustration*

We present a simulation of the impact of a projectile at a speed of 800 m.s$^{-1}$ on a plate in the air taken from [43]. The initial configuration and physical parameters are described in Fig. 4.13 and Table 4.5.

In this simulation, the projectile and the plate are initially adjacent. The projectile and the plate form a single material and are described by the same level set function. Neumann boundary conditions were imposed on the edges of the box. The computation was carried out on 216 processors and took 60 wall-clock hours with a mesh using $600^3$ grid points.

Results are displayed on Fig. 4.14. The elastic material is subject to deformation and oscillations while moving to the right.

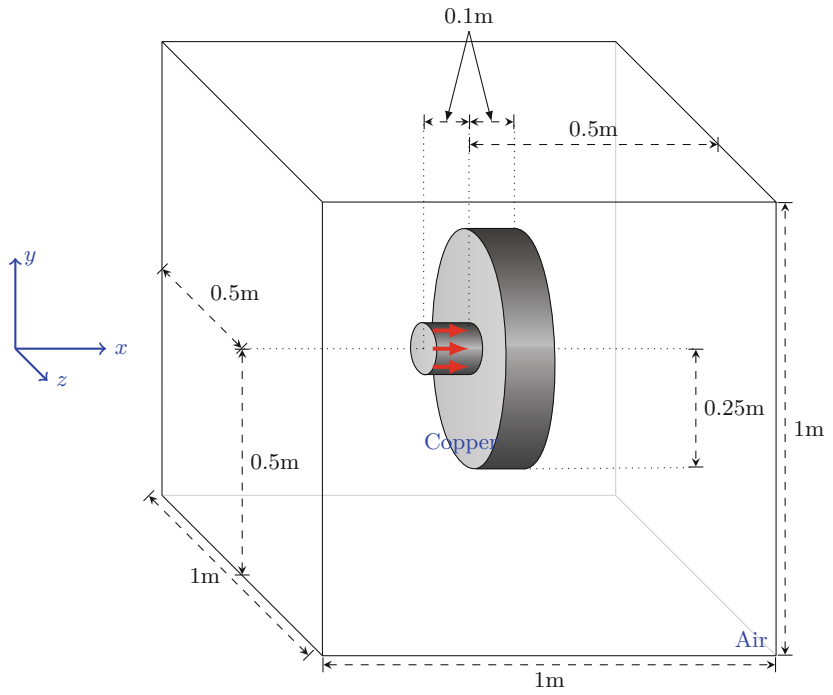


**Fig. 4.13** Initial configuration for the impact test case

**Table 4.5** Physical parameters for the impact test case

| Media | $\rho$ [kg.m$^{-3}$] | $u_1$ [m.s$^{-1}$] | $p$ [Pa] | $\gamma$ | $a$ [Pa.kg$^{-2}$m$^6$] | $b$ [kg$^{-1}$m$^3$] | $p_\infty$ [Pa] | $\chi$ [Pa] |
|---|---|---|---|---|---|---|---|---|
| Copper (plate) | 8900 | 0 | $10^5$ | 4.22 | 0 | 0 | $3.42 \cdot 10^{10}$ | $5 \cdot 10^{10}$ |
| Copper (projectile) | 8900 | 800 | $10^5$ | | | | | |
| Air | 1 | 0 | $10^5$ | 1.4 | 0 | 0 | 0 | 0 |

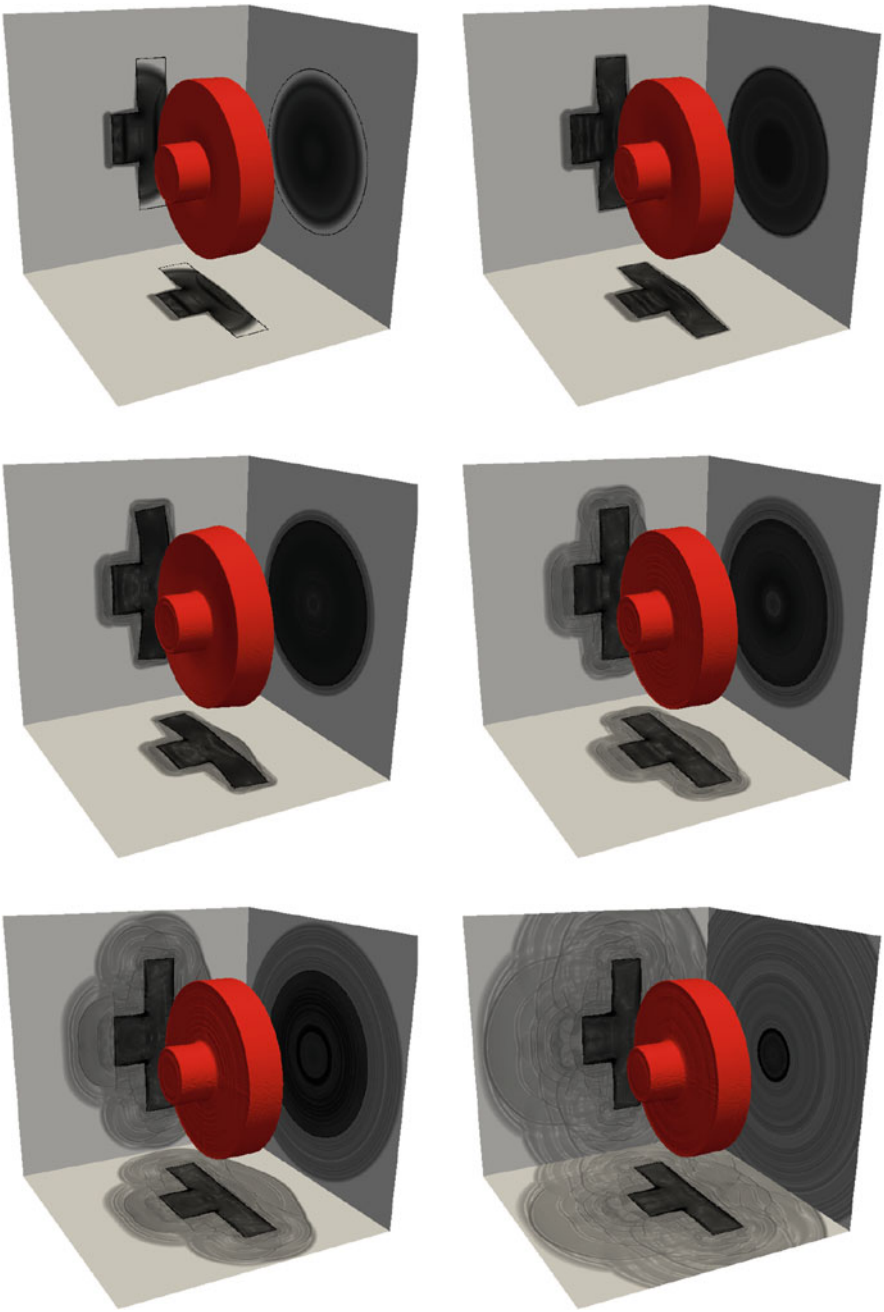

**Fig. 4.14** Impact of a projectile on a cylindrical plate. Schieren images (showing density gradients) of cuts through $x = 0.03\,\text{m}$, $y = 0\,\text{m}$ et $z = 0\,\text{m}$ and zero contour of the Level Set function at times $t = 24\,\mu\text{s}$, $t = 43\,\mu\text{s}$, $t = 88\,\mu\text{s}$, $t = 178\,\mu\text{s}$, $t = 355\,\mu\text{s}$ and $t = 710\,\mu\text{s}$, from left to right, top to bottom. From [43]

# Chapter 5
# Immersed Bodies in Incompressible Fluids: The Case of Rigid Bodies


The traditional way to deal with the interaction of a fluid with a rigid solid is to solve the Navier–Stokes equations in the fluid, using a mesh fitting with the solid boundary, to calculate from the solution of these equations the forces being exerted on the solid, and to make the solid evolve by using these forces.

If one seeks to avoid using an adapted mesh, a fictitious domain approach [74, 75] instead consists in using the Navier–Stokes equations in a computational domain including solids and in treating the constraints of no-deformation of rigid solids using Lagrange multipliers in a variational framework.

Another approach, which would be an extension of the methods developed in this book in an Eulerian framework, can also be to consider this problem of fluid-structure interaction as a limiting case of the elasticity cases seen previously, for example by considering the surface of the solid as an elastic membrane, with a stiffness tending towards infinity. However, this approach can be ineffective for two reasons. On the one hand, it artificially brings into play drastic stability conditions, and, on the other hand, it risks leaving small deformations persist in the rigid solid.

A third approach, suggested by Patankar [126], consists in treating the fluid/solid system like a flow with variable density, and in projecting at each time step the velocity field in the solid phase on the fields corresponding to the rigid displacements. In the following, we will focus on this type of method. More precisely we describe a generalization of the Patankar method in a continuous time formalism based on a penalization method.

Although this part of the book does not heavily rely on the use of Level Set methods, we opted to include it in order to to give a comprehensive study of fluid-structure interaction involving all kind of solid bodies. Moreover, our choice to focus on penalization methods to deal with the fluid-structure interaction in this case is due to the fact that these methods are based on clear-cut mathematical definitions and are simple to implement.

In the sequel, we first recall the definition of the penalization method for a flow around an obstacle having a determined velocity, before turning to the



G.-H. Cottet et al., *Level Set Methods for Fluid-Structure Interaction*, Applied Mathematical Sciences 210, https://doi.org/10.1007/978-3-031-08659-5_5

extension of the method to model the two-way fluid-structure coupling. We then describe extensions of the method to applications where bodies are rigid up to some prescribed deformation. Remarks on the implementation of the method and numerical illustrations complete the chapter.

## 5.1 The Penalization Method for Flow Around Bodies with Given Velocity

This method, originally proposed by Caltagirone [26] and analyzed by Angot, Bruneau and Fabrie [5] consists in solving the following system, in a domain $\Omega$ containing fluid and solid:

$$\partial_t u_\eta + u_\eta \cdot \nabla u_\eta + \nabla p - \mu \Delta u_\eta = \eta^{-1} \chi_S (u^S - u_\eta), \tag{5.1}$$

$$\operatorname{div} u_\eta = 0. \tag{5.2}$$

In these equations, we have assumed the density of the fluid equal to 1, $S$ denotes the solid, $\chi_S$ its characteristic function, and $u_S$ its velocity. The parameter $\eta << 1$ is the penalization coefficient.

The interpretation of this system is simple: apart from the solid (when $\chi_S$ is zero) it reduces to the fluid equation, and in the solid, the preponderant terms of the equation ensure that the speed coincides with that of the solid. The analysis given in [5] confirms that when $\eta$ tends towards zero, the solution of (5.1) tends towards that of the Navier–Stokes equations in the fluid domain, with no-slip boundary on the walls of the solid.

Without going into the details of this result and its proof, we can notice that if we suppose for simplicity that $u_S$ is independent of $t$ and $u_\eta = 0$ on $\partial\Omega$ (we recall that $\Omega$ is the computational domain including the fluid and the solid ), by multiplying Eq. (5.1) by $u_\eta - u^S$ we easily find

$$\frac{1}{2}\frac{d}{dt}\|u_\eta - u^S\|_2^2 + \mu \|\nabla(u_\eta - u^S)\|_2^2 + \eta^{-1} \int_S |u_\eta - u^S|^2 dx = 0,$$

$$u_\eta - u^S \to 0 \text{ dans } L^2([0,T] \times S), \text{ when } \eta \to 0.$$

In what follows, to simplify the writing, we will forget the index $\eta$ in the notation of the approximations of the unknowns.

## 5.2 The Case of the Two-Ways Fluid-Solid Interaction

If the velocity of the solids is not given, but results from the hydrodynamic forces exerted on them, it suffices to use the penalization equation (5.1) and couple it with, on the one hand, an equation expressing the transport of the solid with the fluid velocity, and, on the other hand an equation giving the velocity of the solid as a projection on the rigid displacements of the velocities inside the body. We obtain the following system, considering the case, to simplify the writing, of a single rigid object:

$$\partial_t(\rho u) + \operatorname{div}(\rho u \otimes u) - \mu \Delta u + \nabla p + \frac{1}{\eta}\chi^S(u - u^S) = \rho g \tag{5.3}$$

$$\operatorname{div} u = 0, \tag{5.4}$$

$$u^S = \frac{1}{M_S}\int_\Omega \rho u \chi^S \, dx + \left( J_S^{-1} \int_\Omega \rho (r \times u)\chi^S \, dx \right) \times r, \tag{5.5}$$

$$\partial_t \rho + u \cdot \nabla \rho = 0, \tag{5.6}$$

$$\partial_t \chi^S + u \cdot \nabla \chi^S = 0. \tag{5.7}$$

In Eq. (5.5) $M_S = \int \rho \chi^S$ denotes the mass of the solid and we have included the effect of gravity with the term $\rho g$ in the right hand side of (5.3). As we will see below, the velocity $u^S$ is the velocity of the solid obtained by projection of the fluid velocity inside the body on the rigid motions. The notation $J_S$ above designates the inertia tensor of the solid, defined by

$$J_S = \int_\Omega \rho \chi^S (r^2 \mathbb{I} - r \otimes r) \, dx$$

where $r = x - M_S^{-1} \int_\Omega \rho \chi^S x \, dx$.

In the above system, unlike in the previous case, it is important to distinguish the densities of the fluid and the solid, which leads to add the conservation of mass equation (5.6) for the density $\rho$. If the fluid has a uniform density $\rho_f$ and the solid has a density $\rho_S$ we can obviously do without Eq. (5.6) and directly write

$$\rho = \rho_f + (\rho_S - \rho_f)\chi^S.$$

Equation (5.7) can be replaced by a transport equation on a level set function whose zero level set corresponds to the surface of the object and is positive inside the object:

$$\partial_t \varphi^S + u \cdot \nabla \varphi^S = 0. \tag{5.8}$$

The indicator function of the solid is then given by

$$\chi^S = \mathcal{H}(\varphi^S)$$

where $\mathcal{H}$ denotes the Heaviside function, possibly regularized as we did in the previous chapters.

The proof of the convergence of the solutions of this system, when $\eta$ tends towards 0, towards the solution of the coupled rigid fluid-solid system, is rather technical and we refer the reader to [20]. However, to check the consistency of the method, it is useful and simple to check that the velocity field defined by (5.5) is indeed the projection of $u$ on the rigid displacements.

Let be a velocity field $u$ and a density $\rho$ defined in $L^2(\Omega)$, $\chi^S$ the characteristic function of an open set $S$, and $V(u)$, $\boldsymbol{\omega}(u)$ the average translational velocity and rotation in $S$ defined by (5.5):

$$V(u) = \frac{1}{M_S}\int_\Omega \rho u \chi^S \, dx \ , \ \boldsymbol{\omega}(u) = J_S^{-1} \int_\Omega \rho (r(x) \times u)\chi^S \, dx,$$

where $r = x - M_S^{-1}\int_\Omega \rho \chi^S x \, dx$, and $M_S$ and $J_S$ denote the mass and the inertia tensor defined above.

**Proposition 5.1** *Let $d$ be a rigid displacement, i.e. such that $d(x) = V_d + \boldsymbol{\omega}_d \times r(x)$ where $V_d$ and $\boldsymbol{\omega}_d$ are given vectors of $\mathbb{R}^3$. Then*

$$\int_\Omega \chi^S(x)\,(V(u) + \boldsymbol{\omega}(u) \times r - u(x)) \cdot d(x)\, dx = 0. \tag{5.9}$$

***Proof*** We can write

$$\begin{aligned}
&\int_\Omega \rho \chi^S \left[u - (V(u) + \boldsymbol{\omega}(u) \times r)\right] \cdot \left[V_d + \boldsymbol{\omega}_d \times r\right] dx \\
&= V_d \cdot \int_\Omega \rho \chi^S u \, dx + \boldsymbol{\omega}_d \cdot \int_\Omega \rho \chi^S (r \times u)\, dx - V(u) \cdot V_d \int_\Omega \rho \chi^S \, dx \\
&- V(u) \cdot \left(\boldsymbol{\omega}_d \times \int_\Omega \rho \chi^S r(x)\, dx\right) - V_d \cdot \left(\boldsymbol{\omega}(u) \times \int_\Omega \rho \chi^S r(x)\, dx\right) \\
&- \int_\Omega \rho \chi^S (\boldsymbol{\omega}(u)) \times r) \cdot (\boldsymbol{\omega}_d \times r(x))\, dx \\
&= V_d \cdot (M_S V(u)) + \boldsymbol{\omega}_d \cdot (J_S\, \boldsymbol{\omega}(u)) - V(u) \cdot (M_S V_d)
\end{aligned}$$

$$- V(u) \cdot \left( \boldsymbol{\omega}_d \times \int_\Omega \rho \chi^S r(x)\, dx \right) - V_d \cdot \left( \boldsymbol{\omega}(u) \times \int_\Omega \rho \chi^S r(x)\, dx \right)$$
$$- \int_{\boldsymbol{\omega}} \rho \chi^S (\boldsymbol{\omega}(u) \times r) \cdot (\boldsymbol{\omega}_d \times r)\, dx.$$

As $(\boldsymbol{\omega}(u) \times r) \cdot (\boldsymbol{\omega}_d \times r) = (\boldsymbol{\omega}_d \cdot \boldsymbol{\omega}(u) r^2 - (r \cdot \boldsymbol{\omega}_d)(r \cdot \boldsymbol{\omega}(u))$, we have

$$\int_\Omega \rho \chi^S (\boldsymbol{\omega}(u) \times r) \cdot (\boldsymbol{\omega}_d \times r)\, dx = \boldsymbol{\omega}_d \cdot (J_S\, \boldsymbol{\omega}(u)).$$

Finally, by definition of $r$, $\int_\Omega \rho \chi^S r\, dx = 0$, so that we get

$$\int_\Omega \rho \chi^S (u - V(u) - \boldsymbol{\omega}(u) \times r) \cdot d\, dx = \boldsymbol{\omega}_d \cdot (J_S\, \boldsymbol{\omega}(u)) - \boldsymbol{\omega}_d \cdot (J_S\, \boldsymbol{\omega}(u)) = 0.$$

□

It should be noted that it is also natural to treat the problems of the interaction of fluid with rigid bodies with another method of penalization, namely by penalizing the deformations of the rigid object. In [87] for instance, the variational formulation of the Navier–Stokes equations is classically treated as a minimization problem and a term of penalization of the deformations in the solid is added to the functional to be minimized to ensure a rigid displacement in this one. The disadvantage of this method is that it is likely to leave small deformations in the solid, which can be a difficulty in simulations over long times or in very irregular flows.

To end this section, let us note that, if a main interest of the methods of penalization is to allow to avoid the computations of the forces to determine the dynamics of the fluid-solid system, the method still makes it possible to calculate *a posteriori* and in very simple way these forces. Indeed, according to [5], we can write the following relation for the forces exerted on the solid $S$

$$\int_{\partial S} \sigma(u, p) \cdot n\, ds = \lim_{\eta \to 0} \frac{1}{\eta} \int_\Omega \chi^S (u^S - u)\, dx, \tag{5.10}$$

where $\sigma_{ij}(u, p) = \mu(\partial_{x_j} u_i + \partial_{x_i} u_j) - p\delta_{ij}$ designates the stress tensor. In the above formula, we recall that, by abuse of notation, $u$ denotes the solution of the system (5.3)–(5.7), and depends therefore obviously on $\eta$.

## 5.3 Remarks on the Numerical Implementation

The method described above can be implemented with any discretization method for the incompressible Navier–Stokes equations. Typically, a natural splitting method consists at each time step to:

(i) solve the Navier–Stokes equation:

$$\partial_t(\rho u) + \operatorname{div}(\rho u \otimes u) - \mu \Delta u = \rho g, \tag{5.11}$$

(ii) compute $u^S$ on the basis of Eq. (5.5) using the result of (5.11),
(iii) take into account the penalization term by solving the equation

$$\partial_t(\rho u) = \frac{1}{\eta}\chi^S(u - u^S) \tag{5.12}$$

(iv) add a pressure gradient so as to make the final velocity field divergence free, by solving the equation

$$\Delta p = \operatorname{div} u^*, \tag{5.13}$$

associated with the appropriate conditions at the boundary of the computational domain $\Omega$, where $u^*$ denotes the result of the previous steps,
(v) finally solve the advection equation of the Level Set function giving the fluid-solid interface and the characteristic function of the solid.

Equations (5.11) and (5.13) are solved by taking into account the boundary conditions at the limits of the computational domain (we recall that this domain is independent of the fluid-solid interface).

The time discretization of Eq. (5.12) calls for some remarks. Assuming, for a sake of simplicity of the notations, a uniform density in the fluid-solid system, an explicit discretization of this equation gives the formula

$$u' = u + \frac{\Delta t}{\eta}\chi^S(u^S - u)$$

where $\Delta t$ is the time step, $u^S$ denotes the velocity of the solid defined by (5.5) and $u$ is the velocity resulting from the preceding stages of the algorithm. Equivalently we obtain

$$u' = u\left(1 - \frac{\Delta t}{\eta}\chi^S\right) + \frac{\Delta t}{\eta}\chi^S u^S.$$

We see that in the particular case where $\Delta t = \eta$ one obtains for $u'$ the projection of $u$ on the velocities corresponding to the rigid displacements. In that case the penalization method coincides with the projection method of projection of [126].

In addition, the condition $\Delta t \leq \eta$ appears as a necessary condition to ensure the stability of this step. However, as we will see later, it is important in practice to take very small values for the penalization coefficient $\eta$, to ensure good continuity of the velocity at the solid-liquid interface. With this implementation of the method, this would require a time step which can prove to be prohibitive.

Alternatively, an implicit time discretization for the penalization step is very simple to write and does not entail any additional cost compared to the explicit scheme. It is written, as for the original method with prescribed body velocity [5]

$$u'\left(1+\frac{\Delta t}{\eta}\chi^S\right) = u + \frac{\Delta t}{\eta}\chi^S u^S,$$

or equivalently

$$u' = \frac{u + \Delta t\,\chi^S u^S/\eta}{1+\Delta t\,\chi^S/\eta}. \tag{5.14}$$

This scheme is obviously monotonous, in the sense that if $u_S$ and $u$ are positive, so is $u'$, for any value of the time step. It therefore makes it possible to use small values of $\eta$, and therefore to ensure a good matching of velocities at the walls, without having to use prohibitively small time steps. Below we will show numerical illustrations of these properties.

A final remark concerning the implementation of these methods concerns the monitoring of the solid(s). The transport equation (5.7), even if it is solved with a precise method, can lead to a distortion of the solids, especially as the continuity of velocities at the walls of the solid is not ensured exactly. We can economize on solving this equation and avoid this source of error by using the fact that moving rigid solids is a purely algebraic operation that can be done exactly.

We start by replacing Eq. (5.7) with an advection equation based on the velocity of the solid:

$$\partial_t \varphi^S + u^S \cdot \nabla \varphi^S = 0.$$

Consider the characteristics $X$ associated with the velocity field $u^S$ and set $X_n = X(t_n, x)$ for a point $x$ in the solid. By choosing a constant velocity field between 2 time steps $t_n$ and $t_{n+1}$, we can deduce $X_{n+1}$ from $X_n$ by rotation and translation. More precisely if we define

$$\theta^n = |\boldsymbol{\omega}^n|\Delta t\ ,\ \frac{\boldsymbol{\omega}^n}{|\overline{\boldsymbol{\omega}}^n|} = (\alpha, \beta, \gamma),$$

where $\boldsymbol{\omega}^n$ denotes the rotational velocity of the solid $u^S$ at time $t_n$, consider the rotation around the center of gravity $\mathbf{c}^n$ of $S$ at that time with matrix

$$R^n = \begin{bmatrix} 1-2b^2-2c^2 & 2ab-2cd & 2ac+2bd \\ 2ab+2cd & 1-2a^2-2c^2 & 2bc-2ad \\ 2ac-2bd & 2bc+2ad & 1-2a^2-2b^2 \end{bmatrix}$$

where

$$a = \alpha \sin\frac{\theta^n}{2}, b = \beta \sin\frac{\theta^n}{2}, c = \gamma \sin\frac{\theta^n}{2}, d = \cos\frac{\theta^n}{2}.$$

With these notations, the rigid displacement of $S$ can be written exactly

$$X^{n+1} = \mathbf{c}^n + u^S \Delta t + R^n(X^n - \mathbf{c}^n).$$

We can incrementally calculate the matrices $\mathcal{M}^n$ and the vectors $V^n$, such as

$$X^{n+1} = \mathcal{M}^{n+1} X^0 + V^{n+1}.$$

The above calculations thus make it possible to derive $X^0 = x$ from $X^{n+1}$. To calculate the Level Set function $\varphi$ at time $t_{n+1}$ it is therefore sufficient to do this calculation at each grid point, then to interpolate the initial level set function (built from the solid at initial time) to the corresponding $X^0$ points.

## 5.4 Extensions of the Penalization Method

One advantage of the penalization method described above is the possibility of adding in a seamless fashion to the dynamics of solids external forces other than those coming from hydrodynamics.

A first example is given in [73]. In this case, the point is to add to the velocities obtained by averaging over the solid phase, and therefore resulting from the hydrodynamic forces, a velocity field associated with deformations prescribed a priori in the solid. The targeted application is the swimming of eel fish and the deformations are calculated from models based on a distribution of thicknesses of the solid around an edge, itself defined by a distribution of curvature, variable over time and defining the undulatory movements of the swimmer. By time-differenciation, these deformations allow to define a velocity field in the solid $u_{def}$. This velocity field is added to the velocity field defined by (5.5) and inserted into the penalization term in the right hand side of (5.3). Because $u_{def}$ is generally not divergence-free, the computation of the pressure term in the Navier–Stokes equation must take this divergence into account.

Another extension given in [9, 33] consists in adding an elastic force in the calculation of the velocity of the solid. We can for example consider the case of

an object attached to a spring, held in the direction orthogonal to the spring and free to move in the direction of the spring. In this case, from the position of the center of gravity of the solid the return force of the gives an acceleration of the object in the direction of the spring and the velocity calculated by (5.5) can be updated at each step time by incrementing it by this acceleration. The penalization term of in the right-hand side of (5.3) is calculated from the solid velocity resulting from this operation.

These various extensions will be detailed and illustrated in the following paragraph.

## 5.5 Numerical Illustrations

To introduce this section, let us start with the simple case of the free fall of an object under the effect of gravity in a fluid. Figure 5.1 taken from [20] deals with the case of a two-dimensional cylinder. The velocities are plotted in a horizontal section passing through the center of the cylinder for different values of the parameter $\eta$.

In this example, the system (5.3)–(5.7) is discretized by the penalization method just described, using a staggered grid. Pressure and characteristic function of the solid are calculated at the same point, the velocity components being classically

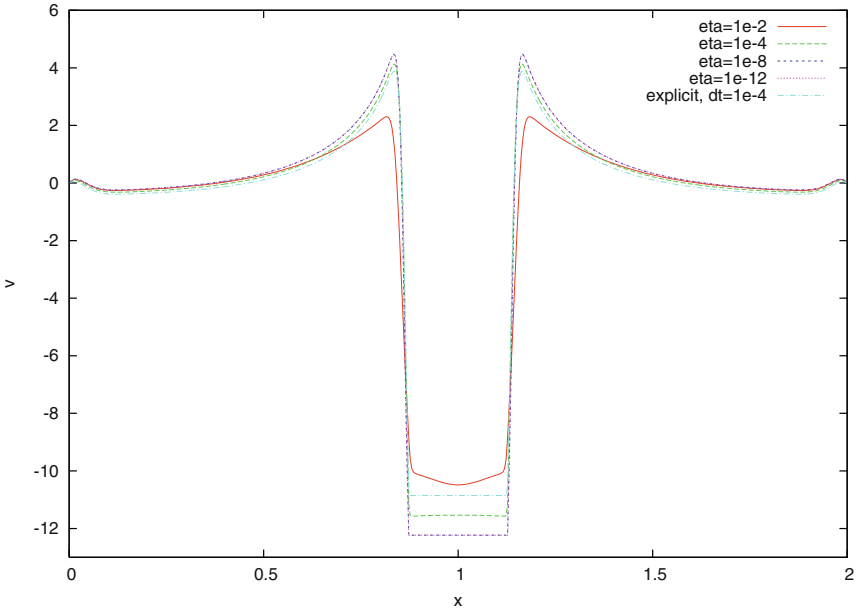


**Fig. 5.1** Velocity profiles for the sedimentation of a cylinder with different values of the penalization coefficient. From [20]

shifted by half a cell to the left or up, which ensures that the zero divergence condition is exactly satisfied. The transport of the characteristic function is solved by a fifth order WENO method. The calculation box is $[0, 2] \times [0, 6]$, the cylinder has a diameter of 0.250 and a density 1.5 in a fluid of density 1. The acceleration of gravity $g$ is taken equal to 980. The grid size is $\Delta x = 1/256$ and the time step is $\Delta t = 10^{-4}$ which corresponds to a CFL around 0.3 at time $t = 0.1$. We can see that the velocity profile converges well when $\eta$ reaches small values (below $\eta = 10^{-6}$), and also that the explicit scheme with $\eta = \Delta t$, which corresponds to the method of [126], under-evaluates the speed of the cylinder by about 10%. This justifies the use of small values of $\eta$ and therefore the use of an implicit method for the penalization equation.

### 5.5.1 *Kissing and Tumbling of Two Spheres*

The second example is borrowed from [34] and corroborates this finding. This is the three-dimensional case known as the "kissing and tumbling" of two spheres. Two spheres initially located one above the other fall by gravity. At first they fall with the same acceleration. In a second stage, the wake produced by the first allows the second to catch up with it. A third phase keeps the two spheres in contact. Finally his system is quickly destabilized and the two spheres separate again. In this experiment the contact between the spheres is taken into account by repulsive forces described in Sect. 6.1.2.

Figure 5.2 represents the vertical speed of the two spheres obtained with the penalization method, the projection method of [126], and the variational method

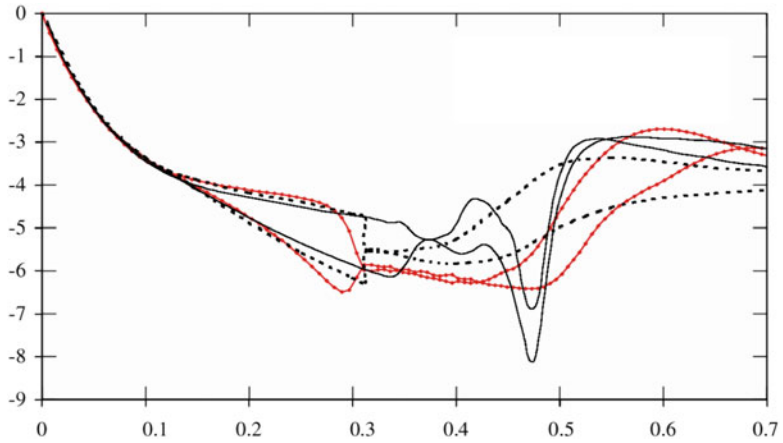


**Fig. 5.2** Evolution of the vertical speeds of two spheres in a "kissing-tumbling" simulation. Results obtained with the projection method [126] (solid line), the fictitious domain method [74] (dotted line) and the penalization method (dashed red line). From [34]

of [74]. We see in this figure that the method of penalization and the variational method of [74] are in good qualitative agreement, in particular for the contact time and the separation dynamics. Only the duration of the contact differs. This is not surprising since the equilibrium of the contact spheres in the vertical position is unstable as soon as the velocity of the of the spheres is large enough. The duration of the kissing phase therefore strongly depends on the response fo the algorithm to this instability. On the other hand the results differ quickly from those obtained with the projection method of [126], although it is conceptually close to the method of penalization. The reason for this difference is probably due to a better accounting of the continuity of the velocity linked to the large values allowed by the implicit method (5.14) in the penalization method, thus confirming the results of Fig. 5.1.

### 5.5.2 *Flows Around Oscillating Obstacles*

The two examples which follow illustrate extensions of the penalization method mentioned in the preceding paragraph. In these examples the numerical method used for the numerical discretization of the Navier–Stokes equations is a semi-Lagrangian method based on a velocity-vorticity formulation of the equations.

Consider first the case of a two-dimensional cylinder mounted on a spring (Fig. 5.3) and subject to a uniform flow transverse to the spring. The motion of the cylinder is constrained along the axis of the spring. If $x_G$ denotes the center of the cylinder and $x_0$ its position at rest, the cylinder therefore undergoes a transverse force equal to

$$F_e = -\frac{k}{m}(x_G - x_0)$$

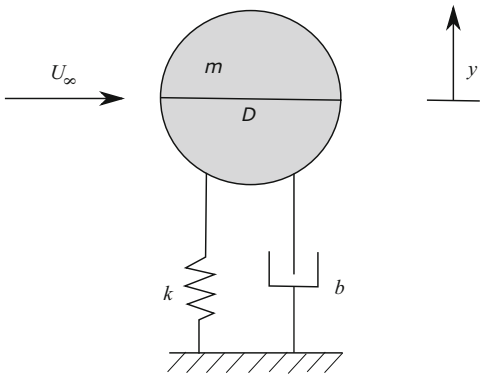


**Fig. 5.3** Sketch corresponding to the oscillation of a cylinder driven by a return force in a transverse flow

where $k$ is the stiffness of the spring and $m$ its mass, with $m = \int_\Omega \rho\, \chi^S\, dx$. In [9] the implemented method can be summarized in the following steps, for each time iteration:

- use the penalization method (5.1) to solve the Navier–Stokes equations with the prescribed obstacle velocity
- use (5.10) to deduce the hydrodynamic forces exerted on the solid
- add the resistance forces of the spring and (possibly) the forces of gravity
- finally use the resulting force to update the position and velocity of the solid.

The approach followed in [33] is to solve the Navier–Stokes equations with variable density (5.3)–(5.7) for the complete interaction problem, and to increment to the velocity obtained by (5.5) the acceleration resulting from the resistance of the spring. To deal with this external force, it suffices to add on the right hand side of Eq. (5.5) the term $-k(x_G - x_0)$ with $x_G = m^{-1} \int \rho x\, \chi^S\, dx$. It is this method that we illustrate below. It is more direct than the method of [9] but requires in the general case to solve the Navier–Stokes equations with variable density.

In the results which follow, the cylinder and the fluid have uniform masses $\rho_S$ et $\rho_f$ respectively, and we use the normalizations of [128] namely

$$m^\star = \frac{\pi}{2}\frac{\rho_S}{\rho_f}\ ,\ k^\star = \frac{2k}{\rho_f}$$

If $f^\star$ is the natural frequency of the system, corresponding to the Strouhal number of the wake of the cylinder, resonance with this frequency is reached for

$$k^\star_{eff} = k^\star - 4\pi^2 f^\star m^\star = 0.$$

The parameters used in these simulations are as follows:

- case 1 (zero stiffness): $k^\star = 0$, $m^\star = 4$,
- case 2 (strong stiffness): $k^\star = 20$, $m^\star = 1$,
- case 3 (close to resonance): $k^\star = 2$, $m^\star = 1$.

Figure 5.4 shows the spring amplitudes for these different cases. After a transient phase during which the wake remains symmetrical and the cylinder remains motionless, very different dynamics are observed depending on the case. Low amplitudes can be observed in the case with zero stiffness (in which case the cylinder can move freely in the direction transverse to the flow under the sole effect of hydrodynamic forces—case 1) or, on the contrary, in the case of very strong stiffness (case 2). In contrast, when mass and stiffness are close to resonance with the Strouhal number of the wake (case 3), stronger oscillations are observed. These differences in spring dynamics are accompanied by changes in the wake (Fig. 5.5). Case 3, close to resonance, exhibits a “narrowed” wake in the direction of flow, corresponding to a higher Strouhal number. In these simulations the computation

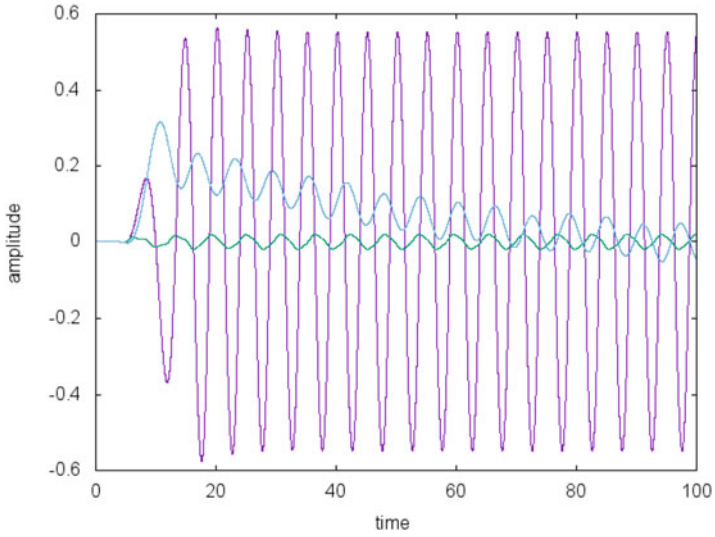


**Fig. 5.4** Oscillations of a cylinder attached to a string for various stiffness and mass values. Case 1 (zero stiffness): blue curve; case 2 (high stiffness): green curve; case 3 (close to resonance): magenta curve

domain is the box $[0, 3]^2$. The cylinder has a diameter equal to 0.2 and is centered at (0.75, 1.5).

The case we have just seen can be extended to a three-dimensional configuration, with a vibrating cylinder free to move in the direction transverse to its axis and to the flow, and subject to an elastic return force. More precisely, if $z$ is the coordinate along the cylinder axis, $y_G(z, t)$ the center of gravity of the section of the cylinder with $z$ coordinate at time $t$, at each time step and on each cross section of the cylinder one adds to the speed obtained by penalization, the acceleration in the transverse direction given by the term $-k(y_G(z, t) - y_G(z, 0))$ where $k$ is the stiffness coefficient.

Figure 5.6 show sections of vorticity and the shape of the cylinder in the reference case without spring ($k = 0$) and in the case $k = 50$. They illustrate again that the deformations of the obstacle have an important effect in its wake. The Reynolds number based on cylinder diameter and upstream velocity is set at the value $Re = 300$. The first case shows the classical three-dimensional structure of the wake, with the presence of longitudinal vortices in the direction of flow that add to the two-dimensional von Karman alley. The case $k = 50$ shows a much more chaotic flow, although the displacements of the cylinder are very small (on the order of 5% of the radius of the cylinder).

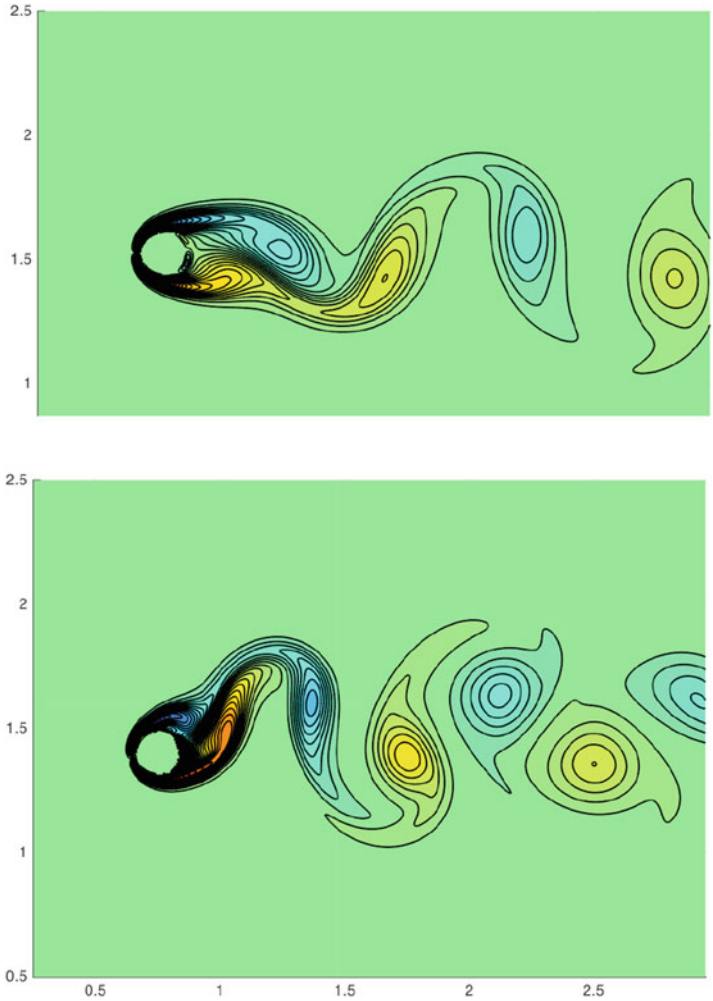


**Fig. 5.5** Wake behind the cylinder in case 1 (zero stiffness, top picture) and case 3 (close to resonance, bottom picture)

### *5.5.3 Anguilliform Swimmers*

The following case is that of anguilliform swimmers studied in [73]. In this application, the velocities resulting from hydrodynamic forces is added to a velocity field resulting from prescribed deformations of the swimmer's geometry.

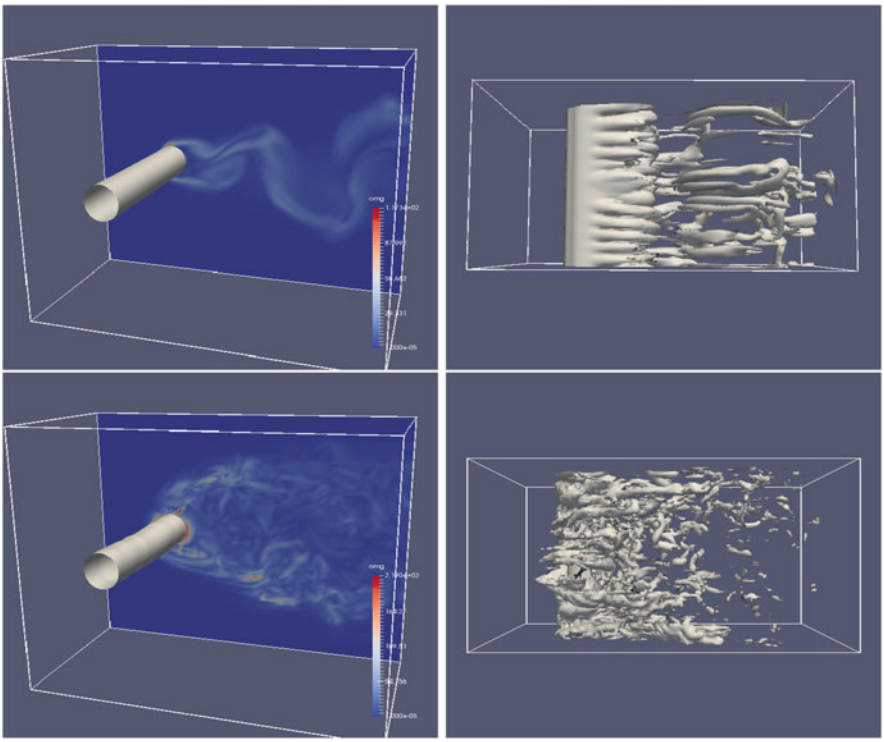

**Fig. 5.6** Vorticity strength in the wake of a vibrating cylinder, in the case with zero stiffness (top picture), and for $k = 50$ (bottom picture). On the left, cross-section in a plane perpendicular to the cylinder axis. On the right, isosurface of the vorticity

These deformations are parameterized as follows. The geometry of the swimmer is defined by half thicknesses $w$ around a central bone, and, for 3D cases, by a height function $h$. For an anguilliform swimmer, the thicknesses are defined through a function of the curvilinear abscissa along the bone by the following formulas, where $L$ is the length of the bone:

$$w(s) = \begin{cases} \sqrt{2w_h s - s^2} & 0 \leq s < s_b \\ w_h - (w_h - w_t)\left(\frac{s - s_t}{s_t - s_b}\right)^2 & s_b \leq s < s_t \\ w_t \frac{L - s}{L - s_t} & s_t \leq s \leq L \end{cases}$$

$$h(s) = b\sqrt{1 - \left(\frac{s - a}{a}\right)^2}$$

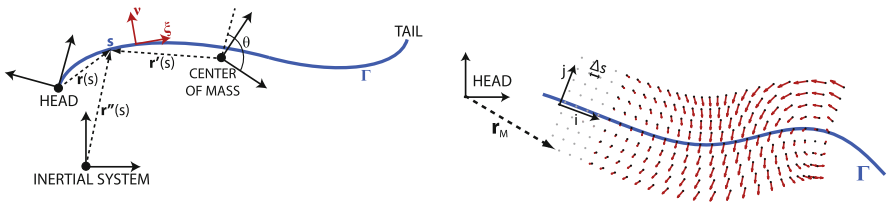


**Fig. 5.7** Local coordinate system used to define the dynamics of a swimmer (left picture) and velocity field around the bone (right picture). From [73]

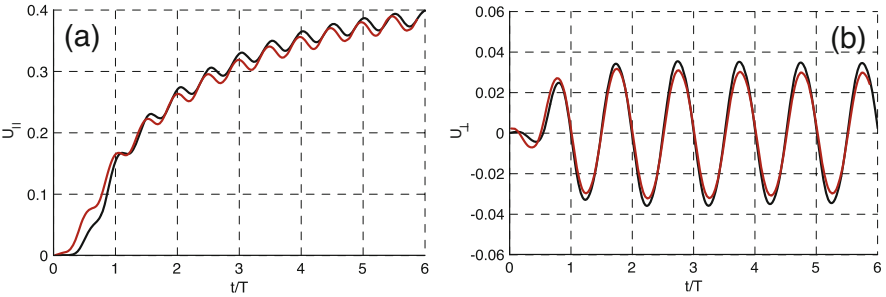


**Fig. 5.8** Longitudinal (left figure) and transverse (right figure) velocities for an anguilliform swimmer obtained by the penalization method [73] (black curve) and he finite volume method [91] (red curve). From [73]

with the following parameters: $w_h = s_b = 0.04L$, $s_t = 0.95L$, $w_t = 0.01L$, $a = 0.5L$ and $b = 0.08L$. The motions of the swimmer are defined by a curvature $H$ oscillating with time according to the formula

$$H(s,t) = \alpha(s) \sin\left(2\pi\left(\frac{t}{T} - \theta(s)\right)\right)$$

where $\alpha(s)$ defines a reference curvature and $\theta(s)$ a phase shift along the bone, defined linearly. The use of a coordinate system attached to the swimmer's head (see Fig. 5.7) then makes it possible by differentiation with respect to time of the Frenet equations

$$\frac{d\mathbf{t}}{ds} = Hn\ ,\ \frac{dn}{ds} = -H\mathbf{t},$$

where $\mathbf{t}$, $n$ are respectively the tangents and normals, then by integration along the bone, to define the velocities along the bone, then by propagation along the normal, in the whole swimmer. This provides the velocity field $u_{DEF}$ which must be added to $u^S$ in the right hand side of (5.12).

Figure 5.8 shows the velocities obtained by this method in comparison with a ALE-type finite volume method [91] where the fluid is meshed at each time-step

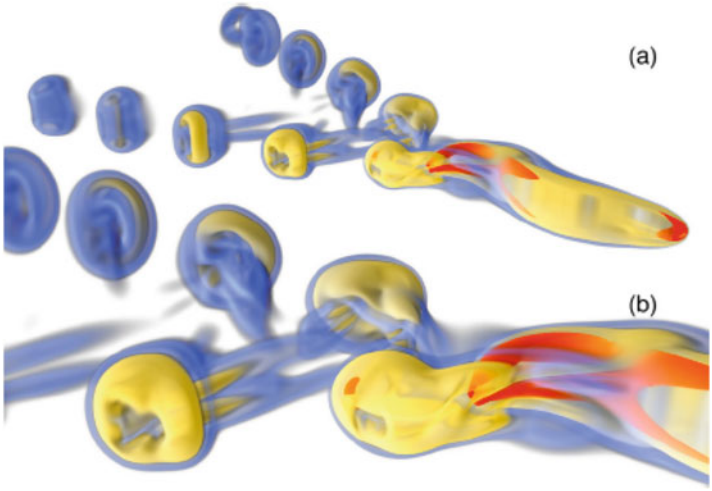


**Fig. 5.9** Vorticity field in the wake of a couple of three-dimensional anguilliform swimmers. From [73]

to fit the swimmer boundary and where the forces are calculated explicitly on its surface.

Figure 5.9 is an example of a wake behind a couple of three-dimensional swimmers. This last example illustrates the fact that the method very simply takes into account the presence of several bodies, unlike methods based on body-fitted meshes. The advantage of this method is that it allows relatively low cost simulations even in complex 3D configurations where several bodies interact through their wakes. This has enabled its use in [73], in combination with stochastic optimization algorithms, to determine optimal swimming modes for individual or group swimmers.

# Chapter 6
# Computing Interactions Between Solids by Level Set Methods


Multi-body systems, such as granular materials, are often dealt with in a discrete way. Contacts and interactions are written as inequalities and systems are described through non-smooth dynamics. An important literature, starting with the work of Moreau [109, 110], has been devoted to this topic and we refer for instance to [54] and the references therein.

In the context of Computational Fluid Dynamics, the question of the interaction between several solids immersed in a fluid can be stated in several ways.

In a first type of application, this question corresponds to the need, purely from the numerical point of view, to avoid the collision, or even the penetration, of objects in a simulation where the objects are led to be confined or to approach solid walls or when the flow is irregular and likely to cause, by accumulation of numerical errors, the solids to come into contact in a non-physical way.

A natural approach proposed in particular in [40, 86, 102] consists in refining the mesh in inter-particle space in order to accurately resolve the flow fields. However, these strategies can turn out to be costly.

It is also possible to model the effect of fluid flow in the interparticle space, when it becomes very small, by lubricating forces [39, 101]. Due to the singular behavior of the forces and the discretization errors in time, this approach seems insufficient and can lead to contacts and overlaps at low spatial resolution.

Other numerical strategies, less respectful of the underlying physics, consist in imposing a constraint on the movement of the objects by means of artificial repulsive forces at short range [34, 75] or by directly applying a minimum distance between the particles [101]. Unlike the refinement strategy, these collision methods allow, in addition to managing overlaps and contacts between particles, to use a coarser discretization, significantly reducing the computational cost compared to the method proposed in [86].

Finally, in other types of applications where we seek to follow more closely the physics of interactions between objects and with flow, we may wish to take into account, for example, electrostatic effects or cohesion forces between particles.



G.-H. Cottet et al., *Level Set Methods for Fluid-Structure Interaction*, Applied Mathematical Sciences 210, https://doi.org/10.1007/978-3-031-08659-5_6

In these different examples, the interactions between objects are reflected by forces exerted on the surfaces of the objects. In an Eulerian method where these surfaces are not followed explicitly, a natural approach is therefore to rely on the formalism described in Sect. 1.4 allowing to translate surface forces into volume forces using Level Set functions, which moreover give the distances between the different objects. This approach is described in Sect. 6.1. If the flow includes a large number of objects, the question arises of the efficient calculation of these interactions, that is to say of avoiding calculation all the two-by-two interactions between objects. Section 6.2 shows how, drawing inspiration from methods developed in image processing, one can limit these calculations to the closest interactions.

## 6.1 Level Set Method to Model Interaction Forces

Level Set methods can be used to detect collision or penetration between objects. If the Level Set function is a signed distance, it evaluates the size of the overlap between the objects. Repulsive forces, depending on this volume, can then be implemented to remove this overlap. This is the method for example used in [27].

The method we describe below is more straightforward, in the sense that the Level Set functions describing the boundaries of the objects are used to calculate repulsive forces that are directly built into the fluid solver.

### *6.1.1 Point Repulsion Model*

To start with, let us consider a point-to-point repulsive force model. To fix the ideas, consider the following model, used in [34]:

$$\ddot{x}(t) = \frac{\kappa}{x(t)} \exp\left(-x(t)/\varepsilon\right). \tag{6.1}$$

In this model the point with coordinate $x(t) > 0$ interacts with the point (obstacle) located at $x = 0$, $\kappa$ is a positive coefficient which gives the stiffness of the collision and $\varepsilon$ is the range of the force. This is a Hamiltonian system with energy given by

$$E(x) = \int_x^1 \frac{\kappa}{s} \exp(-s/\varepsilon)\, ds = \int_{x/\varepsilon}^{1/\varepsilon} \frac{\kappa}{y} \exp(-y)\, dy.$$

This energy makes it possible to assess the thickness of the skin of the obstacle on which the bouncing of objects is made. Let us indeed assume an object at an initial distance $x(0) = x_0$ from the obstacle and with velocity $\dot{x}(0) = v_0 < 0$ directed towards the obstacle. The rebound will take place at a distance $x(t)$ such that $\dot{x}(t) = 0$. If we denote by $x^\star$ this position, we will therefore have, due to the

conservation of energy

$$E(x_0) + \frac{v_0^2}{2} = E(x^\star),$$

that is to say

$$\int_{x^\star/\varepsilon}^{x_0/\varepsilon} \frac{1}{y} \exp(-y)\, dy = \frac{1}{2}\frac{v_0^2}{\kappa}.$$

If we note

$$F_\varepsilon(x) = \int_x^{x_0/\varepsilon} \frac{1}{y} \exp(-y)\, dy\ ,\ \ F(x) = \int_x^{+\infty} \frac{1}{y} \exp(-y)\, dy.$$

and $G_\varepsilon = F_\varepsilon^{-1}$, $G = F^{-1}$, we can therefore write

$$x^\star = \varepsilon\, G_\varepsilon(v_0^2/2\kappa) \simeq \varepsilon\, G(v_0^2/2\kappa) \text{ for } \varepsilon \ll 1. \tag{6.2}$$

This relation confirms that the thickness over which the rebound takes place is of the order of $\varepsilon$. It also shows that in principle the coefficient $\kappa$ can be chosen proportional to the square of the relative velocity of the objects "before contact".

### 6.1.2 Surface Repulsion Model by Level Set Method

Let us now consider the case of a family of objects $\Omega_i$, with boundaries $\Gamma_i$. To extend the point model described above, we can proceed as follows to describe the forces exerted by the object $\Gamma_j$ on the object $\Gamma_i$ for two distinct indices $i$ and $j$:

- extend the dynamical system (6.1) to all the boundary points of $\Gamma_i$ by transcribing its right-hand side into a surface force on $\Gamma_i$ and by using a Level Set function associated with $\Gamma_j$ to determine the direction of this force and the distance to the object $\Omega_j$.
- translate this surface force into volume force using a Level Set function associated with $\Gamma_i$, using the Level Set formalism seen in Chap. 1.

By summing over all the interactions between objects, in the case where the Level Set functions are signed distances to the objects, we obtain the following force model:

$$\mathbf{f}_{\text{contact}}(x) = -\rho \sum_{i,j} \frac{\kappa_{ij}}{\varepsilon} \zeta\left(\frac{\varphi_i(x)}{\varepsilon}\right) \frac{\nabla\varphi_j(x)}{\varphi_j(x)} \exp\left(-\varphi_j(x)/\varepsilon\right).$$

If the Level Set functions are not signed distances (for example when we consider deformable objects and we want use the Level Set functions of the interfaces to define elastic forces as well), we obtain a model by locally approaching the distance to the object $\Omega_j$ par $\frac{\varphi_j}{|\nabla\varphi_j|}$, as we saw in Sect. 1.5.2. By further renormalizing the Level Set functions in the regularization $\zeta$, we end up with the formula

$$\mathbf{f}_{\text{contact}}(x) = -\rho \sum_{i,j} \frac{\kappa_{ij}}{\varepsilon} \zeta\left(\frac{\varphi_i(x)}{\varepsilon|\nabla\varphi_i(x)|}\right) \frac{\nabla\varphi_j(x)}{\varphi_j(x)} \exp\left(-\frac{\varphi_j(x)}{\varepsilon|\nabla\varphi_j(x)|}\right). \tag{6.3}$$

In this equation $\rho$ denotes the density of the fluid-object system, which must be evaluated as a function of the densities $\rho_i$ of the objects by the formula

$$\rho(x) = \sum_i \rho_i \chi_i(x)$$

where $\chi_i$ is the indicator function of $\Omega_i$ ($\Omega_0$ denoting the fluid domain). It is this contact force that is used in the experiment of Fig. 5.2. It should be noted that in this formula the small parameters giving, on the one hand, the thickness of the rebound and, on the other hand, the smoothing of the forces on the surfaces have been taken equal but this is obviously not necessary.

### 6.1.3 *Taking into Account Cohesion and Damping Forces*

In some applications it is desirable to take into account the actual physics of interactions between objects. This is the case, for example, in granular media made up of cohesive sediments found in river beds, coastal systems or mudslides. The grains forming these sediments interact via repulsive forces similar to those seen previously as well as Van der Walls type cohesion forces at very short range. These latter forces are able to ensure the cohesion after contact of agglomerated grains. The specific forms, and in particular their range, of these repulsive and cohesive forces are obviously dependent on the rheology of the grains and the properties of the liquids in which they are immersed.

In the absence of fully satisfactory macroscopic models to describe such flows, direct simulation methods solving the grain-scale flow are becoming increasingly popular [7]. In [145] for example, the grains are spheres of different sizes and the interaction forces are central forces, integrated into an immersed boundary method to process thousands of particles.

One advantage of Level Set methods is that they allow non-spherical particles to be taken into account. A contact model with repulsive and cohesive forces and linear

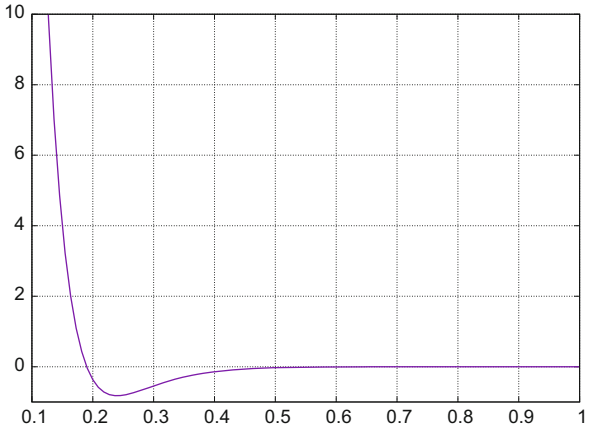


**Fig. 6.1** Profile of a function $g$ taking into account short contact and cohesive forces. The obstacle is at $x = 0$

damping, similar to that used in [145], for particles of any shape can be written as

$$\mathbf{f}_{\text{contact}}(x) = -\rho(x) \sum_{i,j} \frac{\kappa_{ij}}{\varepsilon} \zeta\left(\frac{\varphi_i(x)}{\varepsilon|\nabla\varphi_i(x)|}\right) \frac{\nabla\varphi_j(x)}{|\nabla\varphi_j(x)|} \left[ g\left(\frac{\varphi_j(x)}{|\nabla\varphi_j(x)|}, \varepsilon\right) - \alpha u(x) \right] \exp\left(\frac{-\varphi_j(x)}{\varepsilon|\nabla\varphi_j(x)|}\right). \tag{6.4}$$

In this formula, a damping term controlled by the parameter $\alpha$ has been added to the contact forces. As mentioned earlier, the specific form of the function $g$ must be chosen as a function of the rheology of the media. A typical example of a function $g$ showing the superposition of repulsive and cohesive forces at short range is given in Fig. 6.1.

This type of force and its effect on the dynamics will be illustrated in the following paragraph.

### *6.1.4 Numerical Illustrations*

The reference [34] contains a number of validations of the computation of repulsive forces mentioned in the previous paragraph. Figure 6.2 shows a comparison, for the fall of a disc on a horizontal wall, with a method using a central force acting on the center of the disc [74]. In the case of the Level Set method, the discretization method in [34] is a semi-lagrangian method based on a vorticity formulation and a Boussinesq approximation of the Navier–Stokes equations. In the case of [74] it is a fictitious domain approach with a discretization by finite element methods.

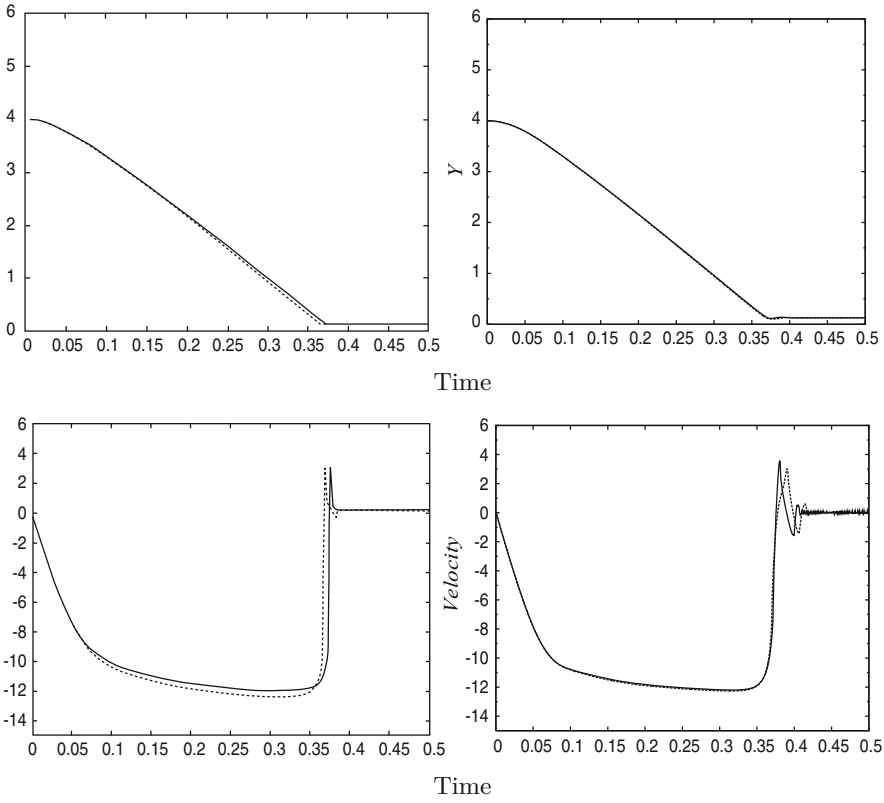


**Fig. 6.2** Sedimentation of a two-dimensional cylinder under the effect of gravity. Comparison of the Level Set approach (left pictures) and the approach in [74] (right pictures) using a central force. Top pictures: height of the cylinder ; bottom pictures: vertical velocity. The grid size is $\Delta x = 1/256$ for the continuous lines and $\Delta x = 1/384$ for the dotted line. From [34]

In these simulations, the physical parameters are as follows

- fluid density 1
- disc density 1.5, disc diameter 0.025
- fluid viscosity 0.01
- gravity 980.

The disc is initially placed at a distance of 4 from the obstacle, in a box of dimensions $[0.2]\times[0.6]$. In this experiment, the parameter $\varepsilon$ is taken equal to the size of the grid cells. From the above analysis the parameter $\kappa$ should be taken from the order of the square of the pre-contact velocity. In the previous experiment the value $\kappa = 30$ was chosen. It should be noted that even in an explicit time discretization, the collision term does not cause stability problems.

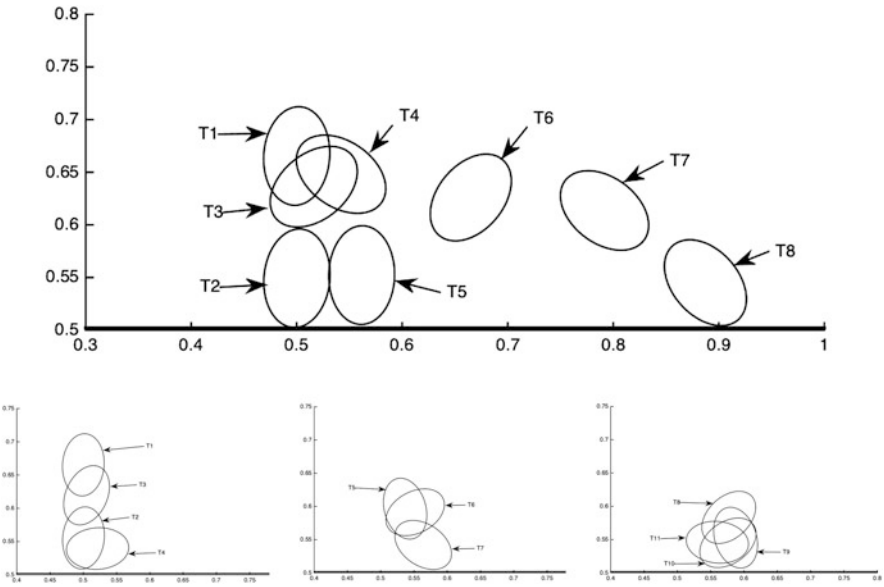


**Fig. 6.3** Elliptic body falling on a plane under gravity. In the top picture, contact by repulsion similar to that in Figs. 5.2 and 6.2, and damping. In the bottom pictures, force with cohesion term and damping given by (6.4) and (6.5). Times $T_i$ refer to successive times of the contact in increasing order

The following example illustrates the handling of cohesive and damping forces in contact between objects. We can see in Fig. 6.3 that the cohesive forces allow the object to stay in contact with the wall after the second bounce. This example also highlights that, unlike central force models, contact models by Level Set methods clearly allow objects to rotate.

In this illustration the function $g$ appearing in formula (6.3) has the following expression:

$$g(x, \varepsilon) = \frac{1}{\varepsilon}\left(3.8 - \frac{x}{\varepsilon}\right) \tag{6.5}$$

In both cases of Fig. 6.3 the damping coefficient is $\alpha = 25$.

## 6.2 An Efficient Method for Dealing with Contacts Between Multiple Objects

### *6.2.1 Motivation*

When we have to deal with the dynamics and the interaction between multiple objects, the use of a single level function to follow the interface of these objects

is possible but problematic: if the mesh is too coarse, interfaces inside a single cell numerically coalesce. A simple alternative is obviously to use a Level Set function for each body. This is what is done in [34], with the difficulty of a high computational cost if the objects are numerous and interacting with each other.

In [147], a formulation using $log_2 N$ level functions to represent $N$ different regions is presented. This model, based on the four-color theorem, considerably reduces the number of Level Set functions and can handle complex topologies. However, reconstructing the distances between two bodies is not simple in the general case, and this model is therefore unable to deal in an efficient way with bodies interacting pairwise and immersed in fluid.

In this section, we describe an approach, based on the deformable multi-geometric, interface capturing model (MGDM) introduced by J. Bogovic et al [17] for image segmentation. This model results in the efficient implementation of formulas of the type of (6.3) for a large number of objects. This approach is detailed in [89].

### *6.2.2 The Algorithm*

The principle of this algorithm is that it requires, regardless of the number of interacting objects, only five fields to

(1) locate and follow each immersed structure,
(2) specify a velocity or force independently on each structure,
(3) handle numerical and/or physical contacts between objects.

This greatly reduces the computational cost, as will be illustrated below. More precisely, a zero level set representing the union of interfaces is transported with the velocity of the fluid. Level Set functions then allow, on the one hand, to label the solids and for each point of the domain to know the index of the closest and the second closest solid to that point. A multi-fast-marching type algorithm is then implemented in a thin band around the interfaces making it possible to update these functions.

This method combines the advantage of the MGDM method, which efficiently captures a large number of bodies and their relative neighbors, and the efficiency of the Level Set contact models seen previously.

In order to validate the capacity of this method to avoid numerical contacts and its efficiency in treating a large number of structures, two applications are explored: settling of rigid bodies and suspensions of biological vesicles. Let us know describe more precisely the method.

#### 6.2.2.1 Label Functions

Let $N$ objects occupying domains $\Omega_i(t) \subset \Omega$, $i \in [1, N]$, and immersed in a fluid occupying the domain $\Omega_{N+1}(t)$. The set of these $N+1$ domains forms a partition of $\Omega$, with $\overline{\Omega_i} \cap \overline{\Omega_j} = \emptyset$ for $i \neq j$ in $\{1, \cdots, N\}$.

At each point $x \in \Omega$, we define the *label* functions $E_0$, $E_1$, $E_2$ as follows:

$$\forall x \in \Omega, \forall i \in \{1, \ldots, N+1\}, \qquad E_0(x) = i \text{ if } x \in \Omega_i,$$

$$E_1(x) = \underset{j \neq E_0(x)}{\arg\min}\, d(x, \Gamma_j), \qquad E_2(x) = \underset{j \notin \{E_0(x), E_1(x)\}}{\arg\min}\, d(x, \Gamma_j).$$

with $\Gamma_{N+1} = \bigcup_{i=1}^{N} \Gamma_i$ corresponding to the fluid-structure interface. The function $E_0$ thus labels the partition of $\Omega$ as $N+1$ different objects, while $E_1$ (resp. $E_2$) identifies the label of an object in this partition closest (resp. of a second closest set) to each point. In the event that several objects are equidistant from a point, the number is that of one of them. In practice, this indeterminacy does not induce any difficulty in the algorithm. We thus have:

$$\begin{cases} E_0(x) = i & \text{if } x \in \Omega_i, \\ E_1(x) = j & \text{if a closest body to } x \text{ is } \Omega_j, \\ E_2(x) = k & \text{if a second closest body to } x \text{ is } \Omega_k. \end{cases}$$

In particular $E_1(x) = N+1$ in each immersed object. $E_2(x)$ is, inside a body, the index of a closest solid, and, in the fluid, a second closest body: if $i \in [1, N]$

$$\forall x \in \Omega_i, \begin{cases} E_0(x) = i, \\ E_1(x) = N+1, \\ E_2(x) = k, \text{ where } \Omega_k \text{ is the immersed body closest to } x. \end{cases}$$

Figure 6.4 is an illustration of the three label cards for five structures immersed in a fluid. The values of $E_1$ show that the object closest to the 5 structures is the fluid. The values of $E_2$ show that for the four peripheral bodies (green, yellow, purple, and light blue objects), the closest object (which is the second closest structure) is the blue body. In addition, the $E_2$ label divides the central blue structure into four regions, each giving the color of the closest structure. We can therefore see that the three label maps provide an interesting local description of the notion of proximity for the whole fluid-structure domain.

Taking advantage of this local description of nearby objects, we can define two associated distance functions.

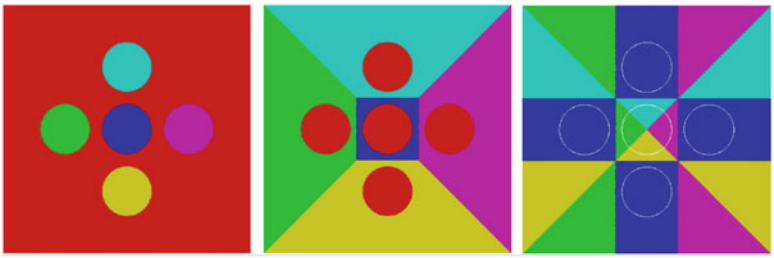

**Fig. 6.4** llustration of the three label functions for a configuration of five bodies, from left to right: $E_0$, $E_1$ and $E_2$. Each object has a specific color given by the values of $E_0$ and red corresponds to the fluid. The white outline represents the boundary of the solids. Within each body, the closest object is the fluid ($E_1$ is red is in these bodies). From [89]

#### 6.2.2.2 Distance Functions

$$\forall x \in \Omega, \qquad \begin{cases} \psi_1(x) = d(x, \Gamma_{E_1(x)}), \\ \psi_2(x) = d(x, \Gamma_{E_2(x)}). \end{cases} \tag{6.6}$$

The distance function $\psi_1(x)$ is the distance from $x$ to the boundary of the first nearest object, noted $\Gamma_{E_1(x)}$, and $\psi_2(x)$ is the distance from $x$ to the boundary of the second closest object $\Gamma_{E_2(x)}$. At any point of the domain $\Omega$, $\psi_1$ captures the union of all interfaces of the bodies and $\psi_2$ monitors the distance to the closest body. As a result, at each point, we obtain for each solid body the distance to the closest other solid. This allows to define a collision model, as avoiding contacts between solids is equivalent to imposing:

$$\forall x \in \Omega, \qquad \psi_2(x) > 0.$$

In the following, we will apply this algorithm to the repulsive forces defined by (6.3). However, it is obvious that it can just as well take into account more general contact forces, such as cohesive forces seen previously or lubricating forces.

#### 6.2.2.3 Dealing with Contact Forces

We start from the collision force model given by (6.3). In this model each solid interface is captured by its own Level Set function. We consider $N$ bodies immersed in a fluid and we denote by $F_{j,i}$ the force applied by the body $\Omega_j$ on the body $\Omega_i$ and by $\varphi_i$ the Level Set function capturing the boundary $\Gamma_i$ of the body $\Omega_i$. The distance from a point $x$ of $\Omega_i$ to the solid $\Omega_j$ is given by $\varphi_j(x)$ and the direction of the force $F_{j,i}$, is obtained directly from $\nabla\varphi_j$. Moreover, to locate the interface

$\Gamma_i$, we use a cutoff function $\zeta$ regularized over a thickness $\varepsilon$ on each side of the interface.

Following (6.3), the short-range repulsive force is expressed as follows (to simplify the writing we assume that the functions $\varphi_i$ are signed distances)

$$\forall x \in \Omega,\ F_{\text{global}}(x) = \rho(x) \sum_{\substack{i,j=1 \\ i \neq j}}^{N} \frac{k}{\varepsilon} \zeta\left(\frac{\varphi_i(x)}{\varepsilon}\right) \frac{\nabla \varphi_j(x)}{\varphi_j(x)} \exp\left(-\frac{\varphi_j(x)}{\varepsilon}\right), \tag{6.7}$$

where $\rho$ denotes the density and $k$ is a repulsive constant which, as explained in the previous section, can be taken proportional to the square of the relative velocities of the corresponding bodies just before the collision.

Interaction forces rapidly decrease exponentially for distant structures, reducing the number of interacting neighbors. Nevertheless, this collision model takes a priori into account all the possible interactions between $N$ bodies, which leads to a computational effort in $O(N^2)$ which quickly becomes prohibitive for large $N$.

To reduce the complexity of (6.7), we modify $F_{\text{global}}$ so as to take into account only the nearest neighbors and express it by means of the two functions $\psi_1$ and $\psi_2$. We set:

$$\forall x \in \Omega,\ F_{\text{label}}(x) = \frac{k}{\varepsilon} \rho(x) \zeta\left(\frac{\psi_1(x)}{\varepsilon}\right) \frac{\nabla \psi_2(x)}{\psi_2(x)} \exp\left(-\frac{\psi_2(x)}{\varepsilon}\right) \tag{6.8}$$

The term $\zeta\left(\frac{\psi_1(x)}{\varepsilon}\right)$ localizes this force on the union of the interfaces, which is expected. More precisely, the force has its support included in $\{x \in \Omega,\ \psi_1(x) \leq \varepsilon\}$.

This collision model takes into account the interaction between the closest bodies at all points. Indeed, as $\psi_2$ is the distance to the second closest object at all points of the fluid/structures domain, if a body is surrounded by other solids, the interaction with the other structures is taken into account on different parts of its interface.

Compared to (6.7), the complexity of the computation is obviously significantly reduced. We refer to [89] and the thesis [88] for a consistency and error analysis between this truncated repulsive force and the original form of the force. In these references, it is shown that the difference between the original force and the truncated force can be controlled when the ratio between the size of the interacting objects (or their minimum curvature radius) and $\varepsilon$ tends towards $+\infty$. This makes it possible to estimate, at least in a simplified coupling model (Stokes-type fluid equations), the error introduced in the final calculation of the velocity by the truncation of the collision forces.

At the algorithmic level, the labels $E_i$ are updated at each displacement of the interfaces by a multiple fast-marching method [17]. The label fields are calculated only in the vicinity of the solid interfaces for $E_1$, and in the vicinity of two close solid interfaces for $E_2$, which significantly reduces the number of calculation points, as shown in Fig. 6.5.

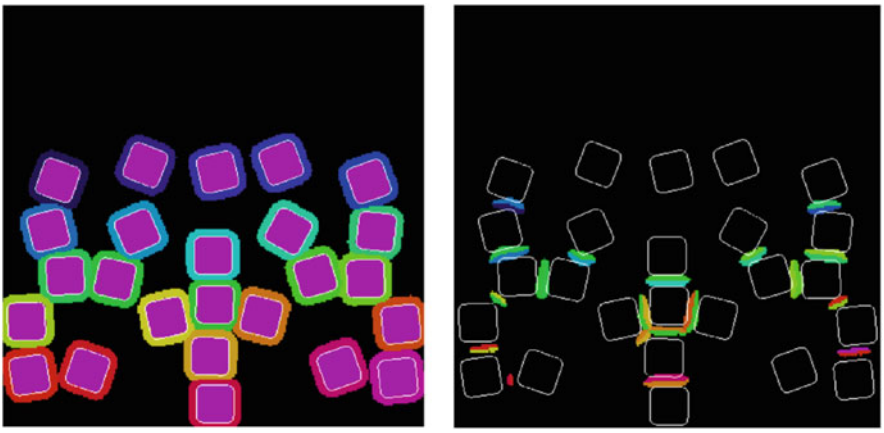

**Fig. 6.5** Illustration of the multiple fast-marching algorithm for 20 objects. Right: $E_1$. Left: $E_2$. The black color corresponds to the uncalculated values of $E_1$ and $E_2$. The white contours correspond to the zero level set of the function $\psi_1$. From [89]

#### 6.2.2.4 Penalization and Complete Model

In addition to reducing the complexity of calculating interaction forces, labels can be used to optimize the penalization step. For that, let us define a new label $E_{0,1}$ which gives at every point of the domain the closest fluid or solid object, that is

$$\forall x \in \Omega, \quad E_{0,1}(x) = \begin{cases} E_0(x) & \text{if} \quad (E_0(x) \neq N+1) \\ E_1(x) & \text{otherwise.} \end{cases} \tag{6.9}$$

In the examples which follow, this label allows to define a regularized characteristic function associated to the $N$ solids though the following formula:

$$\forall x \in \Omega, \forall y \in \Omega, \quad \chi_{E_{0,1}(x)}(y) = 1 - \mathcal{H}\left(\frac{\varphi_{E_{0,1}(x)}(y)}{\varepsilon}\right).$$

Denoting $\rho_{E_{0,1}(x)}$ the density of the solid $\Omega_{E_{0,1}(x)}$ we obtain the overall density function:

$$\rho_x(y) = \rho_f(1 - \chi_{E_{0,1}(x)}(y)) + \chi_{E_{0,1}(x)}(y)\rho_{E_{0,1}(x)}(y).$$

To calculate the penalization term, the value of the rigid velocities is only useful in the objects and their neighborhood of size $\varepsilon$. We thus define a global velocity coinciding with the $N$ rigid velocities $U_i, i \in \{1, \ldots, N\}$ on the solid objects.

More precisely, for all $x \in \Omega$, $y \to U_{E_{0,1}(x)}(y)$ is the rigid velocity of the solid $\Omega_{E_{0,1}(x)}$ obtained by averaging translation and angular velocities (Eq. (5.5)). Setting

$$\forall x \in \Omega, \quad |\ \Omega_{E_{0,1}(x)}\ | = \int_{\Omega_{E_{0,1}(x)}} \rho(z)\, dz = \int_{\Omega} \rho(z) \chi_{E_{0,1}(x)}(z)\, dz \tag{6.10}$$

we get the following formulation: $\forall x \in \Omega,\ \forall y \in \Omega,$

$$\begin{aligned} U_{E_{0,1}(x)}(y) = \frac{1}{|\ \Omega_{E_{0,1}}\ |} \int_{\Omega} \rho_{E_{0,1}(x)}(z)\, \chi_{E_{0,1}(x)}(z)\, U(z)\, dz \\ + \left( J^{-1}_{E_{0,1}(x)} \int_{\Omega} \rho_{E_{0,1}(x)}(z)\, \chi_{E_{0,1}(x)}(z)\, U(z) \times (z - x^g_{E_{0,1}(z)})\, dz \right) \\ \times (y - x^g_{E_{0,1}(y)}). \end{aligned} \tag{6.11}$$

where $J_{E_{0,1}(x)}$ and $x^g_{E_{0,1}(x)}$ are the inertia matrix and the gravity center of the solid $\Omega_{E_{0,1}(x)}$.

In $\Omega_i$, that is to say when $E_{0,1} = i$, this global velocity coincides with $U_i$. The complete model that we consider in the illustrations below therefore corresponds, in the case of immersed rigid solids, to transcribing the model (5.3–5.7) of Chap. 5. It is possible to write it under the more condensed form:

$$\begin{cases} \rho(\partial_t u + (u \cdot \nabla)u) - \mu \Delta u + \nabla p \\ \qquad = \rho g + \frac{1}{\eta}(\chi(U_{E_{0,1}} - u)) + F_{\text{label}} & \text{in } \Omega, \\ \operatorname{div} u = 0 & \text{in } \Omega, \\ \partial_t \varphi + u \cdot \nabla \varphi = 0 & \text{in } \Omega. \end{cases} \tag{6.12}$$

where $\chi$ is a regularized indicator function of the domain occupied by the set of immersed solids, and $U_{E_{0,1}}$ is a rigid velocity on each solid, built thanks to the labels independently on each solid, as in (5.5), then reassembled on the whole domain $\Omega$ (see [88, 89] for more details).

### 6.2.3 Computational Efficiency of the Method

To check the efficiency of the method, we compare in this section the time necessary to calculate the interaction of $N$ immersed disks, on the one hand by considering a collision model with $N$ Level Set functions and on the other hand by the fast method just presented.

In the case of rigid disks, instead of transporting a distance function to the union of the disks and then applying the multiple fast-marching method to it, we transport the centers of gravity and reconstruct the $N$ distance functions. This part of the

**Table 6.1** Average CPU time using $N$ level set functions

| Number of disks | Contact model (6.7) CPU time | Penalization with (6.7) CPU time | Total CPU time |
|---|---|---|---|
| 2 | 0.02 | 0.06 | 0.2 |
| 5 | 0.17 | 0.16 | 0.48 |
| 10 | 0.72 | 0.35 | 1.24 |
| 25 | 4.87 | 0.88 | 6 |
| 50 | 19.25 | 1.75 | 21.5 |
| 100 | 80.8 | 3.9 | 85.3 |
| 400 | 1583.4 | 19.75 | 1605.3 |

**Table 6.2** Average CPU time with the algorithm using labels

| Number of disks | Contact model (6.8) CPU time | Penalization (6.12) CPU time | Labels CPU time | Total CPU time |
|---|---|---|---|---|
| 2 | 0.015 | 0.05 | 0.008 | 0.2 |
| 5 | 0.015 | 0.06 | 0.014 | 0.23 |
| 10 | 0.015 | 0.09 | 0.02 | 0.25 |
| 25 | 0.016 | 0.18 | 0.08 | 0.4 |
| 50 | 0.016 | 0.3 | 0.16 | 0.6 |
| 100 | 0.016 | 0.56 | 0.23 | 0.9 |
| 400 | 0.016 | 2.52 | 2.06 | 4.7 |

algorithm, although dependent on the number of objects, is very fast. We can thus focus on the savings in computational time resulting from the reconstruction of the label functions, then on their use for the computation of the interaction force by (6.8), compared to the computation of the global interaction force by (6.7).

The results presented below correspond to the average of the calculation time of the first ten iterations for either method. This average time is presented in Table 6.1 for the standard method, and in Table 6.2 for the fast algorithm. The model (6.7) is more expensive on the one hand because all the interactions are calculated, but also because the term of penalization in right hand side of the fluid equations also depends explicitly on the number of objects.

### *6.2.4 Numerical Illustrations*

The first illustration relates to the sedimentation of 400 rigid discs of radius $R = 0.01$ in the two-dimensional case. The simulations are performed on a grid of size $512 \times 512$ and the half-thickness of the interface is $\varepsilon = 1.5\Delta x$. The white line indicates the actual numerical size of the particles corresponding to the contour $\psi_1 = \varepsilon$. The coefficient of gravity $g$ is fixed at $-980$, the coefficients $\kappa$ in the

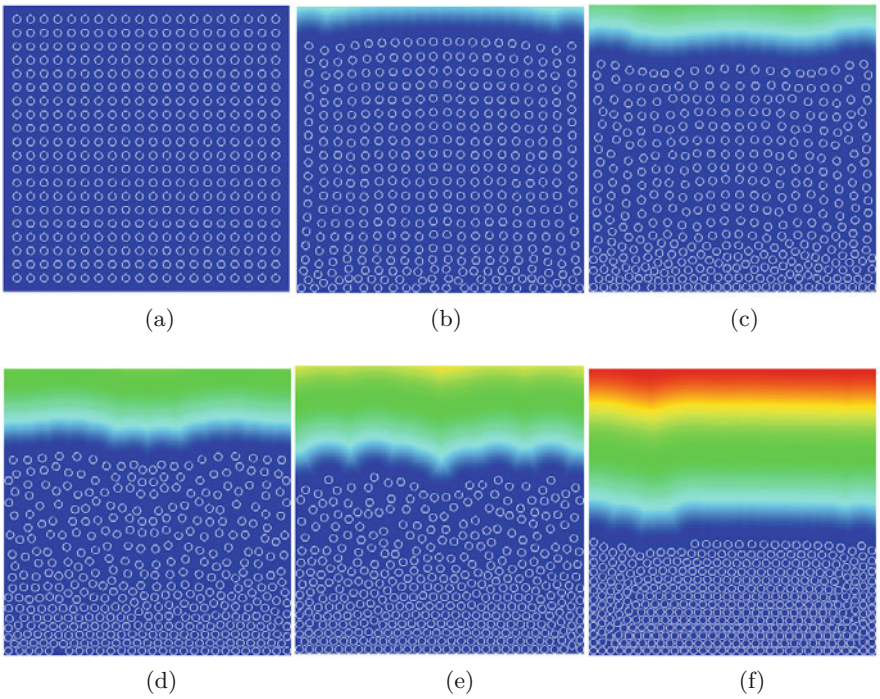


**Fig. 6.6** Simulation of 400 rigid disks under gravity. The white line corresponds to $\varphi = \varepsilon$. The background color represents the distance to the union of the fluid/solid interfaces. From [89]. (**a**) $t = 0.0$. (**b**) $t = 0.75$. (**c**) $t = 1.5$. (**d**) $t = 2.25$. (**e**) $t = 3.0$. (**f**) $t = 6.9$

repulsive force is chosen equal to $-g/10$. The 400 bodies fall and settle, as shown in Fig. 6.6.

The second illustration is an extension to the 3D case. Figure 6.7 shows the settling of 500 rigid spheres of radius $R = 0.01$ falling under gravity using a grid of size $128^3$. The half-thickness of the interface is in this case $\varepsilon = \Delta x$. At the initial stage, there are five layers of 100 bodies at a relative distance $d = 0.1$ (distance between the centers of the two closest bodies). Interactions between bodies occur from $t = 1.5$.

As already indicated, an advantage of the Level Set methods for processing contacts is to be able to take into account non-spherical objects for which central force type models do not work. Figure 6.8 shows the sedimentation of 30 rigid squares of different sizes.

Finally, to illustrate that the method also makes it possible to treat deformable objects, we present a test case of 105 biological vesicles evolving in a Poiseuille flow. The computational domain $\Omega = [0, 4] \times [0, 2]$. The size of the vesicles being small, the simulations are carried out with a fine resolution, on a grid of size $2048 \times 1024$.

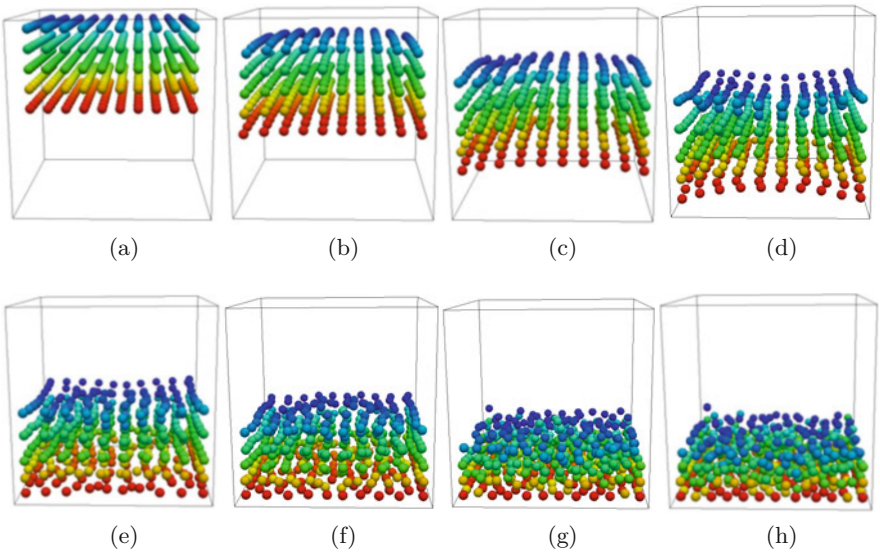


**Fig. 6.7** Simulation of 500 rigid spheres in a $128^3$ grid). Colors represent the labels, from dark blue to red for the solids. From [89]. (**a**) $t = 0.0$. (**b**) $t = 0.5$. (**c**) $t = 1.0$. (**d**) $t = 1.5$. (**e**) $t = 1.8$. (**f**) $t = 2.0$. (**g**) $t = 2.5$. (**h**) $t = 3.0$

The results are represented in Fig. 6.9, the colors indicate the value of the label $E_0$, the white lines correspond to the isolines $\psi_1 = 0$. During the initialization, the region occupied by the vesicles is the left half of the domain, and consists of 7 layers of 15 vesicles. Each vesicle interface corresponds to a Cassini oval with the parameters $a = 0.076$ et $b = 0.08$. The vesicles adopt different shapes, due to the combined effects of the Poiseuille flow induced by the pressure, the elasticity and bending forces and the interactions between the vesicles. For models taking into account bending and elasticity of the vesicles we refer to Sect. 3.6.1.2 and to [89] for the choice of parameters.

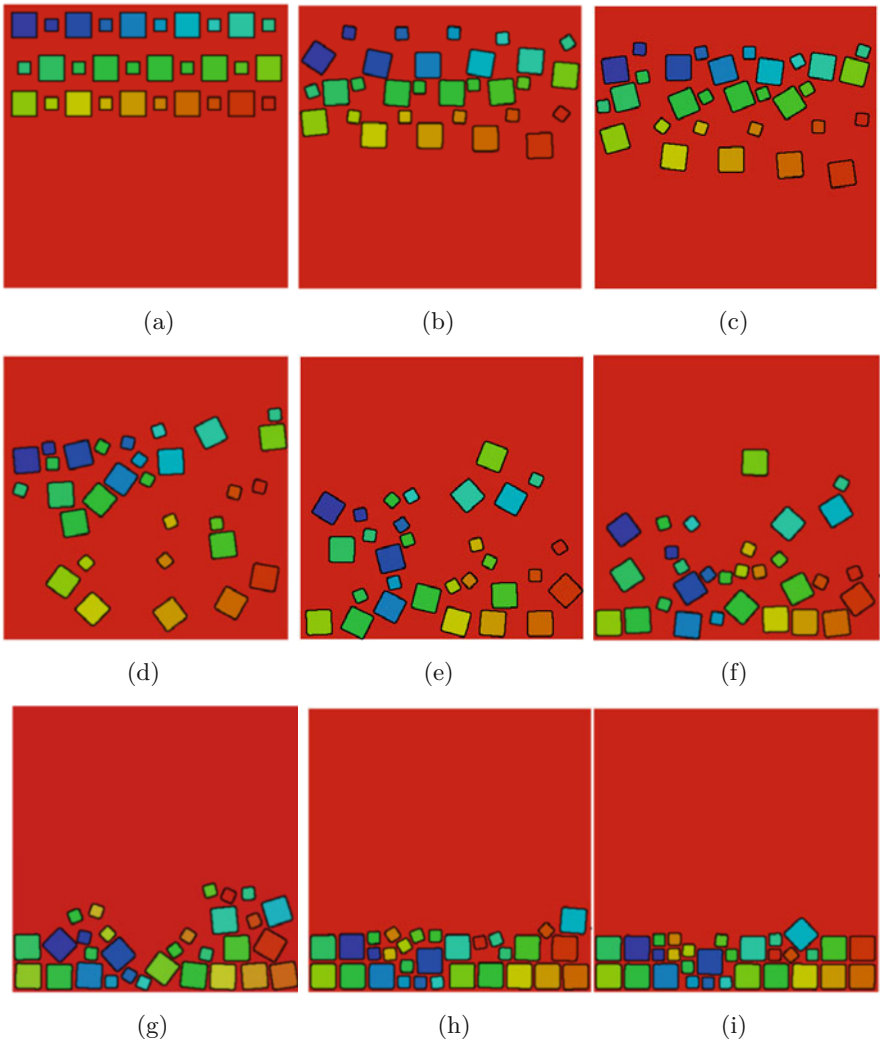


**Fig. 6.8** Sedimentation of de 30 rigid squares of various sizes. From [89]. (**a**) $t = 0$. (**b**) $t = 0.09$. (**c**) $t = 0.11$. (**d**) $t = 0.17$. (**e**) $t = 0.23$. (**f**) $t = 0.25$. (**g**) $t = 0.35$. (**h**) $t = 0.5$. (**i**) $t = 3.18$

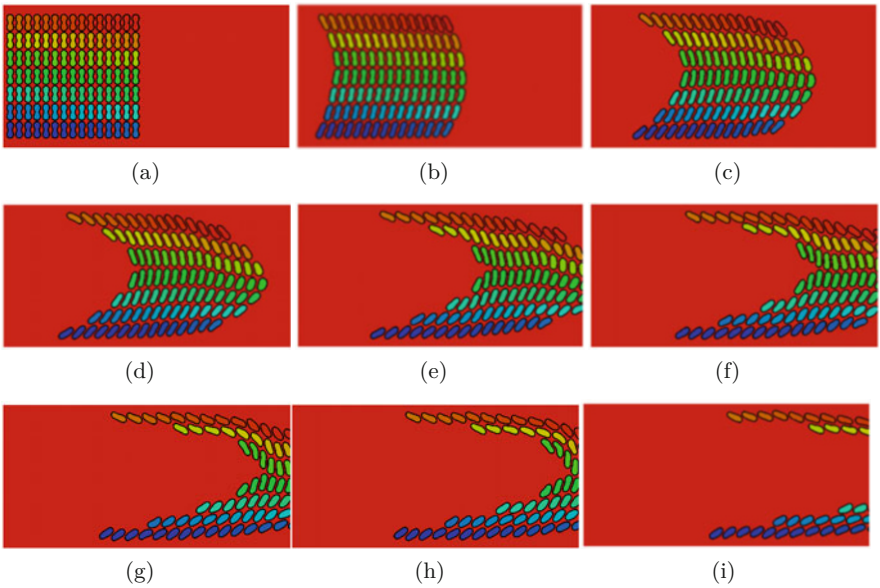


**Fig. 6.9** Simulation of 105 vesicles in a Poiseuille flow, color coded by the values of the label $E_0$. From [89]. (**a**) $t = 0.0$. (**b**) $t = 0.08$. (**c**) $t = 0.14$. (**d**) $t = 0.18$. (**e**) $t = 0.24$. (**f**) $t = 0.28$. (**g**) $t = 0.32$. (**h**) $t = 0.33$. (**i**) $t = 0.42$

# Chapter 7
# Annex

## 7.1 Examples of Curvature Calculations Using a Level Set Function

In this section, we present an explicit calculation of the mean and Gaussian curvatures of an ellipsoid and a torus defined using Level Set functions. These formulas can be used to validate the calculation of the curvature in a numerical code.

### *7.1.1 The Case of the Ellipsoid*

Consider the ellipsoid represented by the following Level Set function

$$\begin{aligned} &\mathbb{R}^3 \longrightarrow \mathbb{R} \\ \varphi : \quad &(x, y, z) \mapsto \left(\frac{x}{a}\right)^2 + \left(\frac{y}{b}\right)^2 + \left(\frac{z}{c}\right)^2 - 1. \end{aligned}$$

The normal is given by

$$n = \frac{1}{\sqrt{\frac{x^2}{a^4} + \frac{y^2}{b^4} + \frac{z^2}{c^4}}} \left(\frac{x}{a^2}, \frac{y}{b^2}, \frac{z}{c^2}\right).$$



G.-H. Cottet et al., *Level Set Methods for Fluid-Structure Interaction*, Applied Mathematical Sciences 210, https://doi.org/10.1007/978-3-031-08659-5_7

Using (1.9), we obtain the mean curvature

$$H = \frac{\frac{x^2}{a^2}(b^2+c^2) + \frac{y^2}{b^2}(a^2+c^2) + \frac{z^2}{c^2}(a^2+b^2)}{a^2b^2c^2\left(\frac{x^2}{a^4}+\frac{y^2}{b^4}+\frac{z^2}{c^4}\right)^{\frac{3}{2}}}$$

and, using now (1.10), the Gaussian curvature

$$G = \frac{\frac{x^2}{a^2}+\frac{y^2}{b^2}+\frac{z^2}{c^2}}{a^2b^2c^2\left(\frac{x^2}{a^4}+\frac{y^2}{b^4}+\frac{z^2}{c^4}\right)^{2}}.$$

### *7.1.2 The Case of the Torus*

Consider a torus, with small and large radius $r$ and $R$ satisfying $R > r$, represented by the following Level Set function

$$\begin{aligned} &\mathbb{R}^3 \longrightarrow \mathbb{R} \\ \varphi : \quad &(x, y, z) \mapsto \sqrt{z^2 + (R - \sqrt{x^2+y^2})^2} - r. \end{aligned}$$

This Level Set function is a signed distance because $|\nabla\varphi| = 1$. The normal is given by

$$n = \frac{1}{\sqrt{z^2 + (R - \sqrt{x^2+y^2})^2}}\left(x\left(1 - \frac{R}{\sqrt{x^2+y^2}}\right), y\left(1 - \frac{R}{\sqrt{x^2+y^2}}\right), z\right).$$

Using (1.9) we get the mean curvature

$$H = \left(2 - \frac{R}{\sqrt{x^2+y^2}}\right)\frac{1}{\sqrt{z^2 + (R - \sqrt{x^2+y^2})^2}}.$$

and, due to (1.10), the Gaussian curvature

$$G = \left(1 - \frac{R}{\sqrt{x^2+y^2}}\right)\frac{1}{z^2 + (R - \sqrt{x^2+y^2})^2}.$$

In the case of the torus these formulas are simplified because $z^2 + (R - \sqrt{x^2+y^2})^2 = r^2$.

## 7.2 Justification of the Results Used for Membranes with Shear

In this section, we are interested in detailing the results concerning the membranes with shear used in Sect. 3.3 of Chap. 3. We will first show what are the equations verified by the invariants then we will show that the first invariant $Z_1$ corresponds to the local variation of area and can be calculated using the gradient of a single Level function Set. We will then present some analytical illustrations in order to justify why the second invariant $Z_2$ measures the shear variations.

### *7.2.1 Proof of the Results Concerning the $Z_1$ Invariant*

Let us begin this section with a lemma which can be seen as an extension of the classical Cayley–Hamilton theorem when the matrix has a zero eigenvalue.

**Lemma 7.1** *Let $\mathcal{A}$ be a symmetric $3 \times 3$ matrix with $0$ as eigenvalue of multiplicity one. Let us denote by $n$ an associated eigenvector. We have the identity:*

$$\mathcal{A}^2 - \mathrm{Tr}(\mathcal{A})\mathcal{A} + \mathrm{Tr}(\mathrm{Cof}(\mathcal{A}))[\mathbb{I} - n \otimes n] = 0. \tag{7.1}$$

***Proof*** It is equivalent to show the lemma in any basis of $\mathbb{R}^3$. Let us consider the orthonormal basis $\mathcal{B}' = (e'_1, e'_2, e'_3) = (\tau_1, \tau_2, n)$ where $(\tau_1, \tau_2)$ is an orthonormal basis of the plane orthogonal to $n$. Let $\mathcal{A}'$ be the matrix $\mathcal{A}$ written in the basis $\mathcal{B}'$ and denote by $\mathcal{A}'_{ij}$ its coefficients.

We have $\mathcal{A}n = 0$ and thus $\mathcal{A}'_{i3} = 0$. Since $\mathcal{A}$ is a symmetric matrix and $\mathcal{B}'$ is an orthonormal basis, the matrix $\mathcal{A}'$ is also symmetric and its structure is given by:

$$\mathcal{A}' = \begin{pmatrix} \mathcal{A}'_{11} & \mathcal{A}'_{12} & 0 \\ \mathcal{A}'_{12} & \mathcal{A}'_{22} & 0 \\ 0 & 0 & 0 \end{pmatrix}.$$

As a result

$$(\mathcal{A}')^2 = \begin{pmatrix} (\mathcal{A}'_{11})^2 + (\mathcal{A}'_{12})^2 & \mathcal{A}'_{11}\mathcal{A}'_{12} + \mathcal{A}'_{12}\mathcal{A}'_{22} & 0 \\ \mathcal{A}'_{11}\mathcal{A}'_{12} + \mathcal{A}'_{12}\mathcal{A}'_{22} & (\mathcal{A}'_{12})^2 + (\mathcal{A}'_{22})^2 & 0 \\ 0 & 0 & 0 \end{pmatrix}.$$

In the basis $\mathcal{B}'$ we have

$$\mathbb{I} - n \otimes n = \begin{pmatrix} 1 & 0 & 0 \\ 0 & 1 & 0 \\ 0 & 0 & 0 \end{pmatrix}.$$

$\mathcal{A}'$ and $\mathcal{A}$ have the same invariants, therefore

$$\begin{aligned} \mathrm{Tr}(\mathcal{A}) = \mathrm{Tr}(\mathcal{A}') &= \mathcal{A}'_{11} + \mathcal{A}'_{22}, \\ \mathrm{Tr}(\mathrm{Cof}(\mathcal{A})) = \mathrm{Tr}(\mathrm{Cof}(\mathcal{A}')) &= \mathcal{A}'_{11}\mathcal{A}'_{22} - (\mathcal{A}'_{12})^2. \end{aligned}$$

It is simple to show that $\mathcal{A}' \mathrm{Tr}(\mathcal{A}') - (\mathcal{A}')^2 = \mathrm{Tr}(\mathrm{Cof}(\mathcal{A}'))[\mathbb{I} - n \otimes n]$ and the announced result follows. □

Let us now recall the definitions given in Sect. 3.3. We follow the deformations in an Eulerian way using the backward characteristics which satisfy the following transport equation

$$\partial_t Y + u \cdot \nabla Y = 0. \tag{7.2}$$

The tensor of the surface deformations is defined by $\mathcal{A} = MM^T$ with

$$M = [\nabla Y]^{-1}[\mathbb{I} - n_0(Y) \otimes n_0(Y)],$$

where $n_0$ denotes the normal to the surface in the initial configuration. The tensor $\mathcal{A}$ can then be rewritten with the right Cauchy-Green tensor $B = [\nabla Y]^{-1}[\nabla Y]^{-T}$ in the form

$$\mathcal{A} = B - \frac{(Bn) \otimes (Bn)}{(Bn) \cdot n}. \tag{7.3}$$

where $n$ indicates the normal to the surface in the deformed configuration. We have $\mathcal{A}n = 0$ thus $\det(\mathcal{A}) = 0$. The invariants $Z_1$ and $Z_2$ are defined by

$$Z_1 = \sqrt{\mathrm{Tr}(\mathrm{Cof}(\mathcal{A}))} \qquad \text{and} \qquad Z_2 = \frac{\mathrm{Tr}(\mathcal{A})}{2\sqrt{\mathrm{Tr}(\mathrm{Cof}(\mathcal{A}))}}. \tag{7.4}$$

The equations verified by these invariants are given by the following proposition

**Proposition 7.2** *Assuming that the vector field $u$ is smooth enough, the invariants verify:*

$$\partial_t Z_1 + u \cdot \nabla Z_1 = Z_1\,[\nabla u] : \mathcal{C}_1, \quad \mathcal{C}_1 = \mathbb{I} - n \otimes n, \tag{7.5}$$

$$\partial_t Z_2 + u \cdot \nabla Z_2 = Z_2\,[\nabla u] : \mathcal{C}_2, \quad \mathcal{C}_2 = \frac{2\mathcal{A}}{\mathrm{Tr}(\mathcal{A})} - (\mathbb{I} - n \otimes n). \tag{7.6}$$

***Proof*** Using (7.2) we get

$$\partial_t([\nabla Y]^{-1}) + u \cdot \nabla([\nabla Y]^{-1}) = [\nabla u][\nabla Y]^{-1}, \tag{7.7}$$

$$\partial_t([\nabla Y]^{-T}) + u \cdot \nabla([\nabla Y]^{-T}) = [\nabla Y]^{-T}[\nabla u]^T, \tag{7.8}$$

then, since $B = [\nabla Y]^{-1}[\nabla Y]^{-T}$,

$$\partial_t B + u \cdot \nabla B = [\nabla u]B + B[\nabla u]^T. \tag{7.9}$$

We also have (7.2)

$$\partial_t(\mathbb{I} - n_0(Y) \otimes n_0(Y)) + u \cdot \nabla(\mathbb{I} - n_0(Y) \otimes n_0(Y)) = 0.$$

Combined with (7.7) this relation yields

$$\partial_t M + u \cdot \nabla M = [\nabla u]M, \qquad \partial_t M^T + u \cdot \nabla(M^T) = M^T[\nabla u]^T. \tag{7.10}$$

Using (7.10) we get (recall that $\mathcal{A} = MM^T$)

$$\partial_t \mathcal{A} + u \cdot \nabla \mathcal{A} = [\nabla u]\mathcal{A} + \mathcal{A}[\nabla u]^T \tag{7.11}$$

where the initial condition is given by $\mathcal{A}(0) = \mathbb{I} - n_0 \otimes n_0$. We can observe that, according to (7.9), $B$ satisfies the same equation with a different initial condition $B(0) = \mathbb{I}$. By taking the trace of (7.11), it results

$$\partial_t\,\mathrm{Tr}(\mathcal{A}) + u \cdot \nabla\,\mathrm{Tr}(\mathcal{A}) = 2[\nabla u] : \mathcal{A} \tag{7.12}$$

then

$$\partial_t\,\mathrm{Tr}(\mathrm{Cof}(\mathcal{A})) + u \cdot \nabla\,\mathrm{Tr}(\mathrm{Cof}(\mathcal{A})) = 2[\mathcal{A}\,\mathrm{Tr}(\mathcal{A}) - \mathcal{A}^2] : [\nabla u].$$

Using the previous equation and the identity (7.1) of Lemma 7.1 we get (7.5)

$$\partial_t Z_1 + u \cdot \nabla Z_1 = Z_1 \frac{[\mathcal{A}\,\mathrm{Tr}(\mathcal{A}) - \mathcal{A}^2]}{\mathrm{Tr}(\mathrm{Cof}(\mathcal{A}))} : [\nabla u] = Z_1[\mathbb{I} - n \otimes n] : [\nabla u].$$

Using (7.12) and the previous equation on $Z_1$ we obtain (7.6). We have $\mathcal{C}_i n = 0$ because $\mathcal{A}n = 0$. □

Let us now show that $Z_1$ measures the local variation of area.

**Proposition 7.3** *Let $u$ be a smooth velocity field and $S_0$ a smooth surface, deformed into $S_t = X(t, S_0)$. Let $(\theta_1, \theta_2) \mapsto \gamma(t, \theta_1, \theta_2)$ be a parametrization of the surface $S_t$ with $\gamma : \mathbb{R}^+ \times U \longrightarrow \mathbb{R}^3$ where $U$ is an open set in $\mathbb{R}^2$. The local variation in area satisfies*

$$\frac{|\partial_{\theta_1}\gamma(t,\theta) \times \partial_{\theta_2}\gamma(t,\theta)|}{|\partial_{\theta_1}\gamma(0,\theta) \times \partial_{\theta_2}\gamma(0,\theta)|} = \frac{Z_1(\gamma(t,\theta),t)}{Z_1(\gamma(0,\theta),0)} = \frac{Z_1(x,t)}{Z_1(Y(x,t),0)} \tag{7.13}$$

*with the notation $\theta = (\theta_1, \theta_2)$ and $x = \gamma(t, \theta)$.*

***Proof*** Let $f : \mathbb{R}^3 \times \mathbb{R}^+ \longrightarrow \mathbb{R}$ be a smooth function. The Reynolds formula for surfaces (2.16) reads

$$\frac{\mathrm{d}}{\mathrm{d}t}\left(\int_{S_t} f\,ds\right) = \int_{S_t} \partial_t f + u \cdot \nabla f + f[\nabla u] : [\mathbb{I} - n \otimes n]ds.$$

Let $g : \mathbb{R}^3 \longrightarrow \mathbb{R}$ a smooth function and $f(x,t) = \frac{g(Y(x,t))}{Z_1(x,t)}$. The expression under the integral becomes

$$\frac{1}{Z_1}\left(\partial_t(g(Y)) + u \cdot \nabla(g(Y))\right) - \frac{g(Y)}{(Z_1)^2}(\partial_t Z_1 + u \cdot \nabla Z_1 - Z_1[\nabla u] : [\mathbb{I} - n \otimes n]).$$

In view of (7.2) and Eq. (7.5) in Theorem 7.2, the first and second terms cancel each other. As a result

$$\frac{\mathrm{d}}{\mathrm{d}t}\left(\int_{S_t} \frac{g(Y(x,t))}{Z_1(x,t)}\,ds\right) = 0. \tag{7.14}$$

Since $\gamma(0,\theta) = Y(\gamma(t,\theta),t)$, Eq. (7.14) becomes

$$\int_U \frac{g(\gamma(0,\theta))}{Z_1(\gamma(t,\theta),t)} |\partial_{\theta_1}\gamma(t,\theta) \times \partial_{\theta_2}\gamma(t,\theta)|\, d\theta = \int_U \frac{g(\gamma(0,\theta))}{Z_1(\gamma(0,\theta),0)} |\partial_{\theta_1}\gamma(0,\theta) \times \partial_{\theta_2}\gamma(0,\theta)|\, d\theta.$$

This result holds for all $g$. We therefore obtain (7.13) and $Z_1$ measures the local variation of area (in both the compressible and incompressible cases). □

We now show that the invariant $Z_1$ can be expressed with a single Level Set function and the Jacobian of the change of variable associated with the deformation noted $J_e$.

Consider $\varphi : \mathbb{R}^3 \to \mathbb{R}$ a Level Set function verifying the transport equation

$$\partial_t \varphi + u \cdot \nabla\varphi = 0. \tag{7.15}$$

We recall that we then have $\varphi(x,t) = \varphi_0(Y(x,t))$ and that the gradient of this relation gives

$$\nabla\varphi = [\nabla Y]^T \nabla\varphi_0(Y) \tag{7.16}$$

Furthermore, we recall that the normal to the surface $\{\varphi = 0\}$ is given by $n = \frac{\nabla\varphi}{|\nabla\varphi|}$.

**Proposition 7.4** *Let $J_e = \det(\nabla Y)^{-1}$. We have*

$$Z_1 = J_e \frac{|\nabla\varphi|}{|\nabla\varphi_0(Y)|}. \tag{7.17}$$

***Proof*** The invariant $Z_1 = \sqrt{\mathrm{Tr}(\mathrm{Cof}(\mathcal{A}))}$ is defined by (7.4). By taking the trace of (7.3), we have

$$\mathrm{Tr}(\mathcal{A})^2 = \left(\mathrm{Tr}(B) - \frac{(B^2 n)\cdot n}{(Bn)\cdot n}\right)^2$$

and

$$\mathrm{Tr}(\mathcal{A}^2) = \mathrm{Tr}(B^2) - 2\frac{(B^3 n)\cdot n}{(Bn)\cdot n} + \left(\frac{(B^2 n)\cdot n}{(Bn)\cdot n}\right)^2.$$

By the Cayley–Hamilton theorem we have

$$B^3 - \mathrm{Tr}(B)B^2 + \mathrm{Tr}(\mathrm{Cof}(B))B - \det(B)\mathbb{I} = 0,$$

from which we deduce

$$\begin{aligned}\mathrm{Tr}(\mathrm{Cof}(\mathcal{A})) &= \frac{1}{(Bn)\cdot n}\Big((B^3n)\cdot n - \mathrm{Tr}(B)(B^2n)\cdot n + \mathrm{Tr}(\mathrm{Cof}(B))(Bn)\cdot n\Big)\\ &= \frac{\det(B)}{(Bn)\cdot n}.\end{aligned}$$

Using (7.16) we get

$$(Bn)\cdot n = \left|[\nabla Y]^{-T}\frac{\nabla\varphi}{|\nabla\varphi|}\right|^2 = \frac{|\nabla\varphi_0(Y)|^2}{|\nabla\varphi|^2}.$$

Using the relation $J_e = \det(B)^{\frac{1}{2}}$ the expression of $Z_1$ reduces to (7.17). We recover the result of Proposition 3.2: in the incompressible case the local variation of area is captured by $|\nabla\varphi|$ since in this case $J_e = 1$. □

### 7.2.2 *Analytical Illustrations for $Z_2$*

We now present some analytical illustrations to show that $Z_2$ defined by (7.4) and (7.3) intuitively gives a "good" measure of the local variation of the shear of a surface. In all the test cases test, we define an initial surface $\Gamma_0 = \{\varphi_0 = 0\}$ and a velocity field $u$ which will move the material points of this surface. We then compute the backward characteristics $Y$ and $Z_1$ and $Z_2$ invariants to see how these Eulerian quantities record the information on deformation.

The test cases and the results are described in Table 7.1. In this first series of test cases (TC1 to TC4), although the material points could move, the initial and deformed surfaces are globally identical ($\Gamma_0 = \Gamma_t$). Moreover, the deformations are uniform in space in the sense that the invariants $Z_i$ on the surface do not depend on the space variables (except for TC4). In the two-dimensional strains, denoted $\alpha$ et $\beta$ (cases TC1 and TC2) the initial surface is the plane $z = 0$. We refer to Sect. 3.3.3 for the corresponding figures with these first two test cases. The velocity field associated with each deformation is represented in the figures below with the corresponding values of $Z_1$ and $Z_2$. The deformation corresponding to $\beta = -1$ is a rotation and as expected it does not induce shear or area variation (see Fig. 3.7). The deformation corresponding to $\alpha = 1$ is a pure expansion and as expected it only yields area variation (see Fig. 3.4).

The deformations corresponding to $\beta = 0$, $\beta = 1$, $\alpha = -1$ only result in a variation in shear (see Figs. 3.8, 3.6, and 3.3). Note that for the deformation $\beta = 0$, we take the limit $\beta \longrightarrow 0$ to define $Y$ and $Z_i$.

The deformation corresponding to $\alpha = 0$ results in variations both in area and shear (see Fig. 3.5). This may seem surprising at first glance, but when a surface

**Table 7.1** Description of the test cases

| TC | $\varphi_0(x, y, z)$ | $u$ | $Y(x, y, z, t)$ | $Z_1$ | $Z_2$ |
|---|---|---|---|---|---|
| 1 | z | $\begin{pmatrix} x \\ \alpha y \\ 0 \end{pmatrix}$ | $\begin{pmatrix} xe^{-t} \\ ye^{-\alpha t} \\ z \end{pmatrix}$ | $e^{t(1+\alpha)}$ | $\mathrm{ch}(t(1-\alpha))$ |
| 2 | z | $\begin{pmatrix} \beta y \\ x \\ 0 \end{pmatrix}$ | $\begin{pmatrix} x\mathrm{ch}(t\sqrt{\beta}) - y\sqrt{\beta}\mathrm{sh}(t\sqrt{\beta}) \\ -\frac{x}{\sqrt{\beta}}\mathrm{sh}(t\sqrt{\beta}) + y\mathrm{ch}(t\sqrt{\beta}) \\ z \end{pmatrix}$ | 1 | $1 + \frac{(1+\beta)^2}{2\beta}\mathrm{sh}^2(t\sqrt{\beta})$ |
| 3 | $x^2 + y^2 - 1$ | $\begin{pmatrix} -yz \\ xz \\ 0 \end{pmatrix}$ | $\begin{pmatrix} x\cos(tz) + y\sin(tz) \\ -x\sin(tz) + y\cos(tz) \\ z \end{pmatrix}$ | 1 | $1 + \frac{t^2}{2}(x^2 + y^2)$ |
| 4 | $x^2 + y^2 + z^2 - 1$ | $\begin{pmatrix} -yz \\ xz \\ 0 \end{pmatrix}$ | $\begin{pmatrix} x\cos(tz) + y\sin(tz) \\ -x\sin(tz) + y\cos(tz) \\ z \end{pmatrix}$ | 1 | $1 + \frac{t^2(x^2+y^2)^2}{2(x^2+y^2+z^2)}$ |
| 5 | $x^2 + y^2 + z^2 - 1$ | $\begin{pmatrix} x \\ y \\ z \end{pmatrix}$ | $\begin{pmatrix} e^{-t}x \\ e^{-t}y \\ e^{-t}z \end{pmatrix}$ | $e^{2t}$ | 1 |
| 6 | $\max(\lvert x\rvert, \lvert y\rvert, \lvert z\rvert) - 1$ | $\begin{pmatrix} 0 \\ x \\ 0 \end{pmatrix}$ | $\begin{pmatrix} x \\ y - tx \\ z \end{pmatrix}$ | see (7.18)–(7.20) | |
| 7 | $x^2 + y^2 + z^2 - 1$ | $\begin{pmatrix} 0 \\ x \\ 0 \end{pmatrix}$ | $\begin{pmatrix} x \\ y - tx \\ z \end{pmatrix}$ | see (7.21) | see (7.22) |

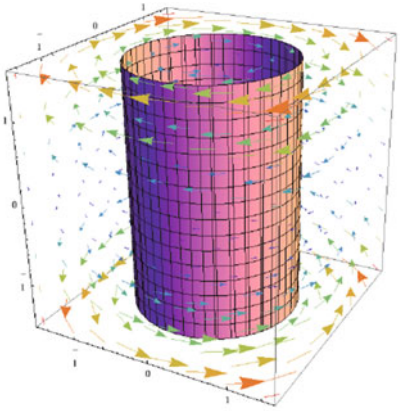

$Z_1 = 1 \qquad Z_2 = 1 + \frac{t^2}{2}(x^2 + y^2)$

**Fig. 7.1** Case TC3: Imposed velocity field $(-yz, xz, 0)$ for the 3D circular shear and initial shape of the cylinder

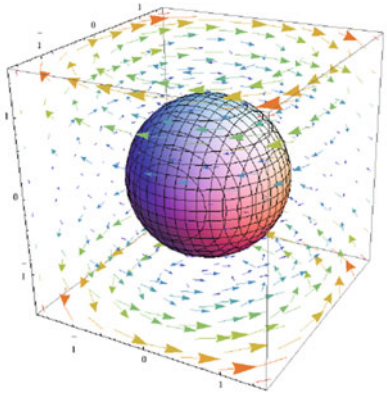

$Z_1 = 1 \qquad Z_2 = 1 + \frac{t^2(x^2+y^2)^2}{2(x^2+y^2+z^2)}$

**Fig. 7.2** Case TC4: Imposed velocity field $(-yz, xz, 0)$ for the 3D circular shear and initial shape of the shpere

is stretched in two directions with different magnitude ($\alpha \neq 1$), it undergoes some shear and therefore, as expected, $Z_2 = \mathrm{ch}(t(1-\alpha)) \neq 1$.

In the three-dimensional circular shear test cases, the initial surfaces are a cylinder (TC3 see Fig. 7.1) or a sphere (TC4 see Fig. 7.2). In each plane $\{z = \alpha\}$ the velocity is a rotation of magnitude $\alpha$. In these test cases, there is a variation in shear but no variation in area. For TC3, $Z_2 = 1 + \frac{t^2}{2}$ is constant on the surface ($x^2 + y^2 = 1$ on the cylinder). This test case is clearly a 3D generalization on a cylinder of the 2D deformation corresponding to $\beta = 0$ and that is why we find the same invariants. For TC4, $Z_2 = 1 + \frac{t^2}{2}(1 - z^2)^2$ on the surface and only depends on the height $z$ which is intuitive ($x^2 + y^2 + z^2 = 1$ on the sphere).

We now present three test cases (TC5 to TC7) where the deformed surface $\Gamma_t$ is different from the initial surface $\Gamma_0$. For the case TC5 corresponding to a three-

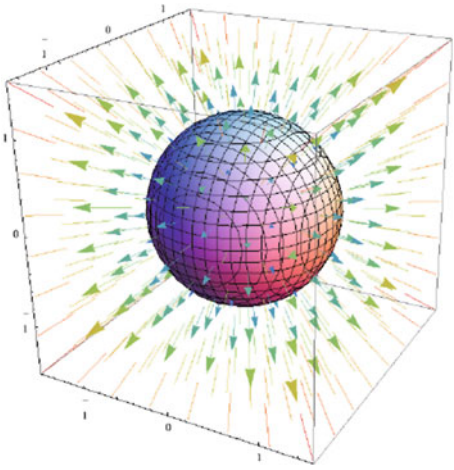

**Fig. 7.3** Case TC5: imposed velocity field $(x, y, z)$ for the 3D expansion and initial shape of the sphere

$$Z_1 = e^{2t} \qquad Z_2 = 1$$

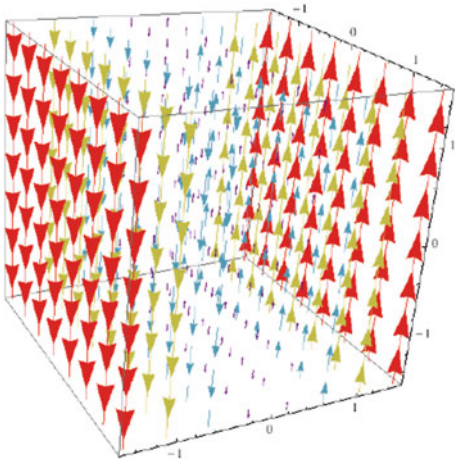

**Fig. 7.4** Cases TC6 and TC7: imposed velocity field $(0, x, 0)$ for the shear deformation

dimensional 3D expansion (see Fig. 7.3), the initial surface is a sphere. In this test case, we only have an area variation.

In the last test cases, the same shear velocity field (see Fig. 7.4) is applied to a cube and a sphere. For the test case TC6, the deformation of the cube (see Fig. 7.5) is given by the zero level set of

$$\varphi(x, y, z, t) = \max(|x|, |y - tx|, |z|) - 1.$$

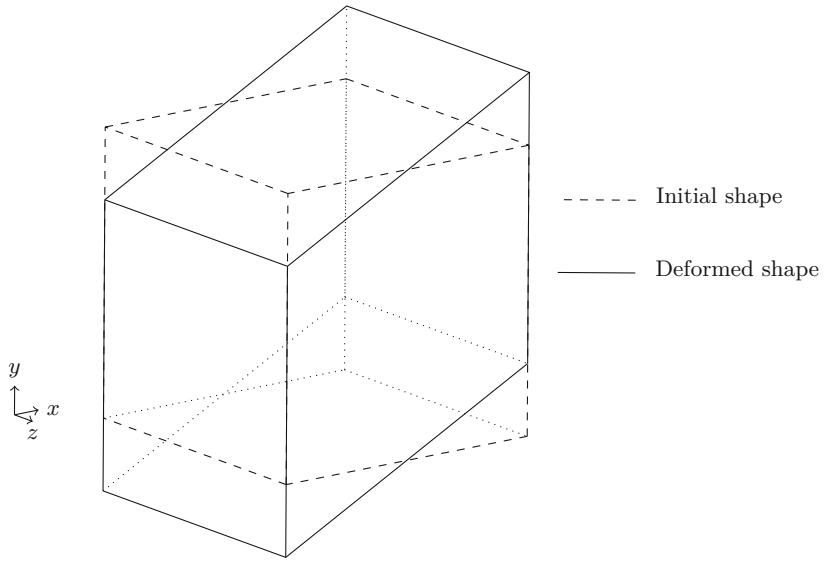


**Fig. 7.5** Case TC6 : initial and deformed cube

Let us calculate the invariants $Z_1$ and $Z_2$ on each plane of the cube. We have the following results

$$\text{On the edges } \{x = \pm 1\} \qquad Z_1 = 1, \qquad Z_2 = 1. \tag{7.18}$$

$$\text{On the edges } \{y - tx = \pm 1\} \qquad Z_1 = \sqrt{1 + t^2} \qquad Z_2 = \frac{2 + t^2}{2\sqrt{1 + t^2}}. \tag{7.19}$$

$$\text{On the edges } \{z = \pm 1\} \qquad Z_1 = 1, \qquad Z_2 = 1 + \frac{t^2}{2}. \tag{7.20}$$

On the edges corresponding to $\{x = \pm 1\}$ there is no variation in area and shear (the edges are just translated). The edges $\{y - tx = \pm 1\}$ are stretched in only one direction and there is a variation in area and shear as in the 2D deformation with $\alpha = 0$. For the edges $\{z = \pm 1\}$ there is variation in shear like in the 2D deformation where $\beta = 0$. For the case test TC7 the deformation of the sphere $\Gamma_t$ is given by thezero level set of

$$\varphi(x, y, z, t) = x^2 + (y - tx)^2 + z^2 - 1.$$

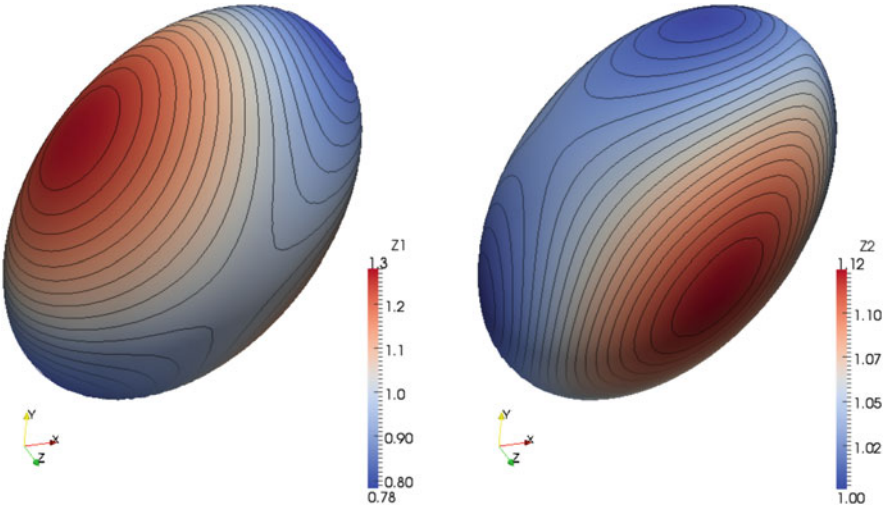


**Fig. 7.6** Case TC7: Level sets of the invariants $Z_1$ and $Z_2$ on the deformed surface at $t = 0.5$

We have

$$Z_1 = \sqrt{1 + t^2 + \frac{t^2(x^2 - z^2) - 2txy}{x^2 + (y - tx)^2 + z^2}}, \tag{7.21}$$

$$Z_2 = \left(1 + \frac{t^2}{2} + \frac{t^2x^2 - 2txy}{2(x^2 + (y - tx)^2 + z^2)}\right)\frac{1}{Z_1}. \tag{7.22}$$

In Fig. 7.6, the iso-level of $Z_1$ and $Z_2$ are plotted on the deformed surface $\Gamma_t$. The results are intuitive: the variation in area reaches its maximum on points along the orthogonal to the $y = tx$ plane, whereas the variation in shear is greater along the $z$ axis.

## 7.3 Justification of the Results Used for the Curves Parameterized in $\mathbb{R}^3$

In this section we are interested to give more precisions on the results used in Sect. 3.4 concerning the parameterized curves. We will first derive an advection equation verified by the invariant $Z_3$ introduced in this section. We will then show that it corresponds to the local variation in length and can be calculated using the gradient of two Level Set functions representing the curve. We will finally see how to approach a line integral by a volume integral and we will calculate the force associated with an elastic curve which responds to a variation in length.

### 7.3.1 Proof of the Results Concerning the Invariant $Z_3$

To begin with, let us recall the definitions given in Sect. 3.4.1. We follow the deformations in an Eulerian way using the backward characteristics which satisfy the following transport equation:

$$\partial_t Y + u \cdot \nabla Y = 0. \tag{7.23}$$

Given an advected curve with tangent vector $\tau_0$ in the initial configuration, the strain tensor along that curve is defined by $\mathcal{L} = \widetilde{M}\widetilde{M}^T$ with

$$\widetilde{M} = [\nabla Y]^{-1}[\tau_0(Y) \otimes \tau_0(Y)].$$

The tensor $\mathcal{L}$ can then be rewritten with the right Cauchy-Green tensor $B = [\nabla Y]^{-1}[\nabla Y]^{-T}$ under the form

$$\mathcal{L} = \frac{\tau \otimes \tau}{(B^{-1}\tau) \cdot \tau}, \tag{7.24}$$

where $\tau$ denotes the tangent vector to the curve in the deformed configuration. The plane orthogonal to $\tau$ is therefore an eigen-space of dimension 2 associated with the eigenvalue 0 of the operator $\mathcal{L}$. The invariant $Z_3$ is now defined by

$$Z_3 = \sqrt{\mathrm{Tr}(\mathcal{L})} = \sqrt{\frac{1}{(B^{-1}\tau) \cdot \tau}}. \tag{7.25}$$

**Proposition 7.5** *Assuming that the vector field $u$ is smooth enough, the invariant $Z_3$ satisfies:*

$$\partial_t Z_3 + u \cdot \nabla Z_3 = Z_3\,[\nabla u] : \mathcal{C}_3, \qquad \mathcal{C}_3 = \tau \otimes \tau. \tag{7.26}$$

***Proof*** Using (7.23) we get

$$\partial_t([\nabla Y]^{-1}) + u \cdot \nabla([\nabla Y]^{-1}) = [\nabla u][\nabla Y]^{-1}. \tag{7.27}$$

We also have with (7.23)

$$\partial_t(\tau_0(Y) \otimes \tau_0(Y)) + u \cdot \nabla(\tau_0(Y) \otimes \tau_0(Y)) = 0.$$

This relation combined with (7.27) gives

$$\partial_t \widetilde{M} + u \cdot \nabla \widetilde{M} = [\nabla u]\widetilde{M}, \qquad \partial_t \widetilde{M}^T + u \cdot \nabla(\widetilde{M}^T) = \widetilde{M}^T[\nabla u]^T. \tag{7.28}$$

Using (7.28) and $\mathcal{L} = \widetilde{M}\widetilde{M}^T$ we get

$$\partial_t \mathcal{L} + u \cdot \nabla \mathcal{L} = [\nabla u]\mathcal{L} + \mathcal{L}[\nabla u]^T, \tag{7.29}$$

where the initial condition is given by $\mathcal{L}(0) = \boldsymbol{\tau}_0 \otimes \boldsymbol{\tau}_0$. One can observe that $B$ satisfies the same equation with a different initial condition $B(0) = \mathbb{I}$. Taking the trace of (7.29), we can write

$$\partial_t \operatorname{Tr}(\mathcal{L}) + u \cdot \nabla \operatorname{Tr}(\mathcal{L}) = 2[\nabla u] : \mathcal{L}. \tag{7.30}$$

We finally obtain from the above equation and (7.25) the desired equation on $Z_3$

$$\partial_t Z_3 + u \cdot \nabla Z_3 = Z_3\, [\nabla u] : \mathcal{C}_3, \qquad \mathcal{C}_3 = \tau \otimes \tau. \tag{7.31}$$

□

Let us now show that $Z_3$ measures the local variation in length.

**Proposition 7.6** *Let $u$ be a smooth velocity field and $\Gamma_0$ a smooth curve, deformed into $\Gamma_t = X(t, \Gamma_0)$. Let $\theta \mapsto \gamma(t, \theta)$ be a parameterization of the curve $\Gamma_t$ with $\gamma : \mathbb{R}^+ \times I \longrightarrow \mathbb{R}^3$ where $I$ is an open set of $\mathbb{R}$. The local variation in length satisfies*

$$\frac{|\partial_\theta \gamma(t, \theta)|}{|\partial_\theta \gamma(0, \theta)|} = \frac{Z_3(\gamma(t, \theta), t)}{Z_3(\gamma(0, \theta), 0)} = \frac{Z_3(x, t)}{Z_3(Y(x, t), 0)} \tag{7.32}$$

*for $x = \gamma(t, \theta)$.*

***Proof*** Let $f : \mathbb{R}^3 \times \mathbb{R}^+ \longrightarrow \mathbb{R}$ be a smooth function. The Reynolds formula for the curves (2.19) reads

$$\frac{\mathrm{d}}{\mathrm{d}t}\left(\int_{\Gamma_t} f\, dl\right) = \int_{\Gamma_t} \partial_t f + u \cdot \nabla f + f[\nabla u] : [\tau \otimes \tau]\, dl.$$

Let $g : \mathbb{R}^3 \longrightarrow \mathbb{R}$ a smooth function and $f(x, t) = \frac{g(Y(x,t))}{Z_3(x,t)}$. The expression under the integral becomes

$$\frac{1}{Z_3}\left(\partial_t (g(Y)) + u \cdot \nabla (g(Y))\right) - \frac{g(Y)}{(Z_3)^2}(\partial_t Z_3 + u \cdot \nabla Z_3 - Z_3[\nabla u] : [\tau \otimes \tau]).$$

Due to (7.23) the first term vanishes. The second also according to Eq. (7.26) in Proposition 7.5. Therefore

$$\frac{\mathrm{d}}{\mathrm{d}t}\left(\int_{\Gamma_t}\frac{g(Y(x,t))}{Z_3(x,t)}\,dl\right)=0. \tag{7.33}$$

As $\gamma(0,\theta)=Y(\gamma(t,\theta),t)$, Eq. (7.33) becomes

$$\int_I \frac{g(\gamma(0,\theta))}{Z_3(\gamma(t,\theta),t)}|\partial_\theta\gamma(t,\theta)|\,d\theta=\int_I\frac{g(\gamma(0,\theta))}{Z_3(\gamma(0,\theta),0)}|\partial_\theta\gamma(0,\theta)|\,d\theta.$$

This result holds for all $g$. We thus obtain (7.32) and $Z_3$ indeed measures the local variation in length (in both the compressible and incompressible cases). □

We now show that the invariant $Z_3$ can be expressed using two Level Set functions and the Jacobian of the change of variable associated with the deformation, still noted $J_e$. Consider two Level Set functions $\varphi^i:\mathbb{R}^3\to\mathbb{R}$ satisfying the equation of transport

$$\partial_t\varphi^i+u\cdot\nabla\varphi^i=0. \tag{7.34}$$

We then have $\varphi^i(x,t)=\varphi_0^i(Y(x,t))$ and the gradient of this relation gives

$$\nabla\varphi^i=[\nabla Y]^T\nabla\varphi_0^i(Y). \tag{7.35}$$

In addition, the tangent to the curve is given by

$$\tau=\frac{\nabla\varphi^1\times\nabla\varphi^2}{|\nabla\varphi^1\times\nabla\varphi^2|}. \tag{7.36}$$

**Proposition 7.7** *Let* $J_e=\det(\nabla Y)^{-1}$. *Then*

$$Z_3=J_e\frac{|\nabla\varphi^1\times\nabla\varphi^2|}{|\nabla\varphi_0^1(Y)\times\nabla\varphi_0^2(Y)|}. \tag{7.37}$$

***Proof*** Combining (7.25), the definition of $B$ and (7.36) we get

$$(Z_3)^{-1}=\sqrt{(B^{-1}\tau)\cdot\tau}=|[\nabla Y]\tau|=\left|[\nabla Y]\frac{\nabla\varphi^1\times\nabla\varphi^2}{|\nabla\varphi^1\times\nabla\varphi^2|}\right|.$$

We obtain the announced result using (7.35) and the relation $A(A^Ta_1\times A^Ta_2)=\det(A^T)(a_1\times a_2)$ (which is nothing but a rewriting of the classical identity $(Aa_1)\times(Aa_2)=\mathrm{Cof}(A)(a_1\times a_2)$). □

### 7.3.2 Area and Co-area Formulas

These formulas generalize the classical formulas for the change of variables which transform integrals between domains of the same dimension.

The so-called area formula concerns the changes of variables for functions of $\mathbb{R}^n \longrightarrow \mathbb{R}^3$ with $n = 1, 2$ or 3. It corresponds to the calculation of volume, surface and line integrals using a parametrization. The co-area formula deals with changes of variables for functions of $\mathbb{R}^3 \longrightarrow \mathbb{R}^p$ with $p = 1, 2$ or 3 and corresponds to the calculation of volume integrals using integrals on level sets. These formulas allow to obtain approximation formulas for surface and line integrals. Results and proofs on the area and co-area formulas can be found in reference works on the subject, for example [58].

In the following propositions, we consider a function $f : \mathbb{R}^3 \mapsto \mathbb{R}$.

**Proposition 7.8** *Let $\theta \mapsto \gamma(\theta)$ be a smooth parametrization of the geometric object under consideration (curve, surface or volume) with $\gamma : U \longrightarrow \mathbb{R}^3$ where $U$ is an open set of $\mathbb{R}^n$ ($n = 1, 2$ or 3). The area formula is:*

$$\int_{\gamma(U)} f = \int_U f(\gamma(\theta))\sqrt{\det([\nabla_\theta \gamma]^T[\nabla_\theta \gamma])}d\theta. \tag{7.38}$$

The matrix $[\nabla_\theta \gamma]$ has size $3 \times n$ and therefore $g(\theta) = [\nabla_\theta \gamma]^T[\nabla_\theta \gamma]$ is an $n \times n$ matrix of general term $g_{ij} = \partial_{\theta_i}\gamma \cdot \partial_{\theta_j}\gamma$. We thus obtain for a curve $\Gamma$ ($n = 1$, $g$ is a scalar) the element of length $\sqrt{\det(g)} = \sqrt{\partial_\theta \gamma \cdot \partial_\theta \gamma} = |\partial_\theta \gamma|$. For a surface $S$ ($n = 2$, $g$ is a $2 \times 2$ matrix) we obtain the surface element $\sqrt{\det(g)} = \sqrt{|\partial_{\theta_1}\gamma|^2|\partial_{\theta_2}\gamma|^2 - (\partial_{\theta_1}\gamma \cdot \partial_{\theta_2}\gamma)^2} = |\partial_{\theta_1}\gamma \times \partial_{\theta_2}\gamma|$. Finally for a volume $\Omega$ ($n = 3$, $g$ is a $3 \times 3$ matrix) we obtain the volume element $\sqrt{\det(g)} = \sqrt{\det([\nabla_\theta \gamma]^T[\nabla_\theta \gamma])} = |\det(\nabla_\theta \gamma)|$.

We now wish to compute the integral of a function on a volume using integrals on the level sets of a vector function $\varphi$.

**Proposition 7.9** *Let us consider a function $\varphi : \mathbb{R}^3 \longrightarrow \mathbb{R}^p$ ($p$ =1,2 or 3). The co-area formula is:*

$$\int_{\mathbb{R}^3} f(x)\sqrt{\det([\nabla_x \varphi][\nabla_x \varphi]^T)}\, dx = \int_{\mathbb{R}^p} \left( \int_{\{\varphi = r\}} f \right) dr. \tag{7.39}$$

The matrix $[\nabla_x \varphi]$ is of size $p \times 3$ and $\widetilde{g}(x) = [\nabla_x \varphi][\nabla_x \varphi]^T$ is a matrix $p \times p$ of general term $\widetilde{g}_{ij} = \nabla_x \varphi^i \cdot \nabla_x \varphi^j$ where we denote by $\varphi^i$ the i-th component of $\varphi$.

In the case $p = 1$, $\widetilde{g}$ is a scalar, $\sqrt{\det(\widetilde{g})} = \sqrt{\nabla_x\varphi \cdot \nabla_x\varphi} = |\nabla_x\varphi|$ and the level sets of $\varphi$ are surfaces.

**Proposition 7.10** *The co-area formula for objects of co-dimension 1 reads*

$$\int_{\mathbb{R}^3} f(x)\,dx = \int_{\mathbb{R}} \left( \int_{\{\varphi = r\}} f(x) |\nabla_x \varphi(x)|^{-1}\,ds \right) dr. \tag{7.40}$$

We recover here the result of Lemma 3.1.
In the case $p = 2$, $\widetilde{g}$ is a $2 \times 2$ matrix and

$$\sqrt{\det(\widetilde{g})} = \sqrt{|\nabla_x\varphi^1|^2|\nabla_x\varphi^2|^2 - (\nabla_x\varphi^1 \cdot \nabla_x\varphi^2)^2} = |\nabla_x\varphi^1 \times \nabla_x\varphi^2|,$$

and the level sets of $\varphi$ are curves.

**Proposition 7.11** *The co-area formula for objects of co-dimension 2 reads*

$$\int_{\mathbb{R}^3} f(x)\,dx = \int_{\mathbb{R}^2} \left( \int_{\{\varphi^1 = r_1\} \cap \{\varphi^2 = r_2\}} f(x) |\nabla_x \varphi^1(x) \times \nabla_x \varphi^2(x)|^{-1}\,dl \right) dr_1\,dr_2 \tag{7.41}$$

In the case $p = 3$, $\widetilde{g}$ is a $3 \times 3$ matrix,

$$\sqrt{\det(\widetilde{g})} = \sqrt{\det([\nabla_x\varphi][\nabla_x\varphi]^T)} = |\det(\nabla_x\varphi)|,$$

and the level sets of $\varphi$ are points. We thus find the classical formula for the change of variables in volume integrals.

### 7.3.3 Volume Approximation of Line Integrals and Calculation of the Elastic Force

We can now deduce a volume approximation formula for a line integral, analogous to formula (1.24) for surface integrals.

**Proposition 7.12** *Let $r \to \zeta(r)$ be a continuous function with support in $[-1, 1]$, such that $\int \zeta(r)\, dr = 1$ and $\varphi^1, \varphi^2$ two functions of class $C^2$ from $\mathbb{R}^3$ to $\mathbb{R}$ such that $|\nabla\varphi^1 \times \nabla\varphi^2(x)| > 0$ for all $x$ in a neighborhood of $\{\varphi^1 = 0\} \cap \{\varphi^2 = 0\}$. We then have*

$$\frac{1}{\varepsilon^2}\zeta\left(\frac{\varphi^1}{\varepsilon}\right)\zeta\left(\frac{\varphi^2}{\varepsilon}\right)|\nabla\varphi^1 \times \nabla\varphi^2| \underset{\varepsilon\to 0}{\rightharpoonup} \delta_{\{\varphi^1=0\}\cap\{\varphi^2=0\}} \tag{7.42}$$

*in the space of measures.*

***Proof*** Under the assumptions made on $\zeta$, we have for any continuous function $g : \mathbb{R}^2 \longrightarrow \mathbb{R}$, using a simple change of variable and the dominated convergence theorem

$$\int_{\mathbb{R}^2} \frac{1}{\varepsilon^2}\zeta\left(\frac{r_1}{\varepsilon}\right)\zeta\left(\frac{r_2}{\varepsilon}\right) g(r_1, r_2)\, dr_1\, dr_2 \underset{\varepsilon\longrightarrow 0}{\longrightarrow} g(0, 0). \tag{7.43}$$

This property states the weak convergence towards the two-dimensional Dirac mass at the point $(0, 0)$. Applying the previous formula to

$$g(r_1, r_2) = \int_{\{\varphi^1=r_1\}\cap\{\varphi^2=r_2\}} f(x)\, dl$$

and using the co-area formula (7.41) in Proposition 7.11 we get

$$\begin{aligned}\int_{\mathbb{R}^2}\int_{\{\varphi^1=r_1\}\cap\{\varphi^2=r_2\}} f(x)\frac{1}{\varepsilon^2}\zeta\left(\frac{\varphi^1(x)}{\varepsilon}\right)\zeta\left(\frac{\varphi^2(x)}{\varepsilon}\right) dl\, dr_1\, dr_2 \\ = \int_{\mathbb{R}^3} f(x)|\nabla\varphi^1(x) \times \nabla\varphi^2(x)|\frac{1}{\varepsilon^2}\zeta\left(\frac{\varphi^1(x)}{\varepsilon}\right)\zeta\left(\frac{\varphi^2(x)}{\varepsilon}\right) dx \\ \underset{\varepsilon\longrightarrow 0}{\longrightarrow} \int_{\{\varphi^1=0\}\cap\{\varphi^2=0\}} f(x)\, dl. \end{aligned} \tag{7.44}$$

which ends the proof. □

Recall that the evolution of the elastic curve is captured by two Level Set functions $\varphi^1, \varphi^2$ which are transported by the velocity field $u$. Moreover, according to Proposition 7.6 the invariant $Z_3$ measures the local variation of the length of the curve and, following Proposition 7.7, can be written using the gradient of these Level Set functions. We now introduce the regularized energy:

$$\mathcal{E}_3 = \int_\Omega E_3(Z_3)\frac{1}{\varepsilon^2}\zeta\left(\frac{\varphi^1}{\varepsilon}\right)\zeta\left(\frac{\varphi^2}{\varepsilon}\right) dx. \tag{7.45}$$

where $\mathcal{E}_3$ is the constitutive law associated with the invariant $Z_3$. The force associated with this energy is given by the following proposition:

**Proposition 7.13** *The principle of virtual work makes it possible to write the temporal variation of* $\mathcal{E}_3$ *as*

$$\partial_t \mathcal{E}_3 = -\int_\Omega F_3 \cdot u \, dx. \tag{7.46}$$

*This leads to the following expression of the force*

$$F_3 = \nabla\left(E_3(Z_3)\frac{1}{\varepsilon^2}\zeta\left(\frac{\varphi^1}{\varepsilon}\right)\zeta\left(\frac{\varphi^2}{\varepsilon}\right)\right) + \operatorname{div}\left(E_3'(Z_3)Z_3\,\mathcal{C}_3\frac{1}{\varepsilon^2}\zeta\left(\frac{\varphi^1}{\varepsilon}\right)\zeta\left(\frac{\varphi^2}{\varepsilon}\right)\right), \tag{7.47}$$

*with* $\mathcal{C}_3 = \tau \otimes \tau$.

***Proof*** After differentiating with respect to $t$ we get

$$\partial_t \mathcal{E}_3 = \int_\Omega E_3'(Z_3)\partial_t(Z_3)\frac{1}{\varepsilon^2}\zeta\left(\frac{\varphi^1}{\varepsilon}\right)\zeta\left(\frac{\varphi^2}{\varepsilon}\right)dx + \int_\Omega E_3(Z_3)\frac{1}{\varepsilon^2}\zeta'\left(\frac{\varphi^1}{\varepsilon}\right)\partial_t\varphi^1\frac{1}{\varepsilon}\zeta\left(\frac{\varphi^2}{\varepsilon}\right)dx + \int_\Omega E_3(Z_3)\frac{1}{\varepsilon}\zeta\left(\frac{\varphi^1}{\varepsilon}\right)\frac{1}{\varepsilon^2}\zeta'\left(\frac{\varphi^2}{\varepsilon}\right)\partial_t\varphi^2\,dx.$$

Using the transport equations on $\varphi^1$ and $\varphi^2$ as well as the relation (7.26) from Proposition 7.5 we get

$$\partial_t \mathcal{E}_3 = \int_\Omega E_3'(Z_3)(-u\cdot\nabla Z_3 + [\nabla u] : Z_3\mathcal{C}_3)\frac{1}{\varepsilon^2}\zeta\left(\frac{\varphi^1}{\varepsilon}\right)\zeta\left(\frac{\varphi^2}{\varepsilon}\right)dx + \int_\Omega E_3(Z_3)\frac{1}{\varepsilon^2}\zeta'\left(\frac{\varphi^1}{\varepsilon}\right)(-u\cdot\nabla\varphi^1)\frac{1}{\varepsilon}\zeta\left(\frac{\varphi^2}{\varepsilon}\right)dx + \int_\Omega E_3(Z_3)\frac{1}{\varepsilon}\zeta\left(\frac{\varphi^1}{\varepsilon}\right)\frac{1}{\varepsilon^2}\zeta'\left(\frac{\varphi^2}{\varepsilon}\right)(-u\cdot\nabla\varphi^2)\,dx.$$

By integrating the second term by parts (the integral over $\partial\Omega$ vanishes because $\zeta(\frac{\varphi^i}{\varepsilon}) = 0$ on $\partial\Omega$)

$$\partial_t \mathcal{E}_3 = -\int_\Omega u \cdot \nabla(E_3(Z_3))\frac{1}{\varepsilon^2}\zeta\left(\frac{\varphi^1}{\varepsilon}\right)\zeta\left(\frac{\varphi^2}{\varepsilon}\right) + \operatorname{div}\left(E_3'(Z_3)Z_3\mathcal{C}_3\frac{1}{\varepsilon^2}\zeta\left(\frac{\varphi^1}{\varepsilon}\right)\zeta\left(\frac{\varphi^2}{\varepsilon}\right)\right)\cdot u + E_3(Z_3)u\cdot\nabla\left(\frac{1}{\varepsilon^2}\zeta\left(\frac{\varphi^1}{\varepsilon}\right)\zeta\left(\frac{\varphi^2}{\varepsilon}\right)\right)dx.$$

Combining the first and last terms and using (7.46) we get the desired result. □

The following proposition allows to decompose the force $F_3$ according to its normal and tangential components.

**Proposition 7.14** *The force $F_3$ defined by (7.47) can be recast, up to a gradient term, under the form*

$$F_3 = \left(\left(\nabla\left(\tilde{E_3'}\right)\cdot\tau\right)\tau + \tilde{E_3'}Hn\right)|\nabla\varphi^1\times\nabla\varphi^2|\frac{1}{\varepsilon^2}\zeta\left(\frac{\varphi^1}{\varepsilon}\right)\zeta\left(\frac{\varphi^2}{\varepsilon}\right). \tag{7.48}$$

*where* $\tilde{E_3'} = \frac{E_3'(Z_3)J_e}{|\nabla\varphi_0^1(Y)\times\nabla\varphi_0^2(Y)|}$

***Proof*** By developing the divergence term in the expression (7.47) and by using the fact that, by (7.36), $(\tau\otimes\tau)\nabla\varphi^i = 0$, we obtain that the force can be written

$$F_3 = A\frac{1}{\varepsilon^2}\zeta\left(\frac{\varphi^1}{\varepsilon}\right)\zeta\left(\frac{\varphi^2}{\varepsilon}\right)$$

with $A = \operatorname{div}(E_3'(Z_3)Z_3\tau\otimes\tau)$. Upon expanding $A$ and using (1.19), we get

$$A = E_3'(Z_3)Z_3Hn + (E_3'(Z_3)Z_3\operatorname{div}(\tau) + \nabla(E_3'(Z_3)\,Z_3)\cdot\tau)\tau. \tag{7.49}$$

Next, we develop the term $\operatorname{div}(\tau)$ with (7.36) :

$$\operatorname{div}(\tau) = \operatorname{div}\left(\frac{\nabla\varphi^1\times\nabla\varphi^2}{|\nabla\varphi^1\times\nabla\varphi^2|}\right) = \frac{\operatorname{div}\left(\nabla\varphi^1\times\nabla\varphi^2\right)}{|\nabla\varphi^1\times\nabla\varphi^2|} - \frac{\nabla(|\nabla\varphi^1\times\nabla\varphi^2|)}{|\nabla\varphi^1\times\nabla\varphi^2|}\cdot\tau. \tag{7.50}$$

The first term is zero because we have

$$\operatorname{div}(\nabla\varphi^1 \times \nabla\varphi^2) = -\nabla\varphi^1 \cdot \nabla \times (\nabla\varphi^2) + \nabla\varphi^2 \cdot \nabla \times (\nabla\varphi^1) = 0. \tag{7.51}$$

Using the relation on $Z_3$ (7.37), we develop the expression $\nabla(E_3'(Z_3)\, Z_3)$ to get

$$\nabla(E_3'(Z_3)\, Z_3) \cdot \tau = \nabla\left(\frac{E_3'(Z_3) J_e}{|\nabla\varphi_0^1(Y) \times \nabla\varphi_0^2(Y)|}\right) \cdot \tau\, |\nabla\varphi^1 \times \nabla\varphi^2| + \frac{E_3'(Z_3) J_e}{|\nabla\varphi_0^1(Y) \times \nabla\varphi_0^2(Y)|} \nabla(|\nabla\varphi^1 \times \nabla\varphi^2|) \cdot \tau$$

Using (7.50) for the second term and the expression of $Z_3$ (7.37) we get

$$\nabla(E_3'(Z_3)\, Z_3) \cdot \tau = \nabla\left(\frac{E_3'(Z_3) J_e}{|\nabla\varphi_0^1(Y) \times \nabla\varphi_0^2(Y)|}\right) \cdot \tau\, |\nabla\varphi^1 \times \nabla\varphi^2| - E_3'(Z_3) Z_3 \operatorname{div}(\tau)$$

Injecting this formula in the expression of $A$ (7.49) gives the final result.

It is interesting to note that the force decomposes only in the basis $(\tau, n)$ and has no component following the binormal vector $b$. Moreover, this decomposition is similar to the expression (3.18) obtained for surfaces. □

## 7.4 WENO Schemes for the Transport Equation

At the heart of the methods presented in this book lies a transport equation of a (possibly multi-dimensional) Level Set function which records the deformations of the medium during its motion along a velocity field calculated by other means. It is therefore important to solve this equation as accurately as possible on Cartesian grids (or on grids that can be reduced to Cartesian grids by changes of variables) encompassing the fluid-solid systems under consideration.

We focus here on finite difference methods as they are routinely used. Many numerical schemes exist for the transport equation: the upwind scheme is the most natural one, but often proves to be too diffusive. The Lax–Wendroff scheme is, on the one hand, more complicated to write in more than one dimension and, on the other hand, generates oscillations around sharp variations of the solution. The method of characteristics suffers from the same defect because of the interpolation involved in its implementation.

In the mid-1980s nonlinear schemes generalizing the upwind scheme were introduced by Harten et al. [83]. These schemes take into account the local smoothity of the numerical solution to determine at which points the finite differences must

be calculated. This idea led to the so-called ENO (for Essentially Non Oscillatory) schemes. Subsequently, the WENO (Weighted Essentially Non Oscillatory) schemes, which consist of taking an optimal combination of discretization stencils, were introduced [90, 129] and then developed in numerous variations [3, 29, 127].

To understand how WENO schemes work, let us consider the one dimensional case, and start from the semi-discrete transport equation

$$\frac{\varphi^{n+1} - \varphi^n}{\Delta t} + u^n \partial_x \varphi^n = 0. \tag{7.52}$$

At node $i$ of a discretization of the domain, the equation is therefore

$$\frac{\varphi_i^{n+1} - \varphi_i^n}{\Delta t} + u_i^n (\partial_x \varphi)_i^n = 0. \tag{7.53}$$

The upwind scheme simply consists in approximating the $x$-derivative of $\varphi$ at node $i$ taking into account the sign of $u_i$. We set $(\partial_x \varphi^-)_i = \frac{\varphi_i - \varphi_{i-1}}{\Delta x}$ and $(\partial_x \varphi^+)_i = \frac{\varphi_{i+1} - \varphi_i}{\Delta x}$ and we write (omitting the superscript $n$)

$$(\varphi_x)_i \approx \begin{cases} (\partial_x \varphi^-)_i & \text{if } u_i > 0, \\ (\partial_x \varphi^+)_i & \text{if } u_i < 0. \end{cases} \tag{7.54}$$

given that the value chosen when $u_i = 0$ does not matter in (7.53). This scheme is stable under the Courant–Friedrichs–Lewy (CFL) condition.

$$\Delta t < \frac{\Delta x}{\max |u|}. \tag{7.55}$$

The WENO scheme we consider in the sequel is of fifth order and uses the values

$$\{\varphi_{i-3}, \varphi_{i-2}, \varphi_{i-1}, \varphi_i, \varphi_{i+1}, \varphi_{i+2}\}$$

to determine an approximation of $(\partial_x \varphi^-)_i$ and

$$\{\varphi_{i-2}, \varphi_{i-1}, \varphi_i, \varphi_{i+1}, \varphi_{i+2}, \varphi_{i+3}\}$$

for $(\partial_x \varphi^+)_i$. Following [129], we set

$$v_1 = \frac{\varphi_{i-2} - \varphi_{i-3}}{\Delta x}, \quad v_2 = \frac{\varphi_{i-1} - \varphi_{i-2}}{\Delta x}, \quad v_3 = \frac{\varphi_i - \varphi_{i-1}}{\Delta x},$$
$$v_4 = \frac{\varphi_{i+1} - \varphi_i}{\Delta x}, \quad v_5 = \frac{\varphi_{i+2} - \varphi_{i+1}}{\Delta x}.$$

Then

$$\partial_x\varphi^1 = \frac{v_1}{3} - \frac{7v_2}{6} + \frac{11v_3}{6}, \quad \partial_x\varphi^2 = -\frac{v_2}{6} + \frac{5v_3}{6} + \frac{v_4}{3}, \quad \partial_x\varphi^3 = \frac{v_3}{3} + \frac{5v_4}{6} - \frac{v_5}{6},$$

are third-order approximations of $\partial_x\varphi^-$. A third-order ENO scheme would choose the best of these approximations by means of a criterion minimizing the third-order divided differences of $\varphi$. Doing so, we get a third order scheme. It was however noticed that by taking an optimal convex combination of the three quantities above to approximate $\partial_x\varphi^-$, one could reach fifth order in regions where $\varphi$ is smooth.

We therefore take an approximation of the form

$$(\partial_x\varphi^-)_i \approx \omega_1\partial_x\varphi^1 + \omega_2\partial_x\varphi^2 + \omega_3\partial_x\varphi^3,$$

where $0 \leq \omega_k \leq 1$ are some weights satisfying $\omega_1 + \omega_2 + \omega_3 = 1$. In regions where $\varphi$ is smooth, it can be easily checked that the optimal choice is $\omega_1 = 0.1$, $\omega_2 = 0.6$ et $\omega_3 = 0.3$. However this choice can turn out to be catastrophic when $\varphi$ is not smooth enough. In this case the original ENO scheme, corresponding to one coefficient equal to 1, and the others equal to zero, would perform better. This remark led to the determination of the weights $\omega_k$ on the basis of some smoothness indicators of the numerical solution.

More precisely, [129] first writes

$$S_1 = \frac{13}{12}(v_1 - 2v_2 + v_3)^2 + \frac{1}{4}(v_1 - 4v_2 + 3v_3)^2, \tag{7.56}$$

$$S_2 = \frac{13}{12}(v_2 - 2v_3 + v_4)^2 + \frac{1}{4}(v_2 - v_4)^2, \tag{7.57}$$

$$S_3 = \frac{13}{12}(v_3 - 2v_4 + v_5)^2 + \frac{1}{4}(3v_3 - 4v_4 + v_5)^2, \tag{7.58}$$

and then defines

$$\alpha_1 = \frac{0.1}{(S_1 + \varepsilon)^2}, \quad \alpha_2 = \frac{0.6}{(S_2 + \varepsilon)^2}, \quad \alpha_3 = \frac{0.3}{(S_3 + \varepsilon)^2},$$

where $\varepsilon > 0$ is a (very) small parameter (for example $\varepsilon = 10^{-6}\max\{v_k^2\} + 10^{-99}$), and finally consider the weights

$$\omega_k = \frac{\alpha_k}{\alpha_1 + \alpha_2 + \alpha_3}, \quad k = 1, 2, 3.$$

These choices give the quasi-optimal weights in the regions where $\varphi$ is smooth, and reproduce an ENO scheme behavior elsewhere. As an example, Fig. 7.7 shows the results obtained by several schemes for the simulation of the one-dimensional transport equation of a prototype function of a distance function. We took in these

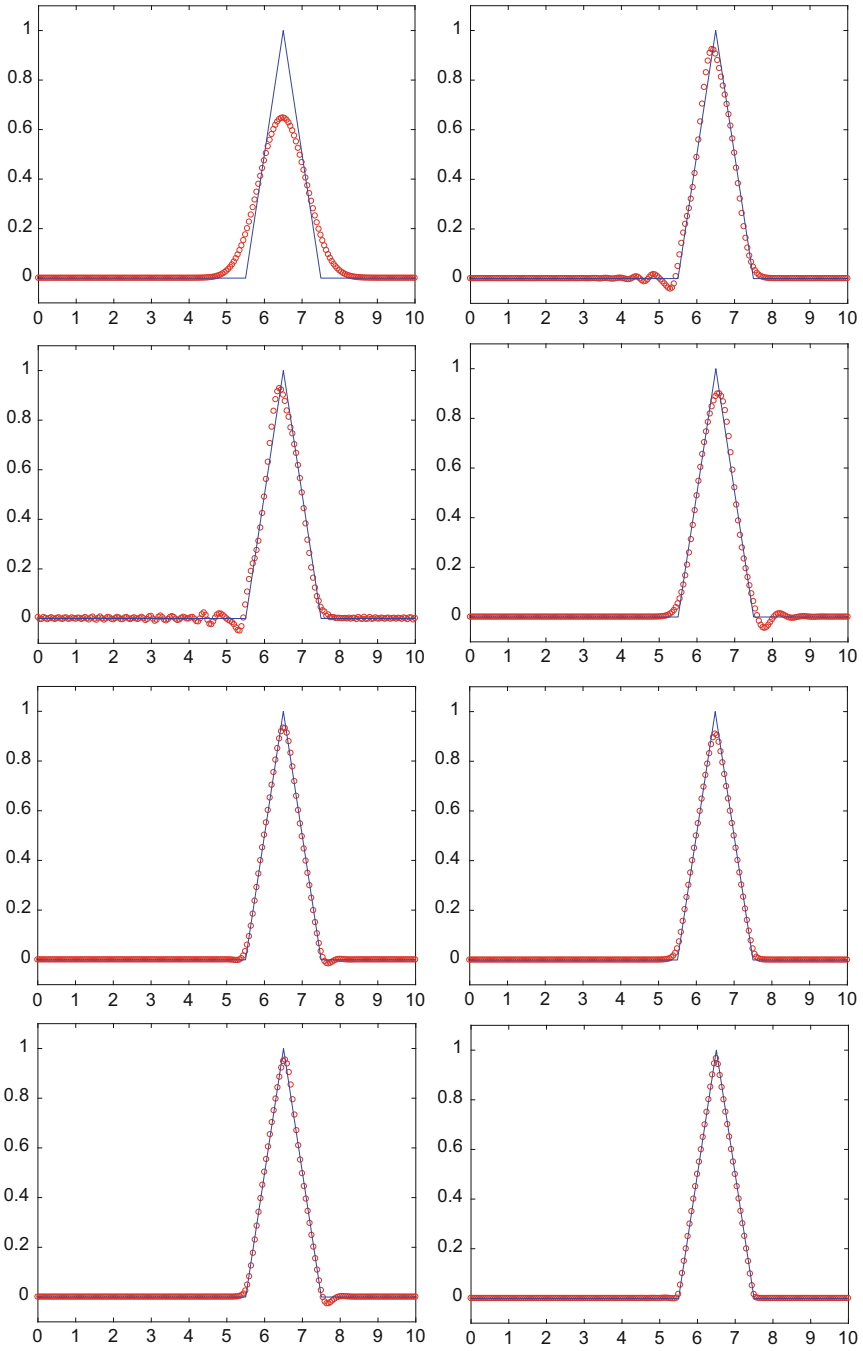


**Fig. 7.7** Illustration of several advection schemes for the transport of a distance function. From left to right, top to bottom, comparison of the exact solution (continuous line) to the upwind, Lax–Wendroff, centered-RK3, Beam-Warming, Fromm, ENO2, ENO3, WENO5 schemes (circles)

examples 200 discretization points on the interval [0, 10], a CFL number equal to 0.2 and a final time $t = 5$ which corresponds to the transport of the solution over half of the domain. The choice of this small CFL number is explained by the fact that in practice the time step is not often imposed by the transport equation, but rather by the diffusion, for an explicit time-stepping, or by the fluid-structure coupling in case of a stiff interface. It is therefore important that the interface transport scheme is not too diffusive at low CFL.

The time-stepping scheme used in this example is an Euler scheme for all the spatial discretizations, with the exception of the centered discretization which is stabilized by an RK3 time-stepping. The WENO scheme performs clearly better than all other schemes, including the sophisticated Fromm and Beam-Warming schemes. We also note that the (W)ENO schemes, like the upstream scheme on which they are based, are the only ones to avoid any post or pre-oscillations.

## 7.5 Some Ideas to Go Further

We list in this section a number of problems that we found interesting for future research. The semi-implicit schemes that we have presented to stabilize the coupling between an elastic membrane and a fluid are currently limited to the case of co-dimension 1 and for energies that depend only on the change of area. Their extension to membranes with shear and to more general elastic solids would make it possible to stabilize the coupling schemes in all cases of fluid-structure interaction. Cases where one has to deal with structures with large stiffness, such as that of the flapping of the elastic rod shown in Sect. 4.3.2, would clearly benefit from such an extension.

The effects of added mass in the problems of fluid-structure coupling under ALE (Arbitrary Langrangian Eulerian) formulation, that is to say where the fluid is treated in Eulerian coordinates and the solid in Lagrangian coordinates, are known in their formulation with explicit time-discretization of the coupling to be very sensitive to added mass effects [32]. This is particularly striking when the density of the immersed structure is close to that of the fluid, which is often the case in biomechanical applications, for example. Essentially it comes from the decoupling of the inertia of the structure and the fluid in the explanation of the numerical scheme. At the cost of many efforts [64, 67, 69] this problem could be circumvented while avoiding a completely implicit resolution. Note that in the case of the completely Eulerian coupling, the inertia part is solved simultaneously for the solid and the fluid, even in the case of a completely explicit scheme. The effects of added mass should therefore be less significant. However, we do not know of any proof of this intuition.

Another case concerns the problems of interface displacements on manifolds, and the associated coupling problems. In [100] the displacement of a curve on a fixed surface is considered, in order to minimize its length. Rather than opting for a general Eulerian representation of curves in space introduced in Sect. 3.4, because the load-bearing surface is fixed a parametric representation of it is used. The curve

is then captured in the parameter space, and the energy is expressed thanks to this representation. The dimension of the resulting problem corresponds to that of the manifold on which the curve moves, and not of the ambient space. Beyond this isoperimetric problem on a manifold, to our knowledge the study of more general energies for problems of flows on surfaces or fluid-structure couplings in this context has not been carried out.

Beyond the fluid-structure interactions, one can make a link between problems of the optimal transport type and the Eulerian mechanics presented in these pages. Indeed, from a measure theory point of view, formula (3.9) simply translates the fact that the measure $|\nabla\varphi_0|^{-1}(x)\delta_{\{\varphi_0=0\}}$ is the push-forward (denoted by #) of the measure $|\nabla\varphi|^{-1}(x,t)\delta_{\{\varphi=0\}}$ by $x \to Y(x,t)$. One thus could reformulate the problem of finding the equilibrium form of an immersed membrane, represented by the Level Set $\varphi$, as minimizing the elastic energy (3.12) among all the functions $\varphi$ verifying $Y\#|\nabla\varphi|^{-1}\delta_{\{\varphi=0\}} = |\nabla\varphi_0|^{-1}\delta_{\{\varphi_0=0\}}$ for a certain field $Y$.

Following [22], this can be formulated as the steady state solution of the problem

$$\partial_t Y + (u\cdot\nabla)Y = 0, \qquad \varphi = \varphi^0(Y),$$

$$-\Delta u + \nabla p = \operatorname{div}\left(E'(|\nabla\varphi|)|\nabla\varphi|\frac{\nabla\varphi\otimes\nabla\varphi}{|\nabla\varphi|^2}\frac{1}{\varepsilon}\zeta\left(\frac{\varphi}{\varepsilon}\right)\right), \quad \operatorname{div} u = 0,$$

with the initial condition $Y(0,x) = x$ and an homogeneous Dirichlet boundary condition on $u$.

Finally, a more general and far reaching class of questions that deserves to be studied concerns the comparison in terms of cost/performance of the methods seen in this book with ALE-type methods. As we have already said, the interest of Level Set methods, and more generally of immersed boundary methods, is a simple consideration of continuity conditions and the possibility of using fast solvers on regular grids. The price to pay is a less precise tracking of the interfaces and the forces they support compared to methods whose meshes are based on these interfaces. To truly and fairly compare the methods, it is necessary to be able to evaluate, with equal or comparable results, the cost of the calculations relating to them, possibly taking into account the efficiency of the parallel implementation of the different algorithms. A first step must consist in choosing test cases which are relevant for the two classes of methods, and in defining a measure of the quality of the results obtained.

# Credits of Figures Reproduced with Permission

Figure 1.3 was published in Springer Science and Business Media, 153, S. Osher and R. Fedkiw, Level set methods and dynamic implicit surfaces, Copyright Springer (2006).

Figures 1.5 and 1.6 were published in Mathematical models and methods in applied sciences, 16(03), G.-H. Cottet and E. Maitre, A level set method for fluid-structure interactions with immersed surfaces, 415–438, Copyright World Scientific Publishing (2006).

Figures 3.9, 3.10, 3.11, 3.12 were published in Journal of Computational Physics, 314, G.-H. Cottet and E. Maitre, A semi-implicit level set method for multiphase flows and fluid–structure interaction problems, 80–92, Copyright Elsevier (2016).

Figure 3.15 was published in Physica D : Nonlinear Phenomena, 241(13), E. Maitre, C. Misbah, P. Peyla, and A. Raoult, Comparison between advected-field and level-set methods in the study of vesicle dynamics, 1146–1157, Copyright Elsevier (2012).

Figures 3.16 and 4.11 were published in Mathematical and Computer Modelling, 49(11), E. Maitre, T. Milcent, G.-H. Cottet, A. Raoult, and Y. Usson, Applications of level set methods in computational biophysics, 2161–2169, Copyright Elsevier (2019).

Figures 3.3, 3.4, 3.5, 3.6, 3.7, 3.8 and 3.18, 3.19, 3.20, 3.21, 3.22, 3.23, 3.24 were published in Communications in Mathematical Sciences, 14(3), T. Milcent and E. Maitre, Eulerian model of immersed elastic surfaces with full membrane elasticity, 857–881, Copyright International Press of Boston, Inc (2016).

Figures 4.3, 4.9 and 4.10 were published in Water Waves, 2(2), J. Deborde, T. Milcent, P. Lubin, and S. Glockner, Numerical simulations of the interaction of solitary waves and elastic structures with a fully Eulerian method, 433–466, Copyright Springer (2020).

Figure 4.14 was published in Journal of Computational Physics, 313, A. de Brauer, A. Iollo, and T. Milcent, A Cartesian scheme for compressible multimaterial models in 3d, 121–143, Copyright Elsevier (2016).



G.-H. Cottet et al., *Level Set Methods for Fluid-Structure Interaction*, Applied Mathematical Sciences 210, https://doi.org/10.1007/978-3-031-08659-5

# References


1. R. Abgrall. How to prevent pressure oscillations in multicomponent flow calculations: a quasi-conservative approach. *Journal of Computational Physics*, 125:150–160, 1996.
2. R. Abgrall and S. Karni. Computations of compressible multifluids. *Journal of Computational Physics*, 169(2):594–623, 2001.
3. F. Acker, R. d. R. Borges, and B. Costa. An improved WENO-Z scheme. *Journal of Computational Physics*, 313:726–753, 2016.
4. G. Allaire, F. Jouve, and A.-M. Toader. Structural optimization using sensitivity analysis and a level-set method. *Journal of Computational Physics*, 194:363–393, 2004.
5. P. Angot, C.-H. Bruneau, and P. Fabrie. A penalization method to take into account obstacles in incompressible viscous flows. *Numerische Mathematik*, 81(4):497–520, 1999.
6. T.-D. Aslam. A partial differential equation approach to multidimensional extrapolation. *Journal of Computational Physics*, 193:349–355, 2003.
7. S. Balachandar and J. K. Eaton. Turbulent dispersed multiphase flow. *Annual Review of Fluid Mechanics*, 42:11–133, 2010.
8. J. T. Beale and J. Strain. Locally corrected semi-Lagrangian methods for stokes flow with moving elastic interfaces. *Journal of Computational Physics*, 227(8):3896– 920, 2008.
9. C. Bernier, M. Gazzola, R. Ronsse, and P. Chatelain. Simulations of propelling and energy harvesting articulated bodies via vortex particle-mesh methods. *Journal of Computational Physics*, 392:34–55, 2019.
10. R. Bhardwaj and R. Mittal. Benchmarking a coupled immersed-boundary-finite-element solver for large-scale flow-induced deformation. *AIAA Journal, Technical notes*, 50, 2012.
11. T. Biben, K. Kassner, and C. Misbah. Phase-field approach to three-dimensional vesicle dynamics. *Physical Review E*, 72(4):041921, 2005.
12. T. Biben and C. Misbah. An advected-field method for deformable entities under flow. *The European Physical Journal B-Condensed Matter and Complex Systems*, 29(2):311–316, 2002.
13. T. Biben and C. Misbah. Tumbling of vesicles under shear flow within an advected-field approach. *Physical Review E*, 67(3):031908, 2003.
14. D. Boffi, L. Gastaldi, and L. Heltai. Stability results and algorithmic strategies for the finite element approach to the immersed boundary method. In *Numerical mathematics and advanced applications*, pages 575–582. Springer, 2006.
15. D. Boffi, L. Gastaldi, and L. Heltai. Numerical stability of the finite element immersed boundary method. *Mathematical Models and Methods in Applied Sciences*, 17(10):1479–1505, 2007.




G.-H. Cottet et al., *Level Set Methods for Fluid-Structure Interaction*, Applied Mathematical Sciences 210, https://doi.org/10.1007/978-3-031-08659-5

16. D. Boffi, L. Gastaldi, L. Heltai, and C. S. Peskin. On the hyper-elastic formulation of the immersed boundary method. *Computer Methods in Applied Mechanics and Engineering*, 197(25):2210–2231, 2008.
17. J. A. Bogovic, J. L. Prince, and P.-L. Bazin. A multiple object geometric deformable model for image segmentation. *Computer Vision and Image Understanding*, 117(2):145–157, 2013.
18. L. Boilevin-Kayl, M. A. Fernández, and J.-F. Gerbeau. A loosely coupled scheme for fictitious domain approximations of fluid-structure interaction problems with immersed thin-walled structures. *SIAM Journal on Scientific Computing*, 41(2):B351–B374, 2019.
19. C. Bost, G.-H. Cottet, and E. Maitre. Linear stability analysis of a Level Set model of immersed elastic membrane. Unpublished. *Preprint HAL* http://hal.archives-ouvertes.fr/hal-00388528/PDF/stability.pdf, 2009.
20. C. Bost, G.-H. Cottet, and E. Maitre. Convergence analysis of a penalization method for the three-dimensional motion of a rigid body in an incompressible viscous fluid. *SIAM Journal on Numerical Analysis*, 48(4):1313–1337, 2010.
21. J. Brackbill, D. B. Kothe, and C. Zemach. A continuum method for modeling surface tension. *Journal of computational physics*, 100(2):335–354, 1992.
22. Y. Brenier. Optimal transport, convection, magnetic relaxation and generalized Boussinesq equations. *Journal of nonlinear science*, 19(5):547–570, 2009.
23. D. Bresch, T. Colin, E. Grenier, B. Ribba, and O. Saut. Computational modeling of solid tumor growth: the avascular stage. *SIAM Journal on Scientific Computing*, 32(4):2321–2344, 2010.
24. P. Burchard, L.-T. Cheng, B. Merriman, and S. Osher. Motion of curves in three spatial dimensions using a level set approach. *Journal of Computational Physics*, 170(2):720–741, 2001.
25. L. Caffarelli, R. Kohn, and L. Nirenberg. Partial regularity of suitable weak solutions of the Navier–Stokes equations. *Communications on pure and applied mathematics*, 35(6):771–831, 1982.
26. J.-P. Caltagirone. Sur l'interaction fluide-milieu poreux; application au calcul des efforts exercés sur un obstacle par un fluide visqueux. *Comptes rendus de l'Académie des sciences. Série II, Mécanique, physique, chimie, astronomie*, 318(5):571–577, 1994.
27. M.-P. Cani and M. Debrun. Animation of deformable objects using implicit surfaces. *IEEE Trans. Visualization Comput. Graphics*, 3(1):39–50, 1997.
28. H. Cartan. *Cours de calcul différentiel*. Hermann, 1977.
29. M. Castro, B. Costa, and W. S. Don. High order weighted essentially non-oscillatory WENO-Z schemes for hyperbolic conservation laws. *Journal of Computational Physics*, 230(5):1766–1792, 2011.
30. Y. Chang, T. Hou, B. Merriman, and S. Osher. A level set formulation of Eulerian interface capturing methods for incompressible fluid flows. *Journal of Computational Physics*, 124:449–464, 1996.
31. L.-T. Cheng and Y.-H. Tsai. Redistancing by flow of time dependent Eikonal equation. *Journal of Computational Physics*, 227(8):4002–4017, 2008.
32. C. Conca, A. Osses, and J. Planchard. Added mass and damping in fluid-structure interaction. *Computer methods in applied mechanics and engineering*, 146(3):387–405, 1997.
33. M. Coquerelle. *Calcul d'interaction fluide-structure par méthode vortex et application à la synthèse d'images*. Thèse de doctorat, Université Grenoble Alpes, 2008.
34. M. Coquerelle and G.-H. Cottet. A vortex level set method for the two-way coupling of an incompressible fluid with colliding rigid bodies. *Journal of Computational Physics*, 227(21):9121–9137, 2008.
35. G.-H. Cottet and E. Maitre. A level-set formulation of immersed boundary methods for fluid–structure interaction problems. *C.R. Mathématique*, 338(7):581–586, 2004.
36. G.-H. Cottet and E. Maitre. A level set method for fluid-structure interactions with immersed surfaces. *Mathematical models and methods in applied sciences*, 16(03):415–438, 2006.
37. G.-H. Cottet and E. Maitre. A semi-implicit level set method for multiphase flows and fluid–structure interaction problems. *Journal of Computational Physics*, 314:80–92, 2016.

38. G.-H. Cottet, E. Maitre, and T. Milcent. Eulerian formulation and level set models for incompressible fluid-structure interaction. *ESAIM: Mathematical Modelling and Numerical Analysis*, 42(3):471–492, May 2008.
39. S. Dance and M. Maxey. Incorporation of lubrication effects into the force-coupling method for particulate two-phase flow. *Journal of Comp. Physics*, 189(1):212–238, 2003.
40. C. Dapogny, C. Dobrzynski, and P. Frey. Three-dimensional adaptive domain remeshing, implicit domain meshing, and applications to free and moving boundary problems. *Journal of Computational Physics*, 252:358–378, 2014.
41. C. Dapogny and P. Frey. Computation of the signed distance function to a discrete contour on adapted triangulation. *Calcolo*, 49(3):193–219, 2012.
42. A. de Brauer. *Simulation de modèles multi-matériaux sur maillage cartésien*. Thèse de doctorat, Université de Bordeaux, 2015.
43. A. de Brauer, A. Iollo, and T. Milcent. A Cartesian scheme for compressible multimaterial models in 3d. *Journal of Computational Physics*, 313:121–143, 2016.
44. A. de Brauer, A. Iollo, and T. Milcent. A Cartesian scheme for compressible multimaterial hyperelastic models with plasticity. *Communications in Computational Physics*, 22(5):1362–1384, 2017.
45. J. Deborde. *Modélisation et simulation de l'interaction fluide-structure élastique : application à l'atténuation des vagues*. Thèse de doctorat, Université de Bordeaux, 2017.
46. J. Deborde, T. Milcent, P. Lubin, and S. Glockner. Numerical simulations of the interaction of solitary waves and elastic structures with a fully Eulerian method. *Water Waves*, 2(2):433–466, 2020.
47. M. C. Delfour and J.-P. Zolésio. *Shapes and geometries: metrics, analysis, differential calculus, and optimization*. Society for Industrial and Applied Mathematics, 2001.
48. J.-P. Demailly. *Analyse numérique et équations différentielles*. EDP Sciences, 2016.
49. M. Demazure. *Catastrophes et bifurcations*. Ellipses Paris, 1989.
50. F. Denner and B. G. van Wachem. Numerical time-step restrictions as a result of capillary waves. *Journal of Computational Physics*, 285:24–40, 2015.
51. R. J. DiPerna and P.-L. Lions. Ordinary differential equations, transport theory and Sobolev spaces. *Inventiones Mathematicae*, 98(3):511–547, 1989.
52. J. Donea, S. Giuliani, and J. Halleux. An arbitrary Lagrangian-Eulerian finite element method for transient dynamic fluid-structure interactions. *Computer methods in applied mechanics and engineering*, 33(1):689–723, 1982.
53. V. Doyeux. *Modélisation et simulation de systèmes multi-fluides. Application aux écoulements sanguins.* Thèse de doctorat, Université Grenoble Alpes, 2014.
54. F. Dubois, V. Acary, and M. Jean. The contact dynamics method: A nonsmooth story. *Comptes Rendus Mécanique*, 346(3):247–262, 2018.
55. B. Engquist, A.-K. Tornberg, and R. Tsai. Discretization of Dirac delta functions in level set methods. *Journal of Computational Physics*, 207(1):28–51, 2005.
56. D. Enright, R. Fedkiw, J. Ferziger, and I. Mitchell. A hybrid particle level set method for improved interface capturing. *Journal of Computational physics*, 183(1):83–116, 2002.
57. S. Esedoglu, S. Ruuth, R. Tsai, et al. Diffusion generated motion using signed distance functions. *Journal of Computational Physics*, 229(4):1017–1042, 2010.
58. L. C. Evans and R. F. Gariepy. *Measure theory and fine properties of functions*. CRC Press, 1992.
59. L. C. Evans and J. Spruck. Motion of level sets by mean curvature. II. *Transactions of the American mathematical society*, 330(1):321–332, 1992.
60. C. Farhat, A. Rallu, and S. Shankaran. A higher-order generalized ghost fluid method for the poor for the three-dimensional two-phase flow computation of underwater implosions. *Journal of Computational Physics*, 227(16):7674–7700, 2008.
61. N. Favrie, S. Gavrilyuk, and S. Ndanou. A thermodynamically compatible splitting procedure in hyperelasticity. *Journal of Computational Physics*, 270(C):300–324, 2014.
62. N. Favrie, S. Gavrilyuk, and R. Saurel. Solid-fluid diffuse interface model in cases of extreme deformations. *Journal of Computational Physics*, 228(16):6037–6077, 2009.

63. N. Favrie and S. L. Gavrilyuk. Diffuse interface model for compressible fluid – Compressible elastic-plastic solid interaction. *Journal of Computational Physics*, 231(7):2695–2723, 2012.
64. M. Fernández, J.-F. Gerbeau, and C. Grandmont. A projection semi-implicit scheme for the coupling of an elastic structure with an incompressible fluid. *International Journal for Numerical Methods in Engineering*, 69(4):794–821, 2007.
65. M. A. Fernández. Coupling schemes for incompressible fluid-structure interaction: implicit, semi-implicit and explicit. *SeMA Journal*, 55(1):59–108, 2011.
66. M. A. Fernández. Incremental displacement-correction schemes for incompressible fluid-structure interaction. *Numerische Mathematik*, 123(1):21–65, 2013.
67. M. A. Fernández, J.-F. Gerbeau, and C. Grandmont. A projection algorithm for fluid–structure interaction problems with strong added-mass effect. *Comptes Rendus Mathematique*, 342(4):279–284, 2006.
68. M. A. Fernández and J. Mullaert. Convergence and error analysis for a class of splitting schemes in incompressible fluid–structure interaction. *IMA Journal of Numerical Analysis*, 36(4):1748–1782, 2015.
69. M. A. Fernández, J. Mullaert, and M. Vidrascu. Explicit Robin–Neumann schemes for the coupling of incompressible fluids with thin-walled structures. *Computer Methods in Applied Mechanics and Engineering*, 267:566–593, 2013.
70. M. A. Fernández, J. Mullaert, and M. Vidrascu. Generalized robin–neumann explicit coupling schemes for incompressible fluid-structure interaction: Stability analysis and numerics. *International Journal for Numerical Methods in Engineering*, 101(3):199–229, 2015.
71. C. Galusinski and P. Vigneaux. On stability condition for bifluid flows with surface tension: Application to microfluidics. *Journal of Computational Physics*, 227(12):6140–6164, 2008.
72. S. Gavrilyuk, N. Favrie, and R. Saurel. Modelling wave dynamics of compressible elastic materials. *Journal of Computational Physics*, 227(5):2941–2969, 2008.
73. M. Gazzola, P. Chatelain, W. M. Van Rees, and P. Koumoutsakos. Simulations of single and multiple swimmers with non-divergence free deforming geometries. *Journal of Computational Physics*, 230(19):7093–7114, 2011.
74. R. Glowinski, T. Pan, T. Hesla, D. Joseph, and J. Periaux. A fictitious domain approach to the direct numerical simulation of incompressible viscous flow past moving rigid bodies: application to particulate flow. *Journal of Computational Physics*, 169(2):363–426, 2001.
75. R. Glowinski, T.-W. Pan, T. I. Hesla, and D. D. Joseph. A distributed Lagrange multiplier/fictitious domain method for particulate flows. *International Journal of Multiphase Flow*, 25(5):755–794, 1999.
76. S. Godunov. *Elements of continuum mechanics*. Nauka Moscow, 1978.
77. J. Gomes and O. Faugeras. Reconciling distance functions and level sets. *Journal of Visual Communication and Image Representation*, 11(2):209–223, 2000.
78. Y. Gorsse, A. Iollo, T. Milcent, and H. Telib. A simple Cartesian scheme for compressible multimaterials. *Journal of Computational Physics*, 272:772–798, 2014.
79. C. Grandmont and Y. Maday. Fluid-structure interaction: a theoretical point of view. *Revue européenne des éléments finis*, 9(6–7):633–653, 2000.
80. A. Gravouil, N. Möes, and T. Belytschko. Non-planar 3D crack growth by the extended finite element and level sets - part II: level set update. *International Journal for Numerical Methods in Engineering*, 53:2569–2586, 2002.
81. B. E. Griffith and N. A. Patankar. Immersed methods for fluid – structure interaction. *Annual Review of Fluid Mechanics*, 52(1):421–448, 2020.
82. B. E. Griffith and C. S. Peskin. On the order of accuracy of the immersed boundary method: Higher order convergence rates for sufficiently smooth problems. *Journal of Computational Physics*, 208(1):75–105, 2005.
83. A. Harten, B. Engquist, S. Osher, and S. Chakravarthy. Uniformly high order essentially non-oscillatory schemes, iii. *Journal of Computational Physics*, 71(1):231–303, 1987.
84. F. Hecht. New development in freefem++. *J. Numer. Math.*, 20(3–4):251–265, 2012.
85. G. Holzapfel. *Nonlinear Solid Mechanics. A continuum approach for engineering*. J. Wiley and Sons, 2000.

86. H. H. Hu. Direct simulation of flows of solid-liquid mixtures. *International Journal of Multiphase Flow*, 22(2):335–352, 1996.
87. J. Janela, A. Lefebvre, and B. Maury. A penalty method for the simulation of fluid-rigid body interaction. In *ESAIM: Proceedings*, volume 14, pages 115–123. EDP Sciences, 2005.
88. M. Jedouaa. *Interface capturing methods for interacting immersed objects*. Thèse de doctorat, Université Grenoble Alpes, 2017.
89. M. Jedouaa, C.-H. Bruneau, and E. Maitre. An efficient interface capturing method for a large collection of interacting bodies immersed in a fluid. *Journal of Computational Physics*, 378:143–177, 2019.
90. G. Jiang and C. Shu. Efficient implementation of Weighted ENO schemes. *Journal of Computational Physics*, 126(1):202–228, 1996.
91. S. Kern and P. Koumoutsakos. Simulations of optimized anguilliform swimming. *Journal of Experimental Biology*, 209(24):4841–4857, 2006.
92. W. Kim and H. Choi. Immersed boundary methods for fluid-structure interaction: A review. *International Journal of Heat and Fluid Flow*, 2019.
93. R. Kimmel and J. A. Sethian. Computing geodesic paths on manifolds. *Proceedings of the national academy of Sciences*, 95(15):8431–8435, 1998.
94. D. J. Korteweg. Sur la forme que prennent les équations du mouvements des fluides si l'on tient compte des forces capillaires causées par des variations de densité considérables mais connues et sur la théorie de la capillarité dans l'hypothèse d'une variation continue de la densité. *Archives Néerlandaises des Sciences exactes et naturelles*, 6:1–24, 1901.
95. L. Lee and R. J. LeVeque. An immersed interface method for incompressible navier–stokes equations. *SIAM Journal on Scientific Computing*, 25(3):832–856, 2003.
96. R. J. Leveque and Z. Li. The immersed interface method for elliptic equations with discontinuous coefficients and singular sources. *SIAM Journal on Numerical Analysis*, 31(4):1019–1044, 1994.
97. P. Lubin and H. Lemonnier. Propagation of solitary waves in constant depths over horizontal beds. *Multiphase Science and Technology*, 16(1–3):237–248, 2004.
98. E. Maitre, T. Milcent, G.-H. Cottet, A. Raoult, and Y. Usson. Applications of level set methods in computational biophysics. *Mathematical and Computer Modelling*, 49(11):2161–2169, 2009.
99. E. Maitre, C. Misbah, P. Peyla, and A. Raoult. Comparison between advected-field and level-set methods in the study of vesicle dynamics. *Physica D: Nonlinear Phenomena*, 241(13):1146–1157, 2012.
100. E. Maitre and F. Santosa. Level set methods for optimization problems involving geometry and constraints ii. optimization over a fixed surface. *Journal of Computational Physics*, 227(22):9596–9611, 2008.
101. B. Maury. A many-body lubrication model. *Comptes Rendus de l'Académie des Sciences-Series I-Mathematics*, 325(9):1053–1058, 1997.
102. B. Maury. Direct simulations of 2D fluid-particle flows in biperiodic domains. *Journal of Computational Physics*, 156:325–351, 1999.
103. B. Merriman, J. K. Bence, and S. J. Osher. Motion of multiple junctions: A level set approach. *Journal of Computational Physics*, 112(2):334–363, 1994.
104. T. Metivet, V. Chabannes, M. Ismail, and C. Prud'homme. High-order finite-element framework for the efficient simulation of multifluid flows. *Mathematics*, 6(10):203, 2018.
105. T. Milcent. *Une approche eulérienne du couplage fluide-structure, analyse mathématique et applications en biomécanique*. Thèse de doctorat, Université Grenoble Alpes, 2009.
106. T. Milcent and E. Maitre. Eulerian model of immersed elastic surfaces with full membrane elasticity. *Communications in Mathematical Sciences*, 14(3):857–881, 2016.
107. G. Miller and P. Colella. A conservative three-dimensional Eulerian method for coupled solid-fluid shock capturing. *Journal of Computational Physics*, 183(1):26–82, 2002.
108. C. Min. On reinitializing level set functions. *Journal of computational physics*, 229(8):2764–2772, 2010.
109. J.-J. Moreau. Fonctionnelles convexes. *Séminaire Jean Leray*, (2):1–108, 1966.

110. J.-J. Moreau. Application of convex analysis to the treatment of elastoplastic systems. In *Applications of methods of functional analysis to problems in mechanics*, pages 56–89. Springer, 1976.
111. R. W. Ogden. Nonlinear elasticity, anisotropy, material stability and residual stresses in soft tissue. In *Biomechanics of soft tissue in cardiovascular systems*, pages 65–108. Springer, 2003.
112. S. Osher and R. Fedkiw. *Level set methods and dynamic implicit surfaces*, volume 153. Springer Science & Business Media, 2006.
113. C. S. Peskin. Numerical analysis of blood flow in the heart. *Journal of Computational Physics*, 25(3):220–252, 1977.
114. C. S. Peskin. The immersed boundary method. *Acta numerica*, 11:479–517, 2002.
115. C. S. Peskin and B. F. Printz. Improved volume conservation in the computation of flows with immersed elastic boundaries. *Journal of computational physics*, 105(1):33–46, 1993.
116. S. Popinet. Numerical models of surface tension. *Annual Review of Fluid Mechanics*, 50:49–75, 2018.
117. J. Qian, Y.-T. Zhang, and H.-K. Zhao. Fast sweeping methods for Eikonal equations on triangular meshes. *SIAM Journal on Numerical Analysis*, 45(1):83–107, 2007.
118. T. Richter. A fully Eulerian formulation for fluid-structure-interaction problems. *Journal of Computational Physics*, 233:227–240, 2013.
119. T. Richter. *Fluid-structure interactions: models, analysis and finite elements*, volume 118. Springer, 2017.
120. R. Ruiz-Baier, A. Gizzi, S. Rossi, C. Cherubini, A. Laadhari, S. Filippi, and A. Quarteroni. Mathematical modelling of active contraction in isolated cardiomyocytes. *Mathematical Medicine And Biology-A Journal Of The Ima*, 31(3):259–283, 2014.
121. G. Russo and P. Smereka. A remark on computing distance functions. *Journal of Computational Physics*, 163(1):51–67, 2000.
122. A. Sengers. *Schémas semi-implicites et de diffusion-redistanciation pour la dynamique des globules rouges*. Thèse de doctorat, Université Grenoble Alpes, 2019.
123. J. A. Sethian. A fast marching level set method for monotonically advancing fronts. *Proceedings of the National Academy of Sciences*, 93(4):1591–1595, 1996.
124. J. A. Sethian. Fast marching methods. *SIAM review*, 41(2):199–235, 1999.
125. J. A. Sethian. *Level set methods and fast marching methods: evolving interfaces in computational geometry, fluid mechanics, computer vision, and materials science*, volume 3. Cambridge university press, 1999.
126. N. Sharma and N.-A. Patankar. A fast computation technique for the direct numerical simulation of rigid particulate flows. *Journal of Computational Physics*, 205(2):439–457, 2005.
127. Y. Shen and G. Zha. Improvement of the WENO scheme smoothness estimator. *International Journal for Numerical Methods in Fluids*, 64(6):653–675, 2010.
128. D. Shiels, A. Leonard, and A. Roshko. Flow-induced vibration of a circular cylinder at limiting structural parameters. *Journal of Fluids and Structures*, 15(1):3–21, 2001.
129. C.-W. Shu. High order ENO and WENO schemes for computational fluid dynamics. In *High-order methods for computational physics*, pages 439–582. Springer, 1999.
130. P. Smereka. The numerical approximation of a delta function with application to level set methods. *Journal of Computational Physics*, 211(1):77–90, 2006.
131. V. A. Solonnikov. Estimates for solutions of nonstationary Navier–Stokes equations. *Journal of Mathematical Sciences*, 8(4):467–529, 1977.
132. J. M. Stockie and B. R. Wetton. Analysis of stiffness in the immersed boundary method and implications for time-stepping schemes. *Journal of Computational Physics*, 154(1):41–64, 1999.
133. J. M. Stockie and B. T. Wetton. Stability analysis for the immersed fiber problem. *SIAM Journal on Applied Mathematics*, 55(6):1577–1591, 1995.

134. K. Sugiyama, S. Li, S. Takeuchi, S. Takagi, and Y. Matsumoto. A full Eulerian finite difference approach for solving fluid-structure coupling problems. *Journal of Computational Physics*, 230:596–627, 2011.
135. M. Sussman and E. Fatemi. An efficient, interface-preserving level set redistancing algorithm and its application to interfacial incompressible fluid flow. *SIAM Journal on scientific computing*, 20(4):1165–1191, 1999.
136. M. Sussman, P. Smereka, and S. Osher. A level set approach for computing solutions to incompressible two-phase flow. *Journal of Computational physics*, 114(1):146–159, 1994.
137. M. Sy, D. Bresch, F. Guillén-González, J. Lemoine, and M. A. Rodríguez-Bellido. Local strong solution for the incompressible Korteweg model. *Comptes rendus Mathématique*, 342(3):169–174, 2006.
138. E. Toro, M. Spruce, and W. Speares. Restoration of the contact surface in the HLL-Riemann solver. *Shock Waves*, 4:25–34, 1994.
139. J. D. Towers. Two methods for discretizing a delta function supported on a level set. *Journal of Computational Physics*, 220(2):915–931, 2007.
140. J. D. Towers. A convergence rate theorem for finite difference approximations to delta functions. *Journal of Computational Physics*, 227(13):6591–6597, 2008.
141. J. D. Towers. Discretizing delta functions via finite differences and gradient normalization. *Journal of Computational Physics*, 228(10):3816–3836, 2009.
142. J. D. Towers. Finite difference methods for approximating heaviside functions. *Journal of Computational Physics*, 228(9):3478–3489, 2009.
143. S. Turek and J. Hron. Proposal for numerical benchmarking of fluid-structure interaction between an elastic object and laminar incompressible flow. *Lecture notes in computational science and engineering, Springer Verlag*, 2006.
144. B. Valkov, C.-H. Rycroft, and K. Kamrin. Eulerian method for multiphase interactions of soft solid bodies in fluids. *Journal of Applied Mechanics*, 82(4):041011, 2015.
145. B. Vowinckel, J. Withers, P. Luzzatto-Fegiz, and E. Meiburg. Settling of cohesive sediment: particle-resolved simulations. *Journal of Flui Mechanics*, 858:5–44, 2010.
146. J. Walter, A.-V. Salsac, D. Barthès-Biesel, and P. Le Tallec. Coupling of finite element and boundary integral methods for a capsule in a stokes flow. *International journal for numerical methods in engineering*, 83(7):829–850, 2010.
147. M. Y. Wang and X. Wang. "Color" level sets: a multi-phase method for structural topology optimization with multiple materials. *Computer Methods in Applied Mechanics and Engineering*, 193(6):469–496, 2004.
148. H. Zhao. A fast sweeping method for Eikonal equations. *Mathematics of computation*, 74(250):603–627, 2005.
149. H. Zhao, J. B. Freund, and R. D. Moser. A fixed-mesh method for incompressible flow-structure systems with finite solid deformations. *Journal of Computational Physics*, 227:3114–3140, 2008.
150. H.-K. Zhao, T. Chan, B. Merriman, and S. Osher. A variational level set approach to multiphase motion. *Journal of computational physics*, 127(1):179–195, 1996.